Seismic Evidence for Hydrocarbon Migration

Martino Foschi

Submitted in partial fulfilment of the

requirements for the Degree of Philosophiae Doctor

Cardiff University

September 2014

DECLARATION

This work has not been submitted in substance for any other degree or award at this or any other university or place of learning, nor is being submitted concurrently in candidature for any degree or other award.

Signed …… (candidate) Date ……

STATEMENT 1

This thesis is being submitted in partial fulfillment of the requirements for the degree of ……(insert MCh, MD, MPhil, PhD etc, as appropriate)

Signed …… (candidate) Date ……

STATEMENT 2

This thesis is the result of my own independent work/investigation, except where otherwise stated.

Other sources are acknowledged by explicit references. The views expressed are my own.

Signed …… (candidate) Date ……

STATEMENT 3

I hereby give consent for my thesis, if accepted, to be available for photocopying and for inter-library loan, and for the title and summary to be made available to outside organisations.

Signed …… (candidate) Date ……

STATEMENT 4: PREVIOUSLY APPROVED BAR ON ACCESS

I hereby give consent for my thesis, if accepted, to be available for photocopying and for inter-library loans **after expiry of a bar on access previously approved by the Academic Standards & Quality Committee.**

Signed …… (candidate) Date ……

"Overhead the albatross hangs motionless upon the air
and deep beneath the rolling waves in labyrinths of coral caves
the echo of a distant tide
comes willowing across the sand
and everything is green and submarine…"

[Echoes - Waters, Wright, Mason, Gilmour - 1970]

Abstract

The migration of hydrocarbons on formation and accumulation on commercially viable oil and gas deposits/reserves/reservoirs. Reflection 2D/3D seismic data can be used to identify the position of these fluids in the subsurface and analyse their habitat and pathways in the context of the basin architecture. A multichannel reflection 2D seismic dataset from a large area offshore Falkland Islands (South American Plate) was analysed to interpret direct hydrocarbon indicators (DHIs) and basin architecture with the aim to find a link between these two elements.

The first results of this research work have led to the definition of a new class of hydrocarbon indicator, here called vertical anomaly cluster (VAC) and observed in the east Falkland Basin. A VAC represents a group of individual hydrocarbon occurrences linked by a vertical migration of hydrocarbons within fine-grained sequences. VACs are interpreted to be low-impact fluid flow phenomena where the migration process exploits pre-existing permeability structures.

In the second part of this research a suite of DHIs, including bottom simulating reflections (BSR), enhanced reflections, pipes, gas chimneys and flat spots have been analysed in the South Falkland Basin. The work demonstrates a significant link between the style of the migration and basin features. In particular it is observed that vertical migration phenomena such as pipes and gas chimneys are clearly linked to the secondary structural features of the basin while the gas hydrate system, composed of BSR and enhanced reflections, is more controlled by primary depositional features. The presence of a mature source rocks suggests that the fluids involved in the formation of the observed DHIs are of thermogenic origin.

The third part of this research was focussed on the analysis of depression structures located in the North east Falkland Basin. The basin hosts other DHIs, such

as VACs, gas chimneys and pipes. The depression structures propagate in depth and are associated with material withdrawal. These structures have therefore been interpreted as mud volcano conduits. The lack of mud edifices has been tentatively interpreted to be related with seabed erosion operated by bottom currents active in the study area. The fluids involved in the withdrawal of the material are interpreted to be related to hydrocarbon generation and expulsion.

The comparison between the results of this research with the wider literature has been used to propose a classification where the style of the migration process and the DHIs are linked to the permeability architecture of the basin. Two styles of DHIs have been defined: (1) permeability-controlled DHIs, derived essentially from low impact migration processes acting in a pre-existing permeability structure (e.g.: VACs, enhanced reflection and BSR), and (2) fluid-controlled DHIs, derived from migration processes able to generate the migration pathways (e.g. pipes, mud volcanoes). Two speculative and, at the time of this research, not tested hypotheses have been proposed to justify the style of the migration process.

The first hypothesis suggests that the style of the migration process is directly linked to the geometry of the deep structures where the hydrocarbon fluids are focussed in relatively small areas. These areas are suggested to be located at structural highs. Once the fluid is focussed in this region then the vertical migration is believed to not be sensitive to barrier and seals within the overlying lithologies. This hypothesis is consistent with the position of fluid-controlled DHIs (e.g. pipes and MVs) at the margin of the hydrocarbon plumbing systems and where the basement structures are relatively shallower. DHIs located in the inner regions are instead of the type sensitive to the permeability structures.

The second hypothesis suggests that the style of the DHIs is function of the time. Hence in this hypothesis, assuming a given region of active fluid migration, the first DHIs to be generated are simple amplitude anomalies which then evolve to VACs. If the migration of hydrocarbons is still active the probable condition of high saturation may trigger some failure within the hosting lithologies and the formation of additional pathways. The newly generated permeability structure may finally be consistent with the one of more dramatic DHI style, such as mud volcanoes.

Author's notes

Thesis Format

The manuscript has been formatted following the rules in force at the Cardiff University. The figures are located at the end of the relative Chapter. The Matlab codes developed during the PhD Course and a number of results and raw images are available electronically on the CD-ROM present in the last page of this manuscript.

Dataset

The present manuscript has been based on a large multi-channel 2D seismic dataset composed of two surveys. The first survey was provided by Geophysical Service Incorporated (GSI, Calgary) and the second by Falkland Oil & Gas Limited (FOGL, London).

The GSI dataset has been loaded with a delay of 9 months with respect to the start of the PhD Course. During this period I developed a number of Matlab applications which have been used during the PhD Course. The FOGL dataset has been requested and successfully loaded during the third year of the PhD Course and allowed to improve the results of two different case studies. These factors have produced substantial changes in the definition of the final structure of the thesis. A chronology of the datasets used during the PhD Course is synthesised in Table α and in Figure π.

Table α Dataset chronology

PhD year	Date	Description	Line colour (Figure π)
1	1st October 2010	Start of the PhD Course	
	4th July 2011	GSI dataset loading. Partial loading of the 2D seismic lines (a subset of the entire GSI lines was missing/not correctly loaded). Use of the GSI dataset at 4s TWT.	black
3	7th January 2013	GSI dataset re-loading and FOGL dataset loading. A complete re-loading of the GSI dataset was done. Complete loading of the FOGL dataset. Use of the FOGL dataset limited at 4s TWT.	red
4	11th March 2014	Partial permission to use FOGL lines over 4s TWT.	green
4	August 2014	Partial permission to use GSI lines over 4s TWT.	blue

Publications

The results of Chapter 3 have been published as: Foschi, M., Cartwright, J. A., Peel, F. J., 2014. Vertical anomaly cluster: evidence for vertical gas migration across multi-layered sealing sequence. American Association of Petroleum Geologists Bulletin, V. 98, No. 9 (September 2014), P. 1859–1884. DOI: 10.1306/04051413121.

Presentations

A number of poster sessions and presentations have been presented at the Cardiff University during the PhD Course. A number of technical presentations have been presented and discussed with the providers of the seismic data and with the companies sponsoring this PhD Course.

Chapter 3 has been presented at two international conferences: (1) AAPG International Conference and Exhibition, 2012 (Singapore), and (2) AAPG-EAGE Geotechnical Workshop, 2013 (Kuala Lumpur).

Some of the results present in Chapter 4 have been presented at the EAGE Workshop, 2014 (Malta).

Other works

During the 3rd year of my PhD Course I have written a chapter of an atlas focussed on the interpretation of direct hydrocarbon indicators (DHIs) and sponsored by the Cap Rock Group. The chapter focuses on the rock physics and on the methodologies to interpret amplitude anomalies and DHIs.

Career progress

On 1st March 2014 I started to work as Post-Doctoral Research Associate (PDRA) at University of Oxford with my supervisor Professor Joe Cartwright.

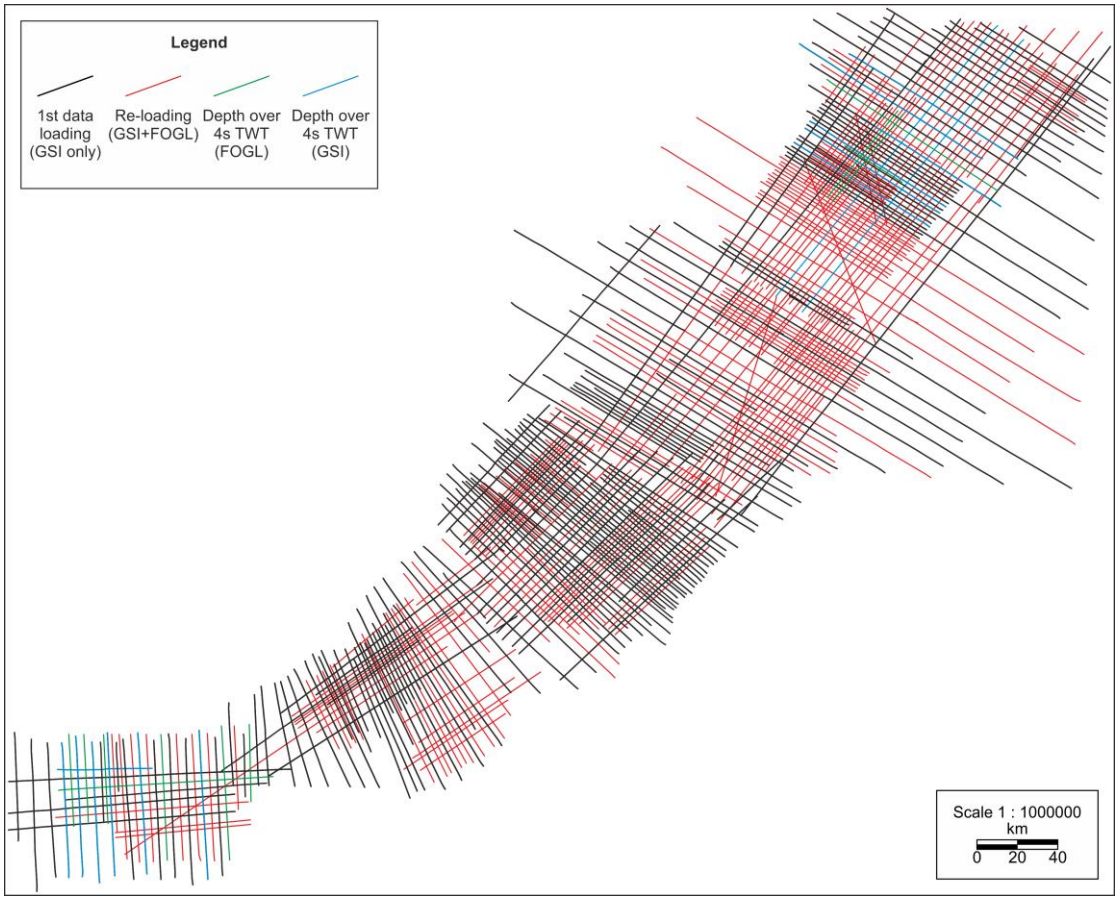

Figure π. 2D seismic grid.

Acknowledgements/Ringraziamenti

During the PhD Course a large number of people constructively contributed to the achievements of this important objective. I would like to thank my main supervisor Professor Joe Cartwright which became an irreplaceable friend and one of the most important people of my life. His knowledge and his guidance lead me to improve in all the aspects of the research methods and allowed me to continue my career in the Academia. I'm grateful with my co-supervisors Frank Peel and Tiago Alves for their suggestion and comments on my work.

I'm really grateful with my sponsor BHP Billiton Petroleum which allowed me to start my PhD Course and complete this project. I'm indebted with Paul Einarsson, COO and Chairman of Geophysical Service Inc., Colin More, Exploration Director at Falkland Oil & Gas Limited, and Noble Energy Inc. and Edison Spa for their support as data providers. I'm grateful with Gwen Pettigrew for the immense IT support at the 3D Lab. I would like to say thanks also to the administrative staff working at Cardiff University and to the people working to make the main building of the Cardiff University a safe place to work.

Thanks go to my colleagues and scientists working at Cardiff University. Huge thanks go to Aldina, Duarte and Maggi which have been always present during my life in Cardiff. Special thanks go to my officemates Ana, Bledd, Chris, David, Iqbal, Kamal and Oluci which helped me to survive during the boring office life. I also say thanks to Ben, Chris, Dan, Hamood, Peter, Tuviere, Usman and all other researchers from past years.

Thanks go to my colleagues at University of Oxford which helped me to settle in the university and in a new city. Thanks go to Claudia for her fundamental help in

reviewing part of this manuscript. Thanks go to Matteo and to the other people of the Shell Group for their outstanding support and experience. Thanks go to my new officemates Graeme, Melanie, Melissa and Phil.

I ringraziamenti piu importanti li vorrei scrivere nella lingua di *Dante*…

Grazie Katia per tutto l'amore che mi hai dato in questi anni. Grazie per tutto il supporto che sei stata capace di offrirmi come moglie, amante, amica, confidente. Grazie per avermi aiutato nei giorni complicati, nei fine settimana passati a lavorare e per aver sopportato molte delle mie dimenticanze. Grazie per avermi avuto nei tuoi pensieri nei periodi di lontanaza e grazie per avermi fatto sentire amato come da nessuna altra persona in questo mondo.

Grazie ai miei genitori, Stefania e Davide, senza i quali non avrei potuto studiare e maturare le mie passioni. Grazie ai miei fratelli, Simone e Daniele, per avermi sempre supportanto nei momenti in Italia e per avermi fatto sentire sempre presente nella vostra vita nonostante la lontananza. Grazie a Manuela e Greta e grazie alle piccole Adele e Viola per aver riempito la nostra Famiglia di gioia e felicita'.

Table of Contents

List of Figures

List of Tables

1. Introduction

1.1. Introduction and rationale

Direct hydrocarbon indicator (DHI) is a term, firstly used by Barry and Shugart (1974) and Millahn et al. (1978), to define specific responses observable on seismic data which are directly indicative of the presence of hydrocarbons. DHIs play a fundamental role in fossil-fuels exploration because they can provide the position of hydrocarbons in the subsurface. The identification and the study of the distribution of hydrocarbons, in association with the stratigraphic and structural features of the basin, may indicate the presence of an active proliferous basin (Andresen et al., 2011) and potentially lead to hydrocarbon discoveries.

DHIs exhibit on seismic data different responses which have been labelled in the last 40 years with different terms (e.g. bright-spot, introduced by Hammond, 1974 or Rutherford and Williams, 1989, among others). The identification of DHIs passes through the seismic interpretation which has, among others, the important objective to discriminate DHIs within a wide range of similar seismic responses. In the last decades, the identification and interpretation of DHIs became more sophisticated by introducing good quality seismic data and especially by developing a number of quantitative techniques to identify, with fewer uncertainties, potential occurrences of hydrocarbons (Mavko et al., 2009).

The increased quality of 2D and 3D seismic data, in association with their wider availability, favoured, among other studies, the research on hydrocarbon migration and hydrocarbon plumbing systems (Cartwright and Huuse, 2005; Cartwright et al., 2007). However, if on one hand a wide number of hydrocarbon migration indicators have been identified in different settings, on the other hand these indicators revealed a poor understanding of the phenomena associated with the migration of

hydrocarbon (Moss and Cartwright, 2010).A large number of works focussed on fluid flow and hydrocarbon migration used successfully the seismic methods to describe DHIs and the hydrocarbon migration processes (e.g. Andresen, et al., 2011; Barry and Shugart, 1974; Cao and Ye, 2011; Cartwright et al., 2007; Clarke et al., 2006; Gorman et al., 2002; Gray et al., 2001; Heggland, 1997; Henriet et al., 1991; Ilg et al., 2012; Jin et al., 2008; Li et al., 2007; Rise et al., 1999; Rollet et al., 2012; Taylor et al., 2000; Xie et al., 2003). The seismic methods, although characterised by limited resolution and poor identification of deep DHIs (Brown, 2004), maintain the ability to describe large scale phenomena and study DHIs in the context of the basin.

The present research work is based on the interpretation and analysis of seismic data. The seismic data is primarily used to detect the position of the hydrocarbon occurrences and define the main characteristics of the studied basin. A detailed definition of these two elements for each studied basin represents the first objective of this research work. The second objective is then to link acoustic characteristics and distribution of the DHIs with the basin architecture. In particular this second objective aims to (1) find any link that can justify the position of the DHIs with respect to the structural and stratigraphical features of the basin, (2) correlate the style of the DHIs with the local migration processes, and (3) correlate the migration processes with the basin architecture.

1.2. Background

The difficulty in finding hydrocarbons by using seismic methods is that DHIs may exhibit different seismic responses, which may or may not be indicative of the presence of hydrocarbons. The most common seismic responses potentially indicative of the presence of hydrocarbons are here documented following the terminology and the descriptions found in scientific literature.

1.2.1. Amplitude anomalies

Seismic amplitude anomaly, or amplitude anomaly (AA), is a general term used to indicate a local increase of acoustic amplitude observable on 2D and 3D seismic data and caused by any reason (Løseth et al., 2009; Sheriff, 1975; Sheriff and Geldart, 1982). Amplitude anomalies associated with increasing amplitude can be named bright amplitude or bright spot. The increase in amplitude can be associated with positive and negative polarities. One of the first images depicting a bright spot on seismic data was documented by White (1977; Figure 1.1).

A decrease in amplitude of both polarities which occurs along a given reflection and caused by any reason is termed dim spot (Brown, 2004; Sheriff, 1975) or dim amplitude (Løseth et al., 2009). Dim spots are as important as bright spots, however they are more complicated to detect on seismic data (Avseth et al., 2009). Bright-spots and dim-spots are often improperly interpreted, especially in oil industries, as indicators of the presence of hydrocarbons (Avseth et al., 2009).

The background amplitude observed on seismic data represents the reference value to discriminate whether a local change in amplitude is associable to an anomaly (Mavko et al., 2009; Sheriff, 1975). At different depth or on different

seismic data, this relationship changes the way to understand if an observed amplitude variation is potentially an amplitude anomaly or not (Brown, 2004).

The main factors that may produce an amplitude anomaly are (1) local variations in lithology, fabric, and diagenesis, (2) presence of compressible fluids (e.g. hydrocarbons), (3) bioturbation, (4) chemical reactions , and (5) overpressure (e.g. Brown, 2004; Mavko et al., 2009; Sheriff, 1975). Other factors not related to geological reasons may affect the seismic response and produce amplitude anomalies. These are mainly associated with acquisition parameters (instruments, array directivity, offset or angle, etc.) and processing (gain control, geometrical spreading correction, migration, etc.).

The amplitude anomalies are often associated with other effects observable on seismic data, such as attenuation, scattering and push down. The attenuation, or more precisely the total wave amplitude attenuation, during the travel in a porous saturated media, is caused by two different processes: matrix loss and fluid loss (Biot, 1962, Mavko et al., 2009, Othman, 1994). Matrix loss is caused by two main causes: (1) grain-grain friction and (2) grain-grain detachments of fluid-induced chemical cementation. Fluid loss is due to relative fluid movement in the solid matrix (Othman, 1994). Any material heterogeneity (point-like, interfaces, etc.) causes a wavefield to be scattered (Huygens principle). The parameters governing the kind of scattering are the wavenumber (or wavelength), the correlation length of the scatters and the propagation distance in the scattering medium. The push down effect is an effect of the presence of fluids which delay the velocity of the seismic waves producing on seismic data an apparent bending which can be observed below amplitude anomalies (e.g. Sheriff, 1975).

1.2.1.1. Amplitude anomaly caused by hydrocarbons

Of particular interest are the amplitude anomalies caused by the presence of hydrocarbons (DHIs). The hydrocarbons on seismic data are visible because of their interaction with the porous rock and the pore fluids. Why?

The seismic data are composed of a number of traces which are the result of the convolution between a source wavelet and a series of numbers named reflection coefficient.

$$trace = W \otimes RC + noise$$

The reflection coefficients are associated with the properties of the rocks and in particular with the product of the velocity and density. This product is named acoustic impedance. For normal incident compressional waves the reflection coefficient associated with two different rocks is expressed as

$$RC = \frac{\rho_2 V_2 - \rho_1 V_1}{\rho_2 V_2 + \rho_1 V_1}$$

If the acoustic impedance of the rocks is increasing downward the polarity of the reflection coefficient will be positive and named hard reflection (e.g. seabed, Opal A-CT transition, etc.). If the acoustic impedance of the rocks is decreasing downward the reflection coefficient will be negative and named soft reflection (e.g. shallow DHIs, base of the gas hydrate stability zone, etc.). The compressional velocity Vp and the shear velocity Vs are defined as:

$$V_p = \sqrt{\frac{K+\frac{4}{3}\mu}{\rho}} \qquad V_s = \sqrt{\frac{\mu}{\rho}}$$

, where K is the bulk modulus, μ is the shear modulus and ρ is the density. Most of the rocks in the shallow lithosphere are porous and the pores spaces are filled with fluids (water-wet). The fluids in the pore spaces contribute to the elastic behaviour of the rock incrementing the incompressibility. The variable that is more sensitive to the properties of the fluids is therefore the bulk modulus K (e.g. Mavko et al., 2009). The density is also sensitive but much less respect to the bulk modulus. The shear modulus is not sensitive since the fluids do not support the shear stress. For this reason the shear velocity is just slightly affected by the presence of fluids.

Why do the hydrocarbons produce an amplitude anomaly? The elastic properties of the hydrocarbons (especially gas) are different with respect to the elastic property of the stratal water. If we replace the stratal water with hydrocarbons in a given portion of a porous medium, the change of the bulk modulus K will locally change the velocity of the seismic wave. The change in velocity will affect the acoustic impedance of the rock and finally the reflection coefficients. This cascade of events is the basis for the generation of an hydrocarbon related amplitude anomaly on seismic data.

1.2.2. Gas chimneys, pipes and other ensembles of amplitude anomalies

The amplitude anomalies described above represent a single seismic element which is, in the vast majority of the cases, a single component of more complex seismic features. A description of the most important groups or ensembles of amplitude anomalies is provided.

The term *seismic chimney* has been introduced by Heggland (1997) to indicate on seismic data a region where the seismic amplitude and phase of the reflections is distorted. Seismic chimneys were defined to be associated with upward migrating fluids. Bjørkum et al (1998) introduced the term *gas chimney* indicating a focal point of upward movement of fluids but interpreted to be mostly associated with exsolution of gas from upward migrating pore-water. After 1998 many authors started to use the term seismic, or gas, chimney to indicate a wide range of seismic responses predominantly characterised by disruption and distortion of the reflectivity pattern and potentially interpretable as associated with different fluid flow processes and not necessarily associated with hydrocarbons (Aminzadeh et al., 2001; Arntsen et al., 2007; Arts and Vandeweijer, 2013; Cathles et al., 2010; Hashemi et al., 2008; Li et al., 2009; Loncke and Mascle, 2004; Meldahl et al., 2001; Petersen et al., 2010; Sun et al., 2012) (Figure 1.2). In this thesis the term gas chimney is defined, following the descriptions of Heggland (1997), as a region of disturbance characterised by distortion of amplitude and phase of the reflections.

Pipes are defined as vertical to subvertical columnar zones of disturbed reflections (Gay et al., 2007- 2012; Leduc et al., 2013; Løseth et al., 2011; Sun et al., 2013) (Figure 1.3). They may exhibit vertically stacked amplitude anomalies with higher amplification with respect to the background reflectivity (Cartwright et al., 2007). Pipes can be divided in dissolution pipe, hydrothermal pipe, blowout pipe and seepage pipe. Of particular interest are those pipes where the migrating fluids comprise hydrocarbons. Pipes allow vertical migration of fluids across low-permeability sediments and for this reason they represent seal-by-pass systems (Cartwright et al., 2007). Pipes size may range in height and diameter from tens of metres to some kilometres and are commonly circular to subcircular in planview (3D

seismic data). The regions surrounding the pipe is often associated with seismic artefacts such as residual noise from migration operation ("smiles"), scattering, attenuation and diffraction (Løseth et al., 2011; Davies, 2003; Cartwright et al., 2007).

Dissolution pipes are observed in areas of evaporite or carbonate rocks. They form by the dissolution of rock which is observed on seismic data as strong reflection attenuation (e.g. Bertoni and Cartwright, 2005). Hydrothermal pipes are associated with igneous intrusions (e.g. sills, laccoliths), and form by the release of hydrothermal fluids (Davies et al., 2002; Svenson et al., 2003). Blowout pipes were first described by Løseth et al (2009) in a basin in the Nigerian continental margin. Blowout pipe may generate from the rapid breaching of top seals on shallow gas accumulations (Løseth et al., 2009). Seepage pipes may appear as blowout pipes but they do not exhibit blowout crater (Cartwright et al., 2007). For this reason seepage pipes are believed to be generated by slow migration of fluids (Løseth et al., 2003).

Mud volcanoes (MVs) are structures associated with the migration and expulsion of sediments and fluids to the Earth's surface (Andresen et al., 2010; Davies and Stewart, 2005; Dimitrov, 2002; Etiope et al., 2009; Graue, 2000; Loncke and Mascle, 2004; Mastalerz et al., 2007; Medialdea et al., 2009; Milkov, 2000; Planke et al., 2003; Prinzhofer and Deville, 2013; Somoza et al., 2012; Stadnitskaia et al., 2008; Stewart and Davies, 2006; Westbrook and Smith, 1983) (Figure 1.4). They can be related to the migration of thermogenic fluids, such as oil and gas, and so can represent a type of seep or leakage phenomenon associated with proliferous basins (Etiope et al., 2009). On the surface, they may produce positive structures characterised by a conical shape. In other cases, they may produce depressions due to the expulsion of the remobilised material and subsequent collapse of the

overburden (Somoza et al., 2012). MVs characterised by bi-conic structures are common and are due to multiple stages of expulsion and collapsing (Stewart and Davies, 2006). Mud volcanoes may or may not present amplitude anomalies which may indicate residual gas phases trapped during the expulsion of mud and other fluids.

1.2.3. Gas hydrates

Gas hydrates are a water rigid structure (ice) with enclosed hydrocarbon, gas and other fluids (Hustoft, 2007). 99% of the natural gas hydrate is methane (Max and Lowrie, 1996). Gas hydrate is produced by bacterial activity within the GHSZ (gas hydrate stability zone), but for many authors, only a small percentage of the total amount. Gas migration and recycling can product the larger amount of gas which is subsequently stored in GHSZ (Clennel, 2000, Demirbas, 2010).

The gas hydrate likely occurs in the free pore space of shallow soft sediment. Porosity, pore size and permeability play a key role in movement and concentration of gas hydrate (Dillon et al., 1997). Gas hydrate can occlude the gas migration because it reduces the porosity of the host medium. Condition of gas hydrate presence is due to focused gas flow and favourable thermodynamic condition (low T and high P).

Bottom-simulating reflector (BSR) is the transition that is present between the rich solid gas hydrate sediment above and little concentrated gas sediment below (Foucher et al., 2002). The BSR detection and description, as the gas in the sediment, is carried out by interpretation of seismic data (Pecher et al., 2001). The BSR shows negative amplitude due to a change of seismic wave velocity: the presence of gas bubble (low velocity) and the presence of crystal-ice (twice as the velocity of the

shallow sediment). Some important features that describe the BSR in seismic data are (1) mimics the profile of the seabed, (2) depth to BSR increase in deep seabed and (3) it cross-cuts the stratigraphic horizons (e.g. Andresen and Huuse, 2011; Bünz and Mienert, 2004; Bünz et al., 2003; Calvès et al., 2008; Carcione and Tinivella, 2000; Gay et al., 2006; Grauls, 2001; Haacke et al., 2007; Holbrook et al., 1996; Horozal et al., 2009; Hovland et al., 2005; Hustoft et al., 2009; Pecher et al., 2001; Petersen et al., 2010; Popescu et al., 2006; Popescu et al., 2007; Shankar and Riedel, 2013; Sun et al., 2012; Tinivella and Giustiniani, 2013; Yoo et al., 2013) (Figure 1.5).

The BSR is a very delicate transition that changes position very frequently. The physical parameters that lead to this behaviour are T and P within the sea-floor sediment. In a static physical condition the BSR depth is a function of the gas chemistry. Every event like fault (e.g. water injection), diapir (thermal conduit, ions dissociation, etc.), mud-injection can change the stability, the position and the continuity of the BSR (Hustoft et al., 2009; Pecher et al., 2001). A usual event that changes the position of the BSR is the bathymetric variation that can change T and P conditions in the shallow sediment. When the sea bottom changes its shape in upward (accretionary margin, salt diapir, sedimentation, etc.) or downward movement (slope failure, erosion, etc.), the change of physical condition can be very quick and in the order of 10.000years (Liu and Flemings, 2007). The new T-P conditions can yield the formation of a new GHSZ and the destruction of the previous GHSZ. During this long-time process, more than one BSR may be detected (Foucher et al., 2002). In some works, a multi-BSRs system composed by 4-5 BSR has been reported (Popescu et al., 2006). The detection of more BSRs is also due to a permanent change of the host sediment yielded by chemical alteration. If T (or P)

falls gas can ex-solve as bubble (effervescence). The opposite effect can occur if the pressure increases (evanescence). It may occur a supersaturation pre-phase before the nucleation of gas (bubble in water; Clennel, 2000). The quick release of gas (effervescence) due to a change of the GHSZ condition may trigger the slope failure in unstable sea floor (Berndt et al, 2005; Sultan et al., 2004).

1.2.4. Fluids, porous media and plumbing systems

The documented seismic features are the response of two key constituents, fluids and porous media. A brief background of fluids, porous media and their role in the plumbing systems is provided.

1.2.4.1. Fluids

The fluids involved in hydrocarbon migration are brine, or stratal water, and hydrocarbons (England et al., 1987). Crude oil is a flammable, viscous liquid, primarily of dark colour. It comprises a complex mixture of hydrocarbons of the following groups: methane (paraffin) - C_nH_{2n+2} (alkanes); naphthene – $C_n H_{2ni}$ (alkynes); aromatic C_nH_{2n-6} (arenes). The major methane-group (methane CH_4; ethane C_2H_6; propane C_3H_8; butane C_4H_{10}) is in a gaseous state at atmospheric pressure and normal temperature. Pentane C_5H_{12}, hexane C_6H_{14} and heptane C_7H_{16} are unstable, as they pass easily from gaseous to liquid state and vice versa. Hydrocarbons with their variations from C_8H_{18} to $C_{17}H_{36}$ are liquids. Hydrocarbons with more than 17 carbon atoms are solids (e.g. paraffin). An “average” crude oil contains about 82-87% carbon, 11-14% hydrogen, oxygen, nitrogen, sulphur,

carbonic acid and less of chlorine, iodine, phosphorus, arsenic and other metals and salts (Mullins and Sheu, 1999).

The hydrocarbons in general can be roughly divided in a gas phase, such as methane, and a liquid phase, the oil. The hydrocarbons are composed of thousands different components that change continuously the property as function of pressure and temperature (England et al., 1987). These parameters are mainly controlled by temperature and pressure which may or may not be depth related.

The water properties depend on the chemical component(s) in solution and on pressure and temperature. The stratal water may contain different components and dissolved minerals. For every T-P condition the water can include gas (e.g. methane) with different concentration in parts per million (ppm). Gas in water can move faster than a two-fluid flow system (Bear and Braester, 1972; Mavko et al., 2009).

The presence of gas (gas accumulation and gas hydrate) changes permanently the chemical composition of the sediment (Foucher et al., 2002). The precipitation and bacterial activity alteration in the sediment can show the same seismic response for a long time even after the complete migration of gas from that area (Francis, 1997; Dillon, 2000). This important chemical change in gas-sediment system is for instance the cause of the multi-BSR theory (Foucher et al, 2002; Popescu et al., 2006). Chemical transitions in the sediments can lead to fluid migration. Long lasting focused seeps can produce biogenic activity (bioherms, shell banks, etc.) that is visible on the water-bottom (Løseth et al., 2009).

1.2.4.2. Porous media

The porous media represents the solid frame where the migration processes take place. The porous media can be imaged as a system (porous system) where the

different geological bodies play different roles during the migration process. When a fluid is travelling in a porous media, a number of hydraulic processes are involved. Regardless of the description of stratigraphic and structural features, many of these processes are led by both physical properties of the medium and fluid(s). The main properties of the porous system (or mediums) are porosity, permeability and pore-shape (Bear and Braester, 1972). These properties are affected by different factors such as lithology, sorting, grain size and shape, diagenesis, cementation, confining pressure and temperature (Mavko et al., 2009).

Porosity

The porosity φ is the ratio between void space U_v and bulk volumeU_b, and is expressed by

$$\varphi = U_v/U_b = (U_b - U_s)/U_b$$

where, U_s is the volume of the solid part within U_b (Bear and Braester, 1972). The permeability is a property of a porous medium that allows the fluid to move through the pore spaces. From Kozeny-Carmen relation the permeability κ is expressed by

$$\kappa = B\frac{(\varphi - \varphi_c)^3}{(1 + \varphi_c - \varphi)^2}d^2$$

, where, φ is the porosity, φ_c is the percolation porosity (the porosity not occupied by residual fluids and that allows the real migration $\varphi \geq \varphi_c$), B is a dimensionless geometrical factor and d is the grain size (expressed in μm). For

instance, the permeability of sandstone with geometrical factor 15, porosity 0.32, percolation porosity 0.035 and average grain size 100 μm will be ~6.8 Darcy (Mavko et al., 2009). It is easy to recognize that by only changing the grain size there will be a large change of permeability.

Permeability and flow rate

The permeability κ is used in the equation of the fluid flow rateQ_x, established by Darcy (e.g. Bear and Braester, 1972), given by

$$Q_x = -A\frac{\kappa}{\eta}\frac{\partial P}{\partial x}$$

, where, A is the cross-sectional area perpendicular to the fluid flow, η is the dynamic viscosity, and $\frac{\partial P}{\partial x}$ is the pressure gradient (expressed also by *grad P* or∇P). κ will be a tensor if the fluid flow occurs in a multidimensional system governed by anisotropies or preferential fluid flow rate. For a multiphase fluid flow the expression will change to

$$V_i = -\frac{k_i}{\eta_i}\nabla P_i$$

, where *i* refer to each phase characterised by relative permeability κ and viscosity η (Mavko et al., 2009). Simultaneous fluid flow of different phases represents the common phenomenon of the migration process. The simultaneous multiphase fluid flow will start if one of the phases involved will reach the threshold of the

irreducible saturation. The involved phases can be two, water oil or gas, or three, water oil and gas. If the fluid migration occurs in pipe conduit or in a fractured media, the equation will be difference due to the different parameters involved and due to the different geometries of the pore shape.

In a pipe like conduit, such as gas-pipe (e.g. Moss and Cartwright, 2011) or gas-chimney (e.g. Arntsen et al., 2007), the flow rate is expressed by the Kozeny-Carman relation for flow (Carman, 1997)

$$Q = -\frac{\pi R^2}{8\eta}\frac{\Delta P}{l}$$

, where, R is the average radius of the pipe, η is the dynamic viscosity, ΔP is the pressure variation and l the conduit length.

For a fractured formation the equation can be simplified to a fluid flow occurring within two parallel walls. The equation in this case will be

$$Q = -\frac{h^3}{12\eta}\frac{\Delta P}{l}$$

, where, h is the average aperture of the fractures, η is the dynamic viscosity, ΔP is the pressure variation and l the fault length or height. It is important to say that the viscosity of the fluid involved can change drastically the flow rate.

In the fractured media the permeability is determined by the aperture of each fault/fracture and by the matrix inside the aperture. The total permeability κ can be expressed therefore as

$$\kappa = \kappa_{aperture} + \kappa_{matrix} = \kappa_{matrix} + \frac{\varphi h^2}{12} cos^2\alpha$$

, where the porosity is given by $\varphi = h/D$; D is the distance between the faults/fractures. h is the aperture and α the angle of the fault (Mavko et al., 2009).

These equations provide a simplification of the real porous systems, however in complex geometries they must be substituted with other and more complicate expressions.

1.2.4.3. Hydrocarbon Plumbing systems

Plumbing systems (e.g. Andresen, 2012; Winefield et al., 2005) represent whatever system composed of a porous medium and fluids in a non-equilibrium condition (potential energy ≠ 0, England et al., 1987). The solid frame part, or porous medium, can be composed of different lithologies with different hydraulic characteristics. The solid frame can be active during the life of the plumbing system and produce drastic changes in the hydraulic behaviour (e.g. faults, Cartwright et al., 2007). The fluids can be of different nature (e.g. water, oil and gas) and move in different directions.

Of particular interest are the petroleum plumbing systems that are the result of the migration of hydrocarbons from the source rock to the shallow section of petroliferous basins. Plumbing systems are dominated by multiple stages of migration and accumulation (Andresen, 2012) which are controlled by the hydraulic properties of the basin. Every elementary portion of a petroliferous basin is indeed regulated by the ratio between inward, I_{ff} , and outward, O_{ff} , fluid flow. This simplification define (1) hydrocarbon occurrences (e.g. reservoirs) when $I_{ff} / O_{ff} > 1$ and (2) hydrocarbon pathways (e.g. pipes) when $I_{ff} / O_{ff} <= 1$.

Plumbing systems can be limited at top by accumulations of hydrocarbons (e.g. reservoirs), but often they reach the surface of the earth exhibiting various features

associated with focused fluid expulsion (e.g. Cartwright et al., 2007; Gay et al., 2007; Rollet et al., 2012). On the seafloor these underlying fluid expulsion phenomena commonly terminate upwards at pockmarks or events which are often observed as sub-circular depressions with diameters ranging from meters to kilometres (Hovland and Judd, 1988). Focussed fluid flow can be associated with fluids other than hydrocarbons and can include remobilised sediments in the flow. Multi-phase flows are seen in a large number of features in both surface, such as mud and sand volcanoes (Eggland, 1997) and in subsurface such as sand injections (Hurst et al., 2007).

In past works as been indicated as primary migration, the movement of hydrocarbon from the generation points (source rock) to the relative high permeable portions of the source rock, meanwhile secondary migration, the movement of hydrocarbon from the source rock to a porous media named reservoir. This terminology is considered obsolete since an infinite number of migration steps, or accumulations of hydrocarbons, are considered present in any hydrocarbon plumbing systems.

The migration of hydrocarbon can be associated with different transport systems. These systems are governed by the forces applied to the fluids. In condition where a pressure gradient is present advective fluid flow will be activated. In condition where a temperature gradient exists, a convective fluid will be present. In a solution containing a soluble compound (e.g. methane dissolved in brine water), if a concentration gradient is present, a diffusive migration will be present (Etiope et al., 2009). In the vast majority of the cases these processes act at the same time. Diffusive flow is considered slower respect to the other transport mechanisms. Løseth et al (2009) summarized three types of fluid migrations based mostly in

advective flow: by fracture, by diffusion and by Darcy law fluid flow. The migration of fluids is dominated by diffusive fluid transport mechanisms and the remaining is focused in fault pathways or hydraulic fracturing (Løseth et al, 2009; Hustoft et al., 2010). Usually the hydrocarbon migration is associated with other mobilization (Cartwright, 2007). Mud, soft sediment, clay, sand and CO^2 are usually transported (they reduce the migration velocity). The migration of fluid can be an active and/or dormant process with different activation timing (random and/or cycle activation) and different amount of gas involved.

1.3. Introduction to the study area

This research work is focussed in a large area offshore the Falkland Islands (Figure 1.6). A brief tectonic, structural and stratigraphycal introduction to the study area is here presented and based on the available published works focussed in the study area (e.g. Fish, 2005; Platt and Philip, 1995; Richards et al., 1996; Bry et al., 2005). A complete description of the study area is present in each result chapter.

1.3.1. Plate tectonic setting

The Falkland Islands are located in the South Atlantic Ocean and 700 km off the Argentinian coast (Figure 1.6). The basins studied in the result chapters are the east Falkland Basin (also referred as Falkland Plateau Basin) located at 100 km to the east of the Falkland Islands and the South Falkland Basin located 200 km to the south of the Falkland Islands.

The Falkland Islands, based on (1) geological, (2) palaeomagnetic reconstructions, and (3) onshore stratigraphy, were located adjacent to the eastern coast of southern Africa prior to the break-up of Gondwana. This event, started in the Jurassic, was followed by the opening of the South Atlantic in the Early Cretaceous (Martin et al., 1982; Martin, 1986; McKerrow et al., 1992; Norton, 1982).

Many authors (e.g. Mitchell et al., 1986; Taylor & Shaw, 1989; Marshall, 1994; Vérard et al., 2012) suggested that the Falkland Islands micro-plate rotated clockwise through up to 180 ° during the formation of the present continental configuration; 120° of which occurred during the early stages of the rifting of Gondwana, and the remaining 60° occurred simultaneously with the opening of the South Atlantic Ocean.

This hypothesis is still under debate (Richards et al., 1996) but although it may have some impacts on the definition of the past tectonic evolution of the study area, it does not have strong implications in the present day tectonic configuration, which is instead part of the aim of this research work.

1.3.2. Geological setting of East and South Falkland Basins

The East Falkland Basin is a rifted continental margin (Ludwig, 1983; Figure 1.6-7) and represents the westernmost portion of the Falkland Plateau Basin (Figure 1.6-7). The basin underlines a thinned continental crust of about 12-16 km (Marshall, 1994; Richards et al., 1996) which thickens westward to 30 km below the Falkland Islands. The decrease in thickness is achieved in c.a. 150km presenting a series of normal faults mainly down-throwing to east and oriented NE-SW (Richards et al., 1996). The faults are indicative of an E-W extension occurred in the Early Jurassic. This extension was followed by post-rift reactivation through the Cretaceous and Cenozoic (Richards et al., 1996). These faults are characterised by throw of 100s of metres. A large sill complex is present in the central and eastern portion of the study area. The sill complex has been dates as Valanginian/ Hautervian in age by Richards et al (2013).

The South Falkland Basin is a partially-filled foreland basin (Figure 1.6-8) and is characterised by (1) Mesozoic extension and (2) Cenozoic compression and infill. The extension is dominated by a preserved normal faults with throw oriented to the north. The faults separate tilted fault-bounded blocks. Most of the normal faults were active during the Jurassic and Early Cretaceous (Richards et al., 1996). The fault system was reactivated during the Cenozoic compression and loading of the Burdwood Bank (Bry et al., 2004, Fish, 2005). Most of the Mesozoic faults trend E-

W to the west and are more ESE-WNW oriented to the east (Richards et al., 1996). The Cenozoic shortening of the SFB is represented by a number of thrust faults and folds which compose the northern portion of the Burdwood Bank. The folds are predominantly north verging and asymmetric. They are more prominent eastward in the area, where they propagate shallow and deform the seabed. The axis of the folds is oriented approximately with the same strike of the Mesozoic normal faults (E-W to the west and ESE-WNW to the east).

1.3.3. Stratigraphy of East and South Falkland Basins

The East Falkland Basin is composed of a sedimentary sequence of an estimated thickness of ~7 km (Zabanbark, 2011) to 11-12 km (Richards et al., 1996) (Figure 1.9). The basement is overlain by a source prone Oxfordian to Early Kimmerdgian succession interbedded with silty-claystones and limestone deposited in relatively small-rifted half grabens, and which are variably intruded by igneous sills recently dated Valanginian-Hauterivian (Richards et al., 2013). The greater part of the Cretaceous interval up to and including the Campanian is dominated by claystones and chalks deposited under pelagic to hemipelagic conditions, in a post-rift setting of thermal subsidence of the margin. This depositional and geodynamic regime continued on through the Cenozoic, but there is increasing evidence from the Oligocene onwards of strong bottom current influence on the depositional system in the form of deepwater erosion surfaces and contourites (Del Ben & Mallardi, 2004).

The stratigraphy of the South Falkland Basin (Figure 1.9) can be subdivided in two main megasequences: (I) Syn and post rift megasequence and, (II) foreland and megasequence (Fish, 2005). The megasequences are separated by a prominent regional unconformity recognised in the entire study area and dated approximately

Upper Cretaceous in age (Del Ben and Mallardi, 2006). The base of the Megasequence I comprises synrift continental (or marginal) marine volcanoclastic rocks intercalated with rhyolitic lavas and intrusive sills and consistent with the Late Jurassic Serie Tobifera succession (Lorenzo and Mutter, 1988; Platt and Philip, 1995). This succession is overlain by shallow marine sandstones and shales of Latest Jurassic-Early Cretaceous age, and then by thick sequences of Early to Late Cretaceous rocks composed of organic-rich, open-marine shales. The megasequence II composes a thick sedimentary wedge filled with slope and basinal shales together with minor siltstones.

1.4. Aims

The main aim of this research work is to improve the global understanding behind hydrocarbon migration using a large seismic dataset from two major basins located to the east and to south of the Falkland Islands. Although this region is under exploration and the primary output of this research will be beneficial for the oil companies operating in these frontier areas, it is hoped that some of the novel methodologies here developed and the results from each chapters, and in particular the ones from the Discussion, will be used and tested in the research focussed on the migration of hydrocarbons in sedimentary basin.

The detailed research aims are as follows:

- To interpret amplitude anomalies and DHIs. This work is carried out in order to discriminate amplitude anomalies associated with hydrocarbons (DHIs) from those related to seismic artefacts and geological causes (e.g. tuning anomalies and diagenetic fronts, respectively). This part will comprise:
    - semi-quantitative seismic interpretation in time domain,
    - seismic interpretation in frequency domain, and
    - amplitude variation with offset (AVO) analysis.

- To interpret structural and depositional elements. This work is done in order to characterise each basin and it is integrated with previous works undertook in the study area.

- To link DHIs with the basin architecture. This will comprise:
    - analysis between the distribution of specific DHIs with structural and depositional elements of the basin, and
    - analysis DHI-DHI (e.g. bottom simulating reflection vs. enhanced reflections)

- To link the style of the DHIs and the migration processes. It is expected that contrasting DHIs, as hinted from their seismic expression, may represent the output of different migration processes.

1.5. Layout

This manuscript is divided in 7 chapters in which have been written theoretical notions, 3 result case histories (Figure 1.10), a discussion on what have been observed in this research work and some main conclusion.

Chapter 1 (this chapter) consists of introduction and background information which covers the knowledge on hydrocarbon migration ,hydrocarbon indicators as observed on seismic data and a brief introduction to the study area.

In Chapter 2 a number of methodologies will introduce the reader to the concepts of the seismic interpretation. A number of qualitative and quantitative methodologies used in this work are described.

In Chapter 3 a large number of staked amplitude anomalies labelled here Vertical Anomaly Clusters (VACs) have been described and analysed in a vast area located in east Falkland Basin.

In Chapter 4 an entire hydrocarbon plumbing system comprising a variety of contrasting DHIs and a prominent bottom simulating reflection (BSR) have been described and analysed in the South Falkland Basin..

In Chapter 5 enigmatic depression structures have been encountered in a northern region of the east Falkland Basin. These depression structures are seen in the shallow section of the basin and are associated with a number of DHIs.

In Chapter 6 the major finding of this research are summarised, compared with the wider literature and discussed. Limitation and future works of this research are documented. Finally, a number of conclusions based on the present work are proposed in Chapter 7.

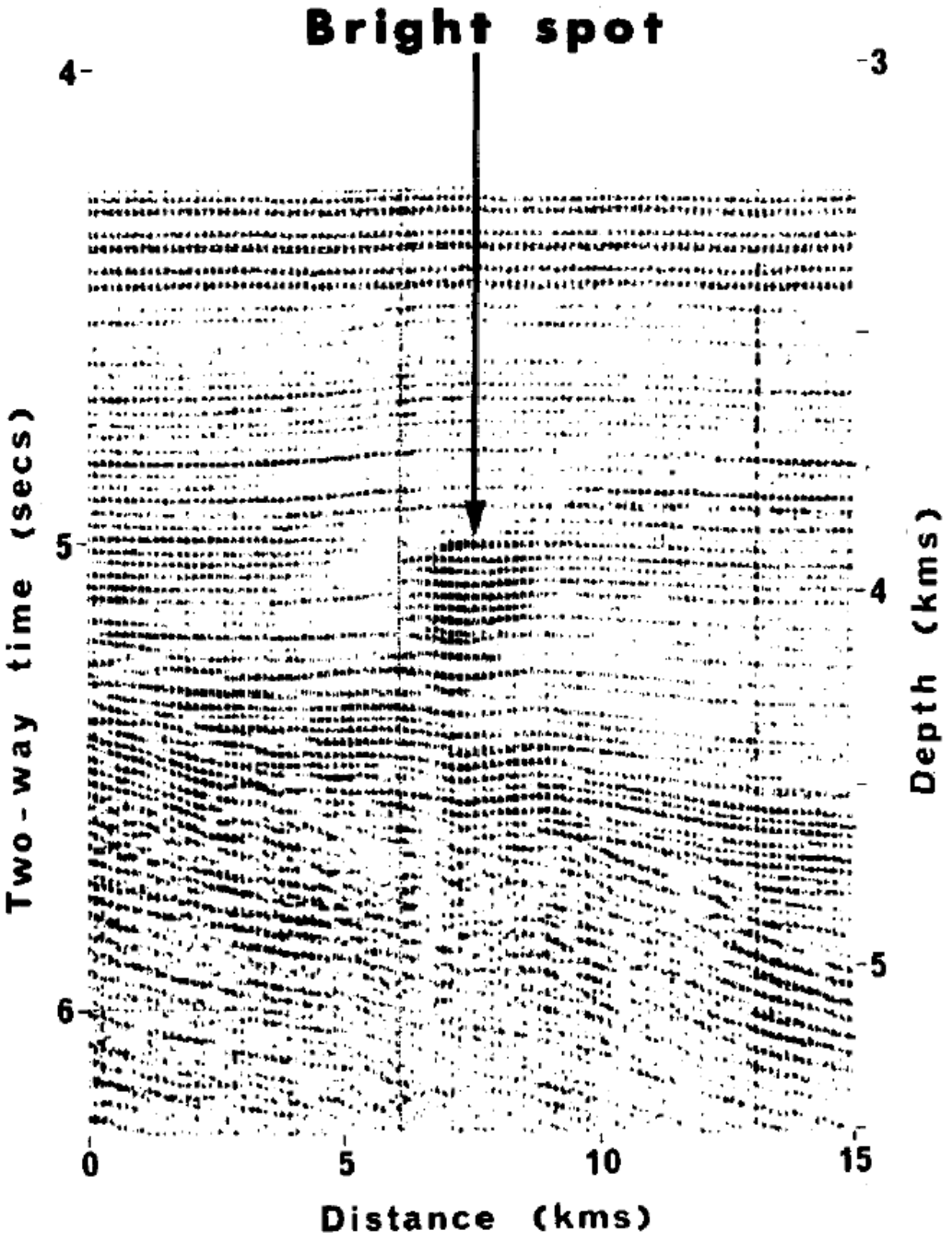

Figure 1.1 2D seismic section depicting bright spots from Gulf of Oman. The seismic features are displayed using variable density method (from White, 1977).

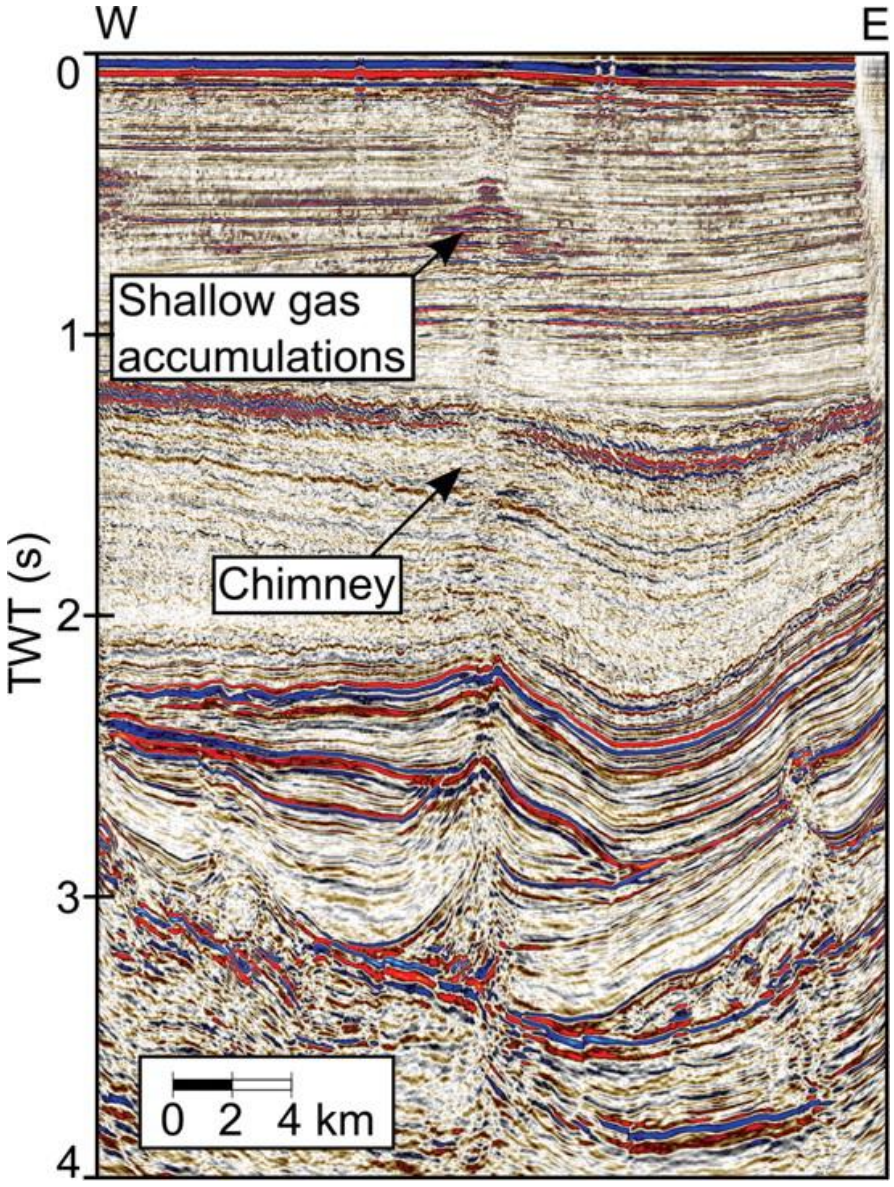

Figure 1.2 2D seismic section showing gas chimney and shallow gas accumulations (from Arts and Vandeweijer, 2011).

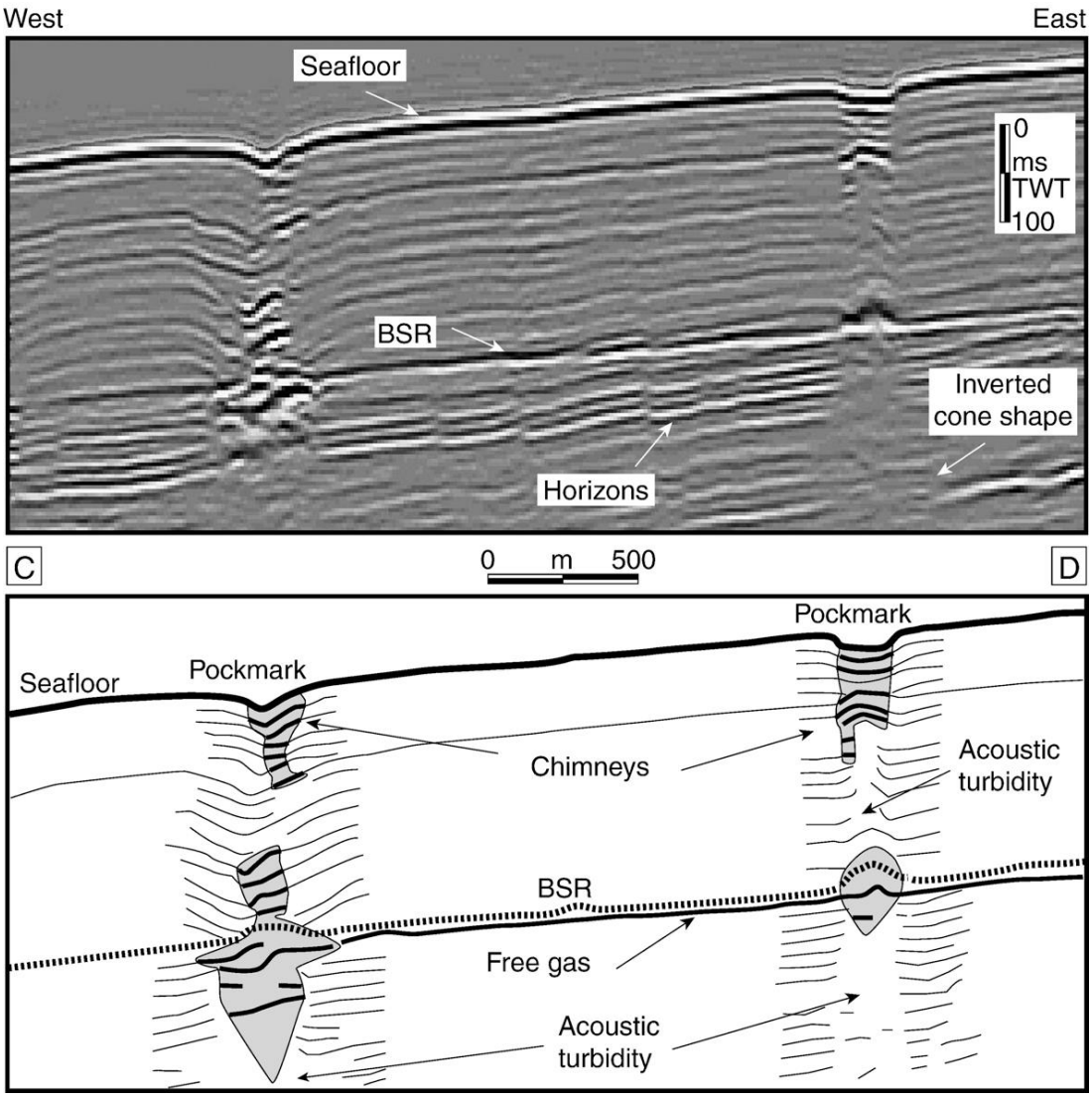

Figure 1.3 2D seismic section and 2D line drawing depicting pipes in Lower Congo Basin. The pipes are columnar features of 200-250ms TWT. They present amplitude anomalies and they terminate at the seabed. The interpretation here suggests that these pipes are rooted beneath the bottom simulating reflection (BSR) (from Gay et al., 2007).

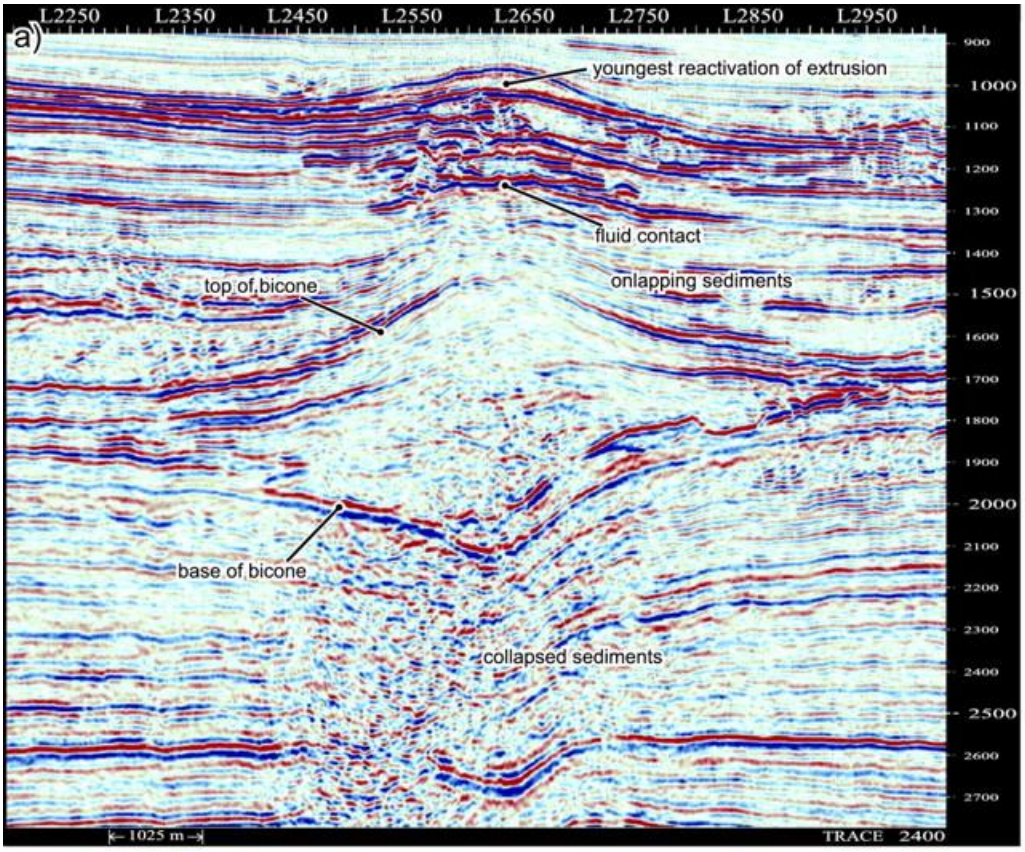

Figure 1.4 2D seismic section depicting a mud volcano. The mud volcano here is characterised by bicone geometry. The mud volcano here presented has been formed through multiple activations (from Davies and Stewart, 2005).

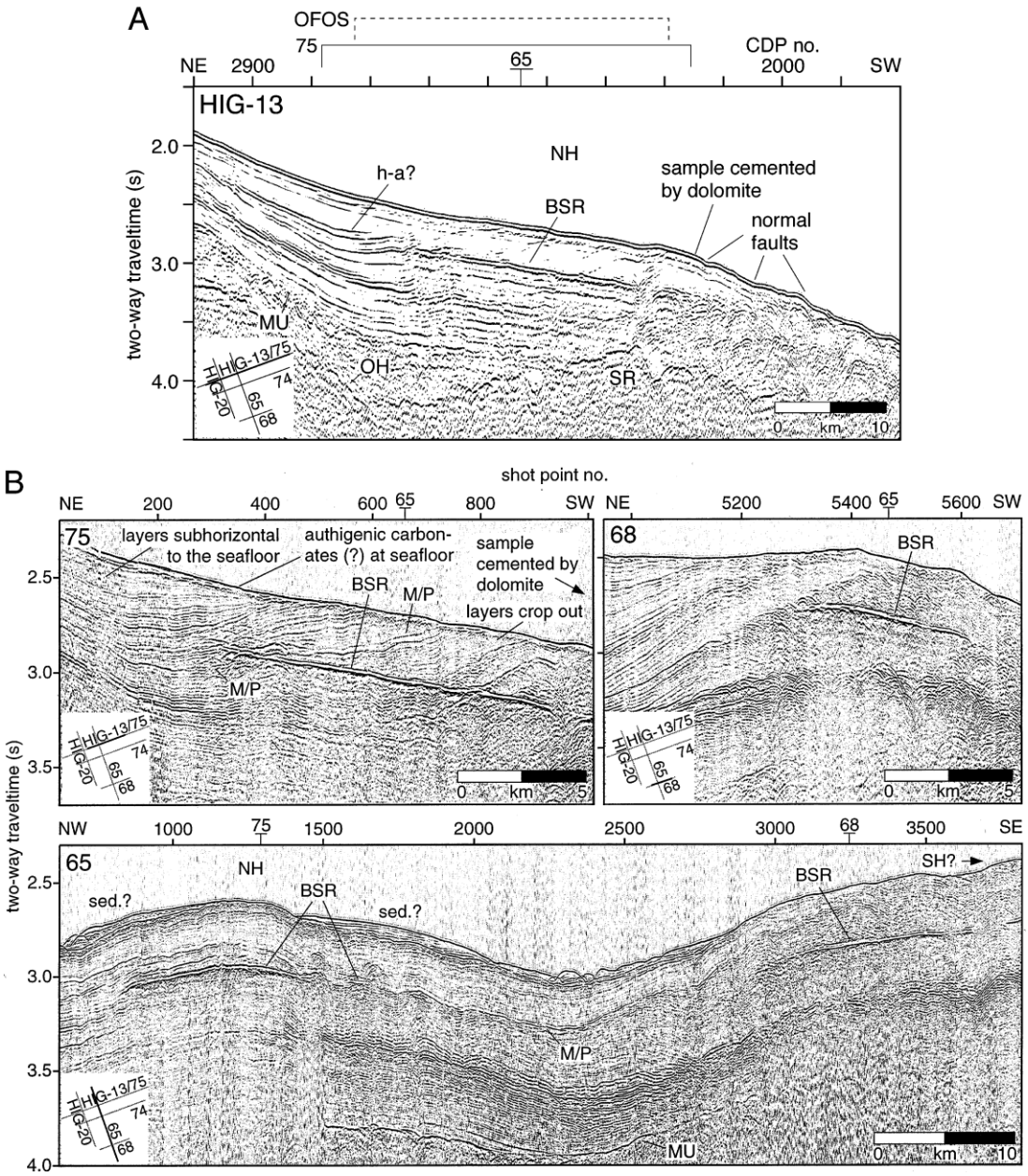

Figure 1.5 2D seismic composite depicting bottom simulating reflections from Lima Basin, Peru Margin. The images exhibit the three diagnostic characteristics of a BSR associated with gas hydrates: negative polarity, seabed-simulating shape and cross-cutting geometry (from Pecher et al., 2001).

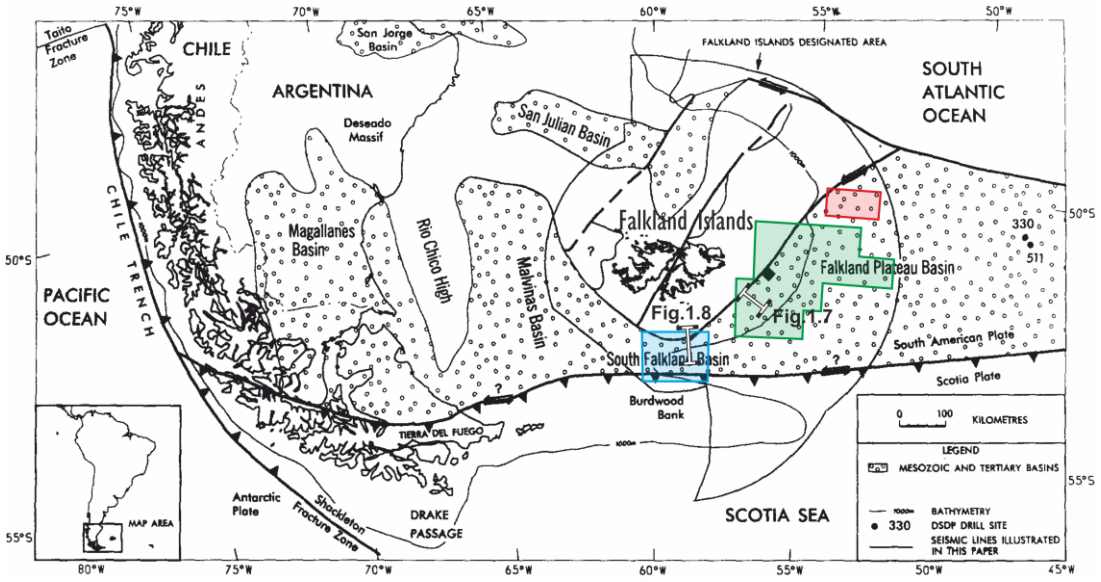

Figure 1.6 Simplified geological map of the of the Southern Atlantic regions with position of the Argentina, Falkland Islands, Falkland Plateau Basin, South Falkland Basin and tectonic and structural elements (modified from Platt and Philip, 1995). Position of Figure 1.7 and 1.8, and approximate positions of the study areas (see Figure 1.10).

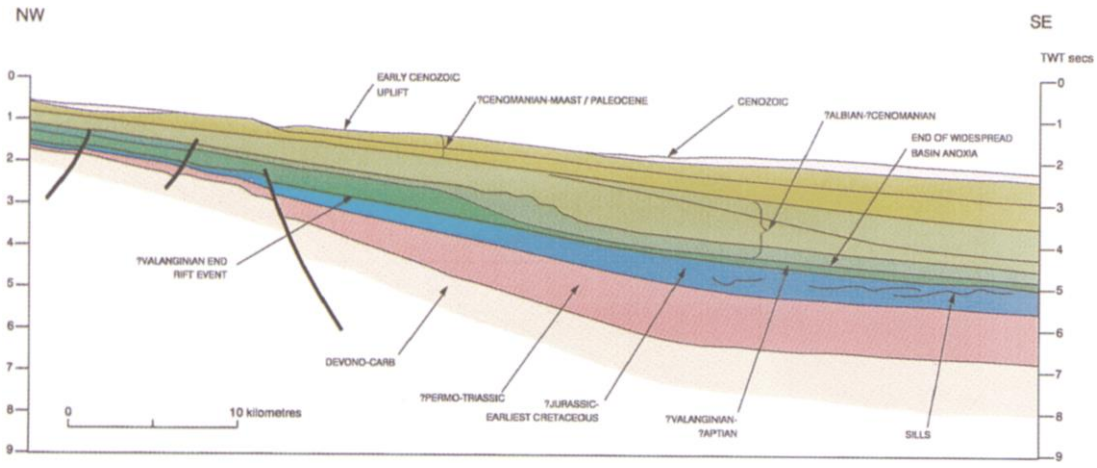

Figure 1.7 Synoptic time section across the westernmost portion of the Falkland Plateau Basin (from Richards et al., 1996; see Figure 1.6 for approximate position).

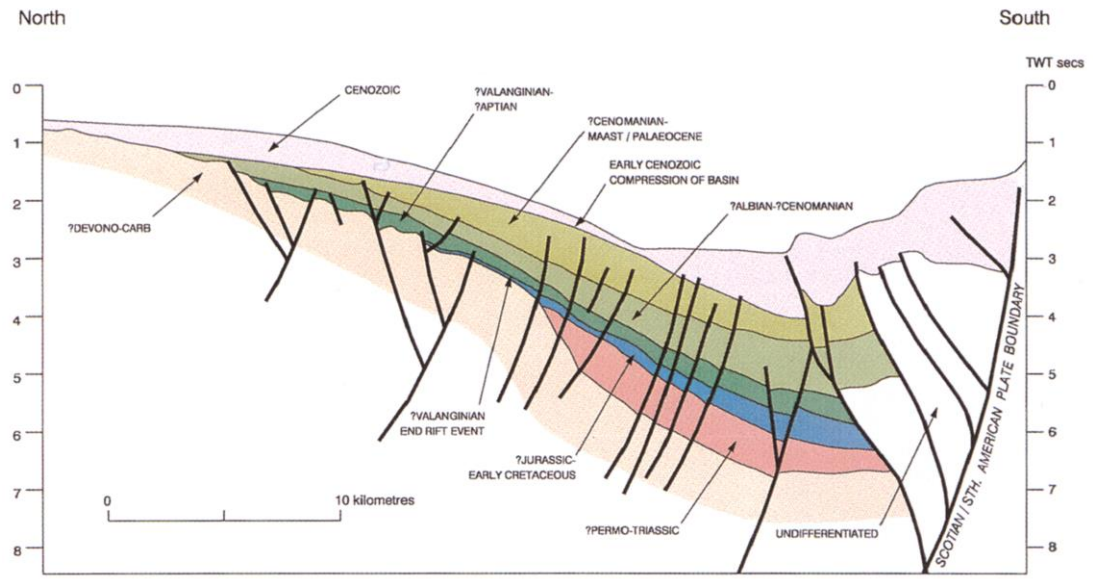

Figure 1.8 Synoptic time section across the South Falkland Basin (from Richards et al., 1996; see Figure 1.6 for approximate position).

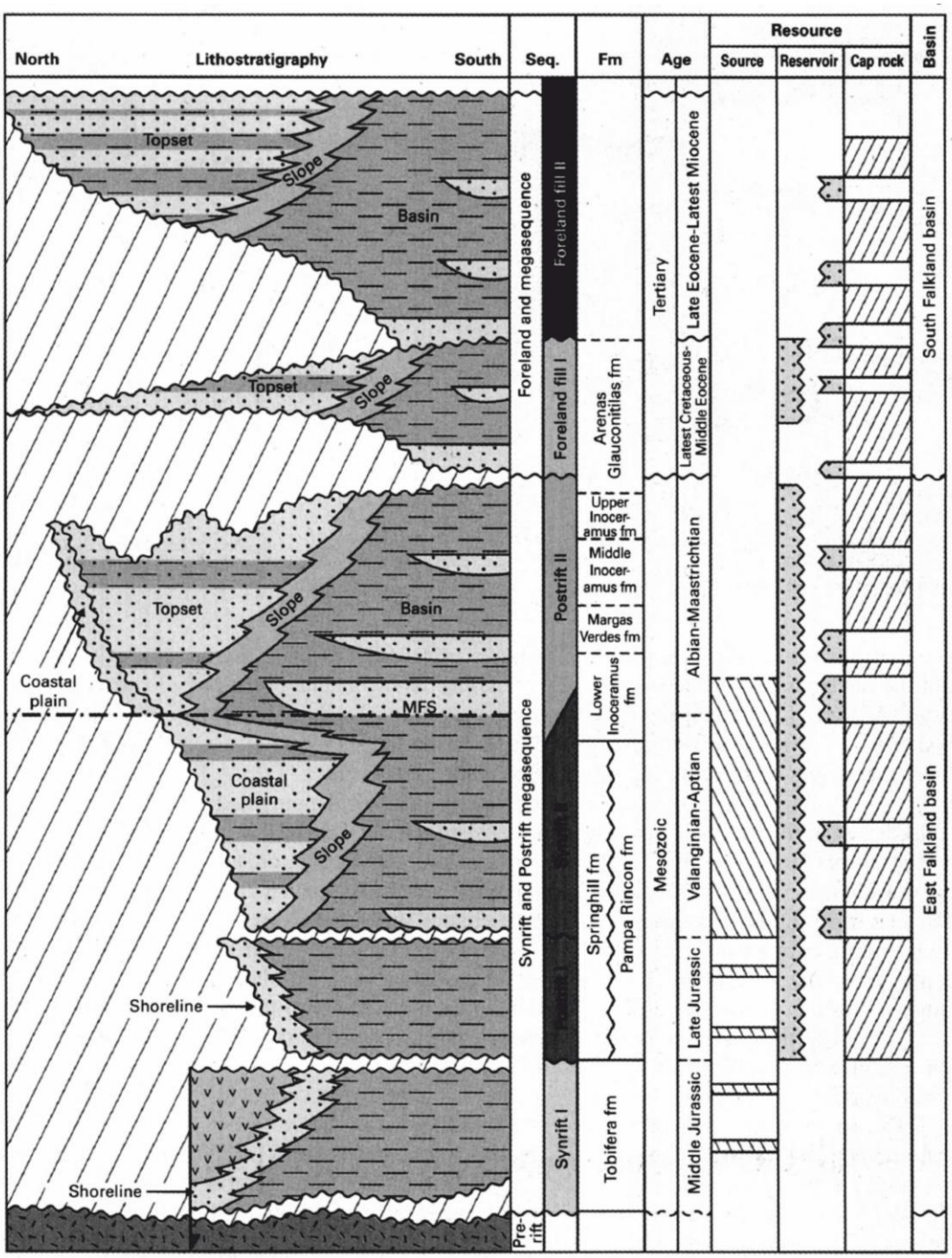

Figure 1.9 Stratigraphic reconstruction of the sedimentary columns of the east Falkland Basin and South Falkland Basin (from Fish, 2005).

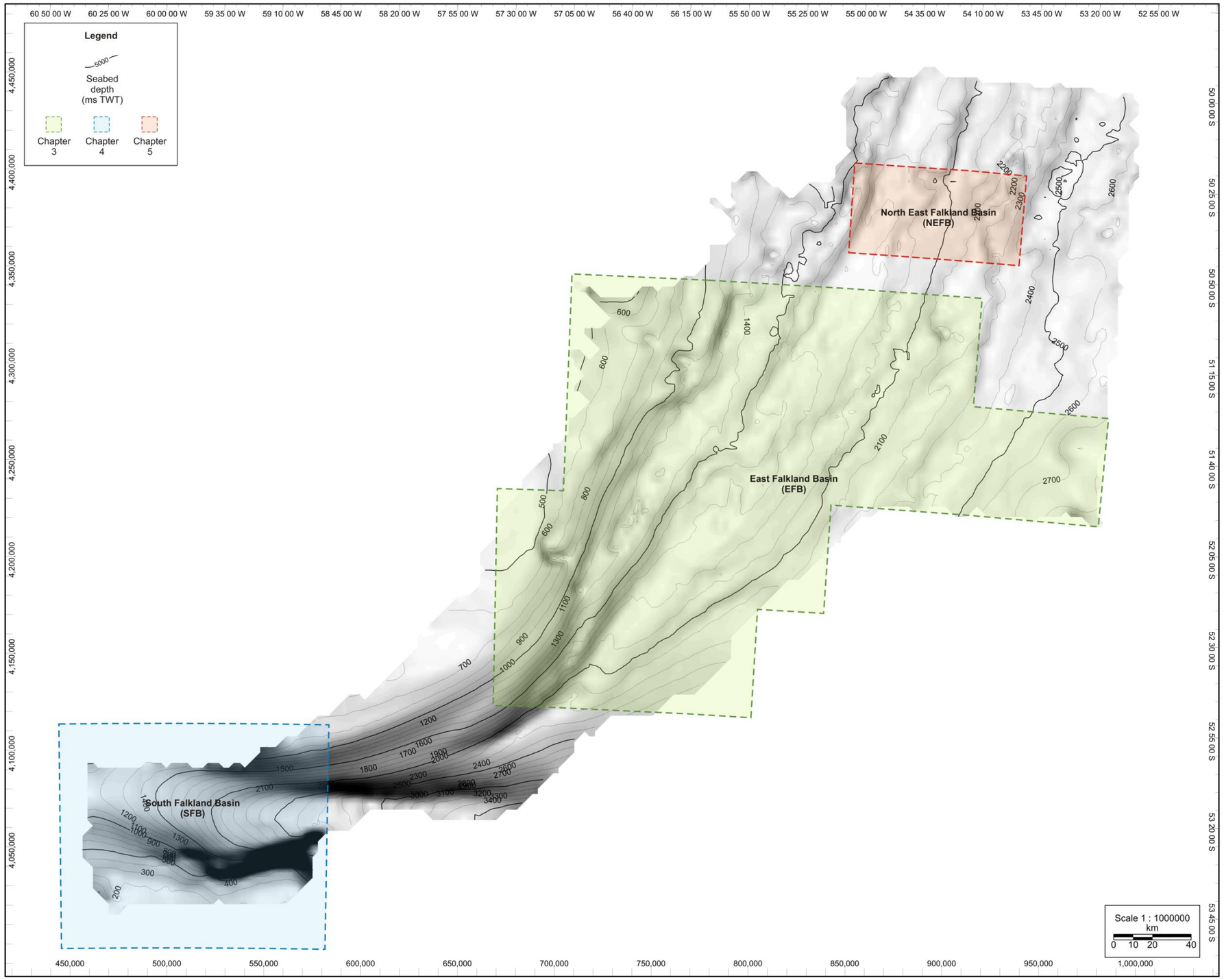

Figure 1.10 Location map of the three study areas described in the present manuscript. The position of the 2D seismic lines and the coast line are not displayed due to data restrictions.

2. Methods

2.1. Introduction

The dataset and the methodologies used in this thesis are essentially those used in the oil companies for exploration of hydrocarbons. The main source of information came from geophysical data that include seismic sections (2D), seismic volumes (3D), wire logs. Other sources of information, such age of the lithologies, lithology or palaeontology, are mainly found in literature including books and papers. In some cases there is access to core data from well sites. Normally the geophysical data (e.g. seismic exploration methodologies) provide large scale information allowing us to describe regional-scale structures. The interpretation of the seismic data however needs to be calibrated with geological data provided by geological campaigns and well logs. All the data and information are interpreted and correlated each other in order to generate geological models of the explored subsurface.

The following subsections will describe first the different data used and then their interpretation.

2.2. Seismic data

The seismic data are nowadays based on a multichannel registration of reflected elastic waves introduced artificially in the subsurface. Different environments required different exploration methodologies. All the data used in this work are 2D seismic data collected in offshore areas (marine environment).

The acquisition is the first step to obtain a seismic section or seismic volume. The entire work is normally carried out directly in the acquisition area (field) and involves a large and expensive number of instruments, devices and qualified personnel. The acquisition required a relative short time (e.g. couple of months) and the largest part of the invested budget (>80%).

The acquisition methods change as function of the field environment (land and/or marine). Since this work has been done on marine data only this exploration methods will be explained.

2.2.1. Marine seismic acquisition and processing

The marine acquisition uses the marine water as elastic media. All operations are performed in water using specially developed ships. The energization (source of elastic wave) is commonly generated by devices named air-guns that create high pressure air bubbles. These bubbles, or spherical waves, hitting the sea floor will transfer the elastic energy from water to sediments and rocks. Every change of the elastic properties of the mediums encountered will separate the elastic energy. Part of these energy will be reflected to the opposite direction of the impinging wave (the impinging wave is not perfectly vertical, the angle of reflection has the same aperture of the impinging angle but in the mirrored direction (Snell Law)) meanwhile the

other part will be transferred to the subsequent mediums. The amount of energy transferred and energy reflected depends to the property of the mediums.

The reflected energy will be recorded by devices named hydrophone. These tools are able to capture the variations of the water pressure coming from the sea floor. The hydrophones are located in arrays named streamers that in their turn are connected to the acquisition ship. For 2D acquisition it is necessary one singular streamer while for 3D acquisition the number of streamer is higher (e.g. 12, 16). The number of hydrophones per streamer is variable and determines the number of channels and the quality of the final seismic image (e.g. narrow or wide angle, fold of coverage, etc.).

The pressure variations detected by the hydrophones are recorded in time. This time represent the travel time that is necessary for the energy to travel from the air-guns to the reflected surface and then to the hydrophones. Conventionally this time is name two-way-travel time (TWT) and is measured in millisecond (ms) or microsecond (μs). The registration time determines the depth of the investigation meanwhile the sampling interval Δt the maximum frequency (Nyquist frequency, $f_N=1/(2\times\Delta t)$). The seismic frequency represents an important parameter because controls the vertical resolution of a given seismic survey (Fresnel zone, Sheriff, 1975).

The seismic acquisition is accompanied by seismic processing that allows us to obtain the image of the subsurface structures of the explored area. Compared to the acquisition steps the seismic processing can require years and many phases of reprocessing and imaging improvements (e.g. from post-stack migration to pre-stack migration).

The basic steps of the seismic processing are (1) the passage from the shot domain to the common depth point domain (CDP), (2) the velocity analysis, (3) the normal move out (NMO), (4) the stack and (5) the migration (in time or depth). Other processes such as muting, deconvolution, multiple suppression, 1D/2D filters, gain controls, static corrections and many other are essentially applied to the seismic processing flow to improve the final result.

2.2.2. Basic properties of the seismic data

The seismic data that will be used in this research are in two-way travel time domain (TWT or TWTT) and associated with reflection of compressional seismic waves (Rpp). Following to common convention of the Society of Exploration Geophysicists (SEG) the seismic data used in this thesis is displayed in zero phase of negative (European) and positive (American) polarity. Zero-phase wavelet is achieved using specific processing steps, such as shaping deconvolution. In zero-phase data the wavelet is symmetric to the zero time (t=0) and it is associated with the maximum energy at the interface separating two different media. American polarity is where a positive peak is associated with an increase in acoustic impedance with depth while European polarity is where a positive peak is associated with decreasing acoustic impedance with depth.

The resolution of the seismic data depends on few key factors such as 1) frequency and 2) velocity of the media. These factors affecting the seismic resolution have been primarily used by Widess (1973) which developed the following relation to calculate the vertical resolution of the seismic data

$$R_v = \frac{1}{4}\frac{V_p}{f}$$

, where Vp is the compressional velocity and f the average frequency. Since the frequency of the seismic data generally decrease with depth and the velocity of the media increase with depth the seismic resolution decreases with depth increasing wavelength and detail of the deep structures (Brown, 2004).

The seismic data can be displayed in variable area (or "wiggle" display, Figure 2.1A) or in variable density (Figure 2.1B-C-D). Different colour maps are normally used at different stage of the seismic interpretation.

2.3. Seismic Interpretation

The 2D and 3D seismic data can be decomposed or transformed to obtain attributes and visualize properties that are not visible in time-amplitude domain. A lot of signal processing techniques, normally used in telecommunication engineering or speech analysis, have been manipulated and subsequently adapted for seismic data.

The multi-domain interpretation method proposed in this work is composed by the standard time-amplitude domain interpretation, which represents the most important way to interpret the seismic data and the frequency domain in both standard and instantaneous versions. These techniques have been also integrated with amplitude variation with offset (AVO) analysis which allows us to characterize quantitatively some observation carried out during the seismic interpretation.

2.3.1. Time Domain

2.3.1.1. Time interpretation and “Bright spot” technique

Every reflection in seismic data, in both 2D and 3D survey, describes the geometrical shape and the physical response of the two mediums involved. It can be used to extrapolate qualitative variations of the acoustic properties or calculate quantitatively the physical characteristics of the mediums.

Since 1970 has been used the bright amplitude technique in which a local increase of seismic amplitude (bright), named seismic anomaly, was used to indicate, with more or less confidence, an accumulation of hydrocarbon (Figure 2.2).

The bright amplitude technique nowadays can be useful to localize particular seismic response caused by hydrocarbons but unfortunately different geological

events can yield similar responses. The positive seismic response, called also “hard” reflections, can be produced by (1) shallow sand in pelagic sediment, (2) carbonate rock in silico-clastic material or (3) cemented sand, among others.

Typical negative response, called in this case “soft” reflections, can be caused by (1) shallow unconsolidated sands in compacted shale, (2) hydrocarbon accumulation, (3) pelagic accumulation or (4) zone of high pressure conditions (Mavko et al. , 2009). These are only a limited number of examples compared to the large number of different responses.

The seismic data is used to generate maps or plots along the reflection or in a given time/depth interval providing the description across a given area about the amplitude variation. The amplitude maps computed in the picked reflection can be manipulated and filtered to increase the visualisation of the desired amplitude features. The time reflection interpretations have been mostly carried out using computer aided interpretation software normally used in the oil industries (Schlumberger Geoframe, ISEXS).

Other techniques for amplitude analysis include root mean square amplitude map (RMS). The use of these maps is considered, for the writer, not useful due to the complete summation of positive and negative values. The general equation to calculate this attribute is expressed by the following equation

$$A_i = \sqrt{\frac{\sum_{i=1}^{N} A_i^2}{N}}$$

, where A_i is the i-amplitude and N is the total number of amplitude values.

2.3.1.2. Amplitude Variation with Offset (AVO)

The "bright amplitude technique" (e.g. Avseth et al., 2009) changed with time and became more quantitative with the amplitude variation with offset analysis (AVO). The AVO analysis represents a method to recognize the change of reflection coefficient with offset caused by the presence of particular fluids in a constant lithological condition (Rutherford and Williams, 1989). The AVO is sometimes difficult to interpret and in some cases does not represent the proof of hydrocarbon presence. Regardless some failure, in which supposed AVO occurrence have not been confirmed by drilling operations,

AVO analysis represents a valuable tool during hydrocarbon exploration (Loizou, 2008). The AVO effect on seismic data can be observed and interpreted in different ways. The best way to analyse the variation of amplitude is watching pre-stack data in which the operator can control the full variation with offset of the analysed reflections composing a CDP. Another way is using range-stack data in which only small range of offset (or angle) can be observed to control the change of amplitude. In range-stack data the CDPs are divided as function of the offset or angle. The stack is performed in a subset of traces located in different portion of the CDP (e.g. near-mid-far). From one singular CDP will be computed different stack traces (e.g. 2 or 3). The stack traces obtained will be composed a multiple stack sections showing the same area but a different offset/angle related response. Watching a pre-stack, NMO-corrected CDP data, it is possible to distinguish four different AVO class (Rutherford and Williams, 1989; Figure 2.2):

- I a strong amplitude positive reflection decrease the amplitude from near to far angle/offset

- II a low amplitude positive reflection decrease the amplitude and change polarity from near to far angle/offset (from positive to negative polarity)
- III a low amplitude negative reflection increase the amplitude from near to far angle/offset
- IV a negative reflection decrease the amplitude from near to far angle/offset

The first three AVO classes have been introduced by Rutherford et al (1989) meanwhile the fourth has been discovered by Castagna (1996). The method used in this work is based on AVO cross-plot technique introduced by Castagna et al. (1998). This method is based on the reduction of data in few parameters per every observed CDP. This parameters computed during this work in range-stack domain are named intercept (*I*) and gradient (*G*). The geometric relationship of these values is shown in Figure 2.4. The observed near and far amplitude values following the curved Zoeppritz function in the *A-θ* domain can be approximated as points composing a line in the $A\text{-}sin^{2(}\theta)$ domain. Every line is therefore described as function of angular coefficient (*G*) and intercept (I; the line value at the axis y (or *X=0*)) and will represented as a single point in the G-I domain. This graphical representation allows us to synthesize and display several observations in a small and unique plot.

The AVO cross-plot values have been calculated using the Shuey approximation (Shuey, 1985) of the full Zoeppritz equation (Zoeppritz, 1919). The Shuey equation, written as

$$R(\theta) = R_0 + \left[A_0 R_0 + \frac{\Delta\sigma}{(1-\sigma)^2}\right] sin^2\theta + \frac{1}{2}\frac{\Delta V_p}{V_p}(tan^2\theta + sin^2\theta)$$

has been truncated at the first two members. The large approximation allows anyway a good fitting of the P-wave reflectivity function and only a small divergence is recognizable at angles over 30-40 degrees.

2.3.1.3. Algorithms

The *G - I* parameters have been implemented in Matlab® using the following equations:

$$G(k) = \frac{A_{fk} - A_{nk}}{sin^2\theta_f - sin^2\theta_n}$$

$$I(k) = A_{nk} - G_k sin^2\theta_f$$

, where A_{fk} and A_{nk} are the extracted amplitude values in far and near angle stack sections, θ_n and θ_f are the fixed angle values used to obtain the far and near angle seismic sections. The G-I cross-plot has been accompanied with a more simple Near Vs Far amplitude cross-plot that represent the relationship between the picked amplitude in near and far angle domain. In both cross-plot methods the main issue is to recognize the background trend representing the lithological response (dry or wet). Usually that trend is passing through the zero cross point (*G=0*; *I=0*) of the *G-I* plot. Every misalignment or variation from it represents an AVO anomaly that can indicate the presence of gas, oil or an anomalous behaviour of the observed rock/sediment.

2.3.2. Frequency Domain

As already seen in other works (Castagna et al., 2003), the presence of fluid in a given permeable medium yields an anomalous decrease of high frequencies (Korneev et al., 2004). The presence of hydrocarbon is the cause of the well-known shadow effect in which the different absorption of frequencies yields the shift of the power spectrum values in direction of the low frequency (Castagna et al., 2003). The anomalous frequency shift, especially at shallow depth, respect to the normal frequency content (or background frequency content) can represent the position of fluids (e.g. gas) but also other heterogeneities (e.g. faults, Ilg et al., 2012).

2.3.2.1. Fast Fourier Transform (FFT)

The seismic data represent a temporal discrete signal (or time series) that is composed of different amplitude values in a given limited time interval. The time series, if they respect some signal properties, can be converted from time to frequency domain and vice-versa (the operation from time to frequency is named analysis meanwhile from frequency to time is named synthesises). The methods to perform the analysis are based on the continuous Fourier Transform equation, written as

$$X(f) = F[x(t)] = \int_{-\infty}^{+\infty} x(t)\, e^{-j2\pi f t} dt$$

, where the $x(t)$ represents a continuous time signal. The registration of the seismic signal and the subsequent elaboration or processing in PCs and workstations, change the property of the seismic data from analogical (continuous) to digital

(discrete). The equation 2.4 is therefore transformed to work in the discrete domain. Many algorithms have been developed to obtain the Fourier Transform in discrete domain. The one we adopted is written as

$$X(j) = FFT[x(k)] = \sum_{k=0}^{N-1} x(k)\, \omega_N^{(j-1)(k-1)}$$

and has been developed by J.W. Cooley and J.W. Tukey in 1964 (Cooley and Tukey, 1965). From a time series composing the digital seismic trace will be obtained his transformation in frequency domain, in the form

$$\begin{bmatrix} x_{t0} \\ x_{t1} \\ x_{t1} \\ \vdots \\ x_{tn} \end{bmatrix} \rightarrow FFT \rightarrow \begin{bmatrix} f_{f0} & f_{f1} & f_{f2} & \cdot & f_{fn} \end{bmatrix}$$

in which t_n represents the number of time samples of the signal (e.g. seismic trace length (to perform the FFT the length of the analysed trace need to be increased to the next square value (e.g. 512, 1024, 2048, 4096, etc) and subsequently truncated the original value). The right series in the equation above is named spectrum and it is continuous for discrete signal and discrete for continuous signal. f_{fn} represents the maximum frequency that can be resolved with a given sampling interval Δt.

The maximum resolvable frequencyf_{fn}, or Nyquist Frequency is obtained by

$$F_{Nyquist} = \frac{1}{2\Delta t}$$

and for a sampling interval of 4ms (the same used to acquire the used seismic survey) the maximum resolvable frequency is 125Hz.

This type of frequency analysis is used to control the frequency content in the analysed seismic dataset. It represents also an essential tool during the filtering operations but does not give any information of the frequency content at different time intervals (or depths).

2.3.2.2. Time-Frequency Representation (TFR)

In order to provide a time or depth-related representation of frequency and understand for instance whether a given amplitude anomaly is associated with specific ranges in frequency a time-frequency representation (TFR; Cohen, 1995) has been used.. An example of this methodology is described using a 2D seismic section shown in Figures 2.5 and depicting gas-related amplitude anomalies.

A TFR is a frequency representation able to provide, for each sampled seismic amplitude value, an entire frequency spectrum (or power spectrum).

$$\begin{bmatrix} x_{t0} \\ x_{t1} \\ x_{t1} \\ \cdot \\ x_{tn} \end{bmatrix} \rightarrow TFR \rightarrow \begin{bmatrix} f_{t0,f0} & f_{t0,f1} & f_{t0,f2} & \cdot & f_{t0,fm} \\ f_{t1,f0} & f_{t1,f1} & f_{t1,f2} & \cdot & f_{t1,fm} \\ f_{t2,f0} & f_{t2,f1} & f_{t2,f2} & \cdot & f_{t2,fm} \\ \cdot & \cdot & \cdot & \cdot & \cdot \\ f_{tn,f0} & f_{tn,f1} & f_{tn,f2} & \cdot & f_{tn,fm} \end{bmatrix}$$

From one singular seismic trace (1D) it is possible to obtain a large number of frequency values (2D). Each row in the TFR display represents an instantaneous spectrum (Figure 2.6). The frequency spectrum needs anyway to be compared with the values in time domain (single amplitude vs single frequency value) and therefore one single frequency value will be associated to the reciprocal time amplitude value.

The iso-frequency sorting represents a common technique to visualize the distribution of the selected frequency in a given portion of the seismic dataset (Castagna et al., 2003, Figure 2.6). The output of this method represents therefore a frequency display where the frequency is fixed with respect to time and space. In a single seismic trace it can be represented as

$$\begin{bmatrix} x_{t0} \\ x_{t1} \\ x_{t1} \\ . \\ x_{tn} \end{bmatrix} \rightarrow TFR \rightarrow \begin{bmatrix} f_{t0,f0} & f_{t0,f1} & f_{t0,f2} & . & f_{t0,fm} \\ f_{t1,f0} & f_{t1,f1} & f_{t1,f2} & . & f_{t1,fm} \\ f_{t2,f0} & f_{t2,f1} & f_{t2,f2} & . & f_{t2,fm} \\ . & . & . & . & . \\ f_{tn,f0} & f_{tn,f1} & f_{tn,f2} & . & f_{tn,fm} \end{bmatrix}$$

, where the frequency *f(t, f=2)* is selected to display its energy throughout the seismic dataset. In real examples the number of the frequency values is related to the number of the trace samples. A trace composed of 2000 samples and a sampling interval of 4ms (125Hz) will give a frequency interval of 0.0625Hz (e.g. ., ., 8, 8.0625, 8.125, 8.1875, ., .). If this operation is repeated for each trace composing a given 2D seismic section (e.g. Figure 2.5) the resulting matrix will hold the same size of the original 2D seismic section but where the amplitude values are related to the energy of the selected frequency. The example proposed in Figure 2.7 represents an iso-frequency representation of the 20Hz content of the seismic shown in Figure 2.5. The iso-frequency puts in evidence the strong amplitude response of the 20Hz associated with the amplitude anomalies observed on the seismic display.

Another way to sort the frequency values is to select for each instantaneous spectrum the frequency peak i.e. the frequency showing the maximum amplitude.

$$\begin{bmatrix} x_{t1280} \\ x_{t1281} \\ x_{t1282} \\ x_{t1283} \\ x_{t1284} \\ x_{t1285} \\ x_{t1286} \end{bmatrix} \rightarrow TFR$$

$$\rightarrow \begin{bmatrix} f_{t1280,f5=0.2} & f_{t1280,f6=1.1} & f_{t1280,f7=0.6} & f_{t1280,f8=0.3} & f_{t1280,f9=0.1} \\ f_{t1281,f5=0.1} & f_{t1281,f6=0.3} & f_{t1281,f7=1.2} & f_{t1281,f8=0.9} & f_{t1281,f9=0.2} \\ f_{t1282,f5=0.4} & f_{t1282,f6=0.5} & f_{t1282,f7=0.1} & f_{t1282,f8=1.1} & f_{t1282,f9=0.1} \\ f_{t1283,f5=0.3} & f_{t1283,f6=0.5} & f_{t1283,f7=0.8} & f_{t1283,f8=0.7} & f_{t1283,f9=04} \\ f_{t1284,f5=0.2} & f_{t1284,f6=0.4} & f_{t1284,f7=0.5} & f_{t1284,f8=0.4} & f_{t1284,f9=0.3} \\ f_{t1285,f5=0.5} & f_{t1285,f6=0.3} & f_{t1285,f7=0.3} & f_{t1285,f8=0.2} & f_{t1285,f9=0.1} \\ f_{t1286,f5=0.2} & f_{t1286,f6=0.5} & f_{t1286,f7=0.1} & f_{t1286,f8=0.4} & f_{t1286,f9=0.2} \end{bmatrix}$$

In this example the seismic trace *X(t)*, here taken, for instance, from samples *X(t=1280)* to *X(t=1286)*, is represented after the TFR, by a frequency matrix here taken from *F(t=1280, f=5)* to *F(t=1286, f=9)*. The frequency-peak series is represented by the samples associated with the maximum energy for each time interval (e.g. *F(t=1280, f=6)*, *F(t=1281, f=7)*, *F(t=1282, f=8)*, etc.). In this case the selection of the value is associated with the energy of the frequency and not by the operator. With this strategy, it is believed to better individuate the frequencies associated with shadow zones. An example of this method is shown in Figure 2.8. The representation clearly shows an evident variation of frequency with depth. The low frequency zones are here located at the same position of the amplitude anomalies observed in the seismic of Figure 2.5. In this case, as expected by the different selection applied, the frequency response puts in evidence that only some of the amplitude anomalies are related to low frequency response. This may suggests that this method is more sensitive to the real variation of frequency of a given region of the seismic rather than to a variation in amplitude. This type of frequency selection has never been used before.

2.3.2.3. Algorithms

The time-frequency representation algorithm used in this analysis is based on the Wigner-Ville distribution (WVD; Cohen,1995; Loughlin et al., 1993; Zhang and Lu, 2009), written as

$$WVD(t,f) = \int_{-\infty}^{+\infty} BA(t,\tau) e^{-j2\pi f\tau} d\tau$$

, where

$$BA(t,\tau) = s\left(t + \frac{\tau}{2}\right) s^*\left(t - \frac{\tau}{2}\right)$$

represents the bilinear autocorrelation function *(BA)* and *s(t)* represents the complex signal (Taner et al., 1979) obtained by

$$s(t) = x(t) + H[x(t)]$$

, where *H[x(t)]* is the Hilbert Transform operator of the seismic signal *x(t)* (e.g. seismic trace). The *s** represent the complex conjugate of the complex signal *s(t)*.

This type of distribution is affected by cross-term interferences (CTI) that appear in the midway between each couple of different frequencies. The issue has been partially overcame modifying the Ambiguity Function (AF), calculated as the inverse Fast Fourier Transform (iFFT) of the BA function

$$AF(t,v) = \int_{-\infty}^{+\infty} BA(t,\tau) e^{j2\pi tv} dt$$

, and re-transforming the modified AF applying a two-dimensional FFT. In this way we obtain a Pseudo-WVD (PWVD), that is written as

$$PWVD(t,f) = \iint_{-\infty}^{+\infty} AF(\tau,v)\varphi(\tau,v)e^{-j2\pi(\tau v-\tau f)}d\tau dv$$

, where $\varphi(\tau,v)$ represents the kernel function (KF) to filter the AF. The KF has been obtained after a convolution and subsequent normalization of a standard Gaussian function.

After the computation every TFR has been smoothed with a triangular shape to increase the legibility of the results. The triangular shape has been convolved with the PWVD

$$PWVD_s = PWVD \otimes T$$

, where $\otimes$ is convolution operator and T is a triangular shape described by

$$T(t,x) = \begin{bmatrix} 1&1&1&1&1&1&1&1&1&1 \\ 0&1&1&1&1&1&1&1&1&0 \\ 0&0&1&1&1&1&1&1&0&0 \\ 0&0&0&1&1&1&1&0&0&0 \\ 0&0&0&0&1&1&0&0&0&0 \\ 0&0&0&0&0&0&0&0&0&0 \end{bmatrix}$$

The convolution operation change the amplitude of the frequency values (due to the convolution operations) and the dimension of the TFR (the size change from M to M+N-1, where M is the size of the TFR result N is the size of the triangular shape). For these reasons every smoothed TFR has been normalized to the original

frequency content and resized to the original dimension. The calculation of the TFR in the 2D and 3D seismic data has been done via project developed Matlab® applications (Appendix B) using the ARCCA (Advanced Research Computing @ Cardiff) cluster at Cardiff University.

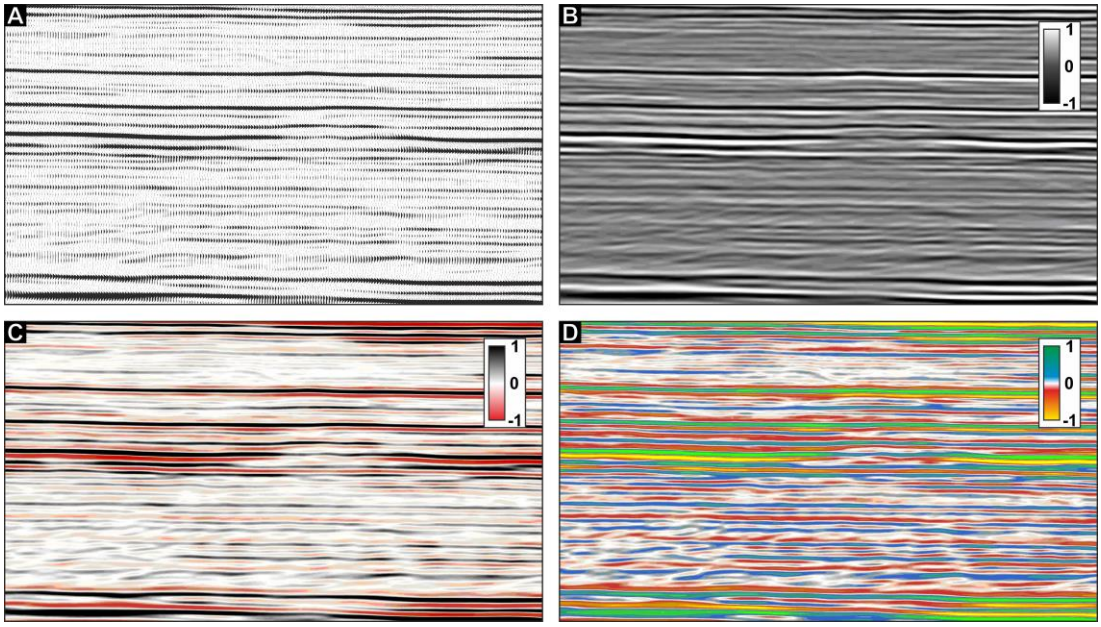

Figure 2.1Variable area (A) and variable density display (B, C and D). In this thesis variable area display will be use in few cases and only when it is necessary to control the shape of the seismic waves. Variable density display will be use in all other cases. Grey colour map (B) will be used to define structural features while the other colour maps (C and D) will be used to better visualise acoustic changes along reflections.

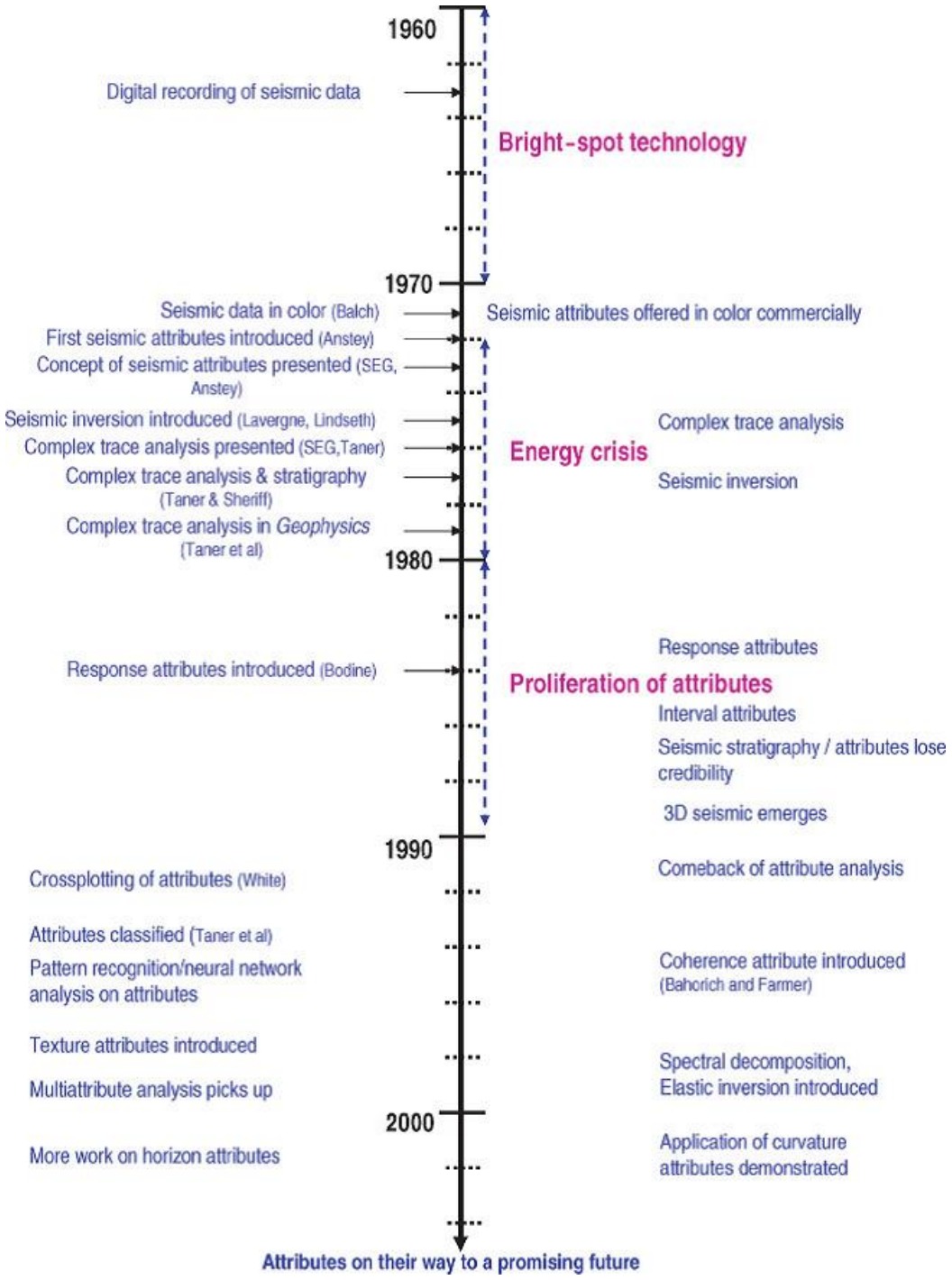

Figure 2.2 Evolution of technologies and methods used to interpret seismic data (from Brown, 2004)

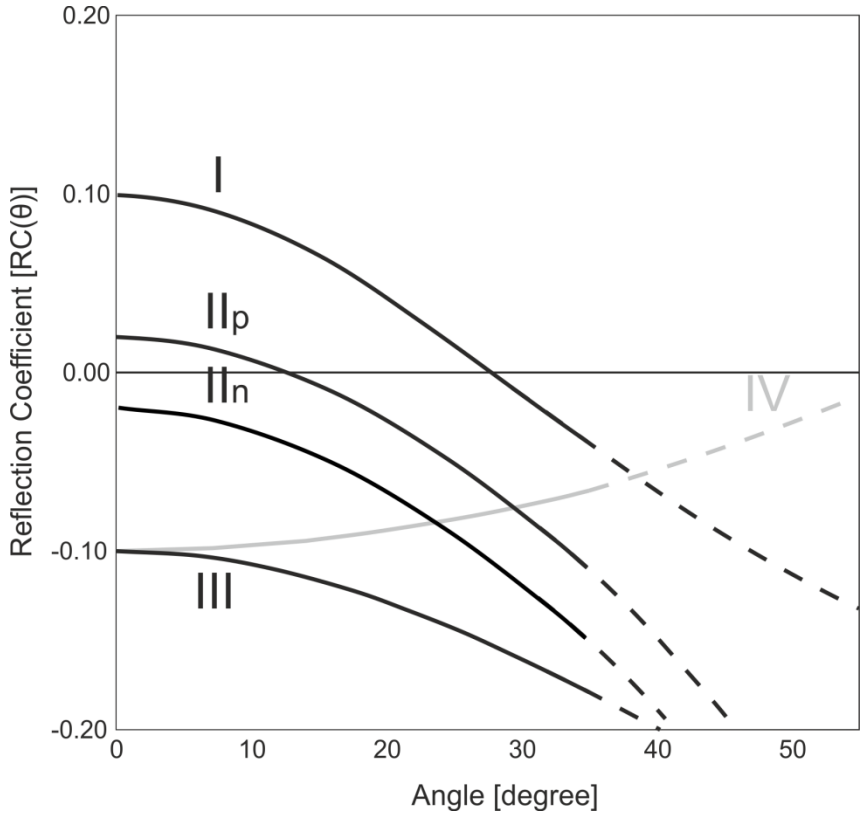

Figure 2.3 Variation of the reflection coefficient RC versus angle of incidence (after Rutherford and Williams, 1989)

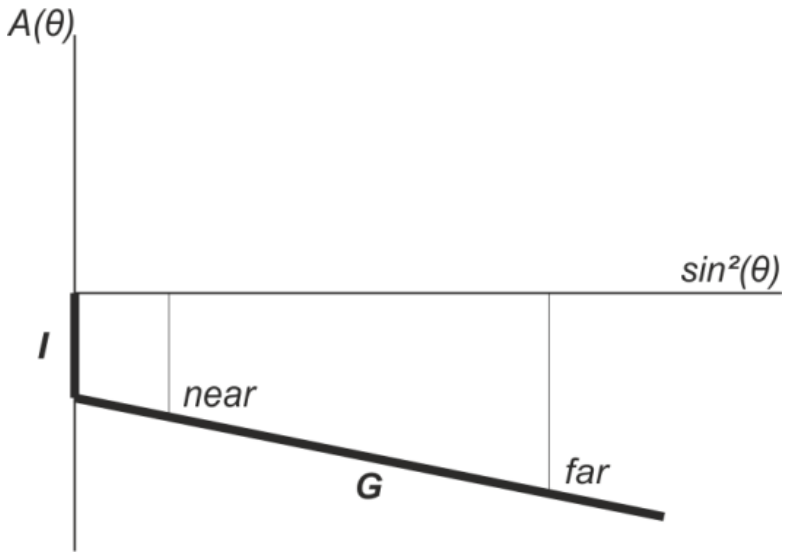

Figure 2.4 Cross-plot A(Θ)-sin2(Θ). The amplitude values estracted in near and far angle (or offset) are plotted in a cross-plot A(Θ)-sin2(Θ). The linear regression of these points provides a gradient G and an intercept I value which are used to generate AVO cross-plots (Castagna, 1996).

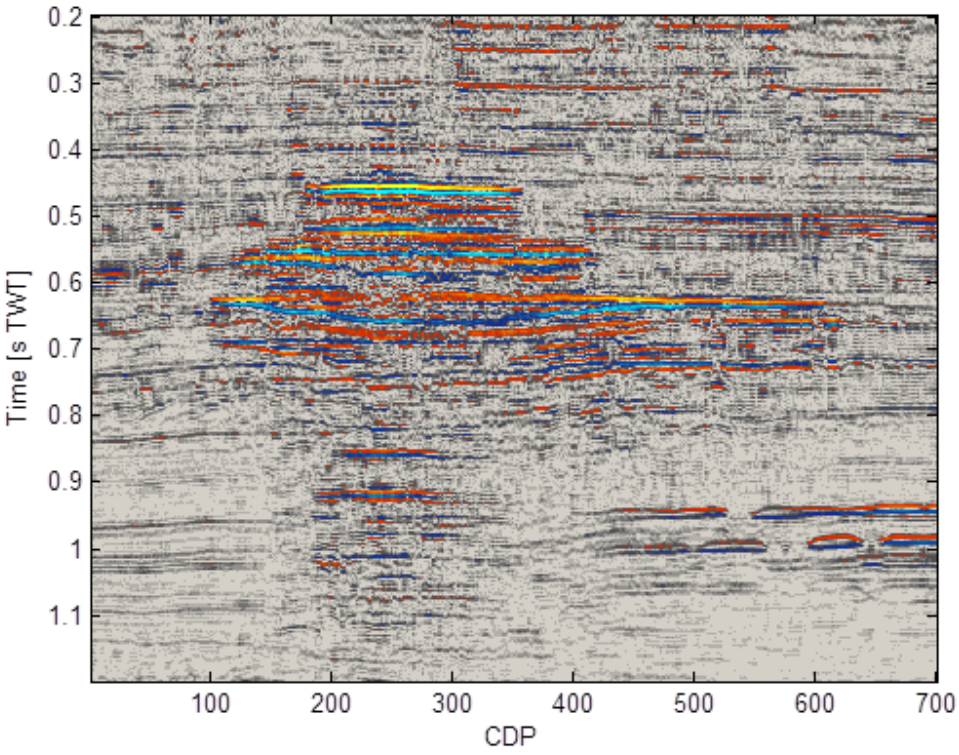

Figure 2.5 2D seismic section depicting stacked amplitude anomalies from Dutch North Sea (van den Boogaard and Hoetz, 2014). The amplitude anomalies, related to biogenic gas, are used to show the response of the pseudo-Wigner-Ville distribution (PWVD).

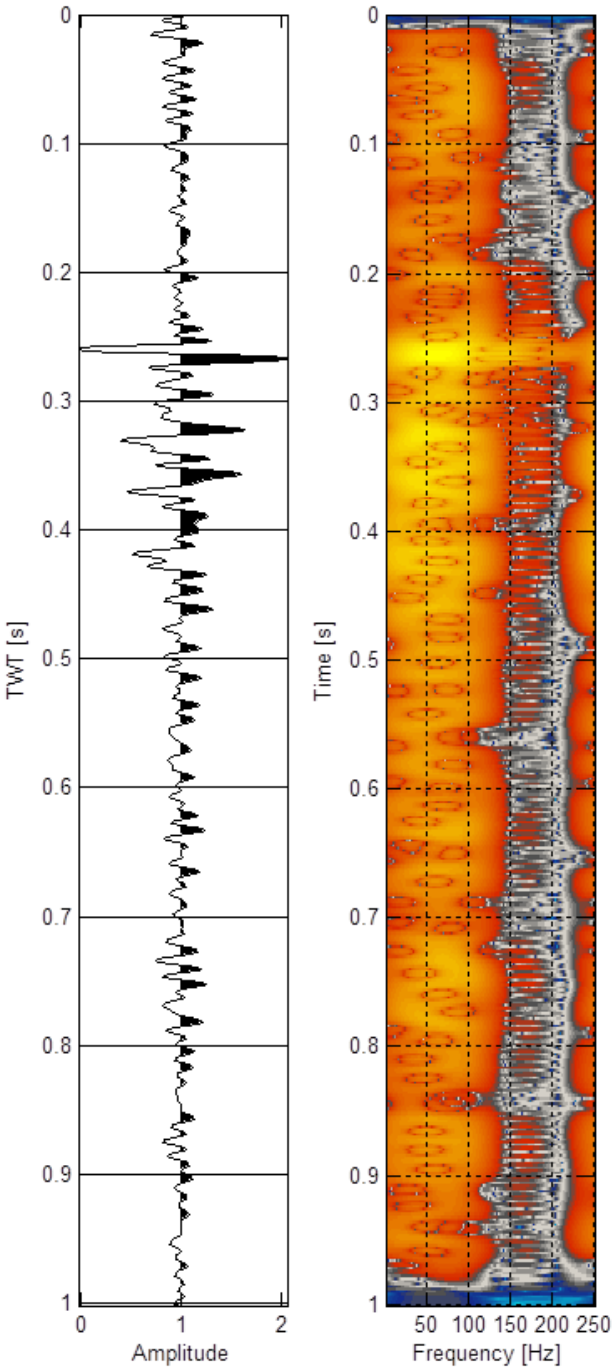

Figure 2.6 Seismic trace (left) and time frequency representation (TFR, right) from CDP 250 in Figure 2.5 using the pseudo-Wigner-Ville distribution (PWVD; see section 2.3.2.2).

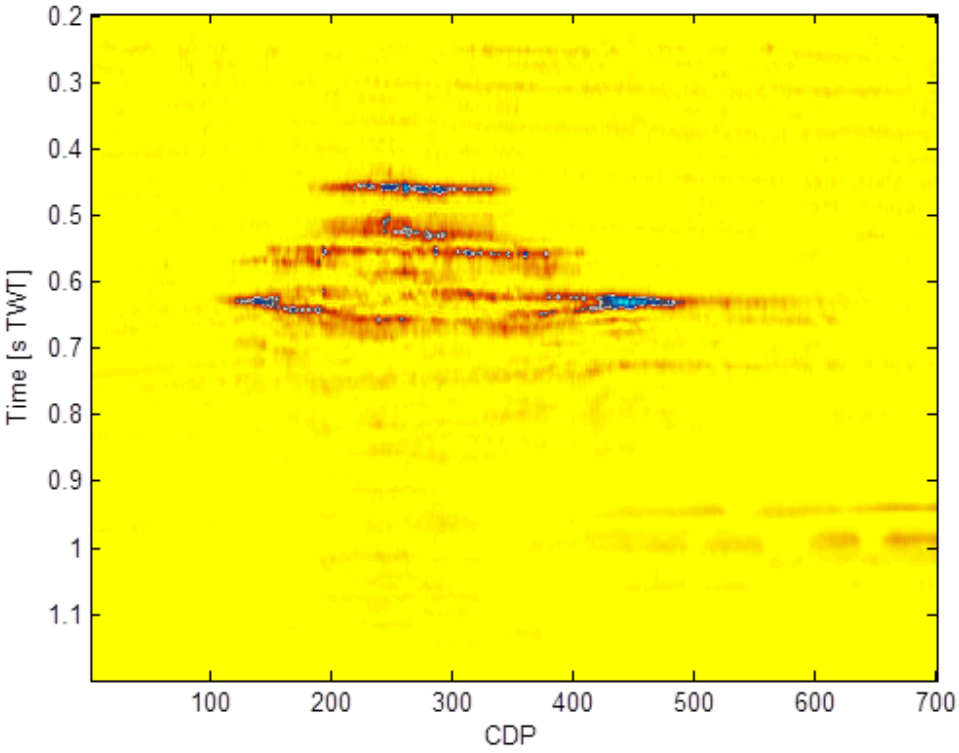

Figure 2.7 Iso-frequency response from the 2D seismic section displayed in Figure 2.5. The response is constructed selecting for each TFR (e.g. Figure 2.6) a single profile for a given frequency value. In this case, the image represents the variation in energy in dB of the 20Hz.

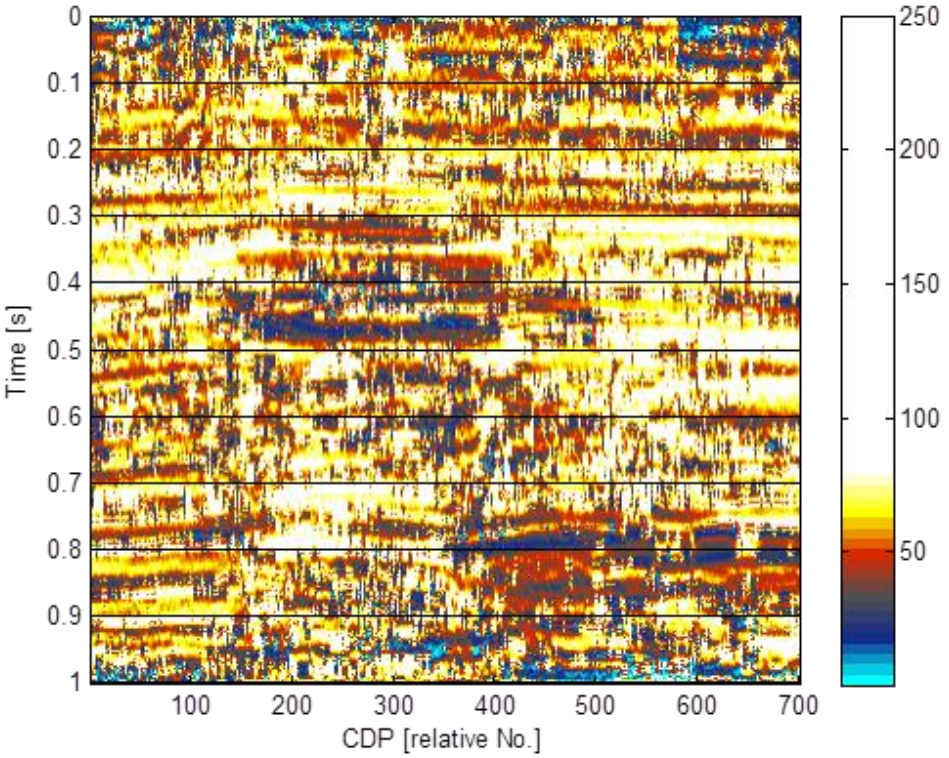

Figure 2.8 Frequency-peak series obtained selecting for each TFR (e.g. Figure 2.6) the series of frequencies associated with the maximum energy in dB. Note that only a subset of the amplitude anomalies is associated with frequency shadow zones. The method highlights also some normal faults present beneath the stacked amplitude anomalies

3. Vertical anomaly clusters: evidence for vertical gas migration across multi-layered sealing sequences

3.1. Introduction

3.1.1. Background

The migration of hydrocarbons within the shallow sections of petroliferous basins has been the focus of increased research activity in recent years, largely because of the wider availability of high resolution 2D and 3D seismic data (Berndt, 2005; Cartwright et al., 2007). In a recent review, Løseth et al. (2009) summarised the main acoustic characteristics of hydrocarbon migration (leakage) on seismic data, and discussed the formation and recognition of contrasting DHI types such as gas chimneys, dim zones, flat spots, bright spots and velocity anomalies. Similarly, more focused research studies have recently been undertaken to try to understand how various types of fluid flow phenomena visible on 2D and 3D seismic data are connected into more holistic petroleum plumbing systems (Andresen, 2012; Moss and Cartwright, 2010; Imbert, 2009).

One of the problems confronting interpreters who seek to recognise and characterise DHIs on seismic data is the plethora of terms applied to hydrocarbon indicators, and the diversity and overlap in definitions and observational criteria used to identify specific DHIs. This problem stems partly from the diversity and spectrum of individual occurrences, and the natural overlap that exists between features that form by the same process, but whose seismic expression is sufficiently different to warrant use of different descriptive terms. This terminological ‘maze’ has perhaps obscured the need to better understand the processes of migration and filling that underpin each DHI.

3.1.2. Aim and rationale

In this chapter, the aim is to describe a newly recognised class of DHI, namely a Vertical Anomaly Cluster (VAC). This is an assemblage of closely related DHIs that would traditionally be labelled as amplitude anomalies or bright spots, but where the assemblage is demonstrably linked by the migration process. The intention here is not to burden the interpreter with yet another term, but rather to identify a systematic grouping of seismically mappable objects that collectively define a linked system that derives from a specific set of factors that control gas migration. By highlighting this assemblage within a new descriptive framework, the aim is to focus attention on the process and to shed light on migration mechanisms.

The approach taken in this study closely follows the multi-interpretation strategy previously adopted in fluid flow studies based largely on seismic data (e.g. Calves et al, 2008, Satyavani et al., 2005) and defined in Chapter 2. This approach maximises the potential seismic data by providing a semi-quantitative analysis of the amplitude anomalies distributed in the target stratigraphic interval combined with a time-frequency representation (TFR) and AVO analysis to evaluate the presence of gas-charged layers (Castagna et al., 1998).

The study presented here is based on a regional 2D survey of the east Falkland Basin (Figure 1.6 and 3.1) has the primary aim of providing an interpretational workflow to analyse the systematics of a vertically stacked suite of amplitude anomalies, with a view to (a) establishing whether they are due to hydrocarbons, and (b) understanding the significance of their spatial relationships within a process context. Secondary aims are to discuss the occurrence of this type of amplitude anomaly cluster within the petroleum system of the basin, explain their genesis and

distribution, and to consider the wider implications of the genetic model for other DHI classes, notably gas chimneys.

3.1.3. Dataset

The primary database used in this study comprises c. 8,000 line kilometres multichannel 2D seismic lines, providing a c. 10 by 10km grid (5km locally) over an area of 10,000km ^{2} of the east Falkland Basin (Figures 1.6 and 3.1C). Well calibration was only possible through long range (c. 400km) correlation to DSDP wells 330 and 511 drilled on the outermost (eastern limit) of the Falklands Plateau (Figure 3.1B). The regional correlation was undertaken by interpretation of multichannel reflection 2D seismic line RC2106-139 stack, collected during the Robert Conrad cruise 21-06 in 1978.

The seismic data were acquired by GSI Inc. in 2005-06. The data were processed using 4 different processing flows: two surveys have been processed using raw and enhanced anisotropic time migration and two by angle-based selection of the CDP gathers traces in near and far angle stack (see Appendix A for the detailed processing flow). The latter were used for AVO interpretation while the former were used primarily for standard seismic interpretation purposes.

All the seismic data were acquired with a sampling interval of 4ms allowing a maximum frequency of 125Hz (Nyquist frequency). The CDP trace spacing is 6.25m (20.50ft) and provides a high lateral resolution. The different processing flows yield contrasting dominant frequencies and hence, vertical resolutions. The vertical resolution, using an average velocity of 2.3km /s (7545ft/s) and assuming that it is given by 1/4 of the dominant wavelength λ (Widess, 1973), ranges between 13.12m (43.04ft, on near-angle stack section) to 21m (68.89ft, on far-angle stack section)

with a theoretical average of 17m (56ft). The data are all processed to zero phase and American polarity (black peak positive; Brown, 2004).

The main focus of this study is the central portion of the dataset and spans the uppermost portion of the basin fill above a level corresponding to 4s TWT.

The seismic-stratigraphic interpretation of the data was based on subdivision into correlatable seismic ‘units’ that were characterised by a combination of distinct reflection configurations and seismic facies rather than a formal sequence stratigraphic approach (e.g. Posamentier et al., 1988; Posamentier et al., 2007). This approach was taken since it was judged more effective in the slope depositional system that was in evidence during the entire interval of interest, and where classical sequence boundaries are lacking.

3.2. Geological setting

3.2.1. Falkland Plateau Basin

The Falkland Plateau (FP) covers an area of ~120,000km ² (excluding the Falkland Island [74,558mi²]) at the southern limit of the Atlantic margin of South America, (Figure 3.1A-B). It is bounded to the north by the Falkland Escarpment composed by the westernmost extension of the Agulhas Fracture Zone, and to the south by the Falkland Trough and the Boordwood Bank. The east Falkland Basin (EFB) represents the westernmost portion of the Falkland Plateau.

The geological evolution of the Falkland Plateau is largely known from the combination of drilling results in DSDP 330 and 511 and single/multichannel seismic data collected during the ‘70-‘80 (Figure 3.2; Ludwig, 1983). The Falkland Plateau was formed during the break-up of the Gondwana during the Early Cretaceous (Platt and Philip, 1995). From the Falkland Island to the east the Falkland Plateau presents a progressive thinning of the continental crust from about 30km thick (Falkland Island included) to 16km in the centre of the plateau (Richards et al., 1996). The decrease in thickness is achieved in c.a. 150km presenting a series of normal faults mainly down-throwing to SE and oriented NE-SW (Figure 3.1B, red lines; Richards et al., 1996). Some of these normal faults are visible in the shallow part of the basin at the east offshore of the Falkland Island (Figure 3.3B) in which the top basement is clearly recognizable due to the strong acoustic response. Further east and in correspondence of the Maurice Ewing Bank (a submarine structural high) the basement, clearly recognisable on seismic data, have been encountered by the DSDP well 330 (Figure 3.2C). Here the basement was calibrated by Barker et al. (1976) where it is composed of granite of Precambrian age (Barker et al., 1976). The

Falkland Plateau Basin is consistent with an interpretation of a rifted continental margin (Ludwig, 1983).

In the central portion of the Falkland Plateau and above the study area, low signal to noise ratio at greater burial depths and prolific igneous intrusion (Richards et al., 2013) masks the top basement marker and make detailed correlation and mapping extremely difficult. The sediment thickness in that portion of the Falkland Plateau is estimated ranging from <7km (4.34mi; Zabanbark, 2011) to 11-12km (6.2-7.4mi; Richards et al., 1996).

The basement is overlain by a source prone Oxfordian to Early Kimmerdgian succession interbedded with silty-claystones and limestone deposited in relatively small rifted half grabens, and which are variably intruded by igneous sills recently dated Valanginian-Hauterivian (Richards et al., 2013) The greater part of the Cretaceous interval up to and including the Campanian is dominated by claystones and chalks deposited under pelagic to hemipelagic conditions, in a post-rift setting of thermal subsidence of the margin. This depositional and geodynamic regime continued on through the Cenozoic, but there is increasing evidence from the Oligocene onwards of strong bottom current influence on the depositional system in the form of deepwater erosion surfaces and contourites (Del Ben & Mallardi, 2004).

The exploration of the Falkland Island basins (Malvinas Basin excluded) started in 1950s with a series of seismic profiles across the Falkland Island. The first important observation regarding source rock and hydrocarbon potential arrived from the DSDP wells drilled 20 years later. From the 1977 to the 2006 GSI, western Geophysical (subsequently Geco-Parakla) and Spectrum acquired a total of more than 40.000 km (24,845mi) of 2D seismic lines. In 1998 six wells operated by different companies (nowadays Desire Petroleum, Argos Resources and Rockhopper

Exploration) have been drilled in the North Falkland Basin. In the last decade, other 5 wells have been drilled in the South Falkland Basin and in Falkland Plateau Basin. The first, Toroa, operated by BHP Billiton resulted dry (coal deposit) meanwhile Darwin, Stebbing, Loligo and Scotia (the first two operated by Border and Southern and the last two by FOGL) showed condensate gas discoveries in good quality reservoirs and gas in poor quality fine-grained reservoirs, respectively.

3.2.2. Seismic Stratigraphy of the Study Area

The gross stratigraphy of the study area is illustrated in a representative seismic profile across the study area (Figure 3.3), which shows a basinward thickening, post-rift sedimentary wedge of Cretaceous and Cenozoic age. The seismic data available to this study was truncated at 4s TWT for confidentiality reasons (see Author's notes), so the underlying basement and syn-rift successions, partially visible on this profile in the westernmost portion of the seismic grid (e.g. Figure 3.3B), are not mappable using the seismic grid. Hence they are excluded from further discussion. Instead, the main mappable interval (Figure 3.3C) is divided into three seismic-stratigraphic 'units', defined from their configuration and seismic facies, and it is these that form the main interval of interest to this study. The chronostratigraphic ranges for these units are based on stratigraphic information in Platt and Philip (1995), Richards et al., (1996) and long-range correlation to the DSDP wells.

3.2.2.1. Unit 1

Unit 1 is thought most likely to be entirely Late Cretaceous in age, based on long calibration with the DSDP well (Figure 3.2), and characterised by low amplitude

reflections that are pervasively offset by closely spaced normal faults. These faults are layer bound and conform to the structural criteria exhibited by layer-bound compaction faults that occur widely in fine grained sediments along continental margins (Cartwright and Dewhurst, 1998; Cartwright, 2011). The gross geometry of this unit is parallel stratified with a maximum thickness of c. 1100m, but it can be systematically subdivided internally into two wedge-shaped subunits of similar gross thickness variation, (1a and b), but which have complementary wedge geometries i.e. the lower wedge (wedge a, Figure 3.3C) thins but the upper wedge (wedge b, Figure 3.3C) thickens downslope (eastwards), respectively. The lower wedge (Unit 1a in Figure 3.3C) has been interpreted as a lowstand wedge by Platt and Philip (1995). The upper wedge resembles a typical slope healing system (Prather, 1998), with thinning and onlap occurring in an upslope direction. The low amplitude response is typical of fine-grained sediments, which accords with the calibration for this interval in the much more distal position occupied by the DSDP wells (Figure 3.2C).

3.2.2.2. Unit 2

Unit 2 is a weakly divergent sedimentary wedge, systematically thickening downslope from c. 500m to c. 1,300m in thickness across the study area that has been dated in the range Upper Cretaceous to Eocene (Platt & Philip, 1995; Fish, 2005).

The unit is characterised by extremely high lateral continuity of constituent reflections that individually have low, moderate or high amplitudes. The laterally continuity and context are both consistent with an interval dominated by hemipelagite deposition in a mid-to-upper slope position (Brown and Fisher, 1977). Equivalent sediments intersected by the DSDP wells further east are found to be

exclusively hemipelagic to pelagic nannofossil chalks to claystones (Figure 3.2C; Barker and Dalziel, 1976).

Unit 2 is bounded at its base by a prominent, laterally continuous, high amplitude soft reflection, termed here Reflection K, and at its top by an equally prominent high amplitude, hard reflection, termed Reflection L (Figure 3.3). Unit 2 is remarkable in one major respect: it hosts a large number of seismic amplitude anomalies (AAs, Figure 3.3C, AA). These are immediately identifiable by the much higher amplitude response compared to the background reflectivity, and the sharp lateral cutoffs in amplitude. To facilitate the quantitative analysis of the distribution of these AAs, the unit is divided into four sub-units (2a-d) simply based on mappable reflections, for convenience, and to allow comparison of the stratigraphic position of AAs across the study area.

There are variable degrees of small scale faulting apparent within some of the sub-units. Typically, small normal faults can be interpreted in 2a-b inclusive, but are rarely seen in subunits 2c-d (Figure 3.3C). These small normal faults are, by analogy with the more pervasive sets seen in Unit 1, considered to be layer-bound compaction faults (sensu Cartwright and Dewhurst, 1998).

3.2.2.3. Unit 3

Unit 3 extends from the top of Unit 2 to the seabed and represents a weakly wedge shaped c. 1000m thick sedimentary succession of probable Cenozoic age. The lower part the Unit 3 is characterized by weak reflections, strongly disrupted by another layer-bound normal fault system (Figure 3.3C, D). However, leaving aside the discontinuity related to structure, the lateral consistency of the amplitude

characteristics of the reflections suggests a pelagic to hemipelagic mode of sedimentation through the interval.

The upper part of Unit 3 exhibits undulating reflections marked by moderate to strong amplitude responses. The reflections are gently concave and eroded at the seabed. These sediments are interpreted as a contourite deposits based on their internal geometry and a comparison with similar packages documented in the South Falkland Basin (Bry et al., 2005). This upper part of Unit 3 is also transacted by the faults propagating upwards from the lower part. The faults are better imaged due to the high amplitude response of the interpreted contourite deposits. At a position typically c.150-200ms TWT below the sea floor is a prominent high amplitude positive reflection that can be traced in this position across the entire study area, and appears to cross-cut stratal reflections in places (Figure 3C, D). From the polarity and the cross-cutting geometry, this reflection is interpreted as a diagenetic reflection, and given the documented presence of siliceous-diatom rich sediments in the lateral equivalent to this Unit in DSDP 330 (Figure 3.2C), this horizon is interpreted as an Opal A-CT transition (c.f. Davies and Cartwright, 2002).

3.3. Amplitude anomalies in Unit 2

3.3.1. General acoustic description

474 amplitude anomalies (AAs) have been interpreted in the study area from the available 2D grid, and all of the mappable anomalies occur within the top 4s TWT. The AAs are recognisable as strong amplifications of the generally low background amplitudes associated with the inferred fine-grained sediments comprising Unit 2 (Figures 3.4, 3.5, 3.6, 3.7 and 3.9). They conform in all respects to seismic amplitude anomalies that are generally referred to as bright spots (Brown, 2004; Løseth et al. 2009).

Individual AAs are in all cases acoustically soft reflections (Figure 3.4B, C). All AAs are represented therefore by increasing negative amplitudes, from soft to soften. The AAs show appreciable amplitude amplification with values an order of magnitude greater than the background amplitude values of the laterally equivalent stratal reflection (Figure 3.4C). Many of the AAs have extremely sharp cut-offs in amplitude at their margins over a few traces (typically 50 - 100m [164 - 304ft]). The AAs are concordant with the stratal reflections, and there is no sign of erosion, or any other form of stratigraphic discordance that could be suggestive of a primary lithofacies variation. Instead, the acoustic response is invariably characterised by a simple amplifications of the primary background reflectivity (e.g. Figures 3.4, 3.5, 3.6, 3.7 and 3.9).

The apparent length of individual AAs is highly variable and ranges from 100m to tens of kilometres. The longest AA measured on seismic section is ~25 km (~15,5mi, Figure 3.5A). The thickness of individual AAs depends on the frequency of the seismic wavelet associated to the amplified reflection, and on the way in which the

waveform changes in response to the process giving rise to the amplification. Since dominant frequency varies survey-by-survey, and local frequency also varies in response to short range attenuation (see below), we can only give a broad range of maximum values for the layer thickness responsible for the amplification of the order of 10-40m.

It is commonly observed that within a single host layer (or subset of different layers), AAs appear as closely spaced individual anomalies. An excellent example of this is shown in Figure 3.5A, where in the lower portion of Unit 2 four separate stacked anomaly group are separated by lateral gaps. Similar patterns are seen elsewhere (e.g. Figure 3.6A), suggesting that this might either be due to a 2D profile intersecting a single, irregularly shaped anomaly, or that there are several discrete anomalies within close proximity amplifying the same background reflection.

3.3.2. Vertical Stacking of Amplitude Anomalies

One of the most important observations of the AAs encountered in the study area is that their vertical distribution systematically arranged in vertical to subvertical clusters or arrays (Figures 3.4, 3.5, 3.6, 3.7 and 3.9). Vertically Anomaly Clusters (VACs) are formally defined in this study as systematic, vertically stacked groups of individually imaged amplitude anomalies that collectively represent a single, identifiable region of seismic amplification of a background reflectivity series. Implicit in this definition is the sense that the stacking arrangement is not coincidental but has a strong causal link.

Systematic vertical clustering is evident in the vast majority of AAs in the study area, and only a few AAs occur as sporadic or isolated occurrences. Some representative examples of VACs are shown in Figure 3.6. Example in Figure 3.6A

has a maximum dimension in this profile of 7km , and the majority of the stronger, more continuous AAs are concentrated at the upper portion of the VAC, with less prominent and smaller AAs in the lower portion. However, all the AAs stack vertically, and the margins of the assemblage of AAs are subvertical, at least in this plane of intersection (2D seismic line). Example in Figure 3.6B there are two VACs of similar size and stratigraphic position, but example 1 has an inward tapering cross-sectional shape, with decreasing width at depth, whereas example 2 has a much more irregular distribution of the individual AAs, with no clear relationship between lateral extent and stratigraphic position. This latter example can be regarded as a type example of an irregular form, whereas examples in figure 3.6A and figure 3.6B-1 are both excellent representatives of regular forms. Note that this descriptive terminology only applies in 2D profile, with the caveat that we are not imaging the full 3D geometry of the VACs.

Lateral margins of VACs in the study area fall into two main types, although there is to some extent a spectrum between these end members. The first type is a sharply defined lateral margin, where either one or both margins has a stacking pattern that results in an almost linear edge to the VAC. Good examples of this can be seen on Figure 3.7. The vast majority of these sharp margins are diagonal (Figure 3.7) but in other cases they can show vertical margins (Figure 3.8B), at least in some sub portions of them. The flat and sharp margins observed in some VACs are associated also to reflection truncation of the underline and overlain unamplified horizons. Evidences of this observation can be seen on Figure 3.7. In that case the sharp margin has been interpreted as a fault that extends in the Unit 2 showing an eastward fault plain dipping (apparently) 24 degrees (@ 2.3km /s [7545ft/s]). The AAs are

truncated at the fault plane, suggesting a close interaction between faulting and seismic amplification.

The second margin type is much more irregular, with considerable overlaps and underlaps in the lateral positions of the individual AAs comprising the VACs. Excellent examples can be observed in Figure 3.4, in which the lengths of the AAs composing the VAC are decreasing upward and in Figure 3.6B-2 in which the AAs are simply stacked vertically with different lengths inside the VAC. The geometrical differences of the VACs associated to their lateral margin and their regular or irregular forms are indicative of an interaction between the AAs composing a given VAC and the geological context. The observed structural setting of Unit 2, characterized by reflection truncation and faults in the lower sub-units, can play a key role in the shaping of the observed margins and in the final geometry of the VACs. This will be discussed later.

In addition to the spectrum of geometrical stacking patterns, there is also considerable variation between individual VACs of the degree of amplification of the host reflectivity. For each VAC, it is possible to define an upper and lower stratigraphic limit for the VAC, with either greater or lesser vertical extent than neighbouring examples (e.g. Figure 3.6B, 1 and 2). However, within the defined upper and lower bounds, there is a large variation in the number of individual AAs within any given VAC. In order to make a quantitative comparison of the degree of amplification of the host interval, we introduce the term, *Stacking Factor*, defined as the proportion of amplified reflections within a specified host interval (bounded by the uppermost and lowermost AAs) out of the total number of background reflections.

Examples of VACs with low and high stacking factor values are shown in Figures 3.4 and 3.6. In low stacking factor examples (Figure 3.4), the individual AAs are relatively widely spaced vertically, and there are often one or more unamplified background amplitude reflections between AAs. However, as stacking factor increases, there comes a point where every reflection in a given interval is amplified such that acoustically hard side lobes of the soft reflections are also amplified to nearly the same degree as the soft reflections (Figure 3.6B-1). Stacking factors are considered in more detail below.

3.3.3. Attenuation and velocity push downs relating to the AAs

Zones of signal disruption are commonly observed beneath and within VACs in the study area, as seen for example in Figure 3.6A. In this example, the disruption recognized by amplitude dimming in the stratal reflections directly beneath the VAC. Background amplitude response is regained immediately outside this zone of dimming. According to Løseth et al. (2009) this dimming effect can be due to gas charging, as widely observed in association with gas chimneys and other gas-charged structures (Sun et al. 2011, 2012a and 2013). The signal disruption seems to apply irrespective of the continuity of the AAs within each VAC, but is certainly more dramatic where the AAs have greater lateral continuity.

Systematic downbending of stratal reflections in the regions beneath VACs is also observed throughout the study area, but particularly beneath and even within VACs with a higher stacking factor. These downbent reflections are generally lower amplitude with respect to their lateral continuations. The vertical extent of the downbending cannot always be ascertained because of truncation of the seismic data, but in some observed case is higher than 100ms TWT (e.g. Figure 3.6B-1). There is

no evidence to suggest that these downbent reflections are deformed into sags or collapse structures. From the geometry, and the close spatial relationship between the VACs and the downbent zone, we interpret these downbent regions as being due to push down, a well-known artefact in regions with localised low velocity anomalies (Brown, 2004). This interpretation suggests a clear link between the AAs in the VACs and the zone of push down, and furthermore that the AAs are linked to low velocity anomalies. Such a connection is well known in regions of shallow gas accumulation or CO2 storage (Arts et al., 2004a-b; Boait et al, 2011).

3.3.4. Spatial Distribution of the Vertical Anomaly Clusters (VACs)

In order to examine the geographical distribution of the observed VACs and correlate them to the basin features a spatial distribution has been carried out. The mapping has been done simply projecting vertically, on an arbitrary horizontal surface (or datum plane), the maximum extension of the singular VACs observed on 2D seismic section (figure 3.8B). Neglecting at this time the limitations of this method, mainly associated to the loss of information of the AA distributions inside the VACs and the inevitable uncertain responses in regions scarcely covered by seismic data, the results revealed some important features.

The projected VACs (black segments, figure 3.8A) are distributed in a (linear) corridor oriented NE-SW (dashed red line, figure 3.8A). The VAC corridor, measured along his longitudinal axis (NE-SW), is c.76km wide, c.225km long. The west margin partially follows the TWT contour of the base of Unit 2 (or K-reflection at 3s TWT). The VAC distribution inside the corridor is inhomogeneous, with local VAC concentrations and empty spaces. The projected VACs, occurring in adjacent and closely spaced 2D seismic lines, have been empirically connected each other and

their resulting shapes analysed. Accepting the limitation of the adopted method and applying an elementary shape analysis in the southernmost part of the basin (better seismic coverage) we can observe that the VACs do not form large groups. The sizes of the shapes range between 4.73 km and 26.5 km. The VAC planforms are variable and present different shapes. For example, VAC 1 and 2 showed in Figure 3.8A display elongated structures trending E-W meanwhile VAC 3 displays a double-blob shaped plain-forms. Also small VACs characterized of more rounded shapes. (Figure 3.8-VAC 4) and different trends respect to the other VACs have been found.

The geographical distribution of the VACs associated to their extrapolated plain-form shapes seem not associated to the stratigraphic features of the basin. The hosting eastward dipping reflections composing Unit 2 do not affect the shape and the orientation of the VACs. Neglecting the useful information from the shape analysis, maybe too simple for a robust discussion, it remains however to link the positions of the VACs to the study area. How we can justify the position of the VAC corridor? Can deeper structures control the positions of the observed VACs in Unit 2?

3.3.5. Quantification of vertical distribution

Earlier, it was noted that there is marked variation in the stacking factor. To quantify the variation, and to examine to what degree specific subunits with Unit 2 acted as preferential hosts for the anomalies, a detailed grid of reflection correlations was carried out on all mappable horizons within Unit 2. The Unit has been therefore divided following the soft reflections (negative amplitude, red-yellow), and for each one has been counted the number of AAs (Figure 3.9A, B and C). The counting has been weighted multiplying every single count (or anomaly in a given reflection)

times the length of the related anomaly displayed on seismic data. This analysis has been carried out in all 2D seismic lines.

Accepting uncertainties encountered during the interpretation of the singular reflections and their correlation in all the study area this method has revealed an inhomogeneous vertical distribution of the AAs inside Unit 2 (Figure 3.9D). The K reflection (reflection 37, Figure 3.9D) hosts the vast majority of the encountered AAs with a cumulative length of 689.27 km (19.24% of all interpreted AAs). Excluding K reflection in the Unit 2 the reflection 21 hosts the highest number of AAs with a cumulative length of 328.06 linear km (9.15%). This layer will be used for further descriptions. Other notable layers are reflections number 17, 20, 22, 27 and 36 that host cumulatively more than 27% of all AAs. From reflection 13 to 37 is hosted more than 94% of the AAs underling a preferential distribution of AAs in the mid-lower portion of Unit 2.

Correlating these simple numerical values with in Unit 2 we can point out that (1) Unit 2b and the lower part of Unit 2c host the largest number of AAs, (2) the low presence of AAs between reflection 33 and 28 is coincident with the central portion of Unit 2a that correspond to faulted weak amplitude continuous reflections and (3) the low number of AAs in the reflection interval 1-12 can be associated to a change of properties in Unit 2d suggesting in correspondence of reflection 12 a potential change of lithology or structural setting.

The close relationship between the amplified portion of the K-reflection and the presence of VACs above suggested us to compare amplitude maps computed on K-reflection and in other reflections inside Unit 2. The aim of this observation is to emphasise the grade of verticality of the VACs and determine whatever different VAC geometry can be correlable to the basin features. The high number of AAs

observed in Reflection 21 (R_{21} hosts the 9.15% of the all interpreted AAs) suggested to use his acoustic amplitude map to maximise the grade of superimposition with K-reflection (19.24%). The distance between the horizons is c.500m. To ensure a good detail of this observation and make reliable observations the maps have been calculated in a sub-area located in the southern portion of the dataset (denser seismic coverage).

The calculated amplitude maps are displayed in Figures 3.10B and C. Both maps are calculated along soft reflections. The K acoustic amplitude map (Figure 3.10B) shows as already observed in the VAC map a patchily amplified area that trend NE-SW. The anomalies, confined in the eastern portion of the map (anomaly boundary, AB), as already mentioned in Figure 3.4C present large variation in acoustic response. The acoustic patchily distribution does not seem to resemble any particular sedimentary structures. The map presents some seismic grid-related acoustic artefacts.

The R_{21} acoustic amplitude map (Figure 3.10C) shows a different response. The northwest portion of the R_{21} map shows an amplified area (A) which trends NE-SW. The amplified portion lies with the same orientation of the impinging onlapping reflections composing Unit 2 (Figure 3.3C, tuning AA). Since the amplified area resulted, in all the cases, as an isolated anomaly, not presenting other amplifications in the underling and overlying horizons and not showing the characteristics associate to the described AAs (sharp cutoffs, push-downs, etc.) it has been interpreted as an effect of tuning (e.g. Partyka et al., 1999) of the R_{21} with the overlying one (reflection 20). Further southeast the R_{21} map shows sub-rounded anomalies organised as clusters (C1 and C2). Isolated tiny AAs are also present in the map.

The superimposition of the two maps has been done projecting only the anomalies below an amplification threshold of -10.000 for both maps and applying the line contours of their acoustic responses.

The result of this operation (figure 3.10D) reveals a partial superimposition of the two maps in which some R_{21} related AAs are located near above the K-reflection ones. Since K reflection host more than 10% of AAs respect to R_{21}, some K-reflection AAs do not show vertical links and vice versa. The relative positions between K-related AAs and R_{21}-related AAs (AA pairs) are variable. Examples of these variable distributions are showed in the AA pairs in P and P1 in which the R_{21}-related AAs are located eastward respect to the K ones beneath. In P2 and P3 the R_{21}-related AAs are located westward respect to the K ones. In area V the AA pairs, regardless the large differences in anomaly extension, are located at the same positions showing a good vertical alignment.

The verticality of the VACs seems not to be influenced by the stratigraphy of the basin, especially by the eastward dipping horizons composing Unit 2. Can therefore the VAC geometry be unrelated to the basin features and be indeed controlled by local structural features?

3.4. Amplitude anomaly analysis

3.4.1. AVO analysis of the amplitude anomalies

From the planform and distribution of the AAs on individual horizons and the spatial distribution of the AAs within VACs, it is difficult to accept an interpretation of the AAs as being entirely due to lithology. Instead, from the observed push down effects, and attenuation beneath the anomalies, it is much more probable that the AAs are due to the presence of a fluid with different elastic characteristics to the one in not amplified portion (fluid substitution). To explore this possibility further, AVO analysis was undertaken on all the profiles for which near- and far-angle stacks were available. 4 profiles were analysed in this way, and in all cases similar results were obtained. To illustrate the results in more detail, we illustrate the AVO analysis using the VAC in Figure 3.11.

The showed line is located in the central part of the study area (Figure 3.1C) and crosses a large, irregular VAC consisting in this profile of a number of strong AAs distributed vertically throughout Unit 2, over a lateral distance of c. 10km . Six distributed AAs (A, B, C, D, E and F in Figure 3.11) were selected for AVO analysis based on their representative high amplitudes, and stratigraphic distribution, since it was important to see if AVO response varied with stratigraphic position.

The first AA lies in the middle of the selected window (Figure 3.11). The relative cross-plot (Figure 3.11A) show a very steep background trend (blue) and an appreciable anomaly trend (yellow). The anomaly trend, not perfectly parallel to the background one, lies between 3020 and 3040ms corresponding to the first soft reflection on the seismic data window. Following the gradient-intercept cross-plot classification of Castagna (Castagna and Smith, 1994; Castagna and Swan, 1997)

that trend is mostly associated to AVO class III. Similar responses have been obtained in other analyses like those observed in the examples C, D. Multiple anomaly trends have been observed also. One example of this kind of response is showed in the AVO analysis in E. The anomaly trend is composed in that case of three parallel sub-trends with decreasing extension and increasing separation from the background one. The example B and F presents a different AVO class IIn/III with anomaly trend located downward respect to the back ground ones. In those cases the background and anomaly trends are very close each other.

3.4.2. Time-Frequency Representation

The AVO analysis points to the likely origin of the AAs as being due to the presence of a compressible fluid may associate to free gas phase. To further evaluate this a Time-Frequency Representation (TFR, Cohen, 1995) was computed for selected profiles where there were VACs of both high and low stacking factor distributed across Unit 2, two representative examples of which are presented in Figure 12A-B. In general, there is a close correspondence between the frequency representation and the stratigraphy, as would be expected in shallow parts of basins. In addition, the TFR response, also as expected (Sheriff, 1975), shows a decrease of high frequencies from a standard value of c. 40Hz over much of the Units 1,2 and 3 , to a low background value of 15-20Hz below Unit 1 (Figure 3.12A-B).

Remarkably however, a number of irregular regions that crudely mimic the stratigraphy can be observed distributed throughout the central parts of the profiles, particularly in Unit 2, and just beneath the K reflection. In nearly every case, these low frequency ‘shadows’ have an average frequency value of <15Hz compared to the background value of c. 40Hz.

These shadow zones are found in nearly every case to be closely related to prominent AAs composing VACs. In most examples, they form small patches of low frequencies around and within AAs. In other cases, the shadow occurs directly beneath an AA, as for example seen particularly clearly S1 (Figure 3.12B) with shadows extending downward for 200ms TWT. In other cases the shadows are accompanied by diagonal patterns as seen on S2 (Figure 3.12A) directly beneath AAs located at the K-reflection and not associated to seismic amplifications showing the same geometry.

In summary, the close juxtaposition of sub-horizontal shadow zones of significantly lower frequencies than background values with associated AAs suggests a direct causative relationship between the presence of the AAs and the attenuation. Since the presence of free gas in porous sediments such as sands or silts is well known to lead to strong frequency attenuation, the Time-Frequency Representation profiles provide strong support for the AVO analysis and other qualitative observations that the AAs can be due to free gas.

3.4.3. Quantitative Analysis of Push Down Effects

To provide a quantitative velocity variation measurement associated to the push-down effects observed beneath VACs a method, derived from the simple equation of the velocity (V=x/t), has been developed and subsequently applied. The measurements should provide some indications about the velocity dispersion associated to VACs.

The velocity variation ΔV can be expressed as the ratio between Vpush, the velocity associated to the push-down, and Vnorm, the velocity associated to an unperturbed area

$$\Delta V = Vpush/Vnorm$$

The velocities expressed can be rewritten in their explicit forms

$$\Delta V = Vpush/Vnorm = (Xpush/Tpush) / (Xnorm/Tnorm)$$

The push-down, in time domain represents an apparent bending of the perturbed horizons (e.g. Løseth et al., 2009), the space X is indeed constant in portions affected or not affected by push-down, therefore Xpush = Xnorm = X. The equation can be rewritten and simplified as

$$\Delta V = (X/Tpush) / (X/Tnorm) = Tnorm/Tpush$$

Using this simplified method to calculate the ΔV for a given VAC we just need to measure the time intervals in the push-down and in the unperturbed areas and calculate the ratio. In order to obtain a percentage value the ratios have been converted using, $\Delta V_{\%} = (1 – Tnorm/Tpush) \times 100$.

An example of this procedure is provided in Figure 3.6A. The Tpush measurements have been done calculating the time intervals at the maximum bending point (P) neglecting less prominent push-down effects. The Tnorm measurements have been done calculating the time interval at the margins of the perturbed areas (N1 and N2) averaging the values. In the example showed the ΔV was 5.84%.

This operation has been carried out in other 18 VACs in which the push down was quantifiable. The calculated ΔVs are variable and range from 1.23% to 10.52% with a mean value of 4.62%. Using an initial interval velocity of 2.3km /s [7545ft/s] the decreased velocities range from 2.27km /s to 2.05km /s, respectively. If the difference in velocity dispersion within the observed 18 VACs, ΔV_{vacs}, is 0.22km /s and it reflects the VAC characteristics can we use the just mentioned variation to understand the relationship between VACs of different size and pushdown effect?

3.5. Discussion

3.5.1. AAs or DHIs?

The observations presented above allow us to build a strong case that the 474 AAs in the study area within Unit 2 are related to the presence of free gas. These observations are summarised below with a discussion of interpretational uncertainties, and the paper then concludes with a discussion of the implications for hydrocarbon exploration in this region and more specifically for hydrocarbon migration mechanisms in dominantly fine-grained stratigraphic successions. Summary of critical observations:

1 Acoustic character and planform geometry.

The universal soft kick response and sharp change of amplitude observed along the reflections composing Unit 2 is consistent with many previous descriptions of bright spots associated with free gas (e.g. Brown, 2004). Similar responses in nearby areas have been described by Baristeas et al. (2012) and interpreted as hydrocarbon leakage indicators. Similar amplitude responses could be linked to the presence of overpressured sands, highly unconsolidated sediments or coal beds (Avseth et al., 2009; Sheriff, 1975). It is very improbable that the AAs could be due to the presence of coal layers, since firstly the depositional setting of Unit 2 is in the mid-upper slope, and not coastal or alluvial as required for the formation of coal layers. Secondly, the anomalies have irregular planform geometry, with many isolated and totally enclosed forms. These do not resemble the expected geometry of coal deposits. Indeed, the planform of the anomalies is hard to explain in any depositional

context, and does not immediately resemble any particular lithofacies association (see for example review by Posamentier and Kolla, 2003; Posamentier et al., 2007). A purely lithological explanation for the AAs can therefore be considered highly improbable.

2 Velocity Push Down

The observation beneath the more prominent VACs (i.e. those with higher stacking factors) of a significant velocity push-down effect ranging from a few percent up to >10% reduction relative to the background interval velocity of Unit 2 (Figure 3.6A) is consistent with the presence of a relatively higher compressible fluid (e.g. gas; Mavko et al., 2009; Løseth et al., 2009). Precise computation of the expected retardation in velocity cannot be made because of the lack of precise calibration of lithology of the host for the anomalies. However, a variation in Vp of 10% over the 1000-1200m thick interval of Unit 2 is at least a good first order match to what might be predicted for gas charged thin sands or silts amounting to say 20% N/G of the gross thickness (Mavko et al., 2009).

3 AVO analysis

The AVO cross-plots of the four profiles with near-far stack pair all exhibit down-to-the-left deviation from the background trends (Simm et al, 2000). This result, interpreted as AVO class III is commonly associated with gas sands (Castagna and Swan, 1997), and in the absence of a more probable lithological argument (see point 1) this is our preferred interpretation of the AVO response.

4 Low Frequency Shadows

The low frequency shadows that are immediately juxtaposed with the AAs argue strongly for attenuation that is directly due to the AAs. Previous studies making similar observations concluded that this effect was due to the differential absorption of frequencies within gas charged layers (Castagna and Sun, 2006; Wu & Liu, 2009). Faults and fractures can generate similar responses (Ilg et al., 2012); however this would not readily explain the concordance of the frequency shadows to horizon-restricted anomalies.

Summary

In conclusion therefore, the acoustic character, velocity slowness, frequency attenuation and planform geometry of the AAs all strongly support their interpretation as being due to the presence of free gas within particular host lithologies in Unit 2. If this is accepted as a plausible argument, what can we now say based on this of the likely reservoir intervals for this gas, and what does the vertical (stratigraphic) and geographical distribution of the anomalies tell us about migration and trapping mechanisms and the distribution and sedimentary properties of the reservoirs? In particular, since the evidence presented overwhelmingly points to the AAs being due to hydrocarbons (i.e. they can be regarded individually as DHIs sensu Millahn et al., 1978) and not as paleo-gas indicators (Francis, 1997), how does the striking vertical stacking of anomalies into VACs occur, and is there any reason to expect this type of clustered DHI more widely in other basins?

3.5.2. AA habitat

Accepting that the AAs are the result of free gas it is now the turn to discuss about their potential habitat. The anomalies are developed exclusively within Unit 2 within the study area. There is no nearby well to calibrate the lithology, so we are forced to rely on long-range correlation of the seismic stratigraphy to the DSDP wells to gain any lithological control. Clearly over such a long distance correlation, there is considerable uncertainty, however (1) the large continuity of horizons in the RC2106-139 line (Figure 3.2), (2) the deposition habitat of the Falkland Plateau (Figure 3.3) and (3) the seismic facies that characterize the seismic response of the top Units in the study area, suggest to do not discard completely the wells information and use them to provide a simplified description of the potential AA habitat in the study area.

The observed seismic facies of the layered Unit 2, associated to hemipelagite deposition in a mid-to-upper slope position (Brown and Fisher, 1977), is indeed in line with the alternation of 10-20cm thick bands composed of claystones and siliceous/calcareous ooze-diatoms rich sediments described in the DSDP wells 511 and 330 (DSDP report). This suggests us to consider a preliminary habitat dominated by binary layering constituted by seal-like layers alternated with reservoir-like layers with variable lithologies and hydraulic properties. Studies of pore throat sizes and permeability of oceanic sediments (e.g. Gamage et al., 2011; Spinelli et al., 2004) support variable permeability for the observed lithologies with range from $1 \cdot 10^{-13}$ - $0.5 \cdot 10^{-14}$ m^2 (siliceous-calcareous oozes) to $0.5 \cdot 10^{-16}$ m^2 -$0.5 \cdot 10^{-19}$ m^2 (hemipelagites; $1 \cdot 10^{-12}$ m^2 $\approx$ 1Darcy). The variability of these lithologies points out that the calcareous and the siliceous ooze imbedded in the hemipelagic succession have the

potentialities to constitute a more suitable habitat to host gas occurrences in the observed binary layering. Since from the seismic (average resolution of 17m [56ft]) we cannot provide any precise location of the mentioned more relatively-permeable lithologies we can however use the information of the AA vertical distribution to obtain their approximate position. The vast majority of the discovered AAs have been mainly founded in the central portion of Unit 2 suggesting in that portion (e.g. from reflection 13 to 27) a more concentration of more relatively-permeable lithologies rather than in the lower (from reflection 28 to 35) and upper portion (from reflection 1 to 12).

3.5.3. Horizontal gas migration

Neglecting at this time the possible mechanisms apt to transfer the observed fluids upward across Unit 2 (it will discussed later), can the shape of the encountered anomalies help in determining any other indications regarding the AA habitat and horizontal migration?

A striking observation of the AAs as revealed by amplitude mapping of the K and R_{21} reflections (Figure 3.10B-C) is their large lateral extent, but lack of preferred orientation of their longest bedding-parallel axis. This suggests that the observed parallel dipping layers composing Unit 2, extremely efficient in generating large gas occurrences (cumulatively more than 3582 linear km of AAs), are not however sufficiently suitable to promote an up-dip migration of gas and generate elongated NW-SE trending gas occurrences. If the migration of gas is not occurring in the up-dip direction what can we say about driving force the possible trapping mechanisms?

The large gas accumulations occurring in the dipping horizons are limited in their vertical extent. In a previously described example (Figure 3.5B) the height of the

longest anomaly has been calculated in 439m, but over a distance of more than 25km (<1deg). This observation poses limited columns of gas, especially in the vast majority of the much shorter AAs distributed in the study area. This feature suggests therefore a limited driving force (buoyancy) of the gas inside the thin reservoir like layers (e.g. Osborne and Swarbrick, 1997; Schowalter, 1979) and a non-predominant NW-SE extension of the AAs. The thin reservoir-like layers can therefore host gas, with enough saturation to generate the observed responses on seismic data (and related effects such push down, frequency shadow, etc.), but allow the generation of occurrences only in particular conditions. Since the gas inside the thin reservoir-like layers is not able to build up enough buoyancy to overcome the capillary entry pressure of the hosting lithologies (Berg, 1975) there must be at least a time-limited condition in which an external source of gas triggers the fluid migration inside those layers and generate the occurrences.

The presence of gas sources beneath K seems in line with the characteristics of the AAs enclosed in the VAC corridor (Figure 3.8). The patchily distributed AAs in that region, observable in the K amplitude map (Figure 3.10B) are characterized by space limited amplifications. This suggest that the gas is not migrating from the eastern margin of the K reflection generating elongated NW-SE AAs (Figure 3.13A), but it is flowing (maybe sub-vertically) from a deeper region intersecting the K reflection and generating on map the mentioned space limited AAs (Figure 3.13A). The presence of gas columns in Unit 1 could justify this hypothesis but since no evidence of fluid migration or AAs have been discovered in the small interval of data between K reflection and the data cut (4s TWT) we cannot provide any further explanation.

The presence of structural features, such faults and fractures, described in Unit 2 (in which they are predominately distributed in the subunit 2a), can attenuate the fluid migration along the relatively permeable layers. Striking examples of sealing faults have been indeed described in Figure 3.7 and also at flat margins (or sub portions of margins, Figure 3.4). The faults seem therefore to be effectively a potential trapping mechanism able to limit the gas displacement and generate the observed sharp AA cut-offs. The presence of the documented irregular VAC margins (Figure 3.6B-2) seem not be associated to faults or fractures suggesting therefore, in absence of sealing faults, a trapping mechanism associated to the singular hydraulic properties of the thin reservoir-like layers. This point will be discussed in the final model.

3.5.4. Vertical link between AAs and vertical gas migration

After the discussion about the horizontal gas migration it is now the turn to discuss about the possible mechanism apt to transfer fluids from a given reservoir-like layer to another one. From the SF analysis has been noticed that the vast majority of the observed VACs are composed of a subset of amplified reflections generally between 1 and 14 on a total of 37, posing a vertical migration mechanism able to cover a distance of 35-500m on a total of 1300m (that correspond to the thickness of Unit 2; 115 to 1600ft on a total of 4250ft). The gas migration is supposed to happen in an upward direction since has been observed a gradual decrease of AAs from the bottom to the upper horizons composing Unit 2 (Figure 3.9). Accepting those observations what we can say about the possible migration mechanism?

In the previously discussed setting, dominated by thin layers with different sealing and permeable properties, we can image that the migration mechanism should work as a cross-stratal migration (e.g. Hood et al., 2002; Hustoft et al., 2010). Taking in account the information from the DSDP well sites, the fluid migration mechanism should work with a series of many short range migration steps from a given reservoir to the next one above (Figure 3.13B). The thickness of these steps is directly associated to the thickness of the seals and therefore in line with the thickness range of the reservoir layers (10-20cm).

From the discussed low driving force inside the reservoir-like horizons (previous paragraph), interpreted as too low to allow up-dip migration, we assume unlikely that the same driving force can generate enough head pressure to fracture the thin seals composing Unit 2 and migrate upward (e.g. Jain and Juanes, 2009; Mandl and Harkness, 1987). This observation is confirmed by the complete absence of any clear vertical conduit such pipes (e.g. Moss and Cartwright, 2010) or gas chimneys (e.g. Loseth et al., 2003) on seismic data. If any evidences of vertical fluid flow have been observed on seismic data can therefore the presence of the observed faults and fractures in the basal horizons of Unit 2 (2a) promote the cross-stratal migration?

Subunit 2a (K reflection excluded), that represent a weakly amplitude package of reflections associated to a large number of faults and fractures, hosts a low number of AAs. In the other hand subunits 2b-c host the vast majority of the AAs and only a limited number of faults. This clear subdivision suggests that the faults and fractures in subunit 2a can work as fluid flow network (Brown, 2000), unable to host appreciable gas occurrences, as already documented in the AA vertical distribution, but allow the gas to reach the central part of Unit 2. Many of the observed faults and fractures end at the lower half of Unit 2 (late Cretaceous, Figure 3.3C) suggesting

their inactivity. This feature can maintain a permanent permeability (Cartwright et al., 2007) during the vertical gas migration. As in many other basins worldwide, a clear relationship between faults and fracture and gas migration have been successfully described (e.g. Cartwright et al., 2007; Loseth et al., 2009; Xie et al., 2003a-b; Ilg et al., 2012), leaving however unsolved, as for our case history, the clear fluid flow mechanism.

3.5.5. Conceptual VAC genesis model

Based on the interpretation of the 2D seismic data and the discussions about the nature of the observed AAs and their link and potential habitat we propose a conceptual model to explain the genesis of the VACs. The model is applicable on all observed VACs and takes in account the stratigraphic and structural setting mainly associated to Unit 2.

In the previous paragraphs we demonstrated that Unit 2 is characterized by (1) parallel dipping layers with thickness of 10-30cm (DSDP well information, Figure 3.2C) composed of fine grained sediments, (2) affected faults and fractures distributed mainly in the lower sub-unit 2a, (3) no evident erosional surfaces (Figure 3.3); in the other hand we discussed that the AAs are characterized by (1) sharp cut-offs (e.g. Figure 3.4), (2) strong vertical relationship (Figure 3.4, 3.5, 3.6, 3.7 and 3.9), (3) distribution in the basal horizons (K) and in the subunit 2b-c, (5) small column heights (Figure 3.5), (4) no clear evidence of gas pipe or gas chimney (the only potential pipe have been observed in Figure 3.7), (6) globular shaped planforms (Figures 3.8 and 3.10). Other important discussed point are (1) the dipping horizons seem not suitable for up-dip migration (Figure 3.7), (2) the sediments can be organized as binary reservoir-seal layering, (3) subunit 2a seems more suitable for

vertical migration (Figures 3.3C and 3.9), (4) faults and fractures can work as trapping mechanism (Figure 3.7).

Using that information we can finally introduce a conceptual model able to explain VAC geometry, genesis and fluid migration mechanisms (Figure 3.14). The model is based on an indicative variation of gas pressure that expresses low and peak pressure conditions. In the first step of the model we introduce an amount of gas at certain pressure from an injection point at the base of Unit 2 (Figure 3.14A). Since no AAs have been discovered beneath K we cannot provide any explanation regarding the pathways taken by the gas to reach that point. The only discussed idea is that K do not promote up-dip gas migration (as for the entire Unit 2) and therefore the gas is assumed flowing vertically from deep portions of the study area (not accessible in this study) to the base of the K. This hypothesis is in line with the patchily distribution of AAs on K amplitude map previously discussed. From the injection point the gas will start to migrate when its pressure will overcome the capillary entry pressure of the K reflection (e.g. Berg, 1975; Figure 3.14B). At that point the gas migrates horizontally driven by the high pressure of the injected gas. The buoyancy force, as already discussed, should be not enough to overcome the capillary entry pressure of the layers in Unit 2 (Schowalter, 1979) suggesting a gas migration strongly dependent to the gas pressure achieved outside Unit 2 (e.g. a gas column beneath Unit 2). Subsequently, if the gas pressure will reach the capillary pressure of some leaking faults (Figure 3.14C); the fluid will continue to migrate horizontally along K and will start to migrate upward along leaking faults. In this case the horizontal migration, higher than the vertical one, will promote the lateral expansion of the VACs. The presence of large capillary entry pressure of some faults (or sealing faults) will stop the vertical and the horizontal migration of gas

generating on seismic the documented VAC flat margins (e.g. Figure 3.7). Since the gas influx is supposed to not be continuous during the time (Loseth, 2009), the pressure at a certain time should drop down with a consequent interruption of gas migration along faults (Figure 3.14D). At that point only the migration along more permeable horizons will dominate the migration process with a consequent further lateral expansion of the gas occurrences. Furthermore the gas pressure will decrease and the gas will not be any more able to migrate along the horizons. In this static or low pressure condition the gas will remain trapped in the pore spaces occupied maintaining the geometry associated to the higher pressure reached. On seismic the response will resemble a group of closely related DHIs linked by the just discussed migration process that have been named in the present manuscript vertically anomaly cluster (VAC).

Given the variability in permeability, structural heterogeneity and possible cyclic or irregular buoyancy pressure evolution at the basal injection point it would be surprising if the vertical gas migration invoked here to explain VACs obeyed a systematic bottom-upwards filling sequence, as exemplified by the CO2 injection into the multi-layered Utsira Formation reservoir in the Sleipner carbon sequestration project in Norway (Arts et al., 2004b). The layer-by-layer but sporadic filling we envisage may well be more widespread in gas migration and leakage across predominantly fine-grained and low permeability multi-layered successions (e.g. Ben-Brahim et al., 1999) than currently recognised. Indeed, the model we suggest is strikingly similar in some respects to that invoked to explain the origin of gas chimneys by Arntsen et al. (2007), and it is interesting to reflect on the gross similarity in external form of some of the VACs described here and gas chimneys described elsewhere, the main difference being that on our data, the internal

configuration is seen to consist of discrete, layer-by-layer amplification of the host units. By documenting the seismic expression of VACs on high quality seismic data here, it is hoped that they will be more widely documented in future as part of the spectrum of DHIs.

3.6. Conclusions

The main conclusions are:

1. The documented vertically stacked amplitude anomalies (AAs) distributed in the east Falkland basin represent direct hydrocarbon indicators (DHIs) associated with presence of gas occurrences.

2. We recognize, and describe for the first time, a vertical clustering of discrete layer-bounded amplitude anomalies, termed here Vertical Anomaly Clusters (VACs).

3. We attribute the development of VACs to dominantly vertical gas migration across a multi-layered low-permeability reservoir interval, in which individual layers are filled successively from bottom to top, and in which small normal faults and fractures provide conduits for cross-stratal migration.

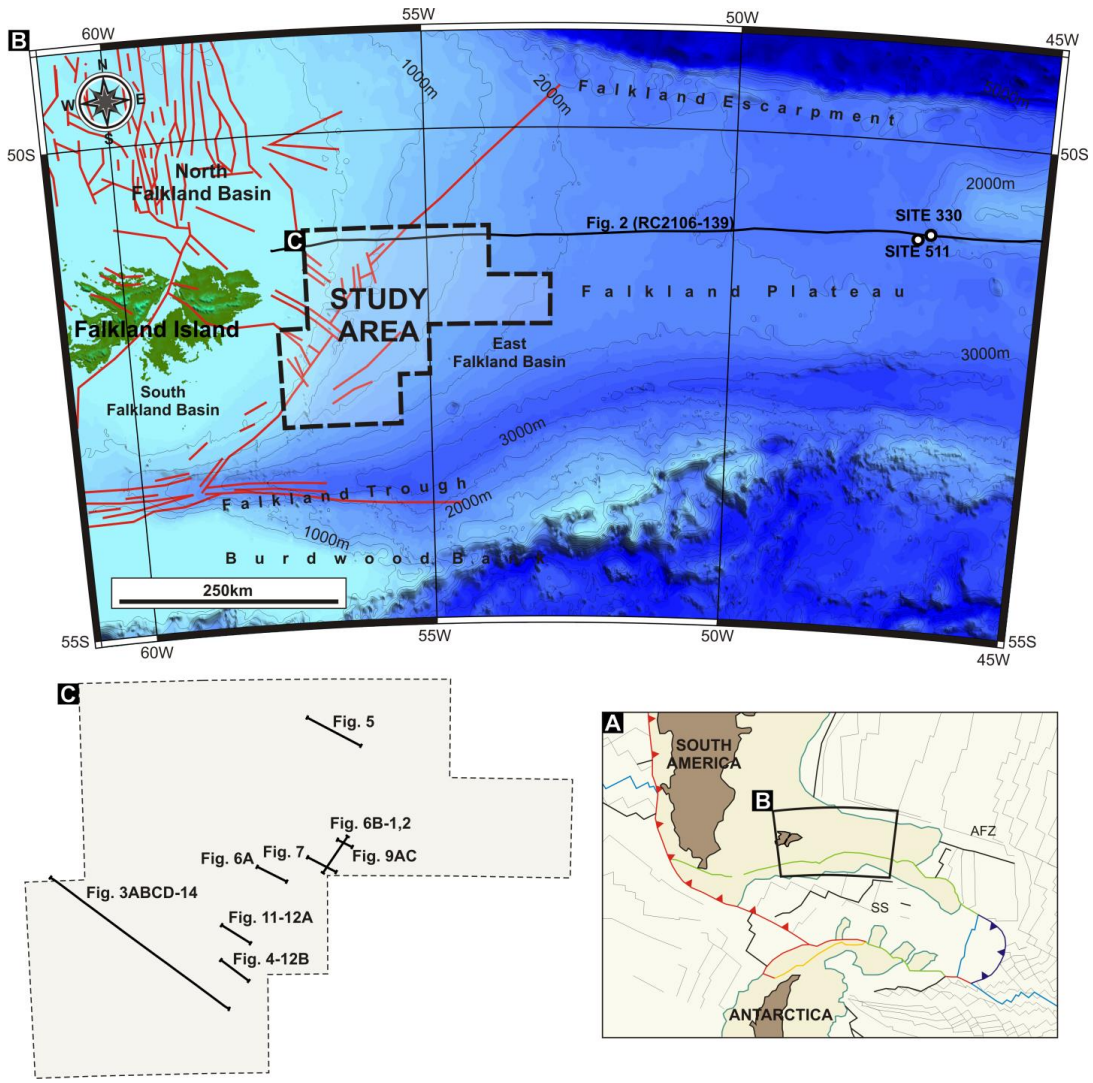

Figure 3.1 Location map (A) of the study area in the South Atlantic region. SS: Scotia Sea, AFZ: Agulhas Fracture Zone; red-blue lines: subduction, light green: inversions, dark green: actual plate margins, light blue: rifts (from Vérard et al., 2012 (mod.)); Bathymetric map (Becker et al., 2009) of the Falkland Plateau Basin (B) with location of the Falkland Basins, Study Area, Line RC2106-139 and DSDP well sites 511 and 330; red lines: main faults (form Richards et al., 1996 (mod.)); Location map (C) of the 2-D seismic lines illustrated.

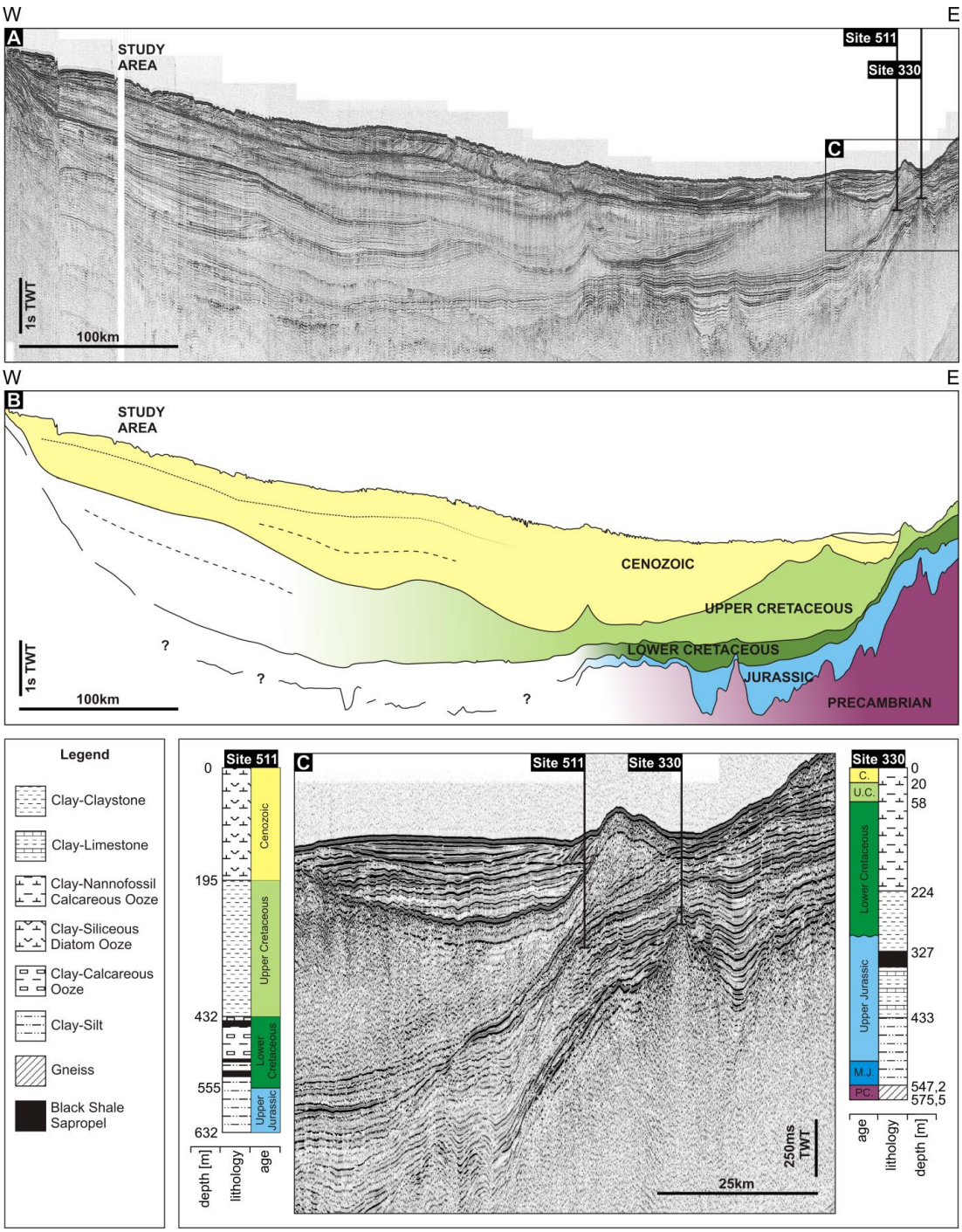

Figure 3.2 Uninterpreted 2D seismic section RC2106-139 (A), interpretation of the main geobodies (B) and DSDP well sites 511 and 330 (C). The key horizons on the 2D profile were calibrated using DSDP well sites 330 and 511. Note the lateral continuity of these key reflections which supported long range correlation to the Study Area (500-600km distant). The main seismic facies observed in the Cretaceous and Cenozoic intervals is typically associated with fine grained sedimentation, and is consistent with the lithologies cored by the two DSDP wells.

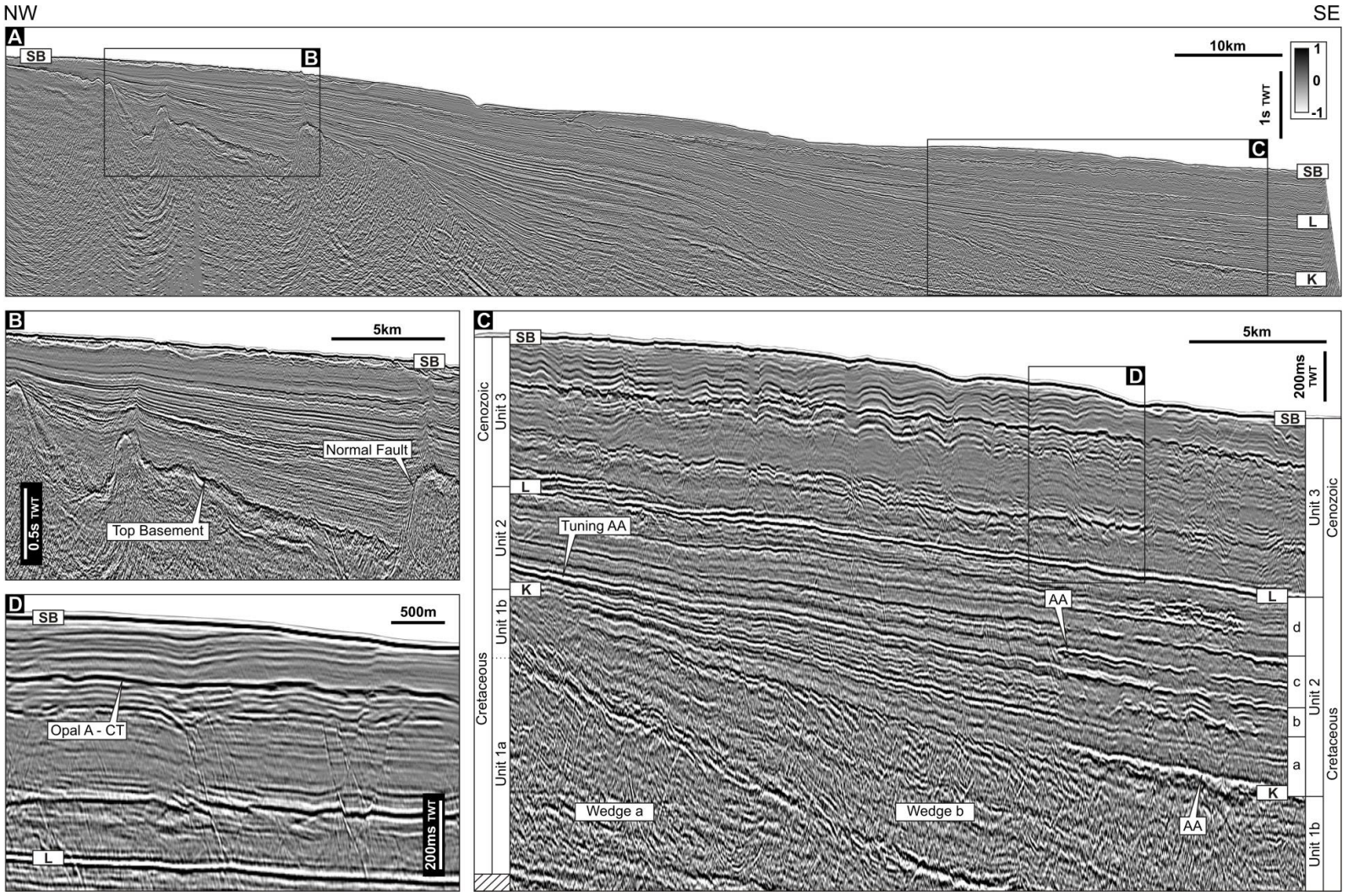

Figure 3.3 Representative 2D seismic line (cut-off at a depth of 4s TWT) passing across the study area (A; see Figure 1C for exact position) showing normal faulted basement and the sedimentary wedging. Close-up of the tilted top basement (B) showing a hard amplitude response (same polarity of the seabed). Close-up of the main mappable Units (C): double-wedge structure (wedge a and b) affected by a strong fault system (Unit 1), onlapping highly continuous reflections with amplitude anomalies (AAs) and tuning amplification (Tuning AA; Unit 2) and polygonally-faulted contourite deposits (Unit 3). Upper section showing contourite deposits and Opal A/Ct transition (D). Data courtesy of GSI.

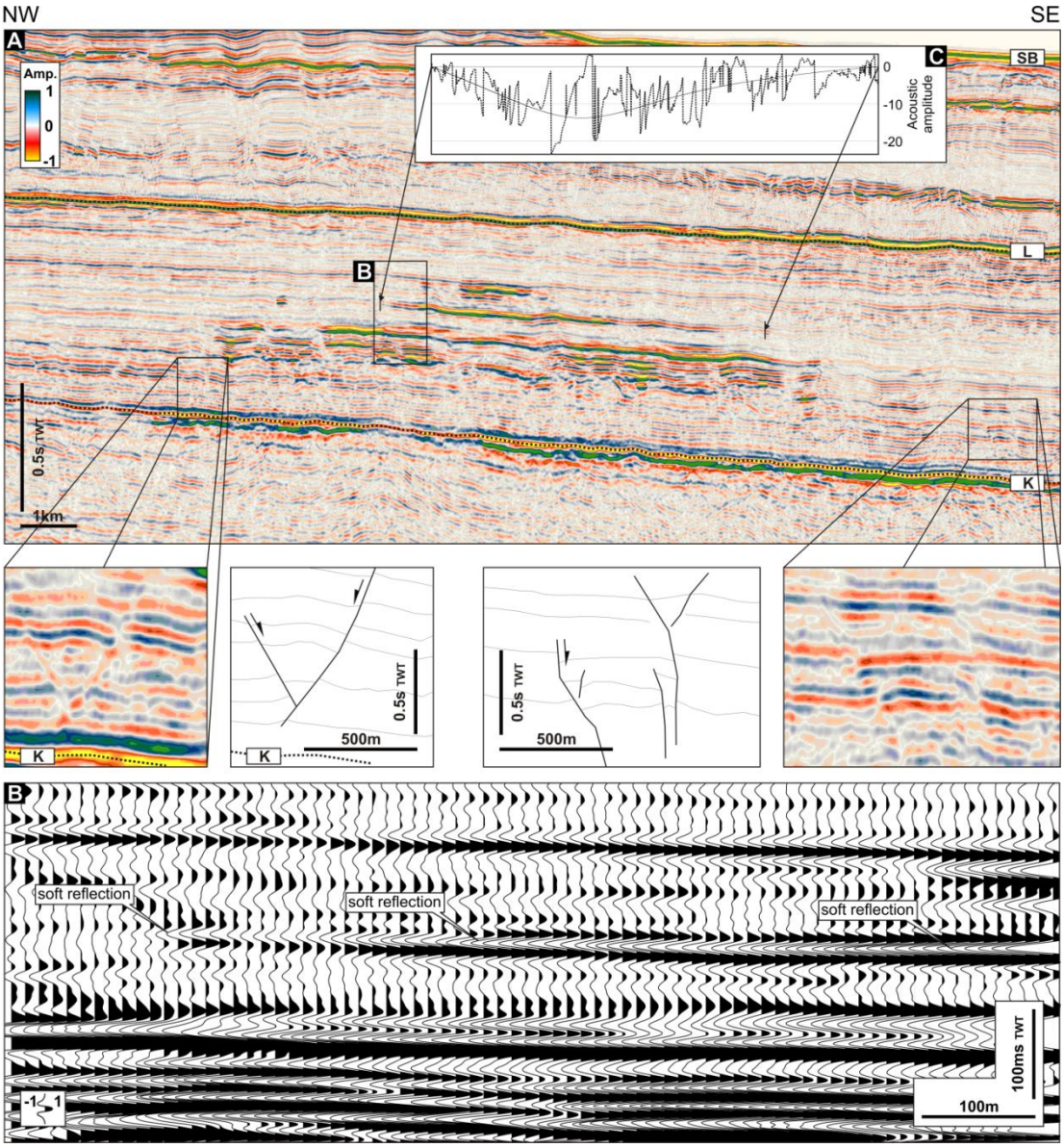

Figure 3.42D seismic section showing vertical amplitude cluster (VAC) and faults (see Figure 1C for location). Unit 2 is included between the reflections K and L and is composed of high laterally continuous reflections showing space limited amplifications (A). The lower portion of the Unit is characterized by faults and fractures showing clear reflection truncations (insets). The amplifications are soft amplitude response (B) and are characterized by strong decrease of amplitude (<-20000, C). Data courtesy of GSI.

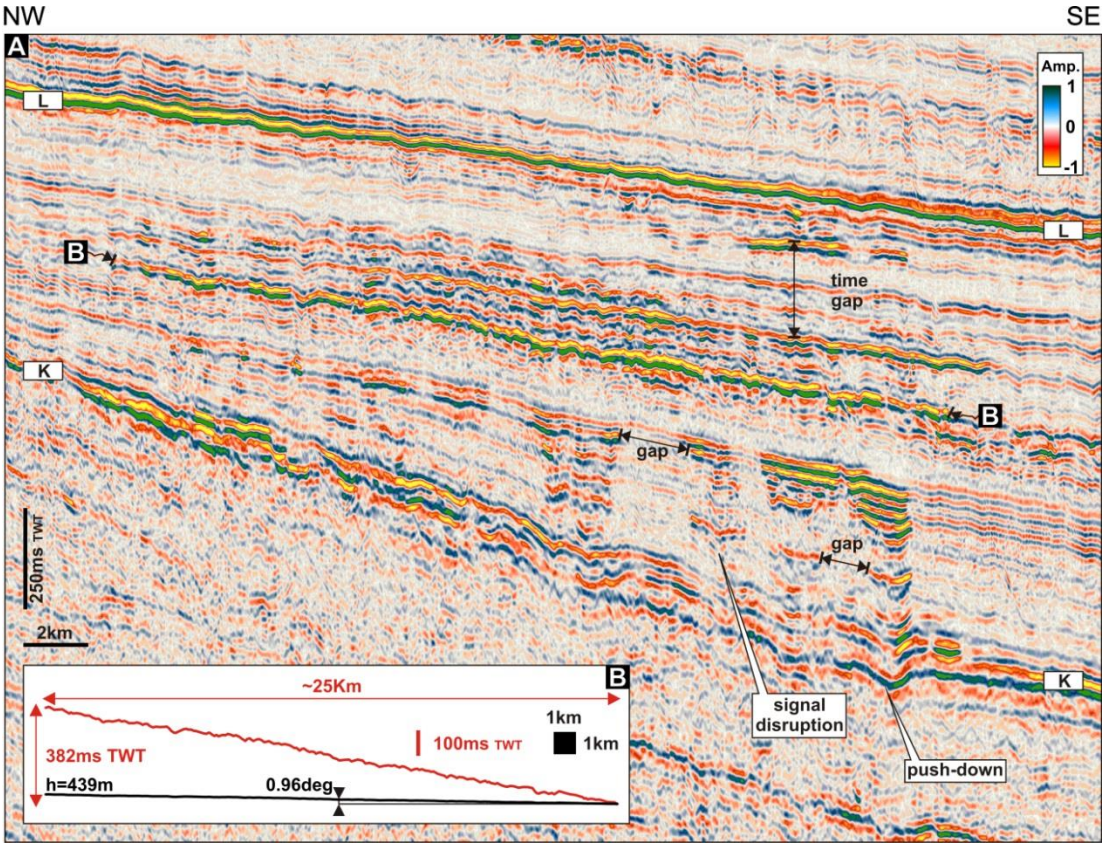

Figure 3.52D seismic section showing a VAC (see Figure 1C for location). The line presents the longest AA discovered in the study area with an approximate length of 25km and a large number of shorter AAs. All AAs are soft reflections (red-yellow). These shorter AAs are separated by gaps occurring along the hosting horizons and time gaps observed as vertical non amplified horizons (A). The longest anomaly has a vertical projection of 330ms TWT (red line) corresponding to c.440m (@ 2.3km /s, black line, B). At normal scale (vertical exaggeration=0, black line) the AA dips at one degree (B). Data courtesy of GSI.

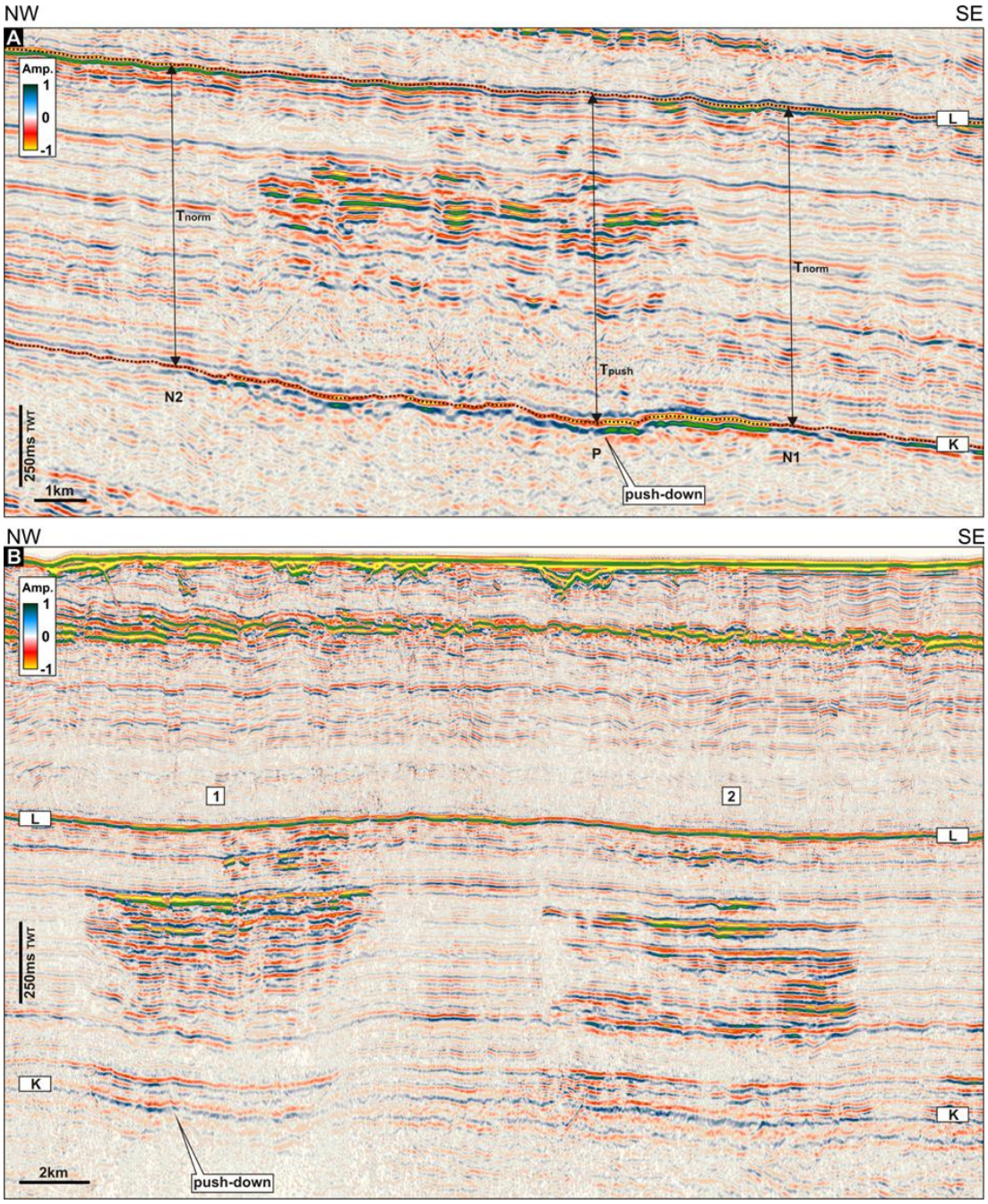

Figure 3.6 2D seismic sections showing a VAC, signal disruption zones and push down (see Figure 1C for exact position). In the top line (A) the AAs composing the VAC within the central part of Unit 2 overlies a zone of signal disruption, accompanied by a push down clearly visible on the K reflection. This line is used as example in the calculation of the variation in Vp from the push down effect (see text). The bottom line (B) hosts two VACs (1 and 2). The VAC 1 is composed of regular margins and extends almost in the entire Unit 2 showing also an appreciable push down (K). VAC 2 exhibits strongly irregular margins. Data courtesy of GSI.

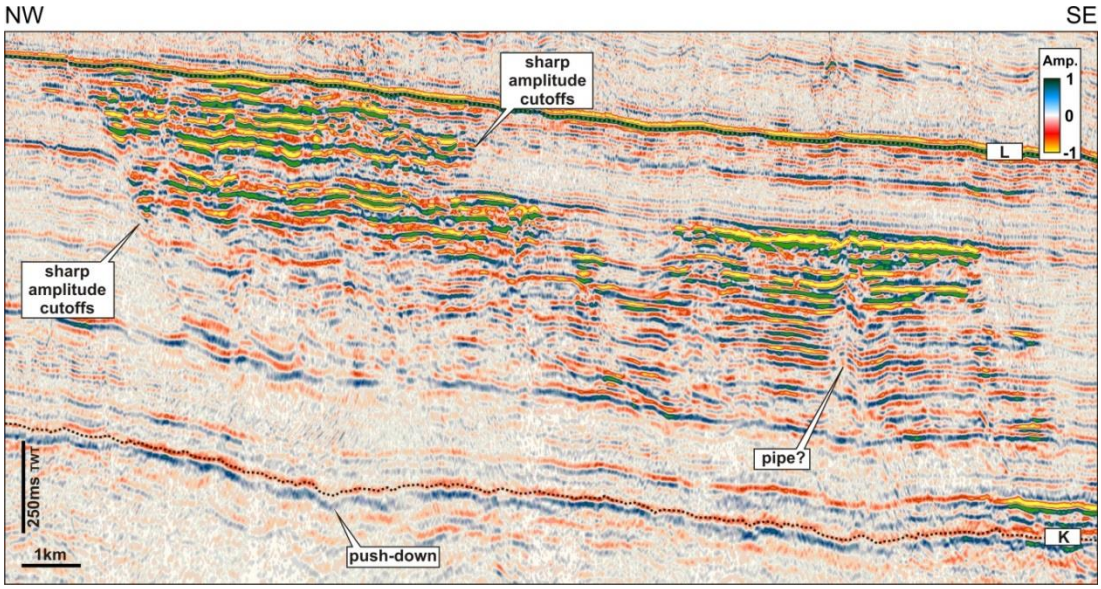

Figure 3.72D seismic section showing detailed imaging of a VAC (see Figure 1C for location). The AAs composing the VAC are truncated generating on seismic sharp cutoffs. The truncation position is interpreted as being demarcated by fault plane. The VAC is associated with a strong push-down clearly recognizable on K. Other sharp AA cutoffs are present at the other margin of the VAC. Internally, a series of deformed convex-up distortions stack vertically, and can be interpreted as a pipe. Data courtesy of GSI.

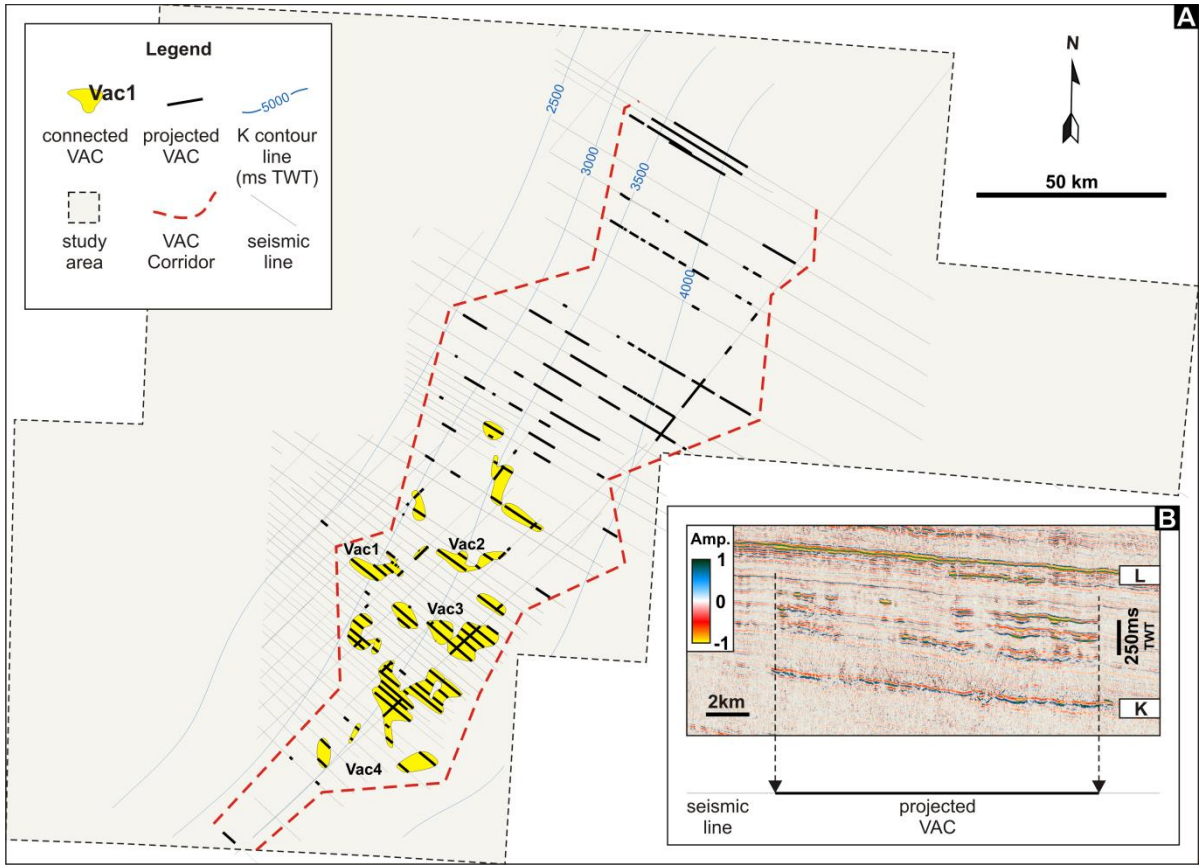

Figure 3.8 Base map of the study area (see Figure 1 for location) with mapped positions of the VACs. The map shows the grid of the available 2D seismic coverage, characterized by variable line spacing. The VACs were mapped using the projection method showed in the example B (see text). The VACs in the study area have been included in the VAC corridor (red dotted lines) that trends NE-SW. Note the contrasting planforms of the VACs interpreted from the seismic grid. Data courtesy of GSI.

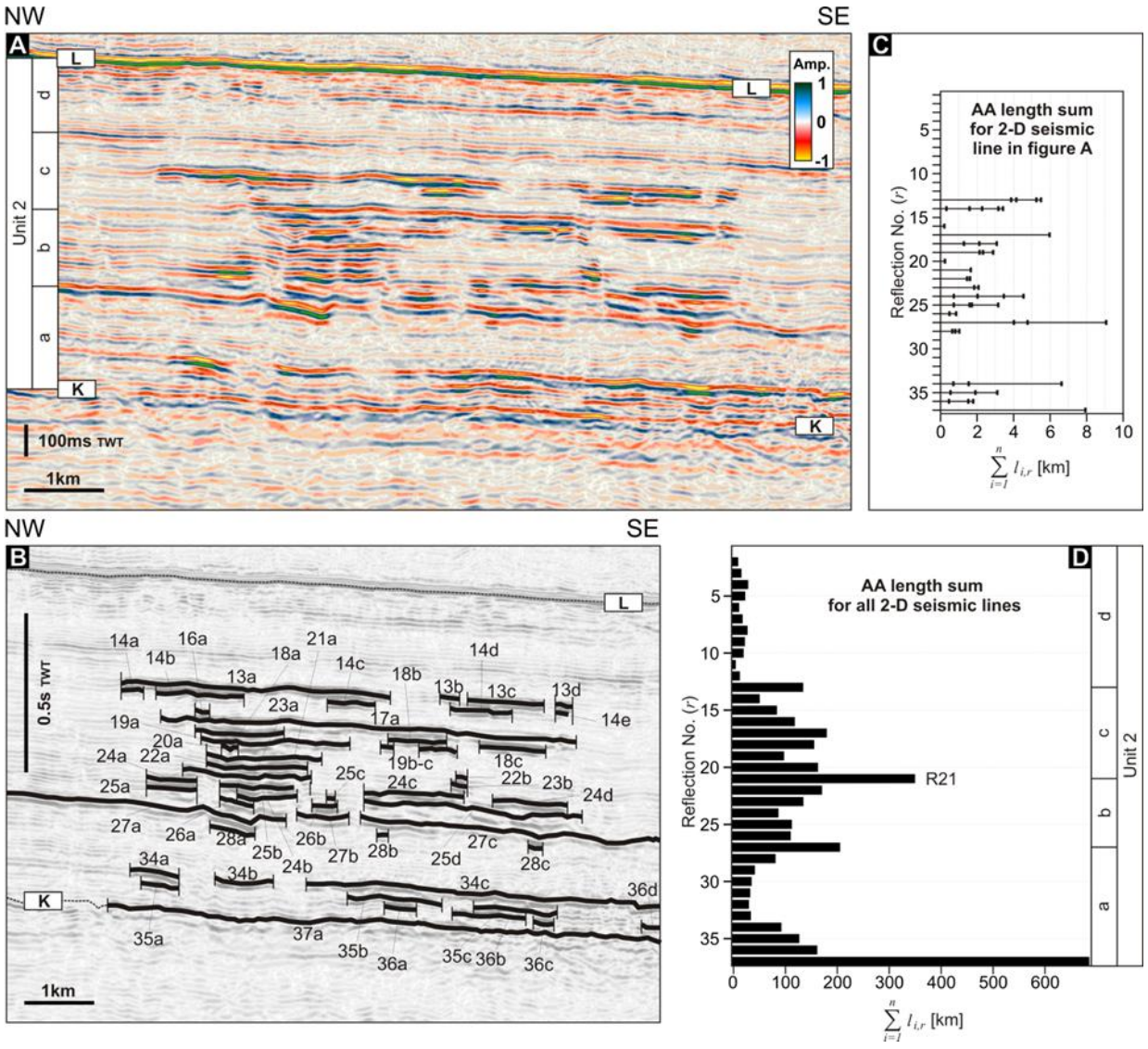

Figure 3.9 (A) 2D seismic section showing a VAC (see Figure 1C for location), AA interpretation and vertical distribution of AAs, and (B) the overall AA distribution calculated throughout the seismic grid as function of their cumulative lengths. The VAC is composed of 50 singular AAs affecting 19 reflections (A-B). The cumulative AA length in km for each reflection r calculated in the shown example is plotted in (C). The overall AA distribution in km calculated in each seismic line (D) shows a clear preferential distribution of AAs in the central reflections of Unit 2. K and the reflection 21 (R21) hosts the largest cumulative length of AAs. Data courtesy of GSI.

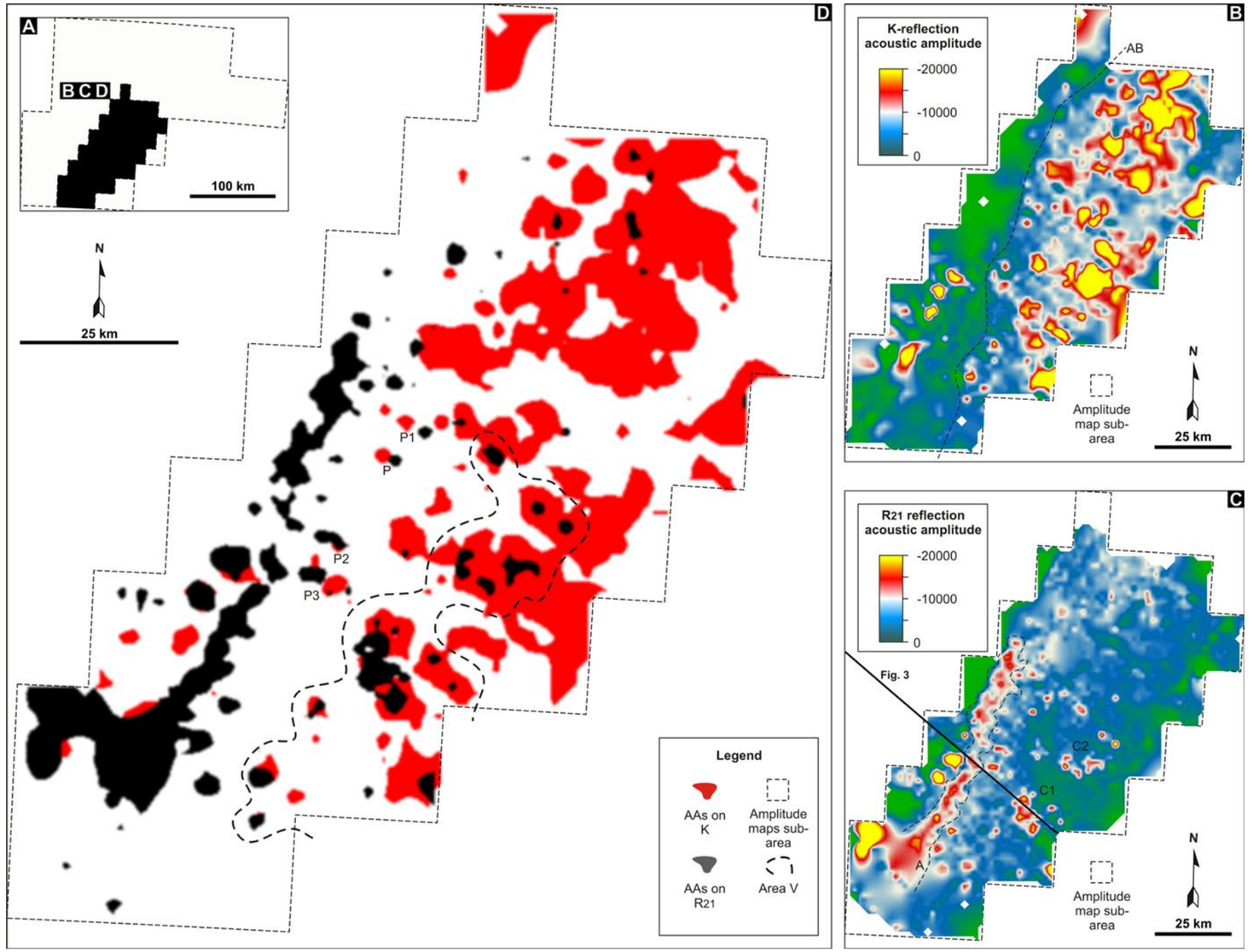

Figure 3.10 (A) Subarea (black area) selected to calculate the amplitude maps of reflections K and R21. (B) Amplitude map calculated from K reflection showing patchily AAs and their preferential distribution in the eastward part of the area (anomaly boundary, AB). (C) Amplitude map calculated from R21 reflection. It shows a small number of AAs characterized by patchily distribution and a tuning amplitude anomaly area at W (A, see reference in Figure 3). (D) Amplitude composite map from K and R21 amplitude maps (see text). The vertical relationship between the AAs of the two maps displays eastward (P, P1), westward (P2, P3) and vertical trends (area V).

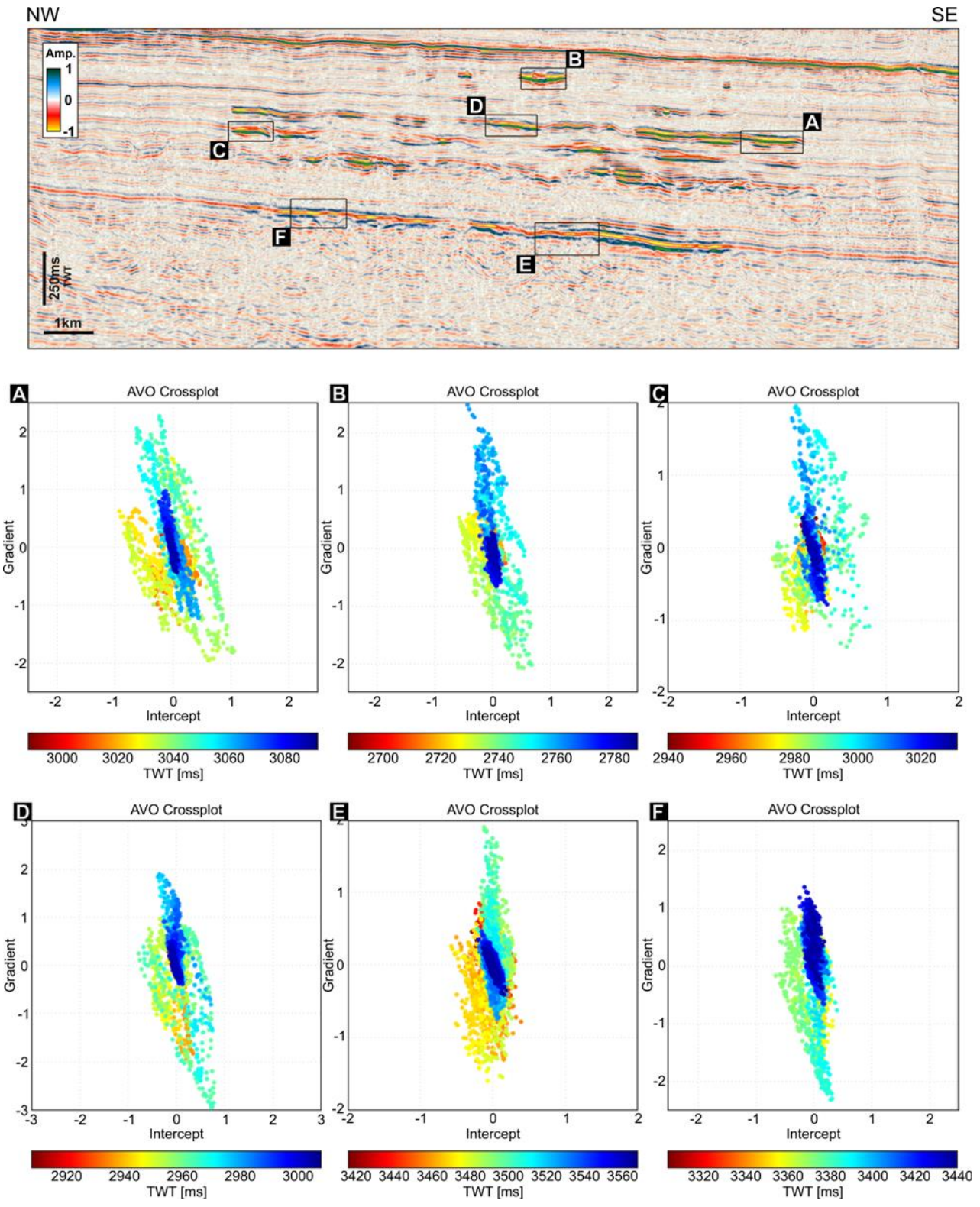

Figure 3.11 2D seismic section showing a VAC (see Figure 1C for exact position) and AVO crossplots extracted from windows A, B, C, D, E and F. The color of the AVO crossplots is function of the time (ms TWT). Events at the top of a given window are colored in red meanwhile at the bottom in blue. A, C, D and E show clear AVO class III responses meanwhile B and F are more uncertain. Data courtesy of GSI.

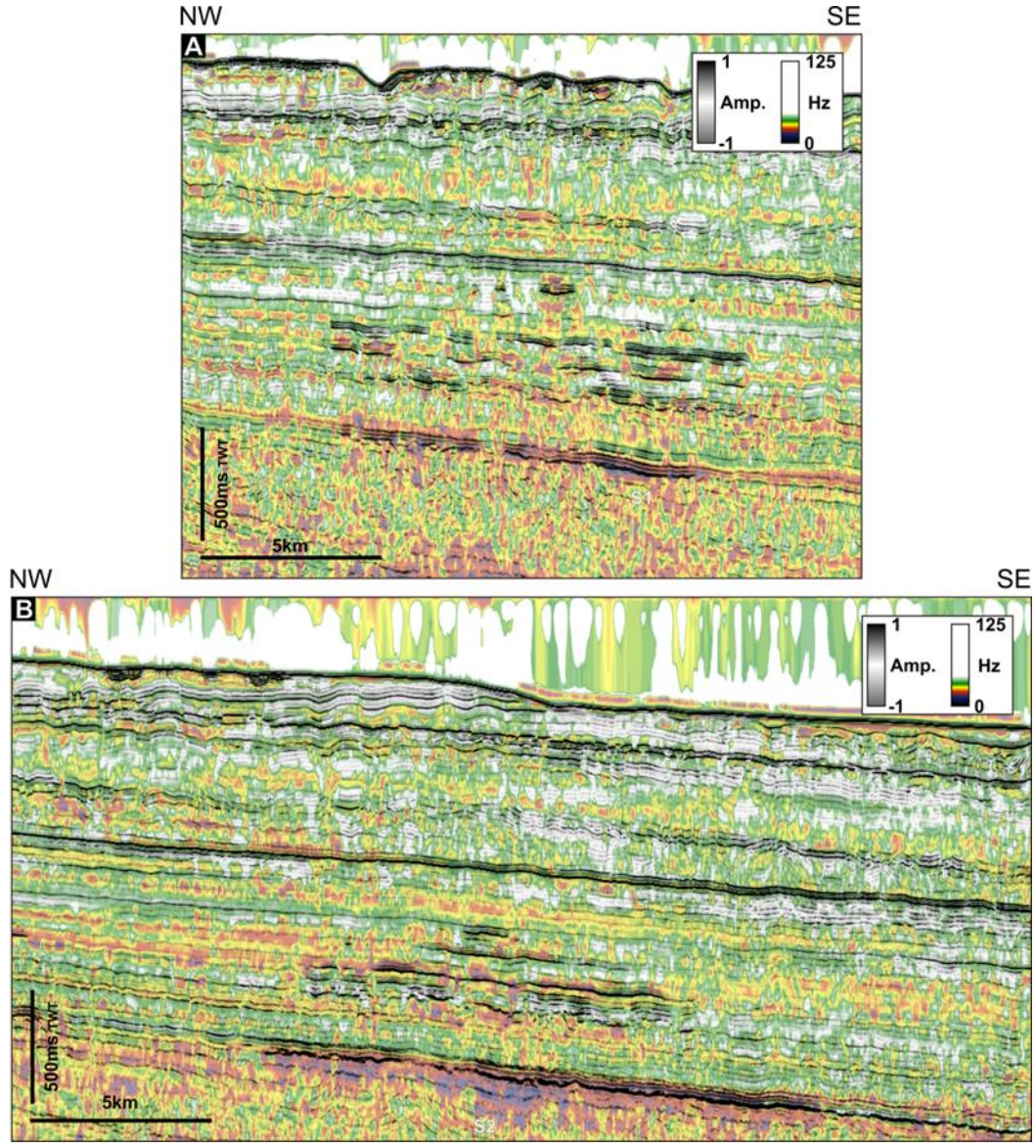

Figure 3.12 2D seismic sections showing VACs (see Figure 1C for exact position) and their time-frequency representations (TFR). The two panels (A-B) are composed of semi-transparent acoustic seismic responses and TFR responses in the background. The TFR are colored from dark violet (0Hz) to white (125Hz). (A) VAC showing patchily distributed frequencies and small shadow effect at the base (S1). VAC showing low frequency patches distributed in the center and shadow zone below K reflection (S2). Note that K reflection is not associated to shadow zones outside the VAC position. Data courtesy of GSI.

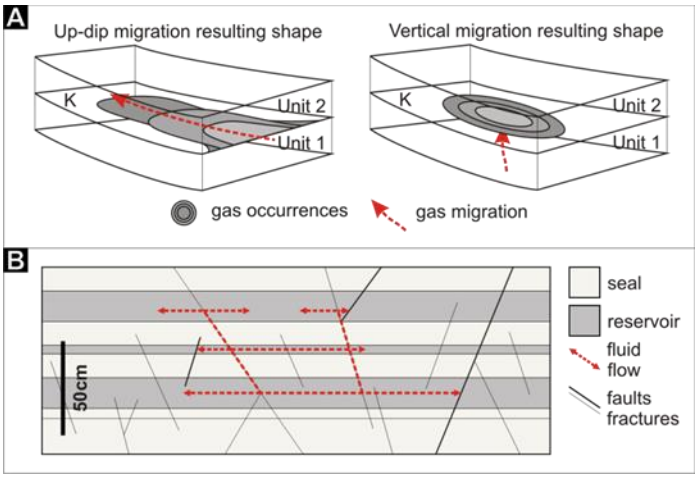

Figure 3.13 (A) Simplified model showing the resulting gas occurrence shapes associated to up-dip migration (left) and vertical migration (right). The patchily distributed AAs on K and R21 (Figure 10B-C) seems associated to the model at right. (B) Simplified model showing binary layering and cross-stratal migration. The migration of gas is supposed to develop as a series of short range vertical migration steps involving the documented faults and fractures and able to connect the reservoir-like layers.

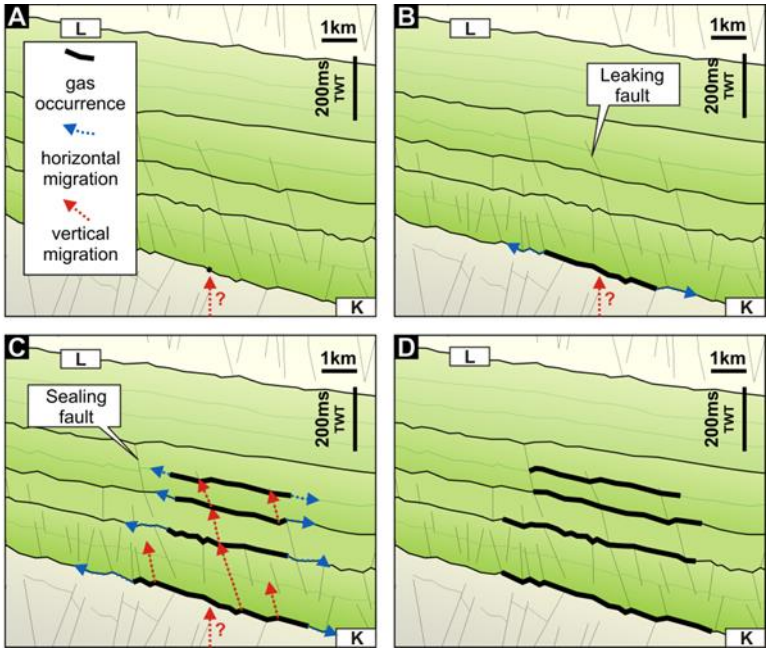

Figure 3.14 Conceptual model showing stages in the development of the VACs. (A) Gas injection at the base of K. (B) Gas exceeds capillary entry pressure of K reflection and starts to migrate horizontally along it. In this stage there is the development of the bases of the vast majority of the observed VACs. (C) Gas exceeds capillary entry pressure of some faults and fractures and migrates vertically. The VACs "grow" vertically following the easiest migration routes in Unit 2. (D) Gas pressure drop and consecutive interruption of the migration. The gas composing the VACs remains in place maintaining the position associated to maximum pressure reached (see text).

4. South Falkland Basin: Hydrocarbon Migration and Plumbing System

4.1. Introduction

4.1.1. Background

Hydrocarbon plumbing systems (e.g. Andresen, 2011 and 2012, Anka et al., 2012 and 2013; Ostanin et al., 2013) are the result of the migration of hydrocarbons from the source rock to the shallow section of petroliferous basins. Hydrocarbon plumbing systems are dominated by multiple stages of migration and accumulation (Abrams, 2005) which are controlled by the hydraulic properties of the basin. Every elementary portion of a petroliferous basin is indeed regulated by the ratio between inward, I_{ff} , and outward, O_{ff} , fluid flow. This simplification define (1) hydrocarbon occurrences (e.g. reservoirs) when $I_{ff} / O_{ff} > 1$ and (2) hydrocarbon pathways (e.g. pipes) when $I_{ff} / O_{ff} <= 1$.

Plumbing systems can be delimited upward by accumulations of hydrocarbons beneath regional seal, but commonly they reach the surface exhibiting various features associated with focused fluid expulsion (Cartwright et al., 2007). On the seafloor these underlying fluid expulsion phenomena commonly terminate upwards at pockmarks or events which are often observed as sub-circular depressions with diameters ranging from meters to kilometres (Hovland and Judd, 1988; Hovland et al., 2002). Focussed fluid flow can be associated with fluids other than hydrocarbons and can include remobilised sediments in the flow. Multi-phase flow phenomena are seen in a large number of features at both the Earth's surface (such as mud and sand volcanoes; Eggland, 1997; Ivanov et al., 2010) and in the subsurface (such as sand intrusions, Mourges et al., 2012).

In the subsurface the presence and the migration of hydrocarbons in the sediments can be observed on seismic data. The Bottom Simulating Reflection (BSR) is a

specific seismic response that is widely associated with the base of the gas hydrate stability zone (BGHSZ, Hyndman and Spence, 1992). On seismic data it is a negative reflection caused by the sharp change of the elastic properties of the porous sediments where gas hydrates overlies free gas and water. The BSR normally mimics quite closely the seabed profile (Pecher et al., 2001; Sloan, 2003) but can exhibit also discordant patterns and multiple reflections (Popescu et al., 2006).

Gas hydrates are lattice-like structures composed of water and gas (typically methane). Other gaseous compounds can be present but usually at low concentrations (Shelander et al., 2010 and 2012). Gas hydrates can originate from thermogenic or biogenic sources. Gas hydrates are stable under low temperature and high pressure conditions and are normally found below the seafloor in almost every continental margin in the world (Liu and Flemings, 2006). It has been estimated that gas hydrate represents the largest resource of methane and that it is an important factor in the climate equilibrium (Ruppel et al., 2005). Changes of temperature (e.g. hot fluids), pressure (e.g. sea level changes, seabed erosions and up-lifts), and gas composition may destabilise the GHSZ with a subsequent re-equilibrium at different depths. This process may generate multiple BSR (Popescu et al., 2006).

Amplitude anomaly on seismic data is an increase of amplitude along a reflection which can be caused by any reason (Løseth et al., 2009, Sheriff, 1975). Amplitude anomalies can be associated with positive and negative amplitude (Avseth et al., 2009). Amplitude anomalies associated with increasing acoustic impedance with depth are labelled “hard” reflections while amplitude anomalies associated with decreasing acoustic impedance with depth are labelled “soft” reflections. Enhanced reflections are amplitude anomalies where the variation in amplitude is consistent

with distance or depth. Enhanced reflections are typically observed beneath BSR and are indicative of the presence of free gas zone (Bünz and Mienert, 2004).

Seismic chimney is on seismic data a region where the seismic amplitude and phase of the reflections is distorted (Heggland, 1997). Gas chimney is indicative of a vertical migration of fluids observed on seismic data (Heggland, 1997). Gas chimney (Bjørkum et al., 1998) represents a similar feature indicating a focal point of upward movement of fluids interpreted to be mostly associated with water and gas.

Flat-spot is a hard reflection which typically exhibits a horizontal profile. It represents a strong evidence of the presence of hydrocarbon in subsurface (Brown, 2004). It can represent the contact between hydrocarbons (above) and water (below). In the situation of a dipping seabed or in reservoirs with lateral migration of water flat-spots may appear as tilted in true section (England et al, 1987).

4.1.2. Rationale and aims

The interpretation of 2D and 3D seismic data and well information is considered the best strategy to recognise hydrocarbons in subsurface (Cartwright and Huuse, 2005) and use their spatial relationship in association with structural and stratigraphic features to understand migration systems in sedimentary basins.

This method has been successfully used in the previous Chapter 3 where the description of hundreds of amplitude anomalies has revealed a systematic upward filling of hydrocarbons (e.g. free gas) in fine-grained successions (VACs, Unit 2). However the survey restrictions (no access below 4s TWT), does not allow a complete description of the factors responsible for the regional distribution of the AAs in the study area (Figure 3.8).

This second case history is focussed in the basin offshore to the south of the Falkland Islands, the South Falkland Basin (SFB). The presence of (1) an active petroleum system (Platt and Philip, 1995; Fish, 2005) that was recently confirmed by an important gas condensate discovery (Borders & Southern Petroleum plc, *RNS Number: 8142B*, 23 April 2012, Appendix A2) and (2) the availability of deeper penetrating seismic data can provide some clues behind the understanding of the distribution of thermogenic fluids in the shallow sequences and perhaps help explain the significance of the previously observed seismic amplitude anomalies observed in Chapter 3.

The primary aims of this chapter are:

- Description of the geological structures
- Description of any amplitude anomaly
- Evaluation of hydrocarbon migration pathways
- Definition of a conceptual plumbing system

4.1.3. Seismic datasets and well information

4.1.3.1. Seismic data

The description presented here of the SFB is based on the interpretation of a large regional 2D seismic dataset (Figure 4.1). The dataset is composed of two surveys provided by GSI and FOGL plc. The GSI survey is composed of 27 2D seismic near- and far-angle stack profiles. The lines are not organized in pairs (i.e. near and far-angle stack sections associated with the same CDP) and for a given 2D seismic

section often only one angle-stack is available. For this reason AVO analysis has been performed only where both stacks where available. The seismic processing applied to this dataset is described in Appendix A.

The FOGL data is composed of 18 full-stack 2D seismic lines and 18x2 near- and far-angle stack 2D seismic lines for a total of 54 lines. The acquisition parameters and the processing flows applied to this dataset are summarized in Appendix A. The combination of surveys gives a variable grid spacing of 2-8km (Figure 4.1).

The polarity of both surveys is SEG American with positive response for increasing acoustic impedance with depth. The seismic data were processed in full- and range-stack yielding different vertical resolutions. The vertical resolution values have been calculated applying Widess relation (Widess, 1973; see Chapter 2) and using an average velocity of $2000 m \cdot s^{-1}$ (Table 4.1). The FOGL dataset was accompanied by velocity data which has been used for time-to-depth conversion.

Table 4-1 Seismic resolutions of the FOGL dataset.

Full stack	Near-angle stack	Far-angle stack
12m	10m	16m

4.1.4. Well data

No direct well calibration was possible in this study because recently drilled wells are not available in the public domain. Some limited well results have been released by the operator who have drilled exploratory boreholes, and where useful, these web-

based reports are cited here and used in the interpretation. Due caution should, however, be applied when considering reports via company websites.

The Darwin discovery represents the most important indication of the presence of a mature source of hydrocarbons in the study area. Darwin was drilled in 2012 by Border & Southern PLC and is located over a kilometre from the seismic database (Figure 4.1). Border&Southern plc released two important press reports in 2012 and 2013 (see Appendix A1, and summary in Table 4.2, and Figure 4.2), in which they confirm Darwin-1 as gas condensate discovery. Importantly they also encountered some prone source intervals at two stratigraphic levels, one immature and one mature.

Table 4-2 Darwin-1 well results.

Position	53°35'43.700''S - 58°45'45.570''W The well is 1.28km from the 2D seismic line 6S-114 and 14.07km from the 2D seismic line 6S-112 (Figure 4.2)
Total depth	4876m
Hydrocarbon shown	From 4633m to 4810m (main reservoir of 84.5m and net pay of 67.8m).
Reservoir properties	Quartz sandstone with lithic fragments and clays (Aptian). Porosity: 22 - 30%
Fluid properties	Ultra-light oil (condensate gas, API gravity 44.5-49°) Saturation: 71.5%
Source rock	Immature Type II/III source rocks above and below the main reservoir (Aptian). Expected mature source rock located 320m below the base of the well (Late Jurassic-Early Cretaceous ext.)

4.2. Regional Geological Setting

The South Falkland Basin (SFB) lies at the southern margin of the South America plate and is located ~200km south of the Falkland Islands. It divides the Falkland Plateau from the Malvinas basin (Richards et al., 1996). The structural style is similar in some aspect to that of the Malvinas basin (Galeazzi, 1998). The SFB trends east west and parallel to the Scotia-South America Plate Boundary (SSAPB) which represents the southern limit of the basin.

4.2.1. Tectonic evolution

Prior to break-up of Gondwana, the SFB was located to the SW of the Karoo Basin (Platt and Philip, 1995; Macdonald et al., 2003; Verard et al., 2012). At that time the Falkland Islands are thought to have been oriented approximately 180 degrees with respect to the present day configuration (Platt and Philip, 1995; Macdonald et al., 2003). Late Permian sediments include deltaic to transitional facies with the localised occurrence of coal deposits and volcanoclastics. These Late Permian sediments are referred to the Lemaire Formation in Argentina (e.g. Caminos et al., 1981) and the Tobifera Formation in Chile (Platt and Philip, 1995; Macdonald et al., 2003). The coal deposits, located at the western margin of the east Falkland Basin, have been drilled by BHP Billiton (FOGL plc AGM Presentation 2012, Appendix A.2).

During the Early Jurassic the South American and Antarctic plates started to move south- west and east, respectively. This early pattern of break-up and plate movement is thought to have been the period of marked clockwise rotation of the Falkland Islands and adjacent basins (Macdonald et al., 2003). The orientation of the

SFB would have changed substantially during this period with rotation ceasing in the Middle Jurassic.

In the Late Jurassic east- west extension of the Falkland Plateau was accompanied by deposition of the later part of the Tobifera Formation. Anoxic sedimentation occurred at this time in the basins around the Falkland Islands and in other regions of the South American Plate (Macdonald et al., 2003). DSDP well sites 511-330 encountered Oxfordian source rocks. Large variations in the age and thickness of the source rock intervals have been observed in other DSDP well sites in the South Atlantic regions (Macdonald et al., 2003).

Rifting and extension of the Falkland Plateau and the SFB is associated with the continued break-up of Gondwana that started in the Late Jurassic (initial breakup at ~155Ma, Verard et al., 2012). The rifting is marked stratigraphically by a relative sea level transgressive stage in which the deposition of a retrogradational sedimentary succession of fluvial, shoreline and shallow marine sandstones occurred. This transgressive unit is the Springhill Formation and potentially represents the best hydrocarbon reservoir in the SFB (Galeazzi, 1998).

The early post-rift stage (Early Cretaceous) is accompanied in the South America plate by the opening of the South Atlantic Ocean with a higher circulation of water and the supposed end of the anoxic period in the South American basins (Davison, 1999). In the late post-rift phase (Late Cretaceous) a reorganization of the plates generated a widespread unconformity (~70Ma, Macdonald et al., 2003; Late Maastrichtian, Fish, 2005, Zabanbark, 2011) observed in the SFB but also in other areas of the Falkland Plateau (e.g. Del Ben and Mallardi, 2004). In the same period the relative movement between the Antarctic and the South American plates triggered the fragmentation and spreading of the Andean Cordillera, generating the

Scotia Ridge (Bry et al., 2004). After this period the sedimentation in the basin was controlled mostly by the erosion of the Andean Cordillera and Falkland Islands (Fish, 2005).

The continuous motion of the plates facilitated the opening of the Scotia Sea, which commenced at ~26Ma (Cunningham et al., 1996; Verard et al., 2012). The opening of the Scotia Sea triggered the inversion between the South America and newly formed Scotia plates with collision and shortening, achieved in an E-W sinistral strike-slip motion and a N-S compression (Bry et al., 2004). The generation of the Burdwood Bank is consistent with N-S compression.

The continuous thrusting and the increasing in thickness of the Burdwood Bank increased the loading on the rifted basement in the north with a consequent flexural response (Bry et al., 2004, Fish, 2005) and reactivation of the Early Cretaceous fault system. This relative movement between the South America Plate and the Scotia Plate continues to the Recent (Bry et al., 2004).

4.2.2. Well tie

To tie the well information to the seismic grid two 2D seismic lines, 6S-114 (Figure 4.4) and 6S-112 (Figure 4.5) were used. These dip-lines are the closest to the well 61/17-1 (Figure 4.3 and 4.2) on which the deeper structures can be clearly interpreted. Since the well information is mainly associated with the deeper portion of the basin, far-angle stack sections were preferred due to the higher content in lower frequencies yielding a better signal to noise ratio at depth. The 2D seismic lines were converted in depth using the seismic velocity data provided by FOGL plc.

The well was projected with a total distance of 1.28 km to the 2D line 6S-114-depth (Figure 4.3 and 4.4). The well site is located a few tens of meters south of the

footwall crest of the interpreted normal fault F (Figure 4.4). On seismic, due to muting operations at the southern margin of the 2D line, the fault F and the projected well are not included. For this reason the 2D seismic line 6S-112 (Figure 4.5) was selected. The well information is projected to this line for a distance of 14.07 km. The projection axis was parallel to fault F (Figure 4.3). It was considered reasonable to project along the large distance between the well and the selected seismic line because of the linear geometry of fault F (Figure 4.3B).

On the 2D seismic line 6S-112 the projected information is located close to footwall crest of fault F which is visualised in this line. The reservoir interval coincides with a series of southward dipping high amplitude reflections (Figure 4.4C). These reflections overlie low amplitude reflections. The horizon separating these two acoustically different packages was named B1-reflection and it is recognisable as a laterally correlatable positive amplitude reflection. The high amplitude response of the reservoir-related reflections is expected from a sand-rich reservoir imbedded in deep sea source rocks (see Section 4.2.1 and Figure 4.2). The reservoir interval dated Aptian in age may coincide with the Springhill Formation. The latter is described as a retrogradational sedimentary succession of fluvial, shoreline and shallow marine sandstone (see Section 4.2.1; Galeazzi, 1998).

The interpretation of the Darwin reservoir was also compared to a figure taken from a presentation published by Border and Southern plc (Figure 4.2, see Appendix A2). The well 61/17-1 is located nearby a normal fault and intersects dipping high amplitude reflections. These reflections overlie a package of low amplitude reflections. The structures exhibited in the 2D seismic line 6S-112 (Figure 4.4) and in the presented figure show a close similarity.

4.2.3. Structural setting interpreted from seismic data

The structural setting of the SFB is described with reference to a representative 2D profile across the basin (Figure 4.4). The structural interpretation partly follows those presented by previous workers in the basin (e.g. Bry et al., 2004; Fish, 2005; Ghiglione et al., 2010; Platt and Philip, 1995; Richards et al., 1996 and 2006).

The SFB is dominated by (1) Mesozoic extension and (2) Cenozoic compression and infill.

The extension of the SFB is observed on seismic data as a series of preserved normal faults with throw oriented to the north (Figure 4.4). The faults separate tilted fault-bounded blocks. Most of the normal faults were active during the Jurassic and Early Cretaceous (Richards et al., 1996). Later reactivations of the fault system are documented (Richards et al., 1996) and are also visible on seismic data where some faults are seen to reach the seabed (Figure 4.4). The reactivation can be associated with the documented loading of the Burdwood Bank and the consecutive flexuring of the rifted basement in (Bry et al., 2004, Fish, 2005). Most of the faults terminate however at the top of the syn-rift marked by a regional unconformity (Horizon C, described later).

The interpretation of the most prominent normal faults was done using 2D seismic lines (Figure 4.6). Most of the Mesozoic faults trend E-W to the west and are more ESE-WNW oriented to the east.

The Cenozoic shortening of the SFB is represented by a number of thrust faults and folds which compose the northern portion of the Burdwood Bank (Figure 4.4). The folds are predominantly north verging and asymmetric. They are more prominent eastward in the area, where they propagate shallow and deform the seabed. The axis of the folds is oriented approximately with the same strike of the

Mesozoic normal faults (E-W to the west and ESE-WNW to the east). The lack of signal below the anticlines precludes any interpretation of the deeper structures.

4.3. Seismic stratigraphy

The interpretation of the stratigraphic units present in the SFB has been undertaken by synthesising a seismic interpretation of the regional limited published work focussed in the study area (Fish, 2005; Platt and Philip, 1995). The recognition of the unit boundaries has not been based on direct correlation with well sites. Due to the lack of properly calibrated stratigraphic information a detailed litho and chronostratigraphic description of the units involved has not been possible. A simple subdivision of the basin into two major units (already defined in Bry et al., 2004) is proposed and described below.

4.3.1. Acoustic Basement (Horizon B)

The acoustic basement is interpreted here as Horizon B (Figure 4.4 and Figure 4.6), which throughout the area is recognizable as a prominent, laterally correlatable positive reflection. Locally some coherent reflections are observed beneath Horizon B, but in general this marker separates the overlying reflective sedimentary basin-fill from a featureless reflection free interval (CR, Figure 4.5). Horizon B dips south-eastward with a maximum depth of 6.5s TWT. Horizon B may represent the top of the Precambian Cape Meredith Complex overlain by quartzitic Gran Malvina Group (Platt and Philip, 1995) or the top of the eroded Permo-Trias/Devonian basement (Richards et al., 1996).

4.3.2. Regional Unconformity (Horizon C)

The regional unconformity is interpreted in this study as Horizon C. It is defined here as the local expression of a regional unconformity recognized in all the Falkland basins and in the Falkland Plateau (e.g. Del Ben and Mallardi, 2004). The unconformity may be the expression of the plate reorganization occurred during the Late Cretaceous (Fish, 2005; Platt and Philip, 1995). The unconformity is recognized from its moderate to high amplitude response and systematic truncation of underlying reflections (Figure 4.4).

4.3.3. Unit 1

Unit 1 is bounded at its base by Horizon B and at its top by Horizon C (Figure 4.4). It comprises the Mesozoic syn-rift megasequence previously defined. Unit 1 is characterized internally by two different seismic facies which are separated by Horizon B1. The Unit was divided in two subunits:

- sub-unit 1a, bounded at the base by Horizon B and at the top by Horizon B1, and
- sub-unit 1b, bounded at the base by Horizon B1 and at the top by Horizon C.

Sub-unit 1a is composed of low amplitude laterally continuous reflections. In some restricted regions the reflections partially onlap Horizon B. The dominant seismic facies is consistent with an interpretation of fine-grained sedimentation (Brown and Fisher, 1977). The subunit exhibits southward thickening with variable thicknesses ranging between 100 and 600m. With reference to previous interpretations (Fish, 2005, Richards, et al., 1996) the Sub-unit 1a may include

Tobifera Formation (Fish, 2005) and Serie Tobifera (Platt and Philip, 1995) and would therefore be dated as approximately Middle Jurassic to Early Cretaceous. The subunit may also be associated with the Late Jurassic-Early Cretaceous mature source rocks expected below the base of well 61/17-1 (Figure 4.2).

Subunit 1b is composed of lateral continuous parallel stratified reflections which exhibit moderate to high amplitude reflections. High amplitude reflections are associated with the reservoir interval encountered by the well 61/17-1. The high amplitude reflections observed on seismic profiles can be interpreted as indicating the presence of sand beds embedded with finer-grained sediments. Some of the finer-grained sediments may have source potential, as observed in the descriptions of well 61/17-1 (Figure 4.2). Sub-unit 1b thickens slightly to the south with values ranging between 700-900m. The top of Sub-unit 1b exhibits truncated reflections in the upslope regions and incised canyons in the middle slope (described later). The sub-unit hosts a few but important amplitude anomalies that will be described later. Based on the well calibration 61/17-1 and previous works (Fish, 2005; Platt and Philip, 1995, Bry et al., 2005), Sub-unit 1b is approximately dated as Aptian to Upper Cretaceous in age.

4.3.4. Unit 2

Unit 2 represents a sedimentary asymmetric wedge bounded at its base by Horizon C and at its top by the seabed (Figure 4.4 and 4.5). It represents the Cenozoic foreland basin megasequence defined previously. It is predominantly composed of onlapping, laterally continuous reflections characterized by variable amplitude response from weak to moderate. The sedimentary fill comprising Unit 2 is largely divergent, with maximum thicknesses of approximately 2.8km .

Unit 2 is important in the context of the study because it exhibits amplitude anomalies, enhanced reflections and a continuous seabed simulating negative reflection which was previously observed by Richards et al. (1996) and interpreted as a bottom simulating reflection (BSR, described later).

The laterally continuous reflection pattern of Unit 2 is truncated in a number of cases by elongated bodies characterised by chaotic reflectivity. These bodies occur mostly in the central portion of Unit 2, immediately adjacent to the northern footwall of the Falkland Thrust. These bodies are interpreted as mass transport deposits (MTDs). These MTDs are not correlatable within the 2D grid.

In the shallower section of Unit 2 the reflection geometry exhibits an undulating pattern. These sediments are characterised by moderate and weak amplitude, and are similar in their seismic facies to bottom currents deposits or contourites (e.g. Rebesco et al., 2008). These sediments have been previously interpreted by Bry et al. (2005) as contourites and are probably composed of fine grained sediments (c.f. Stow et al., 2009).

The lack of direct well calibration precludes any specific chronological interpretation of Unit 2. It has been approximately dated as Cenozoic in age by Bry et al. (2004) and in absence of any well data I follow this interpretation.

4.4. Fluid-related acoustic features

The study of seismic features distributed in the SFB has been based on the acoustic properties as observed on seismic data. These seismic features will be described in terms of acoustic response, geophysical properties, distribution and interaction with the stratigraphical and structural features of the basin.

4.4.1. Bottom Simulating Reflection (BSR)

A discontinuous, negative polarity reflection is observed over much of the study area that exhibits diagnostic characteristics of a Bottom Simulating Reflection, of the type associated with the base of the Gas Hydrates Stability Zone (BGHSZ). The presence of BSR in the study area has been briefly documented in some works where it has been linked to the BGHSZ (Richards et al., 1996). This putative "BSR" is described in detail below, and its association with structures and other fluid flow indication is discussed.

4.4.1.1. Acoustic description and distribution

Three main diagnostic observations (1) polarity, (2) relationship with the seabed and (3) relationship with the sedimentary and structural features are used by many previous studies to identify a BSR (e.g. Brooks et al., 1991; Ecker et al., 1998; Helgerud et al., 1999; Korenaga et al., 1997; Satyavani et al., 2003; Shelander et al., 2012). These three major observations will be here documented in order to validate the interpretation of the BSR in the study area.

Polarity

On seismic data the BSR exhibits segments of negative reflection, with different levels of continuity, which approximately mimic the shape of the seabed (BSR, Figure 4.7A). In detail however, these reflection segments are unconnected each other, showing gaps and irregular vertical distance to the seabed.

The polarity response of the BSR was evaluated by extracting traces from 2D seismic lines. In a representative example, five traces are extracted and plotted in Figure 4.7B. The traces have been chosen in different portions of the line and in different basinal settings. In trace T1 (Figure 4.7A-B) the BSR exhibits zero-phase negative loop followed by enhanced reflections beneath. In traces T2, T3 and T4 the BSR exhibit isolated strong negative amplitude response with amplification approximately 1.5 times higher than the seabed reflection (positive). In trace T5 the BSR shows multiple negative reflections. These reflections (Figure 4.7A) mimic the seabed surface maintaining the trend of the more continuous and extended BSR. These amplitudes are potentially associated with development of multiple BSRs (e.g. stable and paleo-BSRs, Popescu et al., 2006) or with different BSRs (e.g. GHSZ of Structure 1, 2 and B; Lu and Sultan, 2008, Sloan, 2003). However, the polarity of the BSR, regardless of the different amplification, is clearly characterised by negative reflection and so it corresponds to the expected response of the BGHSZ.

Relationship to Seabed

Generally the BSR tracks parallel to the seabed, but locally there are small regions where it deviates from this relationship. A direct comparison of the seabed

and BSR surfaces has been undertaken. This observation has been carried out mapping the bathymetric contours of the seabed (blue lines, Figure 4.9) and the time structure contours of the interpreted BSR (red-orange lines, Figure 4.8).

The BSR and the seabed surface have similar shapes. The BSR contour mimics the seabed geometry especially in the southern region (Figure 4.8C). Further north, the contour pattern of the BSR tends to diverge from the seabed. The BSR contour pattern shows clear divergent pattern with respect to the seabed (crossing contours, Figure 4.8A). In the northern area, the BSR exhibits also domed shaped features (DSB, Figure 4.8B). These observations contrast to the parallelism the BGHSZ and the seabed in the southern portions. The presence of irregular features in the north is described in detail below.

Relationship with basin and distribution

The BSR is interpreted over a large region based on the interpretational criteria previously discussed in this section. The identification of the BSR is strongly affected by the frequency of the seismic data. On far stack section the BSR exhibits a suspicious strong continuity in comparison to the near offset seismic profile. This is due to the large content in low frequency but also to Class III AVO effects (Carcione and Tinivella, 2000; Horozal et al., 2009).

The distribution of the BSR is shown in Figure 4.9, where the vast majority of the interpreted anomalies are focussed in the centre of the study area. Two main regions trending E-W (at north and south) exhibit a high continuity of the BSR anomalies. Between these regions the BSR is more discontinuous and presents areas of uncertain identification mainly caused by concordant patterns with the stratigraphy. Three main regions can be defined and are described in detail below.

Region A, in the north, is mostly characterised by BSR anomalies that are recognised as amplitude cut-off of enhanced reflections lying beneath (described later). The presence of free gas beneath GHSZ yields on seismic data a prominent amplitude cut-off due to the decrease of acoustic impedance (Helgerud et al., 1999). Representative examples are present in Figure 4.10, 4.11 and 4.12. In the first example (Figure 4.10 A-B) the amplitude of the enhanced reflection beneath are cutted by a seabed-simulating boundary. The BSR can exhibits localised variations in depth (respect to the profile of the seabed) that can be caused by many factors (Clennell, 1999). In those cases the amplitude cut-off boundary does not simulate the seabed. A representative example is shown in Figure 4.12 A-B, where the amplitude cuff-off boundary exhibits a dome-shaped profile.

Region B is where the BSR anomalies are recognised within MTDs and partially in discordant reflection configuration. The BSR within mass transport deposits (MTDs) is detected due to seabed simulating-pattern of the BGHSZ that is in contrast with the chaotic reflectivity patterns that characterise many MTDs. Interesting examples of the BSR within MTD are present in Figure 4.11. In detail, the BSR terminates within the MTD with gentle amplitude cut off (Figure 4.11A-B). The immediate region beneath the BSR exhibits an amplified chaotic reflection pattern. This feature increases the ease of recognition of the BSR. Examples of BSR not associated with an amplified chaotic reflection within MTDs are observed. A representative example is proposed in Figure 4.11 C where the BSR exhibits a simple seabed-simulating negative reflection that cross-cuts the MTD. In the region the BSR is not often easily identifiable because the seabed, and so the BSR, are concordant to the stratal reflection. The region presents therefore many gaps due to

interpretational uncertainties. The absence of gas hydrate in these regions is however not excluded.

In Region C, in the south the BSR anomalies are mostly identified due to truncation of steep enhanced reflections associated with the thrust-fold belt system. Folded structures or obliquity of stratal reflections with respect to the seabed are the easiest diagnostic setting to interpret a BSR (Rajput et al., 2009 and 2012). Examples of a BSR in discordant sedimentary patterns are shown in a representative example in Figure 4.10 and 4.12. The BSR exhibits a weak continuity that is associated with a lower amplitude response with respect to the previous examples. BSR is also recognisable in sediment waves (Figure 4.10). In these cases the BSR is interpretable because it simulates the profile of sediment waves at the seabed crosscutting the sedimentary structure beneath.

4.4.1.2. BSR forward modelling using Geothermal Gradient Depth BSR Profiles (GGDBSRs)

A forward modelling of the expected position of the BSR in depth has been carried out in order to test whether the BSR position as observed conforms to the probable range of BGHSZ positions expected for the uncertainties in temperature, salinity and other variables.

The position of the BGHSZ has been calculated using a Matlab application based on the following equation developed by Lu and Sultan (2008),

$$P_{(T,S)} = \exp((C_S \cdot S + D_S) \cdot T) \cdot \exp(E_S \cdot S) \cdot F_S$$

, where S is the salinity (range $0 < S < 0.050$ mol NaCl / mol H_2O),

- Cs= 0.1711726397,
- Ds= 0.1046133676,
- Es= −34.14836102,
- Fs= $1.010769956 \times 10^{-9}$,

(constants), and which requires (1) water pressure between 1500-40000KPa, (2) water temperature between 273.15-290.15K, and (3) 100% methane composition.

Temperature and salinity data used in the calculation are based on pre-drilling reports of the oil companies working in the study area (see Appendix A.2). One profile for temperature and one for salinity have been used for the entire area (Figure 4.13). This assumption implies a stratification of water in which T and S only change vertically. The temperature and pressure ranges observed in the study area are inside the limits of the equation (Lu and Sultan, 2008; Figure 4.13). Gas composition of the hydrate is assumed to be 100% methane. This assumption is reasonable in the absence of detailed local data and is based on data from the great majority of the gas hydrate deposits discovered worldwide (e.g. Sloan, 2003). Also in the case of a biogenic source for the gas this assumption can be accepted. Biogenic gas generally contains only up to 2% of other gases, such as ethane, propane, butane, and pentane (Rice, 1993).

The workflow used to model the BGHSZ is synthesised in the following block diagram:

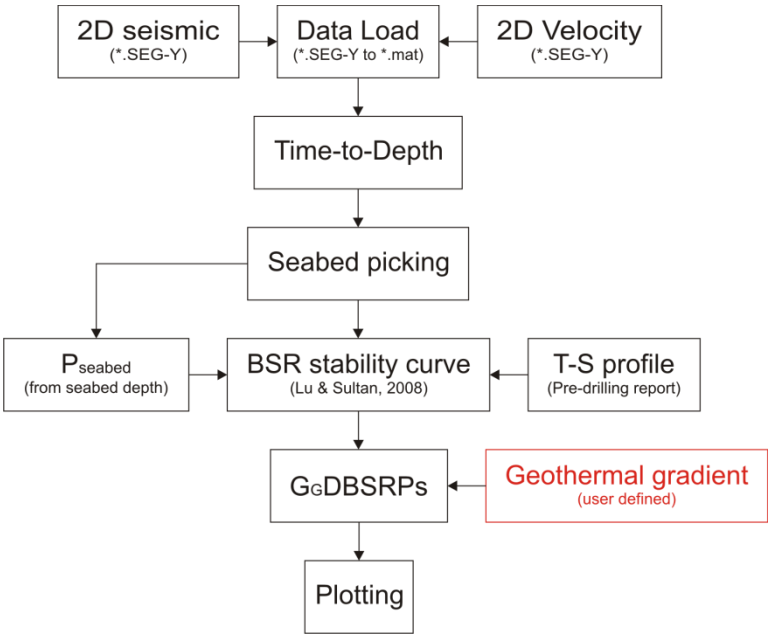

This workflow is applied and plotted directly on the 2D seismic profiles in order to compare the depth of the interpreted BSR with the depths of the modelled G_GDBSRs. Since the G_GDBSRs are based on fixed and homogenous physical properties, any local variation in depth between them and of the interpreted BSR represents a local physical anomaly of the basin which can be caused by variations in temperature, pressure, salinity and pore size.

The workflow has been applied on a number of 2D seismic lines where velocity data were available (FOGL lines). The geothermal gradients are selected for each seismic section in a way that the observed BSR falls in the depth range of the G_GDBSRPs. The geothermal gradients used to calculate the G_GDBSRPs in this profile are 25, 30, 35, 40, 45 and 50°C/km . Two representative examples are proposed to illustrate the approach taken (Figure 4.14 and 4.15).

In the first example (Figure 4.14), the 2D line crosses from the basin axis to the southern region (north-south). The BSR can be identified easily on the seismic profile and can be clearly seen to exhibit a smooth boundary, that crudely mimics the

seabed but which clearly does not follow a single depth value beneath the seabed. Two regions of domal shallowing of the BSR are visible in the basin axis located above the upper tip regions of two prominent basement normal faults. There is no visible shallowing above the buried fold where the BSR is consistent to 30°C/km (Figure 4.13).

The modelled G_GDBSRPs mimic the seabed shape. In the south the BSR is consistent with a geothermal gradient of 25°C/km (Figure 4.14A). From south to north the BSR is consistent with different G_GDBSRPs from 25 to 40°C/km . In the north the domal shallowing of the BSR is consistent with G_GDBSRP calculated on a geothermal gradient of 45°C/km (Figure 4.13B). The depth variation between the BSR at the domed feature and the depth of the G_GDBSRP associated with the geothermal gradient in the south (25°C/km) is 254m.

In the second example (Figure 4.15) the 2D profile crosses the basin longitudinally (east- west). The BSR is easily identified as segments of negative polarity that simulates the seabed shape. Isolated BSR anomalies are observed in the east. A clear domal-shallowing of the BSR is visible at the centre of the 2D seismic profile (DSB, Figure 4.15A). It lies above a prominent basement high which sharply ends with a basement normal fault. The normal fault is geographically linked to the end of the BSR segment. In a similar way other two isolated BSR segments further east are crudely located above two basement normal faults.

The modelled G_GDBSRPs closely simulate the seabed shape with a constant increase of distance with depth. The BSR coincides with the 35°C/km G_GDBSRP in the west. In the central area of the seismic profile the BSR coincides with 40°C/km and 45°C/km G_GDBSRPs. These regions of BSR shallowing are located above a large basement structural high. The domal shallowing of the BSR (DSB, Figure

4.15B) associated with a geothermal gradient of 45°C/km produces a local decrease of depth of 95m with respect to the background value of 35°C/km observed in the west. In the east the isolated BSR segments coincide with the 40°C/km G_GDBSRP.

These results confirm that the BSR clearly exhibits local variations of depth which are unrelated to the shape of the seabed. Different explanations can be found to account for the local anomalous shallowings of the GHSZ. Interaction of GHSZ and upward flow of warm fluids generate a rough BGHSZ with vertical gas intrusions (e.g. Yoo et al., 2013; Wood et al., 2002). The observed BSR is smoothed and it does not exhibit any seismic evidence of vertical fluid intrusions. The presence of salt diapir is known elsewhere to locally perturb the position of the BGHSZ due to local increase of salinity of the stratal water (Ruppel et al., 2005). The lack of salt bodies in the basin exclude this possibility. Variations in sea level can destabilize the GHSZ and produce a shift of the entire BSR (Svenson et al., 2003). The BSR exhibits however local shallowings which are not therefore consistent with this explanation. The domal-shwallowing of the BSR can be ultimately related to the properties of the basin and in particular with the geometry of the deep structures.

In order to provide a better interpretation of what is observed on seismic data, two isochronal maps, associated with the deep basin structures, have been calculated: (1) one map between seabed and the acoustic basement (Horizon B; this map represents the isochronal map of the sedimentary package) and, (2) the second one between the Upper Cretaceous regional unconformity (Horizon C) and the acoustic basement (Horizon B; this map represents the isochronal map of Unit 1). These maps are compared with the isochronal map of the GHSZ calculated between the seabed and the interpreted BSR (Figure 4.16).

In window 1 the GHSZ map (Figure 4.16A) exhibits a number of regions trending NE-SW where the GHSZ thins smoothly (GHSZ thinning, Figure 4.16A). These regions are located in the same regions where the sedimentary package exhibits evidence the minimum thickness (sed. thinning, Figure 4.16B). In window 2 the GHSZ map (Figure 4.16A) exhibits also narrow regions of thinning (fault thinning, Figure 4.16A) which are associated with faults (see Figure 4.8). These narrow regions are geometrically related to with the narrow thinning observed on the isochronal map of Unit 1 (Figure 4.16 C). It is important to note that the isochronal map of the GHSZ is not exhibiting any variation in thickness associated with buried canyons (Figure 4.16 C).

The localised variations in depth of the BSR are therefore interpreted to be consistent with the geometry and the depth of the deep structures and especially with the acoustic basement. This observation supports what already observed on seismic profiles, where domal shallowing of the BSR was observed above structural highs (Figures 4.14 and 4.15).

4.4.2. Enhanced reflections beneath the BSR

Enhanced reflections (ER; e.g. Sun et al., 2012a) are defined as amplitude anomalies where the amplification is dependent on depth and/or distance. ERs are not associated with phase rotation or signal disruption. ERs associated with gas hydrate systems may exhibit the maximum amplification at the BGHSZ. The amplification of dipping reflections decreases in this case with depth and away from the BGHSZ.

Numerous ERs have been recognised in the South Falkland Basin. They are associated with the BSR and their distribution is consistent with that of the BSR

(Figure 4.9). The most prominent ERs are distributed in the northern portion of the study area (Region A, Figure 4.9) but also in the southern region above and between the thrust-fold belt anticlines (Region C, Figure 4.9).

At the BSR the enhanced reflections appear as truncated reflections with a sharp amplitude cut-off response (red arrows, Figure 4.17a). The BSR and the enhanced reflections exhibit in discordant stratigraphy a roof-tile configuration similar to that described by Calves et al. (2008) from the Indus Fan (Figure 4.17a B). The response is however interpreted as an artefact caused by the convolution operations with a non-spike wavelet (e.g. Kronecker delta function). The real geometry of the gas hydrate transition is considered not to exhibit the "steps" seen on the seismic display.

If the upper limits of the enhanced reflections are easily recognizable due to the BSR, the lower edges are not identifiable. Factors such as (1) decreasing amplitude with depth, (2) presence of faults and (3) unconformities make it challenging to interpret precise amplitude cut-offs at the lower margin of the ERs.

The polarity of the ERs is uniformly soft with a prominent single soft loop (or wavelet, Figure 17b). The presence of amplified hard loops is associated with enhanced soft reflections present above or below the ER taken as reference (Figure 17b C). In some cases however it is possible to recognize large differences between top and base loops of the wavelets suggesting that a constructive interference with hard loops is present (e.g. Widess, 1973). In a representative example displayed in variable area mode (Figure 17b D) the base of the layers n and n+1 are indeed amplified with respect to symmetric waveforms (dotted line, Figure 17b D). This response is interpreted as a potential response from the base of the layers.

The amplification of the ERs seems in a number of cases to increase constantly in an up-dip direction. However some exceptions have been observed. In order to

evaluate in a more robust way the relationship between the geometry and the reflection seismic amplification, amplitude extractions passing at the centre of the soft loop of the enhanced reflections have been carried out.

This analysis is described with reference to a set of 4 representative examples (Figure 4.18). P1 profile shows the presence of an amplified area comprised between two main amplitude cut-offs ACO1 and ACO2 (8.27 km). The maximum amplification next to ACO1 is associated with the BSR which represents also the top of the ER. ACO2 exhibits a low amplification and is related to the deeper portion of the ER (148ms TWT). In P1 the increase in amplitude is associated with a decrease of depth. P2 shows a similar pattern but in this case the amplitudes are subject to a strong decrease at ACO2 which may suggest a variation in the layer properties or a variation in fluid content. P3 is characterised by three amplified regions. All of them exhibit amplification variations that are, considering large differences in amplitudes, decreasing with increasing depth. In P4 the amplified region presents again a decreasing amplification with depth. The analyses carried out in other ERs are consistent to what observed in the described examples. The ERs are therefore associated with variation of amplitudes which are inversely proportional to the depth.

The interpreted enhanced reflections, characterised by (1) sharp amplitude cut-off at the BSR (2) soft amplitude response and (3) variation in amplitude with distance and depth, are consistent with many descriptions of ERs associated with free gas charged layers beneath the BGHSZ (e.g. Calves et al., 2008; Hustoft et al., 2009; Li et al., 2013; Sun et al., 2012; Yoo et al., 2013). However the lack of clear hard loops makes the definition of the bottom boundaries of potential gas charged layers uncertain. Only in a few cases (Figure 17b D) has it been possible to identify

asymmetric wavelets that could represent an interaction with the bottom gas layers and the overlying positive loop of the ERs (Widess, 1973).

Importantly, the geometrical characteristics of the ERs, constrained by the analysis of the extracted amplitude values (Figure 4.18), are fundamental for the determination of the behaviour of a potential free gas phase. Applying a velocity of 1.6-1.7 km /s (FOGL velocity data) the analysed ERs are characterised by column heights of 25-125m. These values are comparable to those observed in Black Ridge by Hornbach et al (2004) for fault reactivation and hydrocarbon migration across GHSZ. Therefore the observed columns of potential free-gas may release gas through GHSZ.

However the strong variation in amplitude responses, underlined by the previous analyses, suggests that the gas columns are not continuous as hinted on seismic display. Also the lack of clear lower edges makes uncertain the definition of some of the measured columns of gas. The lack of evidences of hydraulic fracturing and especially the lack of fluid expulsion structures such as pipes or gas chimneys at the updip point of the observed ERs (e.g. red arrows, Figure 4.17a) may suggest that the free gas zone is not able to breach the gas hydrate bearing sediments.

4.4.3. Pipes

Pipes are defined on seismic as vertical zones of signal disturbance that may or may not be associated with amplified reflections. Pipes are normally circular or elliptical in 3D seismic data and are associated to deformed reflections (Cartwright et al., 2007). A small number (4) of pipes have been interpreted in the study area. They

are described with reference to two representative seismic profiles shown in Figure 4.19 and 4.20.

4.4.3.1. Acoustic description

The best example of a pipe is P1 observed entirely within Unit 3 (Figure 4.19, P1). From its base close to the BSR to the seabed it represents a zone of disturbed or incoherent reflections with width of c.350m and with a vertical extent over 200m. The pipe is composed of 4-5 sections characterised by different cross sectional width which are not aligned in cross section (Figure 4.19 E). It reaches the seabed and terminates at a large pockmark with a diameter of c.250m. The reflections lying just outside the pipe are bent downward mimicking the seafloor depression. The partially coherent reflections inside the pipe are characterized by well-defined downward bending of < 10ms TWT. From the BSR to the lower boundary of the enhanced reflections the pipe is not easily recognizable. Chaotic reflections and the presence of high angle normal faults throwing towards the centre of the pipe complicate the interpretation. The root of P1 has not been therefore recognised and is partially obscured by transmission artefacts (c.f. Hovland, 1983; Moss et al., 2012).

The non-coaxial geometry of the pipe is interpreted as evidence of the potential multiple activation of the pipe. The faulting around and inside the pipe could possibly be associated with collapse of the centre of the pipe, potentially due to the expulsion of fluids. Similar structures have been reported by Moss and Cartwright (2010) in the Namibia Basin. Beneath the base of the enhanced reflections the pipe exhibits a disrupted signal "tail" (DSZ, Figure 4.19 B-C) that dims almost completely the underlying reflections. A similar problem in identifying the root of pipes was discussed by Moss et al., 2010.

In contrast pipe P2 is represented by a series of vertically stacked amplitude anomalies with a central dim zone of slightly discontinuous reflection character. The anomalies stacked vertically are disposed axio-symmetrically. P2 terminates at the seabed in a small pockmark, and as such this structure conforms to small diameter pipes described by Moss et al., 2010. At the BSR the pipe is intersected by a small normal fault. The columnar disturbance interpreted as pipe disturbs the high amplitude reflections beneath the BSR. These are deflected into small depressions along the pipe axis (Figure 4.19).

Below the high amplitude reflections a narrow tail of disrupted acoustic character is present (DSZ, Figure 4.19), but in this case the geometries beneath it are well imaged. The root of the pipe is again not precisely imaged, a common problem with this type of features (Hustoft et al., 2009), however in this case some possibilities of the position of the root of P2 are considered (T1 and T2 Figure 4.19 C). In the first interpretation the root (T1) is placed at the BSR in which case all the disturbed reflections along the vertical zone beneath the BSR would have to be considered as transmission artefacts. In the second interpretation the root (T2) is located at the base of the set of enhanced high amplitude reflections located for c.150ms TWT beneath the BSR. It is interesting to note that the downward projection of the pipe axis coincides with the upper tip region of the large basement-rooted normal fault precisely at the base of the stacked enhanced reflections, at position T2 on Figure 4.19 C. In this second interpretation the "tail" of disrupted reflectivity (DSZ) would extend downward only from position T2.

Looking at P1 in detailed view (Figure 4.19 D) the pipe axis is interpreted as cross cutting the BSR at point T1. The pipe axis intersects a prominent fault zone at position T2, and the disrupted signal "tail" (DSZ) is interpreted to extend to the top

of the acoustic basement (Horizon B). The interpretation here favours the probability that the root of pipe P1 is close to or at the intersection with the normal fault zone. In contrast with pipe P2, this pipe roots some way within the enhanced reflections. This raises the question of to what extent the enhanced reflections and the normal faults are implicated in the origin of these two pipes.

The remaining two pipes (P3 and P4) are both observed in the 2D seismic line shown in Figure 4.20. They exhibit similar characteristics to pipe P1. Between the seabed and the BSR, P3 is recognisable as a discrete columnar shaped zone of small amplitude anomalies and disrupted host stratigraphy. It is c. 560m in diameter, larger respect to P1. Some reflections cross P3 with little disruption, notably the BSR. It is possible that the 2D profile does not transect the axis of the pipe, hence giving a mixture of in-plane and out-of-plane reflections (Figure 4.20 C). Beneath the BSR the pipe is imaged as a series of narrow upward amplified reflections. These reflections are remarkably characterised by decrease of dominant frequency. These are associated with strong attenuations making it complicated to recognise the underlying structures and therefore the position of the root.

Pipe P4 is interpreted as a pipe, but most probably intersect the structure where the profile is some distance from the pipe axis and hence it does not have a particularly obvious expression in a vertical sense (Figure 4.20). Pipe P4 is characterised by an irregular vertical region of signal disturbance. Within P4 some amplified reflections are present but in general the pipe does not represent a drastic change of amplitude. P4 does not reach the seafloor and it is unconnected to the underlying BSR. Also in this case the regions beneath P4 are clearly deformed by the strong attenuation and low frequency response observed beneath P3. The root of the pipe is again unrecognisable.

Importantly, the positions of pipes are associated with a notable shallowing of the BSR in all the cases. The positions of pipe P1, P2 and to some extent P3 are also closely associated with basement rooted normal faults propagating upward into Unit 2.

The few but extraordinary pipes discovered in the shallow section of the South Falkland Basin are largely comparable, in terms of geometry and acoustic characteristics, to those described by Gay et al. (2006 and 2007) in Lower Congo Basin. In that example they represent focussed fluid expulsions of mixed thermogenic and biogenic gases and oil. Similar columnar zones of disrupted or offset reflections have also been reported by Hustoft et al. (2009) in NW offshore Svalbard, Løseth et al. (2011) in offshore Nigeria, Macelloni et al. (2012) from Gulf of Mexico, and all these cases they indicate migration of fluids from the subsurface to the seabed. Fluid flow expulsions are also associated with sediment remobilization and generation of edifices such mud volcanoes and mounded structures (Lonke and Mascle, 2004; Somoza et al., 2012). The absence of any mud structures at the top of the observed pipes and in the subsurface suggests a low or negligible presence of solid materials being transported upward with the fluids. The presence of pipes in the South Falkland Basin therefore represents a strong evidence of fluids expulsions (water, gases, etc).

4.4.3.2. Pipe and BSR relationship

As seen on seismic data the BSR presents, in the region surrounding the pipes, limited areas of local shallowing (Figure 4.20). Anomalous regions of domal shallowing of the BSR have also been observed in the time map of the BSR in Figures 4.8 and 4.16. Is the domal shallowing of the BSR related to the pipes? In

order to evaluate this question the distribution of the pipes has been associated with the isochron map of the seabed to the BGHSZ (Figure 4.21).

Major thickness reductions of the GHSZ are localised in the southern and western margins and as already observed in Figure 4.8 are associated with the seabed profile. In these regions and in the central portion of the study area the GHSZ exhibits a smoothed pattern. The pipes are distributed in the north-west region of the interpreted BSR (Figure 4.21 A) and in these regions the most prominent local shallowing are located. At the northern margin of the GHSZ the dome-shaped features associated with P2 and P1exhibit an elongated NE-SW trend (Figure 4.21 B). These features are parallel with each other and are oriented with the same strike as the prominent basement normal faults. The height of these domes, considering a background level at these areas of about 275ms TWT, is approximately100ms TWT with the highest values associated with the pipe positions. Further west, the dome-shaped features associated with pipes P3 and P4 are associated with a normal fault that extends for approximately 20km with a strike of ENE-WSW.

These observations provide additional context of the link between (1) pipes and BSR and (2) structural features of the acoustic basement. These points are discussed later.

4.4.4. Seismic anomalies in the deep basin

A set of amplitude anomalies comprising dim amplitude zones, disrupted signal zones and flat-spots have been interpreted in the deeper buried part of Unit 2 and Unit 1, below the lower limit of the shallower families of enhanced reflections associated with free gas trapped beneath the BSR. These are described in detail

below based on interpretation of the seismic amplitude response and attribute analysis.

4.4.4.1. Dim- and disrupted-signal zones

The dim amplitude zones appear on seismic as well defined regions where the general amplitude of reflections is much lower than their background values (e.g. Løseth et al., 2009). They can exhibit irregular margins that are not related to the background reflectivity patterns.

In a representative example (Figure 4.22A) the dim zone can be easily recognised in areas of moderate amplifications associated with enhanced reflections and MTDs. The amplitude of the reflections is firstly dimmed inside the dim amplitude zone and subsequently returns to the background values (dim reflections, Figure 4.22 B).

Dim amplitude zones are commonly associated with the presence of gas charged layers (Løseth et al., 2009). The dim reflections seen in the study area (e.g. Figure 4.22 B) represent a clear decrease of acoustic impedance and this may be caused by the replacement of water with hydrocarbons or by the localised increase of porosity (Mavko et al., 2009). The presence of high amplitude reflections and MTDs above the dim amplitude zones could locally attenuate the response of the horizons located directly beneath them by attenuation. However, the geometry of the dim reflections is not consistent with the presence of high scattering amplitude bodies because this would have generated a vertical dim amplitude shadow. The lack of any other quantitative observations does not allow the validation of whether this seismic response is indeed associated with hydrocarbons.

Disrupted signal zones, defined as areas of signal disruption associated with intermittent amplifications have been observed in the deeper section of Unit 2.

Representative examples are shown in Figure 4.23 (DZa and DZb). The signal disruption zones, DZa and DZb, extend vertically showing a slightly appreciable increase of amplitude of the background reflectivity. This effect is associated with a partial disruption of the reflections. DZa exhibits a narrow area and is roughly rooted at the Horizon C, and above a normal fault propagating from the basement (Horizon B). DZa reach the BSR at his top. DZb is characterised by a wider shape respect to DZa. It is rooted above a normal fault above Horizon B and its top terminates below the enhanced reflections.

The peak-frequency TFR display shows horizontal (HFS) and vertical frequency shadows (VFS) closely related to DZa and DZb (Figure 4.23 C). The frequency response at DZa exhibits vertical and horizontal features. The horizontal frequency structures simulate the geometries of the sedimentary pattern with frequency drop between 10 and 20Hz. The frequency response at DZb shows a vertical cluster of horizontal frequency shadows (HFS). They are related mostly with the upper part of the disrupted zone with values around 10Hz.

The observed disrupted signal zones, located at the top of the foot wall crests, are interpreted as regions associated with the presence of ascending fluids (Løseth , 2009). These seismic features are similar to other well-known gas migration features, such as gas chimneys (e.g. Arntsen, 2007) or with the seismic expression of CO_2 injection in the North Sea (Arts et al., 2004a-b). The lack of strong reflection amplification, expected in the limited regions that are associated with fluid substitution, can be attributed to the depth of the observed objects that reduces the acoustic effect of the presence of fluids (Domenico, 1974). The TFR response observed in DZa and DZb features are consistent with frequency shadow effects documented by Castagna et al. (2003). The presence of horizontal low frequency

features can be associated with gas charged layers (HFS, Figure 4.23 C) meanwhile the sub-vertical ones (VFS, Figure 4.23 C) could plausibly be related to faulting (Ilg et al., 2012).

4.4.4.2. Flat-spot

A potential flat-spot has been recognised in two 2D seismic lines that transect it longitudinally (Figure 4.24 A) and transversally (Figure 4.24 B). In cross section it can be described as a moderate hard reflection with an almost perfect horizontal surface. It is divided in segments of equal amplification and it lies beneath a convex upward low amplitude soft reflection. Both reflections exhibit discordant patterns with respect to the background reflectivity suggesting they may represent lateral events projected in the seismic plane.

In dip-section the flat-spot exhibits a horizontal hard reflection with a completely discordant trend respect to the background reflectivity (Figure 4.24 B). This characteristic represents strong evidence of a potential fluid contact (e.g. gas-water contact or oil-water contact). The flat-spot is laterally bounded by a northward dipping normal fault which propagates from Horizon B to the base of Unit 2. The soft reflection above the flat spot observed in Figure 4.24 B seems to change polarity in the area above the flat spot suggesting again the presence of a substituting fluid (Mavko et al., 2009.).

The flat-spot has been investigated further using AVO analyses using the available near-far stack section pair in order to determine the nature of the anomaly. Limited windows have been selected in specific regions to reduce the noise of background reflectivity. In AVO cross-plot 1 and 2 (Figure 4.24) the results can be described as a dominant background response located at the centre of the plot (G=0;

I=0). Clear anomalous trends are not observed. AVO cross-plot 3 shows again a dominant background trend but in this case a clear anomaly trend can be observed in the bottom left region of the cross-plot (3rd quadrant). Following the classification of Castagna et al. (1998) this result is clearly associated with AVO class III response.

The interpreted flat-spot is a strong evidence that support the presence of thermogenic gas in the study area (or at least at the depth of the seismic object). The segmented hard reflection, observed also in wiggle display, could possibly be associated with other structures like Opal A/Ct and highly consolidated sands (Aveseth et al, 2009). The pressure-temperature stability conditions related to Opal A/Ct, a chemical transition associated with digenesis of silica-rich sediments (Davies and Cartwright, 2002) and the hard response on seismic data, are not however consistent with the depth of the documented flat spot. A potential paleo digenetic boundary (e.g. paleo opal/A/Ct) is also discarded due to the small lateral extent of the feature. The presence of highly consolidated sands bodies are not consistent with what observed in Figure 4.24 where the flat-spot exhibits a clear discordant trend respect to the observed dipping reflections of Unit 1. Again, the presence of the soft amplitude response above the flat spot is consistent with what is expected by a decrease of acoustic impedance from cap rocks to reservoir intervals (Mavko et al., 2009). In Figure 4.24 B the particular amplitude response above the flat-spot resemble a typical amplitude reversal universally associated with deep gas layers (Sheriff, 1975). Finally, the AVO class III response strongly suggests the association of the observed anomaly with compressible fluids.The presented and discussed flat-spot is probably a hydrocarbon reservoir and hence also a DHI.

4.5. Discussion

In the previous sections it has been interpreted that the observed range of seismic anomalies are mostly associated with hydrocarbons. In this section all these DHIs will be analysed in order to build up a strong case that they are potentially part of a single hydrocarbon plumbing system active in the South Falkland Basin (SFB).

4.5.1. Pipe formation as shallow indicator of an active petroleum system

Pipes represent the potential expression at the seabed of an active petroleum system in SFB. The first strong implication for their formation is the presence of a source of fluids (Moss and Cartwright, 2011). The position of the source of fluids can reveal how pipes are formed and vice versa. The close relationship observed between pipes, the BSR and the basement normal faults will be discussed to explore their interrelationship in the context of pipe formation and the potential origin of the fluids involved.

4.5.1.1. Pipe formation

The possible formation of pipes is discussed taking as reference previously explained mechanisms for formation of pipes and other leakage features observed worldwide on seismic data. These mechanisms are related to gas hydrates (or gas hydrate provinces) and faults, and include:

1) Pipe formation due to pressure build-up of the free gas zone beneath the GHSZ (e.g. Liu and Flemings, 2007; Figure 4.25 A);

2) Pipe formation caused by fault activation triggered by free gas column within the free gas zone (Hornbach et al., 2004; Figure 4.25 D)
3) Pipe formation due to GHSZ instability
4) Pipes formation caused of focused fluid flow along faults (e.g. Xie et al., 2003a-b; Figure 4.25 B);
5) Pipe formation caused by vertical fluid migration rooted at basement structural highs (Figure 4.25 E)

These mechanisms are discussed below and with reference to synthetic models shown in Figure 4.25.

Pipe formation due to pressure build-up of the free gas zone beneath the GHSZ (1)

The formation of the pipes can be caused by pressure build-up of the free gas zone beneath gas hydrate bearing sediments (Figure 4.25 A). As suggested by Liu and Flemings (2006) gas may concentrate in shallower regions of the free gas zone and enter, due to the high gas pressure, into GHSZ and propagate vertically forming gas chimneys. As observed in Figure 4.21 pipes are located at the regions of domal shallowing of the BSR which are potentially associated with local higher thicknesses of the free gas zone (or enhanced reflections, see section 4.4.2). These conditions are favourable for the formation of higher column of gas and therefore for the formation of pipes (Luo et al., 2012).

The measurements carried out in Figure 4.18 showed in the free gas zone gas columns of 25-125m (see section 4.4.2) which are spread horizontally for many kilometres (profile P1 length is 20 km, Figure 4.18) and with apparent angles less

than 1 degree. At this distance, a gas layer should have a high saturation in order to maintain pressure and gas column continuously connected (Berg, 1975; Stauffer, 1979; Wan et al., 2014). These observations, taking in account also the lack of clear gas-water contacts, suggest that the free gas beneath the GHSZ would not be able to generate enough buoyancy forces to migrate into in the gas hydrate bearing sediments. Similar arguments have been discussed by Flemings et al., (2003) in the Black Ridge Basin. This point is also supported by the complete absence of fluid flow indicators (e.g. leakage phenomena; Løseth , 2009) at the up-dip points of the observed enhanced reflections (e.g. red arrows, Figure 4.17 B) and leads us to consider pipes formation caused to pressure build-up of the free gas zone beneath the GHSZ implausible.

Pipes formation caused by fault activation due to free gas column within the free gas zone (2)

Formation of pipes can be associated with GHSZ instabilities caused by fault slip triggered by critic pressure of the free gas zone (Hornbach et al., 2004). This mechanism is similar to the one previously discussed, however in this case the gas has to trigger a pre-existing fault (e.g. basement normal fault) which requires a minor gas pressure build-up.

As observed in the previous analysis (Figure 4.19 C-D) pipes P1 and P2 could have been formed in some way by the active slip of basement normal faults and the consequent release of gas across the GHSZ.

In two different points was observed that the P2 axis transects a shallow fault at the BSR at point T1 (Figure 4.19 C) and a deeper fault propagating from the basement (Horizon B) at point T2 (at the base of the enhanced reflections, Figure

4.19 C). The position T1 suggests that the formation of the pipe could potentially have been associated with fault activation at the GHSZ, but the presence of a deeper and prominent normal fault (position T2) suggests instead a potential rooting of the pipe below the BSR. This case is supported by the geometry observed at P1 where the pipe axis transects a number of enhanced reflections at T2 implying again that the formation of the pipes is potentially rooted below the BSR. These observations suggest that the formation of the observed pipes is not related to fault activation triggered by pressure build-up of the free gas zone below the GHSZ.

Pipes formation due to GHSZ instability (3)

Release of gas associated with GHSZ instability can be produced by variations in temperature, pressure and salinity (e.g. Sloan, 2007). The observed BSR in the south region above and within the fold-thrust belt anticline structures, exhibits seismic evidence of multiple BSRs interpreted as paleo-markers of the past positions of the BGHSZ. Arguing that the most recent GHSZ is associated with the more developed BSR at the top (Figure 4.7), the paleo-BSRs indicate that the seabed has been uplifted in the past years to the actual position. The uplift of the seabed is consistent, in that region, with the N-S compression between the Scotia and the South America Plates previously documented (e.g. Bry et al., 2004). In the northern region the GHSZ shows in most of the cases a single BSR (e.g. Figures 4.7, 4.10, 4.12, 4.14 and 4.15) implying that the uplift of the seabed was active mostly in the southern region. The lack of any multiple BSRs and the large number of enhanced reflections terminating sharply at the observed BSR are strong evidence that the BSR observed is the actual and stable position of the GHSZ.

Pipes formation caused of focused fluid flow along faults (4)

The close relationship observed within specific pipes and the position of prominent normal faults propagating from the deep acoustic basement (Horizon B, Figure 4.21) is worthy of further discussion. Since the fluids present within the free-gas zone are not enough sufficient to build up the necessary gas pressure and breach the BGHSZ, it is expected that the formation of pipes is potentially produced by migration of gas within the observed normal faults (Capuano, 1993; Fisher et al., 2001; Ilg et al., 2012; Manzocchi et al., 2010). Direct evidences of fluid flow along faults were not clearly observed due to the limitations of the seismic methods, however the close position between normal faults and pipes (Figure 4.21) and taking in account the previous discussed possibilities (see section 4.5.1.1), the documented faults may support the migration of fluids from the deeper Units (e.g. lower portion of Unit 1) to the shallow sequence and contribute actively in the formation of pipes.

Fault-related pipe formation mechanisms are poorly understood but documented in a large number of cases worldwide (e.g. Berndt et al., 2003; Ilg et al., 2012; Hovland and Judd, 2007; Hustoft et al., 2007).

Pipe formation caused by vertical fluid migration rooted at basement structural highs (5)

Pipes can be an expression of vertical migration of hydrocarbon rooted in proximity of basement structural highs. This hypothesis suggests a pipe formation similar to other vertical fluid flow features such as disturbed signal zones observed in Figures 4.22 and 4.23 which are highly comparable to other vertical evidence of

hydrocarbon migration observed worldwide (e.g. Heggland, 1997; Hashemi et al., 2008; Schroot et al., 2005).

Following these example the pipes could be related to these type of hydrocarbon migration which are characterised by the rooting at local structural shallows of the acoustic basement. However, as observed in Figure 4.19 the pipe axes intersect normal faults and the GHSZ implying that the migration of hydrocarbon forming the pipes is not sensitive to the presence of faults and GHSZ. This implies therefore a complete bypass of these migration obstacles and that the root zone is in such way connected to the seabed.

As observed by Løseth et al (2011) in the Niger Delta pipes can penetrate fault zones maintaining straight vertical pathways and produce vent structures at the seabed. As observed by Cathles et al. (2010) in Storegga Slide offshore Norway pipes can penetrate the GHSZ and produce pockmark at the seabed. These examples make feasible the case that the observed pipes could potentially have been formed by vertical gas migration rooted at the observed shallower region of the acoustic basement and that the presence of faults and GHSZ plays a limited role in their formation.

Summary

These discussed points suggest that the formation of the pipes is not related to fault slip of the GHSZ and that the presence of gas in the free-gas stability zone (enhanced reflections) is not sufficiently efficient to breach the BGHSZ. The stable condition of the GHSZ within the pipe regions (Figure 4.21) suggests again that GHSZ instabilities are not responsible for the formation of the observed pipes.

The suggested mechanisms for the formation of the observed pipes are therefore related to the migration of hydrocarbons within fault zones or migration of hydrocarbon rooted at the structural shallow of the acoustic basement.

The limited number of pipes observed in the fault zones (Figure 4.21) is suggested to be influenced by the coarse spacing of the 2D seismic grid. It is expected that a larger number of pipes may be present in fault zones. The seabed could potentially resemble previously documented fault-related pockmarks fields (e.g. Hovland, 1983; Pinet et al., 2010) where regularly spaced pipes, occurring along fault planes generate aligned pockmarks at the seabed.

It is finally suggested that the fluid involved in the formation of pipe have deep origins and potentially related with the thermogenic hydrocarbon documented in association of Darwin discovery and the observed flat-spots. A discussion of the origin of the fluids is therefore needed to support the formation of the pipes.

4.5.2. Origin of fluids within the free gas zone and GHSZ

The documented enhanced reflections (section 4.4.2) were interpreted to be associated with free-gas zone which represent a common phenomenon associated with the formation of gas hydrates (Sloan, 2003). The formation of a free-gas zone first and the formation of a widespread gas hydrate region require the presence of biogenic or thermogenic gas. The potential origin of gas can be related to (1) generation of biogenic gas within the shallow basin or (2) migration of thermogenic gas from deeper structures to the base of the enhanced reflection package. These possibilities are discussed below.

4.5.2.1. Biogenic gas within free-gas zone and GHSZ

The generation of biogenic gas in the basin cannot be determined due to lack of essential parameters such amount of immature organic matter, temperature and other information (Rice, 1993). Some considerations are however proposed.

Biogenic gas accumulates in marine sediments where sedimentations rates exceed ~50m/MY and organic matter is preserved. With sedimentation rate lower than 50m/MY organic matter is consumed and methane is not produced. Assuming that the sediments involved in the generation of biogenic gas are dated from Upper Cretaceous (66MY) to Quaternary (0-2.5MY) and that Unit 2 exhibits thicknesses of 2.5km , the resulting approximate sedimentation rate is 40m/MY. Lower sedimentation rates, ranging between 3.3m/MY and 33m/MY, are also reported in other parts of the Falkland Plateau (DSDP 330-329; Ludwig, 1983).

The geometry of the sedimentary thickness is not consistent with the distribution of the gas hydrates. The northern margin of the interpreted BSR is indeed southward divergent with respect to the geometry exhibited by the both basement and sedimentary body (Figure 4.16) and in contrast to basin centred gas systems (Law, 2002). The generation of biogenic gas, assuming a uniform distribution of organic matter, would be more uniformly distributed (Law, 2002). Again, on 2D seismic data it has been observed that the distribution of the BSR presents gaps and areas in which enhanced reflections are not present (Figure 4.15). Also the distribution of the enhanced reflection is not regular beneath the BSR but developed mostly at the northern margin of the GHSZ (Figure 4.10, 4.12 and 4.14). Maturation of biogenic gas should be more uniform and generate almost equally developed enhanced reflections.

These observations suggest that the gas involved in the formation of free-gas-zone and gas hydrates is associated to the presence of thermogenic hydrocarbons coming from the deep structures. The lack of essential parameters does not allow us to exclude the presence of biogenic gas and evaluate its concentration in the observed DHIs. Mixed gas system with biogenic and thermogenic gases are widely reported (e.g. Gay et al., 2007; Shurr and Ridgley, 2002).

4.5.2.2. Thermogenic gas within free-gas zone and GHSZ

The free-gas zone and the GHSZ can be associated with fluids migrating from the deeper structures to the base of the free-gas zone. Indicators of fluid migration routes within Unit 1 and 2 are potentially related to dim amplitude and disrupted signal zones (Figures 4.22 and 4.23). The presence of these fluid flow structures, as already discussed, resemble typical seismic features, such gas chimneys (Løseth et al., 2009) or other vertical fluid migration systems (Arts et al., 2004a).

Since at the depth of the observed dim amplitude and disrupted signal zones (Figures 4.22 and 4.23) biogenic gas is not produced (>600m; Shurr and Ridgley, 2002) the migration features will involve only thermogenic fluids. The Darwin discovery and the flat spot (Figure 4.24) are indeed strong evidence of the presence of thermogenic hydrocarbons coming from the expected mature source rock located immediately below the well site 61/17-1 (Figure 4.2).

This case suggests that thermogenic fluids migrate from the deeper portion of Unit 1 and 2 at the base of the free-gas zone and allow the formation of gas hydrates

4.5.3. Source rock

The plumbing system, in order to provide fluids for the generation of the documented DHIs needs to be associated with a source of fluids. Most of discussed points suggest that the origin of the fluids is associated with thermogenic fluids and so related to the deeper units of the basin containing the expected mature Oxfordian source rock (Figure 4.2).

The source rock is imbedded in Unit 1 which is widely distributed in the basin. Assuming a geothermal gradient of 30°/km and using the velocity information provided by FOGL an estimation of the distribution of the mature source rock has been carried out. The measurement is based on the interpreted acoustic basement (Horizon B, Figure 4.6) and so involves only the northern area of the basin.

The result of this operation (Figure 4.26), assuming uncertainties on the real distribution of the organic matter and his concentration in Unit 1, shows that the mature source rock could have generated the observed DHIs and is distributed in a narrow elongated area oriented E-W. The mature source rock is supposedly also present also below the southern area beneath and within the thrust-belt anticlines.

The result shows that the observed DHIs are localised only partially above the mature source rock. The relationship between deep source of fluid and DHIs is therefore strongly dependent on deep migration routes capable of transferring the hydrocarbon fluids northward and up-dip. The fluid flux from the source rock to the normal faults and the DHIs should cover in certain case almost 20 km laterally. Up-dip stratal migration can cover over 100 km (England et al., 1987) making this suggested plumbing option a reasonable proposition. One of the potential up-dip migration routes could be associated with the sand rich sediments composing the

base of Unit 2 that as already stated represent an analogue of the Darwin reservoir (Figure 4.2) and covers almost the entire basin (Figure 4.4).

4.5.4. Plumbing System

The discussed DHIs and their fluid flow interactions are here summarised in the proposed conceptual plumbing system acting in the South Falkland Basin (Figure 4.27). The plumbing system will be described below starting from the deep source rocks to the shallowest evidences of fluid flow.

1. Hydrocarbons are generated from the mature source rock distributed in Unit 1. The generation of hydrocarbons and the presence of thermogenic gas are necessary to justify the Darwin discovery and other key DHIs (e.g. flat spot).

2. The generated fluids migrate northward along key reservoir-like layers. The hydrocarbons are supposed migrating up-dip for few 10s of kilometres. The updip migration mechanism is supposed to transfer a certain amount of hydrocarbons to relatively shallower positions of the basin. These shallower positions, such as footwall crests of basement normal faults, are expected to be the regions of hydrocarbon focussing. The properties of the carrier beds can be associated to what discovered in the Darwin reservoir (Figure 4.2). These lithologies are potentially related to the middle reflections of Unit 1. Other carrier beds are however potentially located within the Unit.

3. The normal faults intersecting the mentioned carrier beds act as vertical conduits transferring vertically the hydrocarbons to the shallower portions of the basin. No direct evidence has been discovered to support this hypothesis.

4. The gas reaches the base of Unit 2 generating subsequently on seismic the documented disrupted signal zones (or gas chimneys). From these points, the gas will migrate upward generating the documented free gas zone (enhanced reflections). Some biogenic gas can be generated within the enhanced reflection package. Once the gas reach the BGHSZ generates the gas hydrates and on seismic the documented BSR.

5. The gases, respect to point 4, can however migrate along the normal faults directly to the shallower portion of Unit 2 and generate the documented pipes.

4.6. Conclusion

The main conclusions are:

1. The South Falkland Basin hosts an active petroleum system.
2. From the undrilled source rock, below the base of the well 61/17-1, to the seabed the plumbing system exhibits a series of seismically recognizable amplitude anomalies that represent Direct Hydrocarbon Indicators.
3. The DHIs are mostly consistent with thermogenic fluids. Biogenic gas cannot be excluded because of the lack of essential parameter.
4. The normal fault system is discussed to be the main vertical fluid flow network allowing the migration of hydrocarbon and the connection of the observed DHIs in the different sections of the basin.
5. The widespread BSR has been interpreted as the base of the GHSZ. It presents a number of domal shallowing, which are interpreted to be caused by the relative shallow position of the acoustic basement. Further analyses are required to support this interpretation.

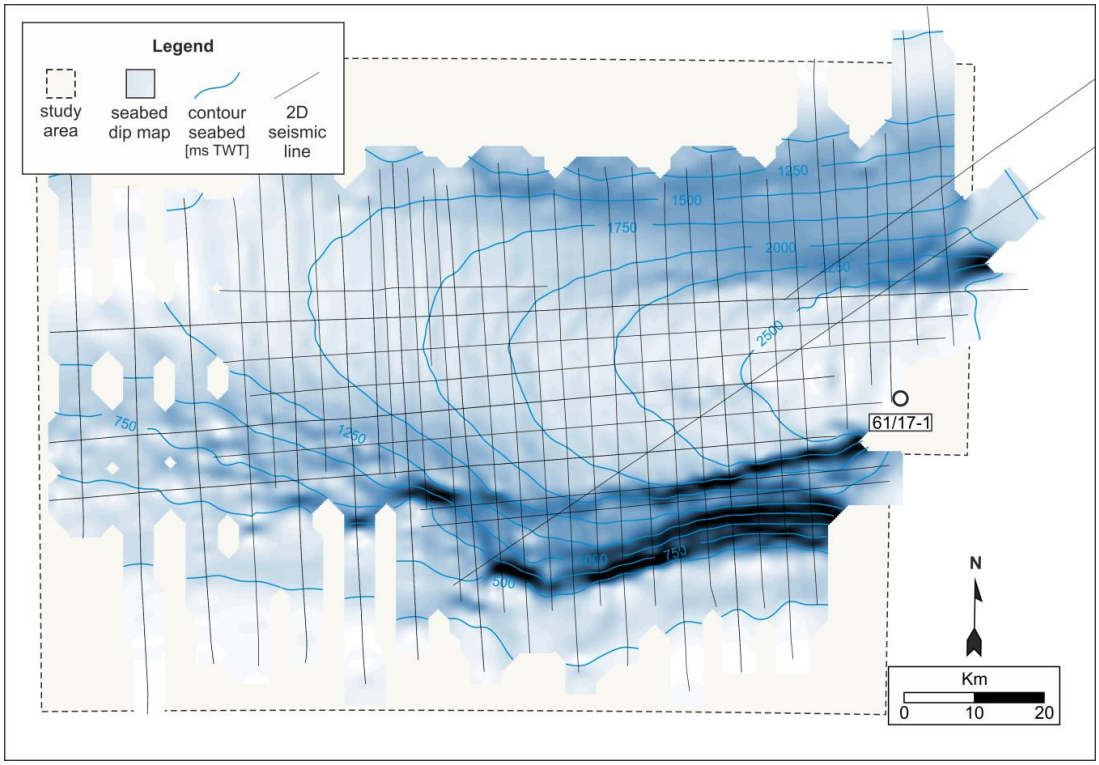

Figure 4.1 Basemap of South Falkland Basin (SFB). Dip map of the seabed and contouring of the depth in ms TWT. The well 61/17-1 is located approximately 1.25km to the east of the 2D seismic grid. 2D grid spacing variable between 2 and 8 km .

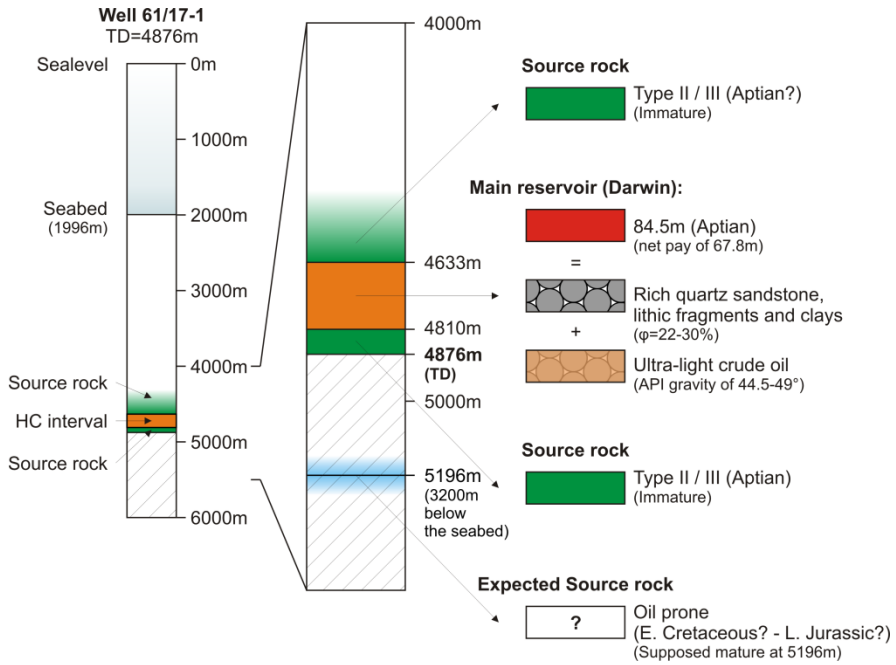

Figure 4.2 Well 61/17-1 indicating the position of Aptian source rocks (green, immature), Darwin reservoir (orange) and expected mature source rock (light blue). Total depth: 4876m below the sea level (water depth 1996m).

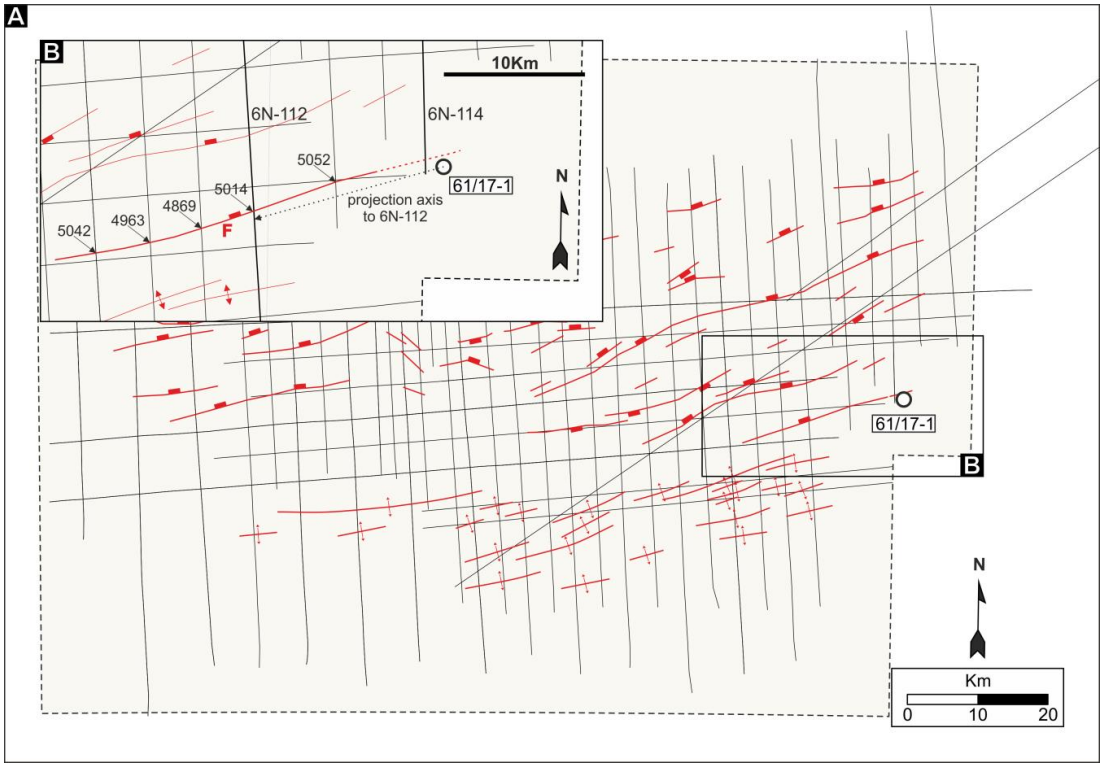

Figure 4.3 Basemap of SFB. The basemap (A) shows the position of well 61/17-1, the 2D seismic grid and the position of the interpreted structural features (red drawings, see section 4.2.3). In the close-up (B) the position and the projection of the well 61/17-1 on the 2D seismic line 6S-112 (Figure 4.4) and 6S-114 (Figure 4.5). The projection axis is parallel to the normal fault F which exhibits a linear NE-SW orientation and a limited variation in depth (black numbers in ms TWT).

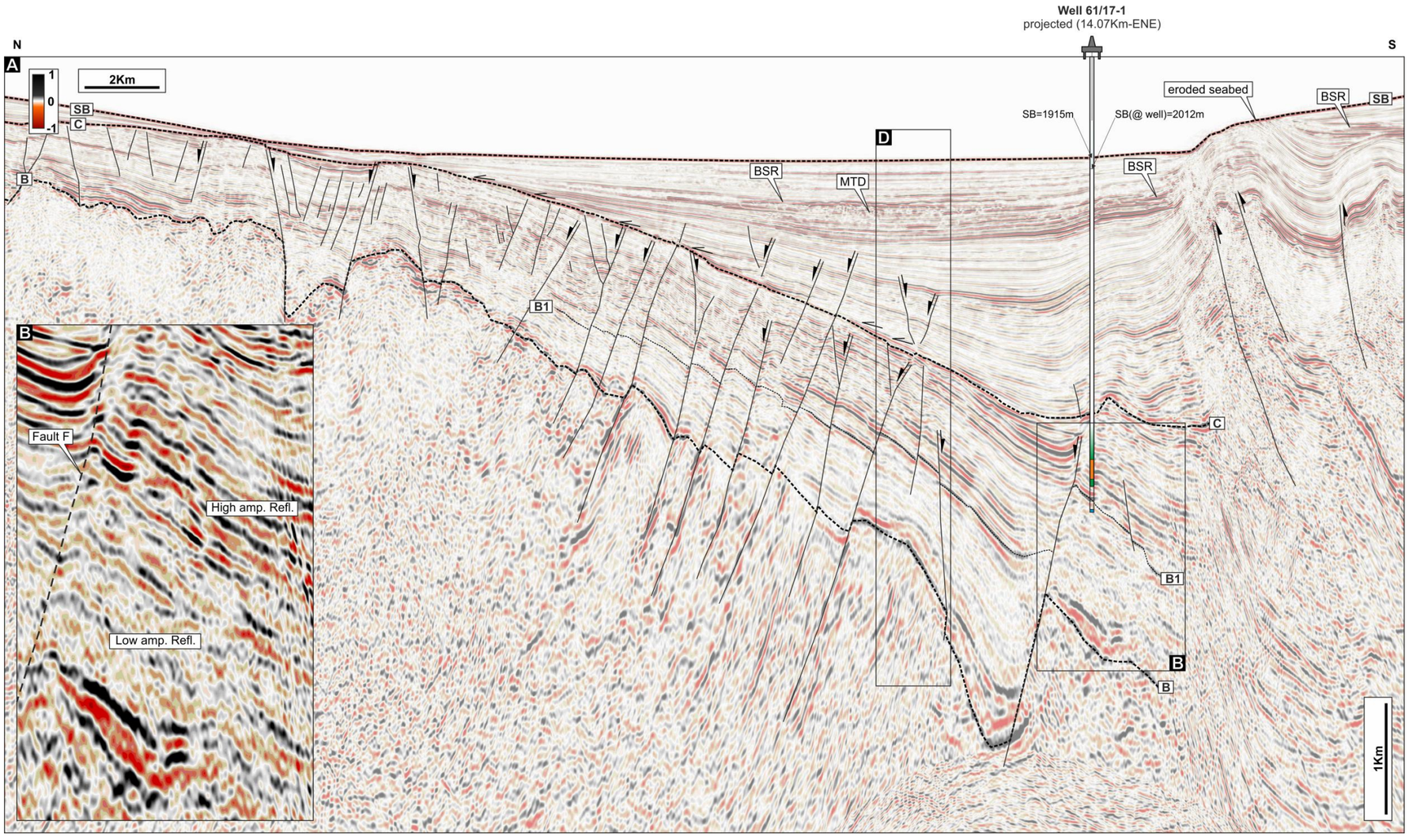

Figure 4.4 2D depth-seismic section 6S-112 (A, see Figure 4.3 for line location) showing the interpretation of normal faults, thrust faults and main horizons. The projected well 61/17-1 lies approximately at the footwall crest of fault F (B). The well is displayed with the same colour code of Figure 4.2 where orange is used to represent the reservoir interval, green represents the Aptian source rocks above and below the reservoir interval and blue represents the expected mature source rock. Interpretational uncertainties (question marks) below the Falkland Thrust. The basin is consistent with an interpretation of a partially filled rift basin at north (Syn-rift and foreland basin) and a thrust-fold belt system at south (Falkland Thrust) (C). The Darwin reservoir (orange, Aptian) is approximately associated with a series of bright amplitude reflections dipping to the south (A-B). The expected position of the mature source rock interval (see Figure 4.2) is may associated with a series of low amplitude reflections beneath Horizon B1. D, representative seismic interval used in Figure 4.5.

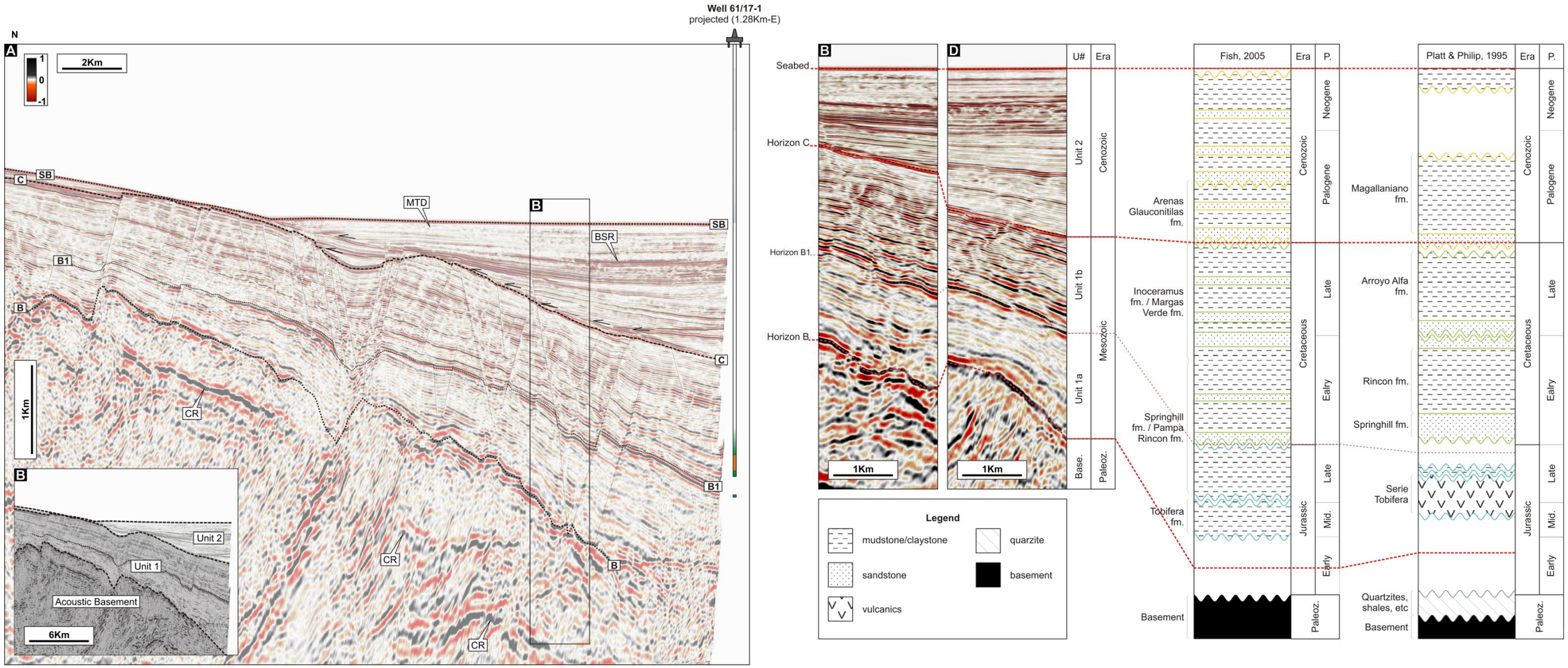

Figure 4.5 2D depth-seismic line 6S-114 composite (see Figure 4.3 for line location) showing the interpreted horizons and the position of the well 61/17-1. The well lies outside the 2D seismic line. The well is displayed with the same colour code of Figure 4.2 where orange is used to represent the reservoir interval, green represents the Aptian source rocks above and below the reservoir interval and blue represents the expected mature source rock. Coherent reflections (CR) beneath the acoustic basement (B) have been observed. Close-ups C and D (see Figure 4.4) showing the principal seismo-stratigraphic units interpreted using previous works focussed in the SFB (Fish, 2005; Platt and Philip, 1995). Two main units are identified. Unit 1a is characterised by fine grain sequence and may include volcanics. Unit 1b is composed of fine grained sediments embedded in a coarser bed set. It includes Darwin-like reservoir interval. Unit 2 is mostly composed by fine grained sediments.

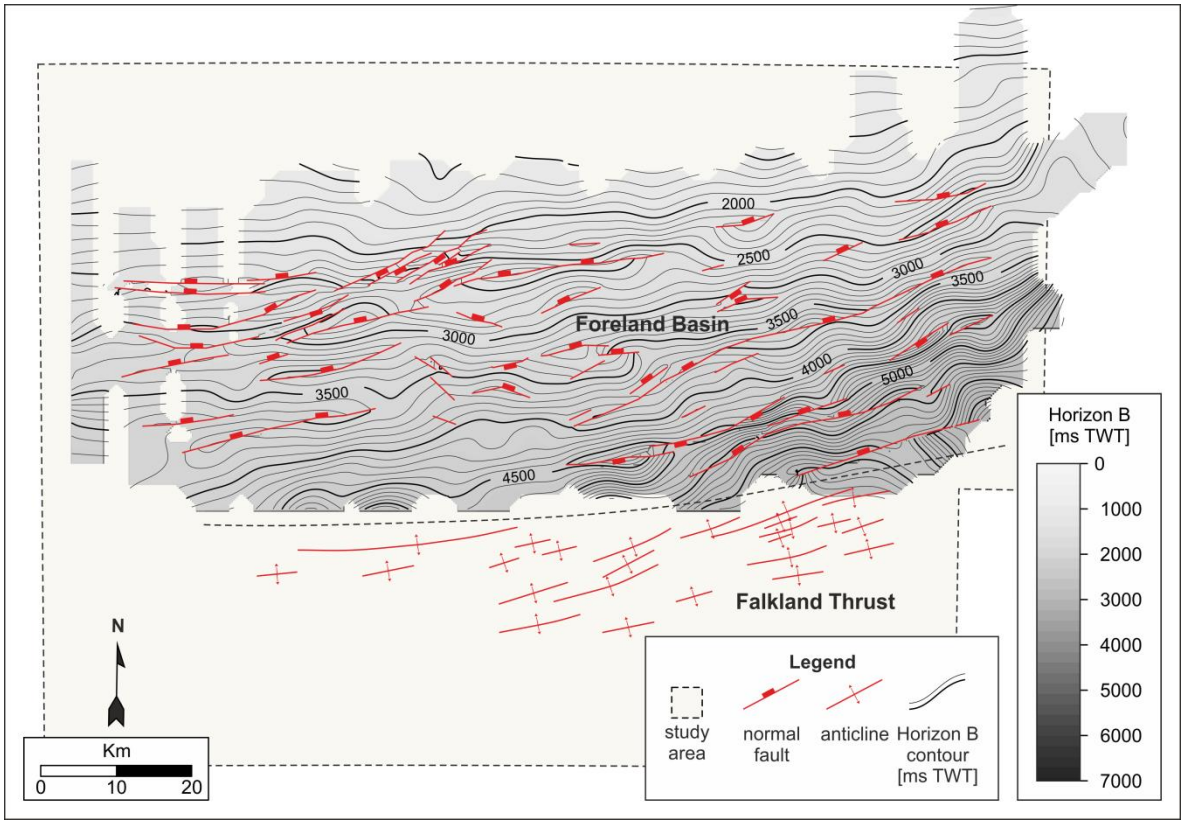

Figure 4.6 Time-structure map of the acoustic basement (Horizon B). The acoustic basement was interpreted only in the northernmost portion of the study area due to signal loss beneath the Falkland Thrust. The basement dips south-eastward and exhibits a prominent normal fault system oriented mostly east- west. The basement reaches a maximum depth of c.6500ms TWT. The Falkland Thrust is characterised by a series of thrust-fold belt anticlines oriented east-west.

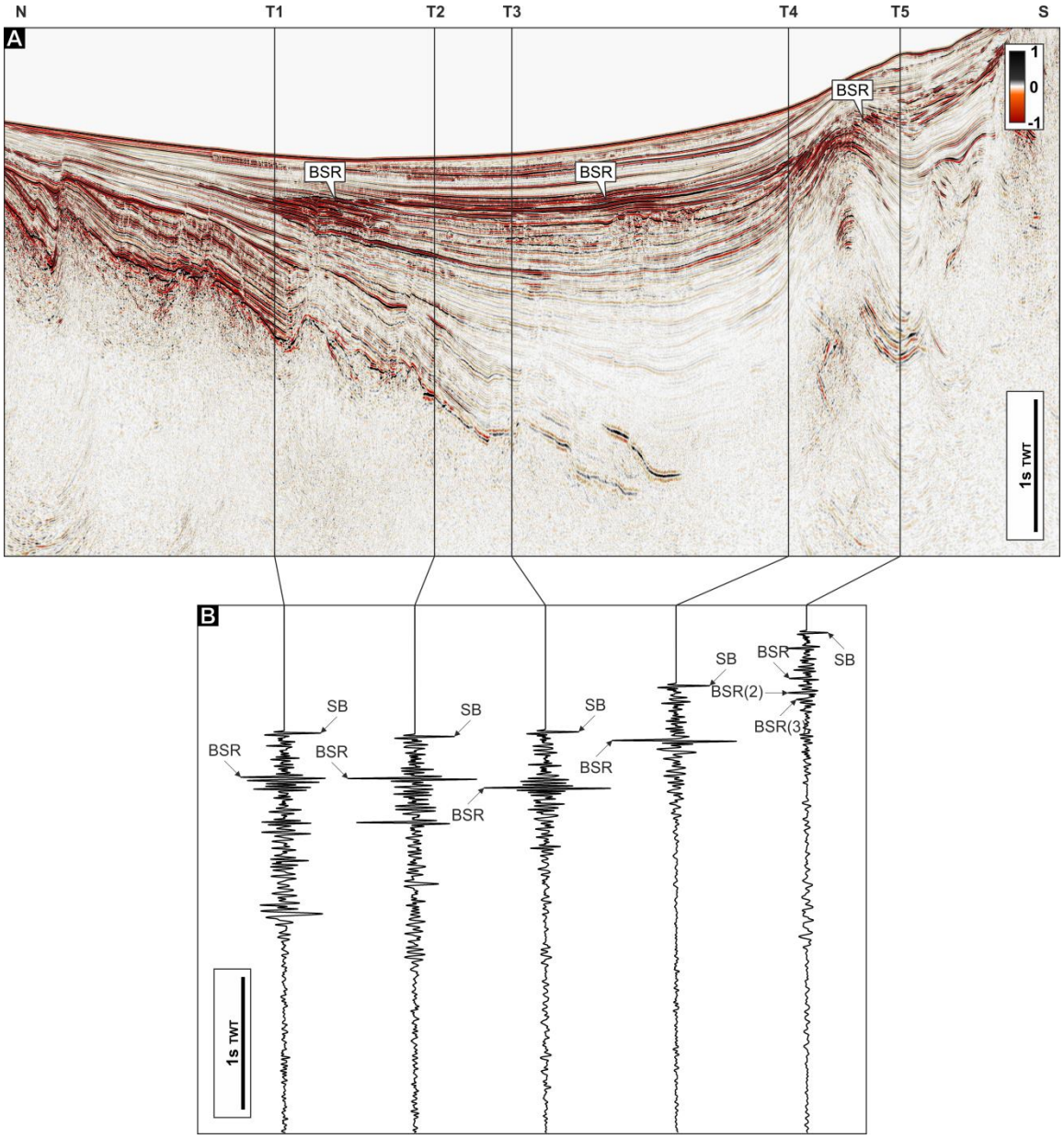

Figure 4.7 2D seismic section and polarity responses of BSR. Five seismic trace (B) have been extracted from a representative 2D seismic profile (A). The seismic traces have been selected at different settings. In all the cases the BSR polarity is consistent to negative amplitude responses. Multiple BSR events are present in the Falkland Thrust as observed in the southern trace extracted. Data courtesy of GSI.

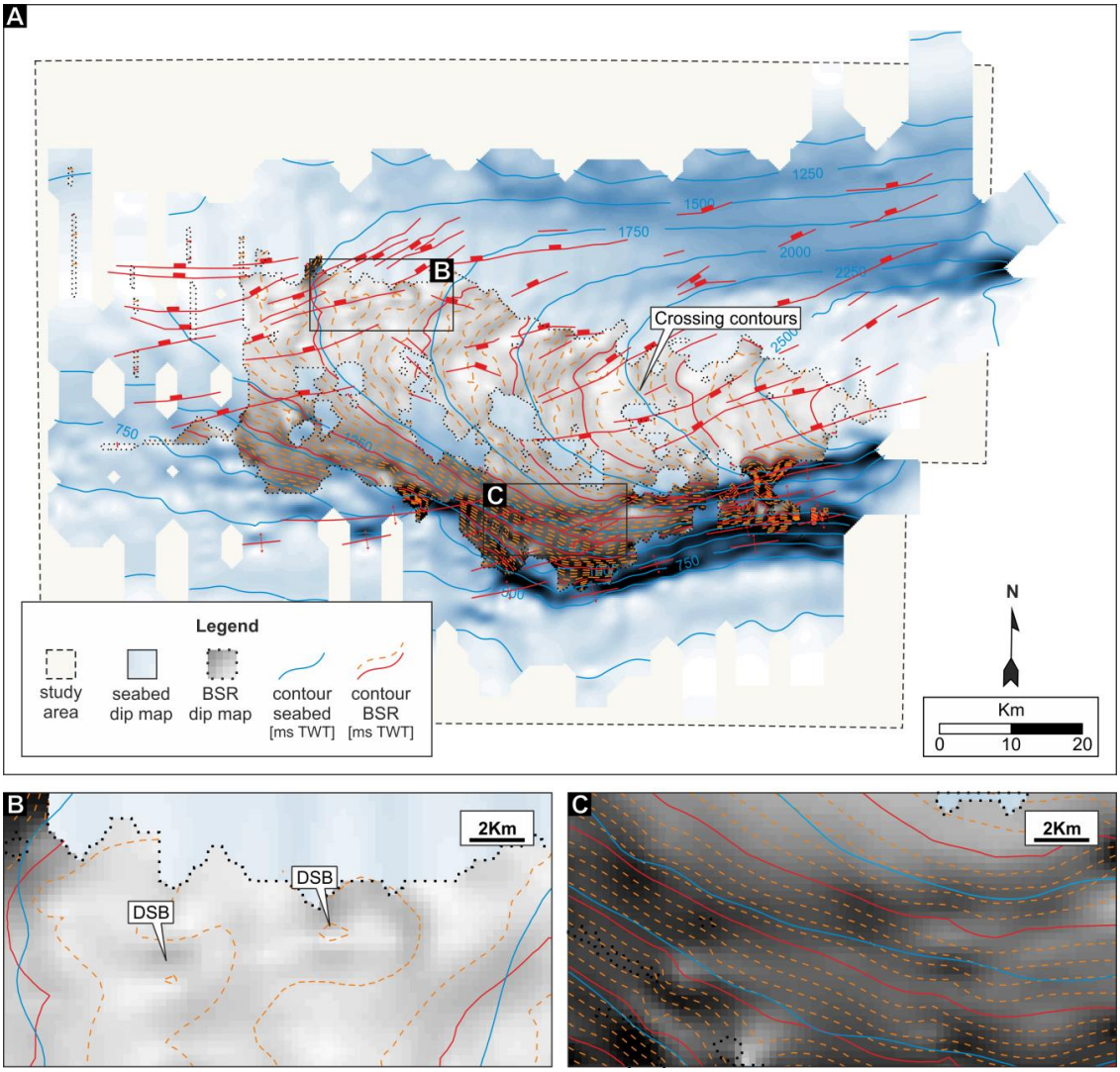

Figure 4.8 Time map of seabed and BSR. The BSR distribution occupies the central region of the study area. The BSR presents irregular margins as interpreted from the 2D seismic grid (A). In the northern region (B) the GHSZ exhibits domal-shallowings of the BSR (DSB) which are not consistent with the shape of the seabed. In the southern region (C) the BSR is clearly consistent with the shape of the seabed as clarified by the parallel contours.

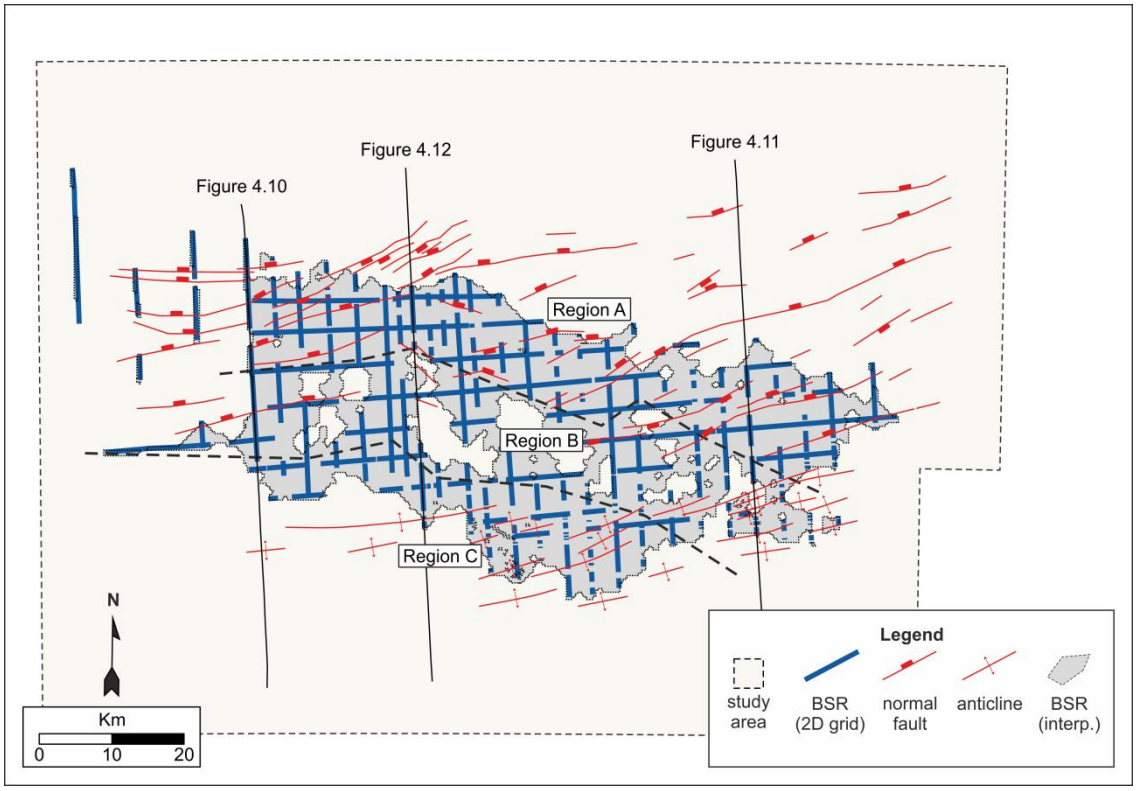

Figure 4.9 BSR distribution map, definition of the regions and position of the representative 2D cross sections used to describe the identification of the BSR on seismic data. The BSR is identified and interpreted over a large number of 2D seismic lines (blue lines). The interpolated distribution (grey area) exhibits continuous and patchy patterns.

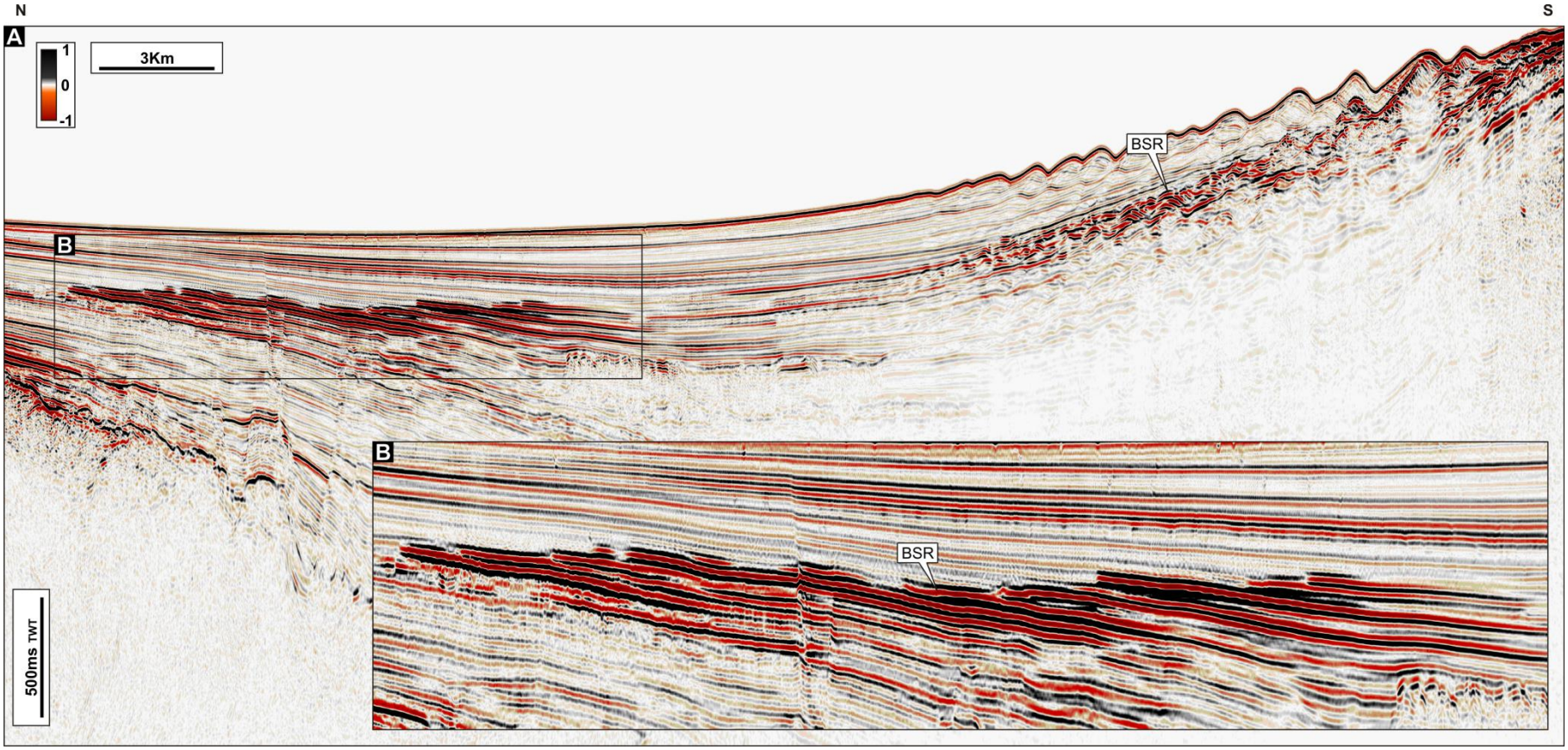

Figure 4.10 BSR composite. Representative 2D cross section oriented north-south showing the bottom simulating reflection (BSR).The BSR is not continuous within the basin and is segmented in a number of regions. The BSR does not have a regular distance respect to the seabed. Domal-shallowing of the BSR is observed in B. BSR clearly cross-cut the reflection package close to thrust region. Data courtesy of GSI.

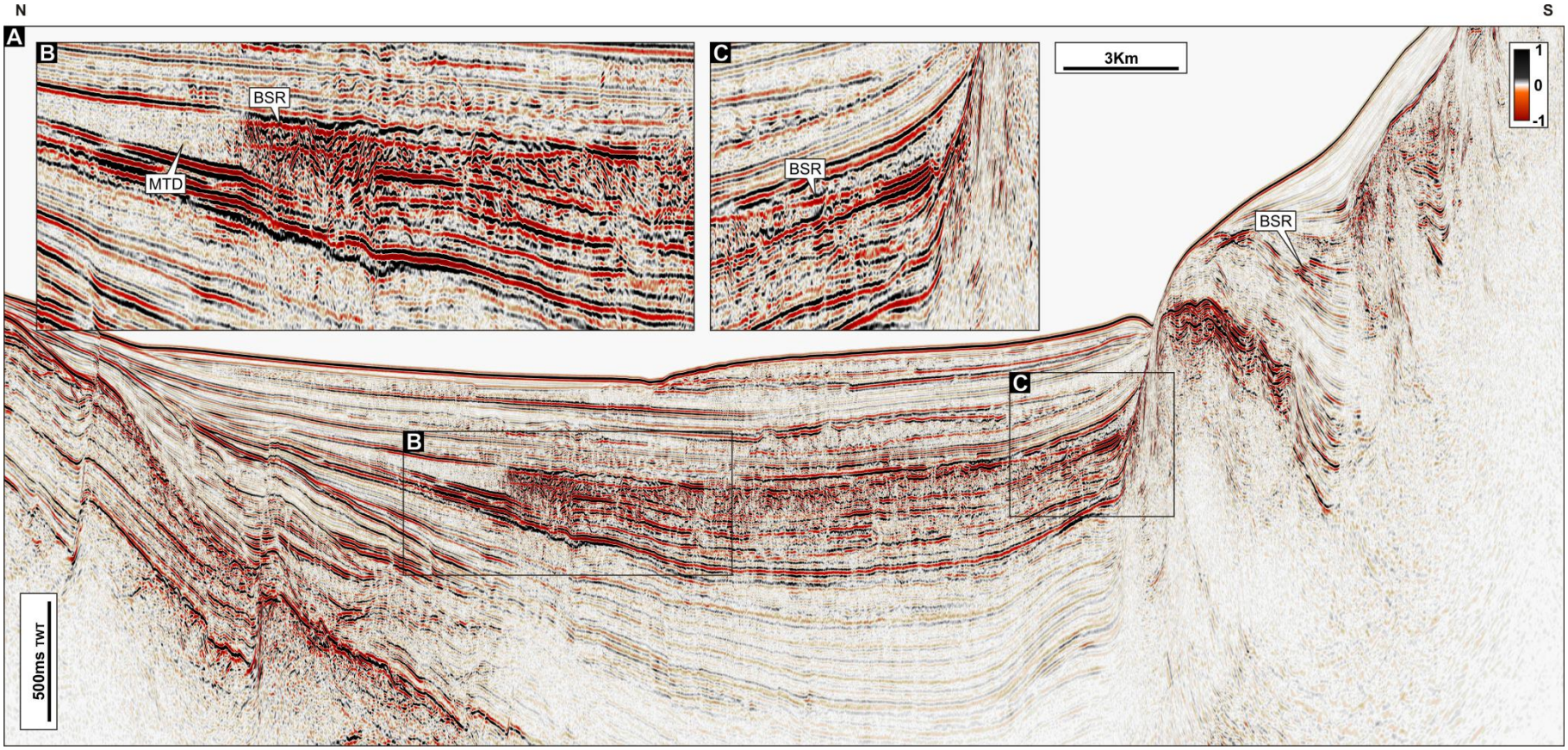

Figure 4.11 BSR composite. Representative 2D cross section oriented north-south showing the bottom simulating reflection within a laterally extended MTD. The BSR stands out as a prominent negative reflection which crosscut the MTD. The latter appear as a weakly chaotic body (B). The amplitude of the MTD is clearly amplified beneath the BSR. The MTD and the BSR seem stopped by the northern flank of the Falkland Thrust (C). Some BSR segments are also present within the thrust-folds. Data courtesy of GSI.

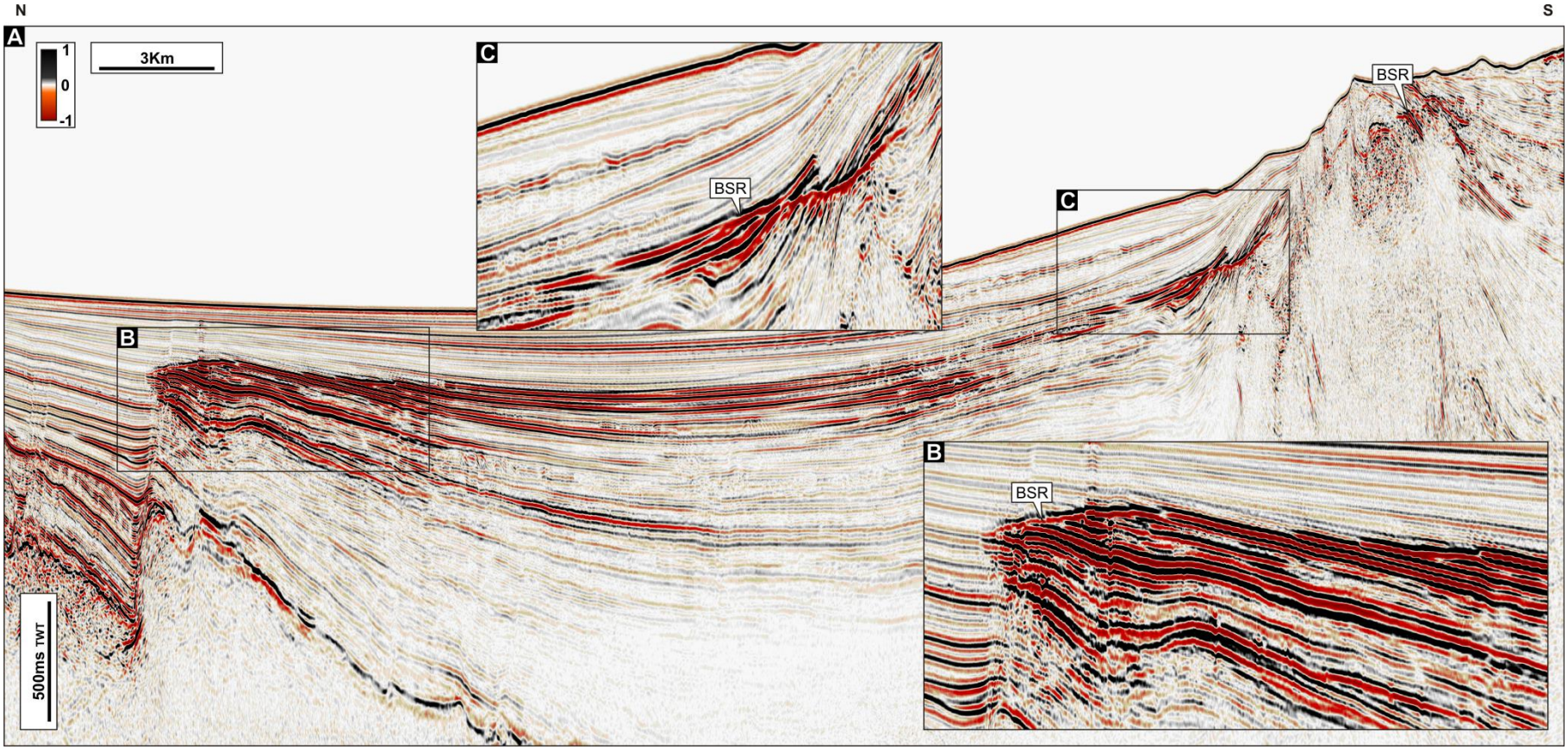

Figure 4.12 BSR composite. Representative 2D cross section oriented north-south showing the bottom simulating reflection (BSR).The BSR is not continuous within the basin and is segmented in a number of regions. The BSR does not have a regular distance respect to the seabed. Domal-shallowing of the BSR is observed in B. BSR clearly cross-cut the reflection package close to thrust region. Data courtesy of GSI.

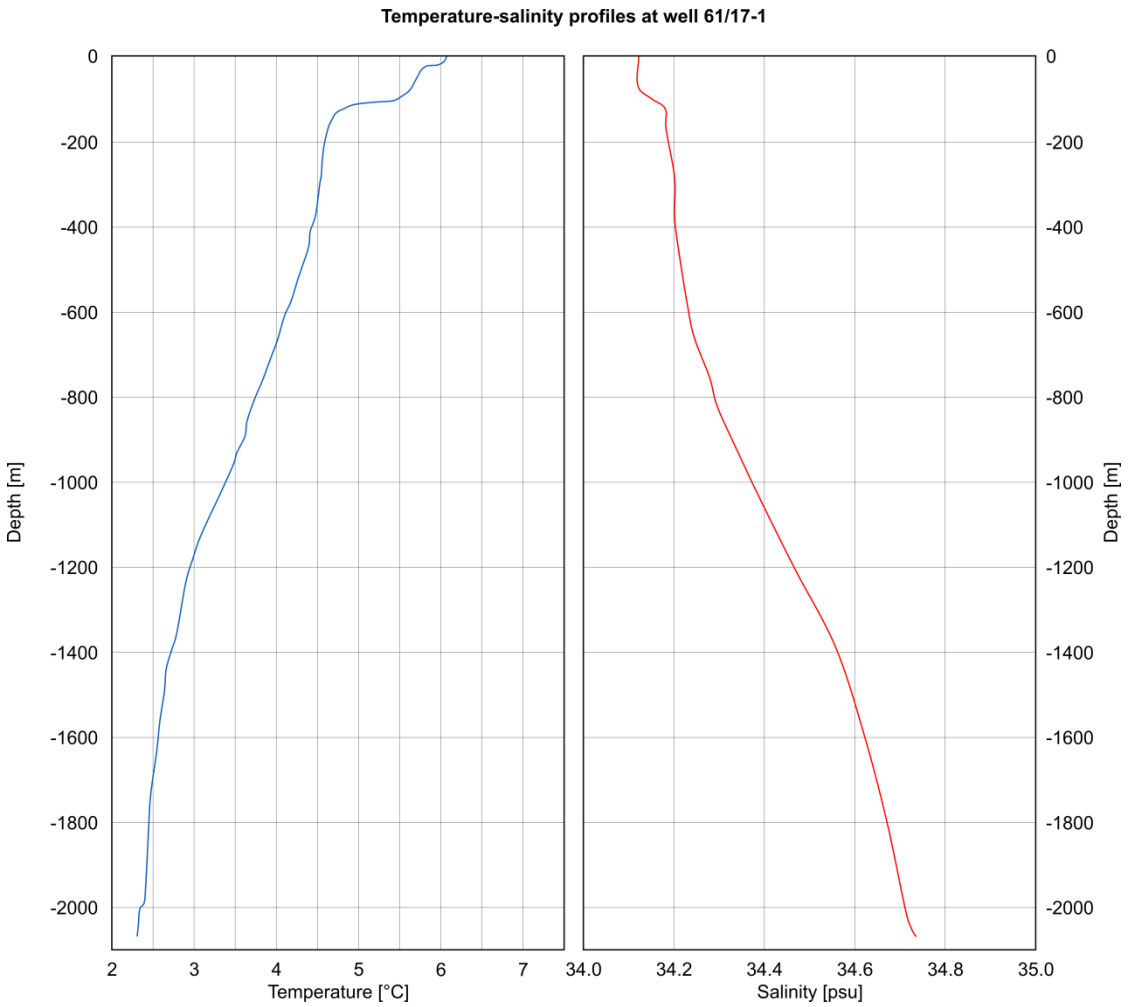

Figure 4.13 Temperature and salinity profiles used for the calculation of the GGDBSRPs. The curves have been interpolated to get a value every 1m. The curves have been graphically extracted from pre-drilling reports (see Appendix A).

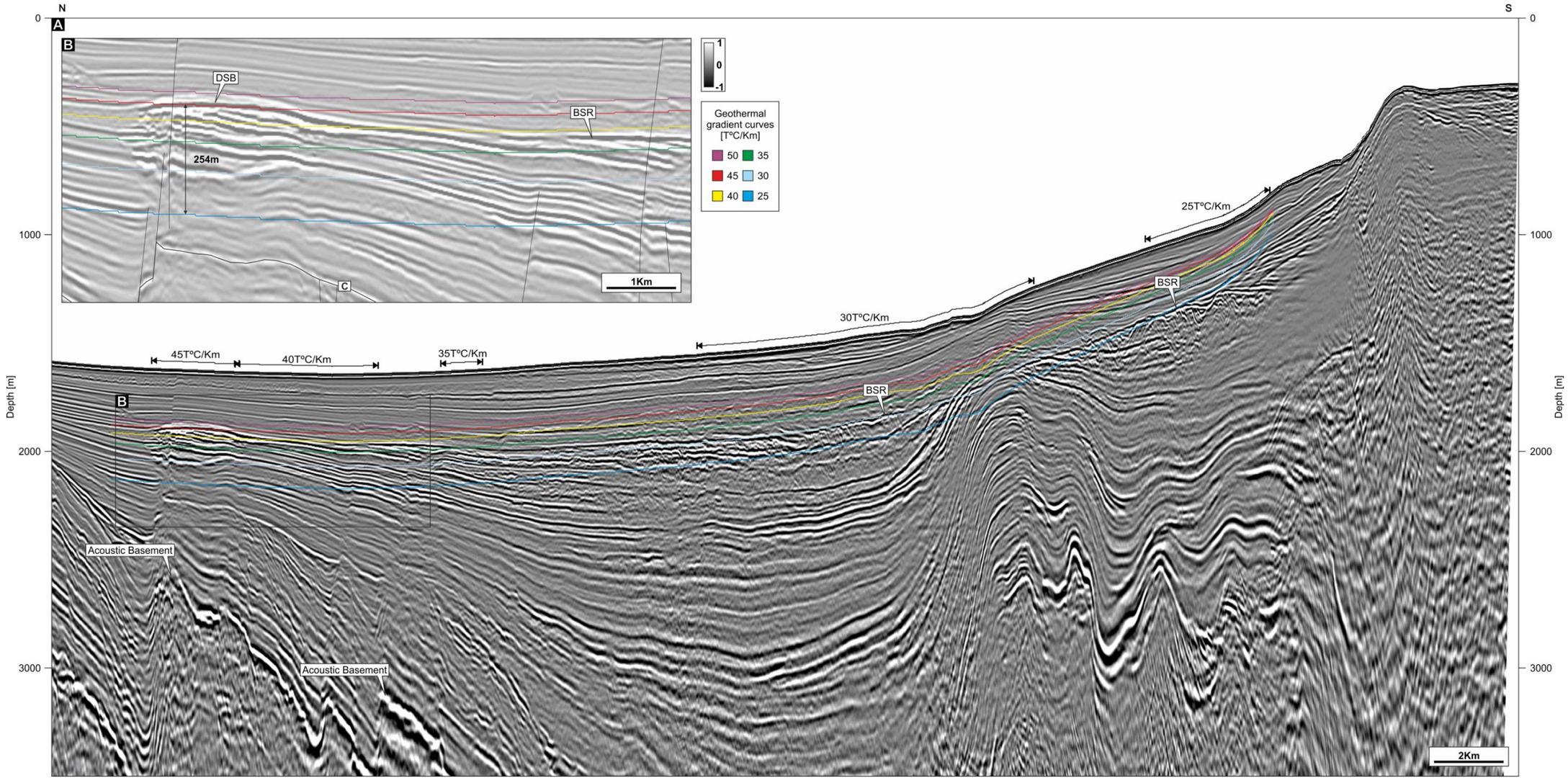

Figure 4.14 Geothermal gradient depth BSR profiles (G_GDBSRPs) calculated in a representative 2D depth seismic section oriented north-south. The BSR intersects the modelled GGDBSRPs at different values which are associated with different stabilities. At north the BSR exhibits a domal shallowing (DBS) which is located right above a prominent footwall crest of the acoustic basement (depth c.2500m). Taking as reference the stability of the GHSZ at south (25°C/km) and north (45°C/km) the BGHSZ is apparently located 245m above the lower geothermal gradient stability.

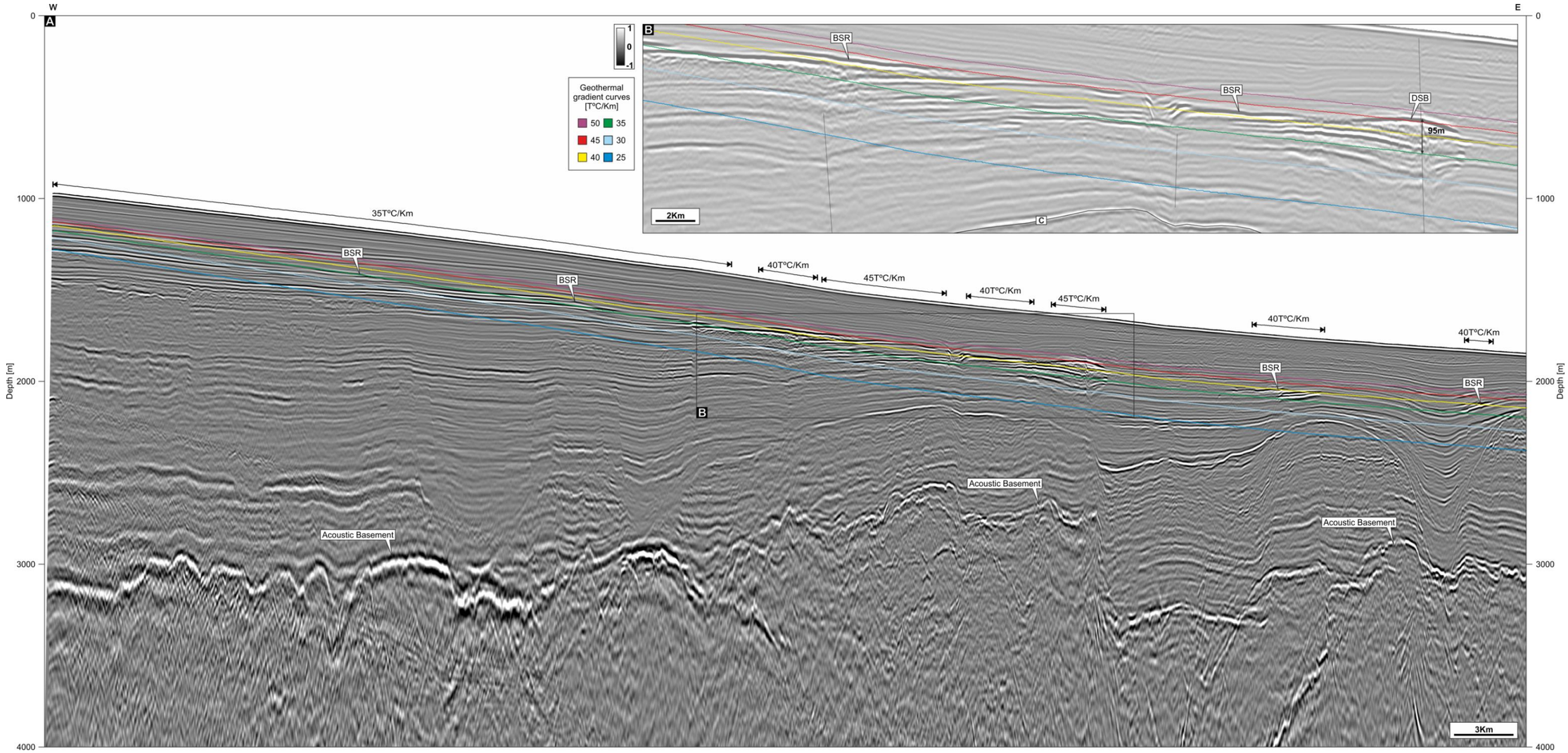

Figure 4.15 Geothermal gradient depth BSR profiles (G_GDBSRPs) calculated in a representative 2D depth seismic section oriented west-east. The BSR is consistent with a G_GDBSRP of 35°C/km in the westernmost portion of the basin. In these regions the acoustic basement depth is over 3000m. Further east the BSR is consistent with higher geothermal gradient values (40-45°C/km). In these regions the acoustic basement is shallower (<3000m). The GHSZ of these regions (DBS, B) is located 95m above respect to the observed stability at west. At east the BSR is intermittent and localised only above basement normal faults.

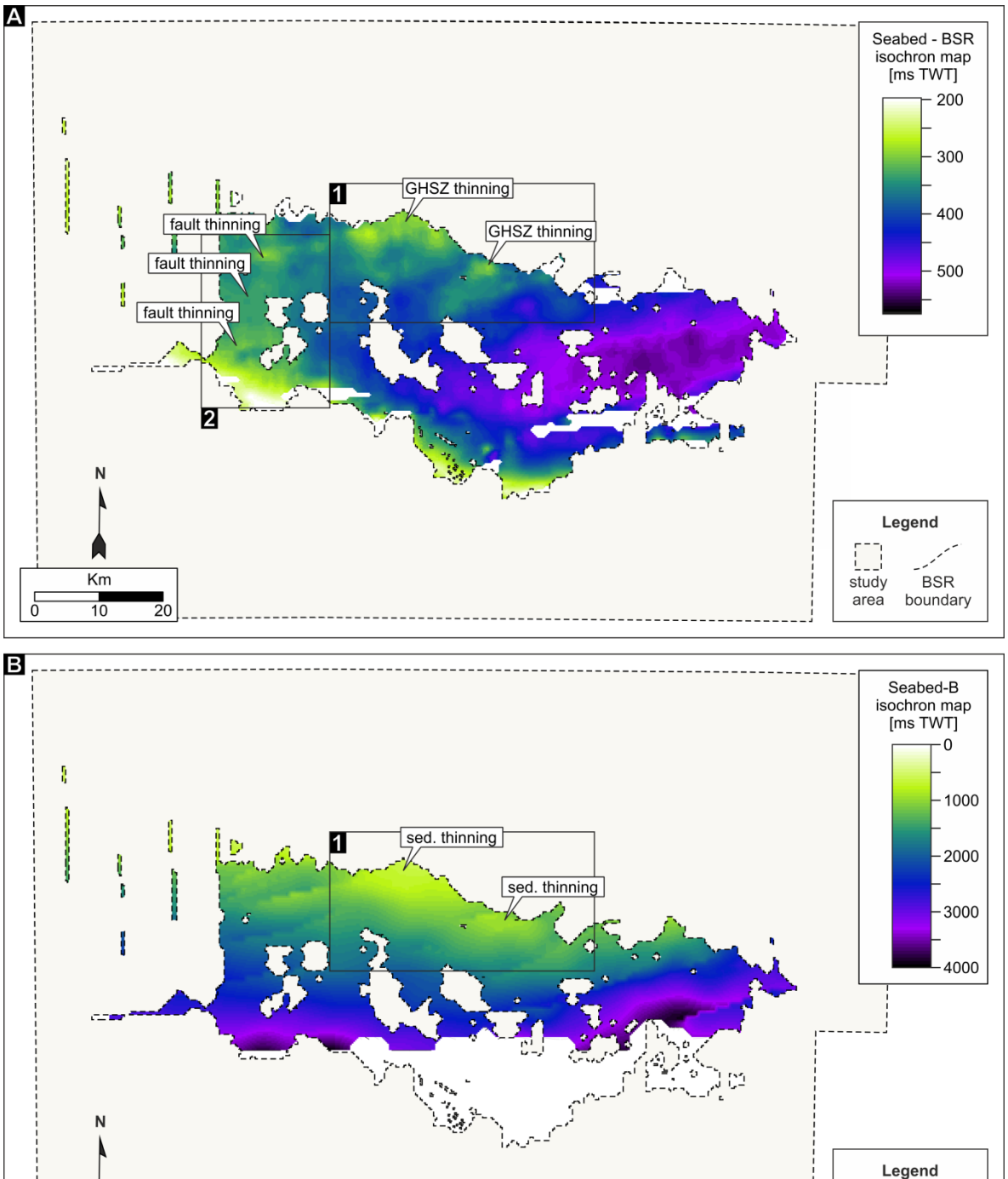

Figure 4.16 Map composite. Isochron map between BSR and seabed (A). In window 1 (A-B) the isochron map between BSR and seabed thins in a number of regions which reflect the variations in sedimentary thickness (B). In window 2 (A-C) fault related thinning observed in the isochron map between BSR and seabed (A) are related to the isochron map of Unit 1 (C). Note that canyon features (C) do not perturb the BSR which therefore is more susceptible to the variation of the gross sedimentary thickness and therefore to the depth of the interpreted acoustic basement (Horizon B).

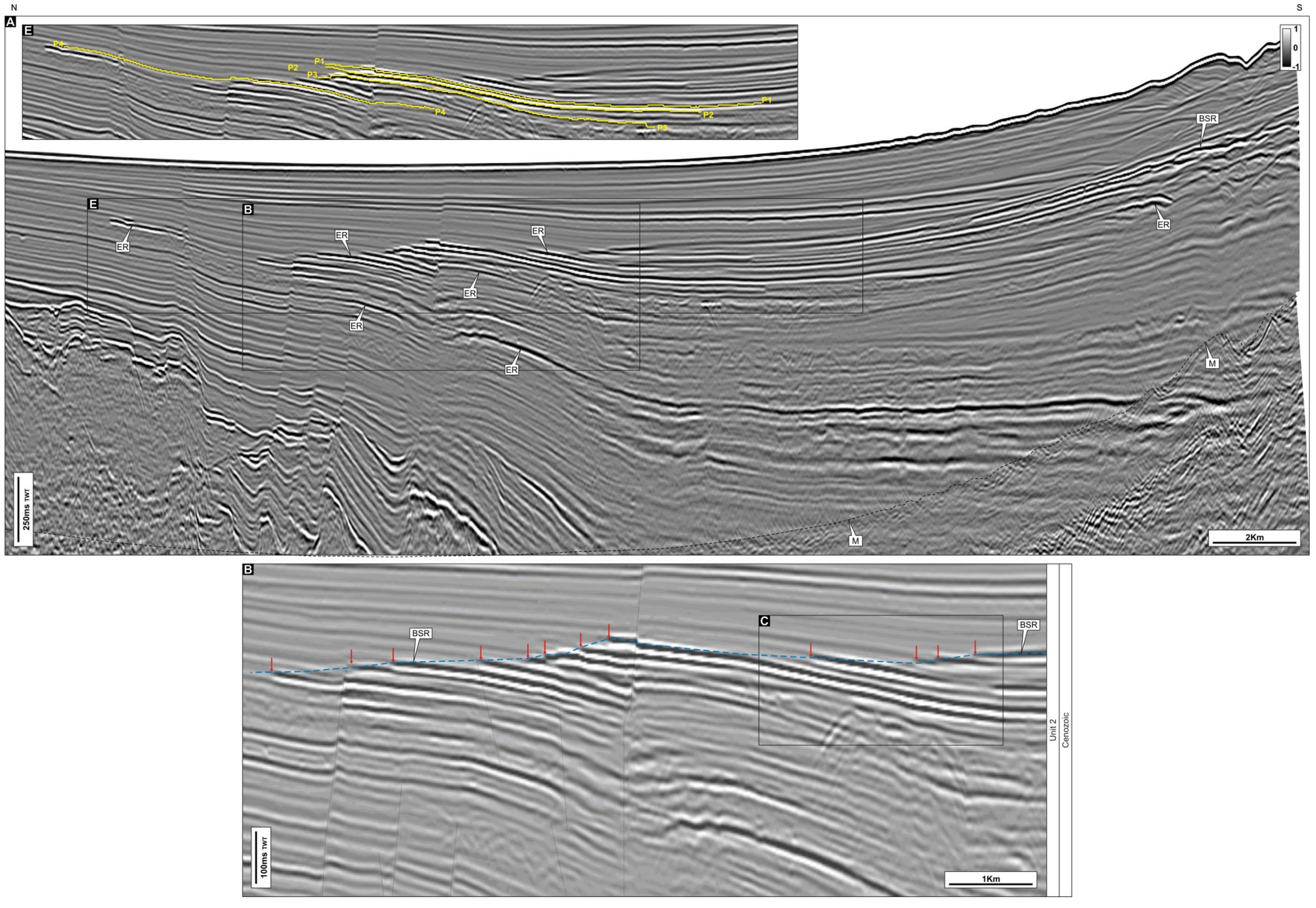

Figure 4.17a 2D seismic section depicting representative examples of enhanced reflections (ER) in SFB. ERs are mostly observed beneath the BSR (A). Some isolated ERs are also observed at different depths. ERs are clearly stopped at the BSR (red arrows, B) where they exhibit a “roof-tile” configuration. Position of the analysed ER profiles in Figure 4.18 (E). Data courtesy of GSI.

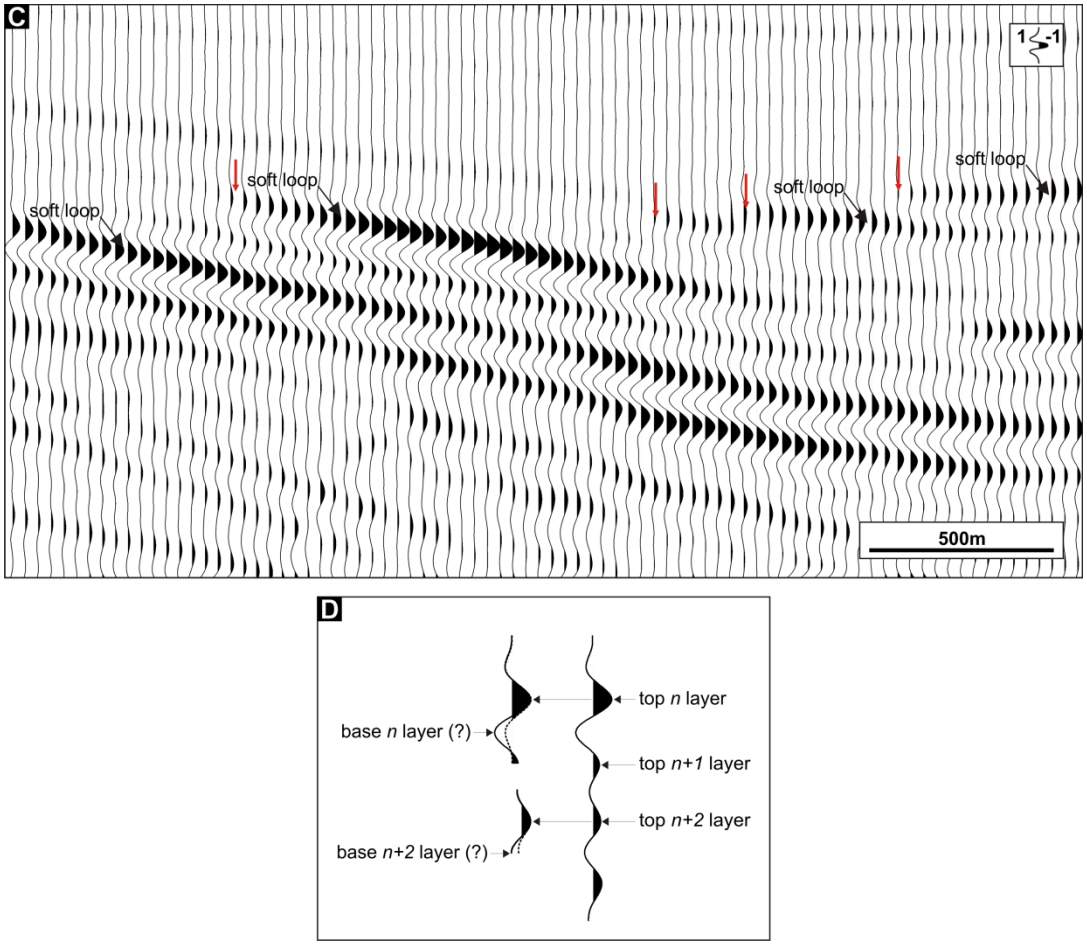

Figure 4.18b Representative selection of ERs from Figure 4.17a (C). The ERs exhibit mostly only soft, or negative, loop (C). They are followed by positive side loops associated with positive side loops. These layers are in some cases amplified and may associated with the base of the layers. Data courtesy of GSI.

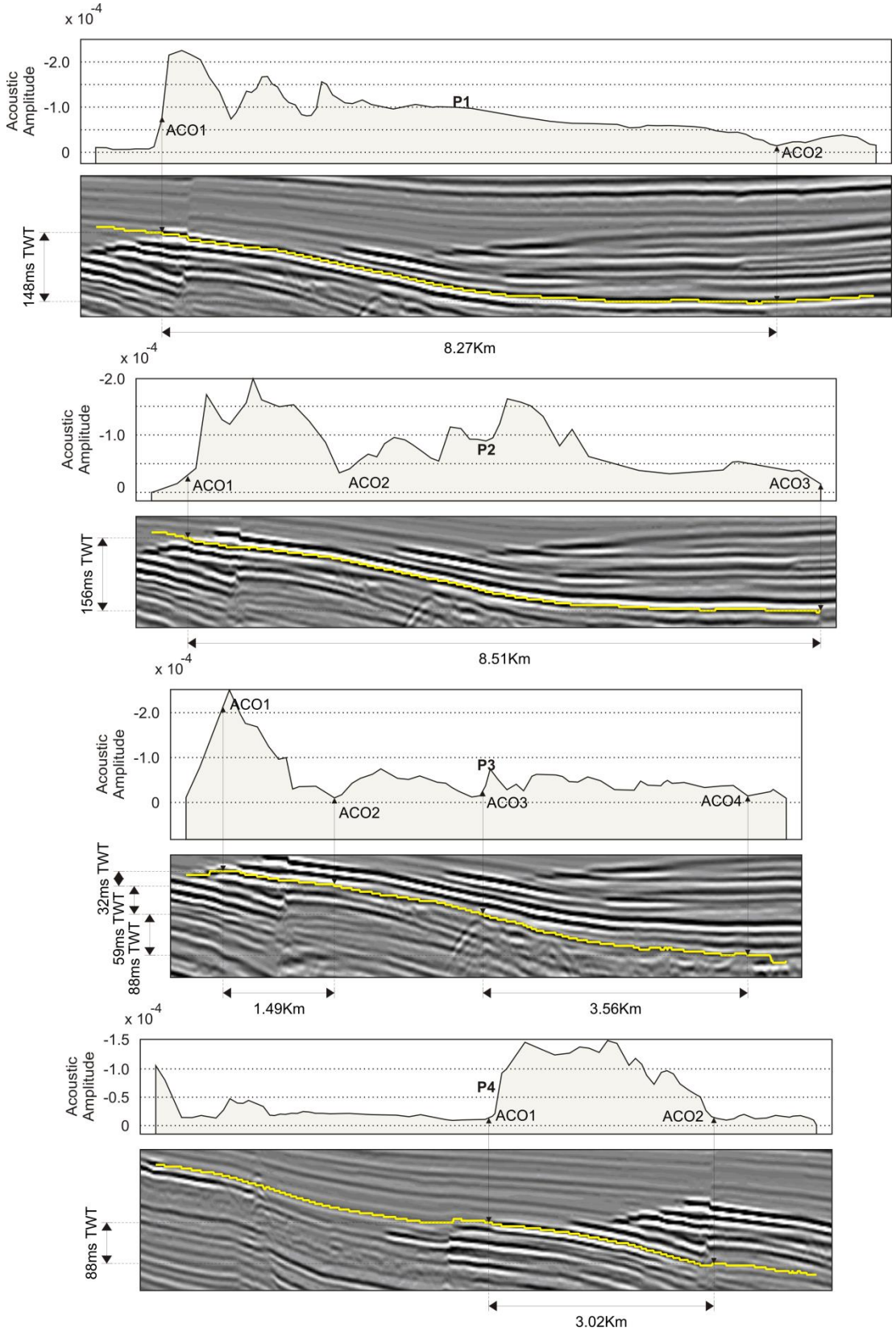

Figure 4.18 Enhanced reflection structure-amplitude analyses (ER profiles location in Figure 4.17a E). ERs are analysed in terms of geometry and amplification which provide indication about the possible column of gas involved (see text). Data courtesy of GSI.

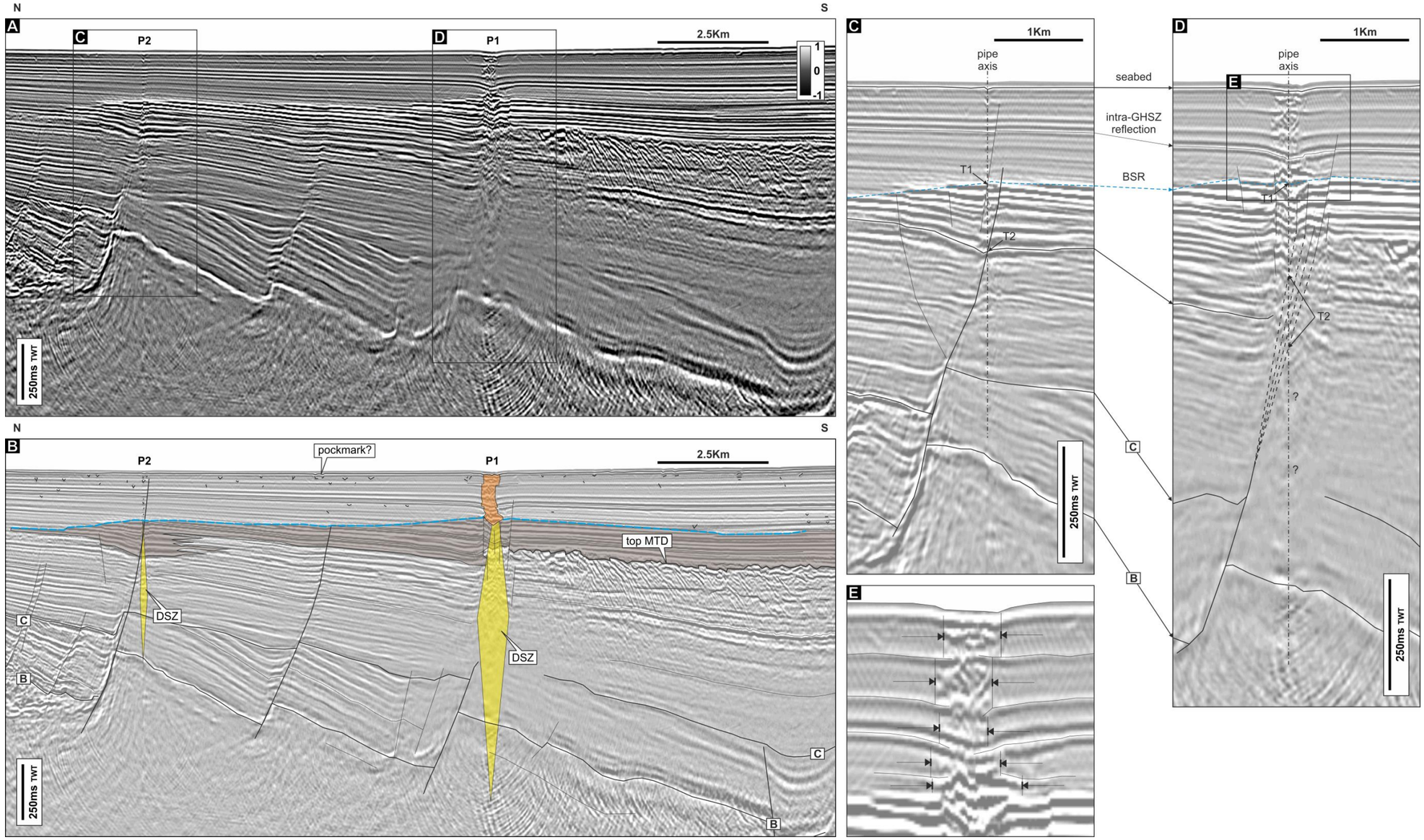

Figure 4.19 2D seismic section crossing pipes P1 and P2. Pipe P1 and P2 stand out as vertical regions of signal disturbance (A). Regions of amplified reflectivity (brown shade) are distributed beneath the prominent BSR (blue dashed line) (B). Disturbed signal zones propagate from the interpreted pipes (orange shade) downward for c.2s TWT (yellow shade). Interpretational uncertainties do not permit a precise definition of the roots of the pipes. Pipe root points at the BSR (T1, C-D) and below the BSR (T2, C-D) are interpreted along the pipe axes (dashed vertical lines, see text). Interpretational uncertainties are indicated (?). Pipe P1 is composed of a number of sections characterised by different cross sectional lengths (or diameters) and axis (E). These sections seem associated with the different layers composing the shallow section of basin (E). Data courtesy of GSI.

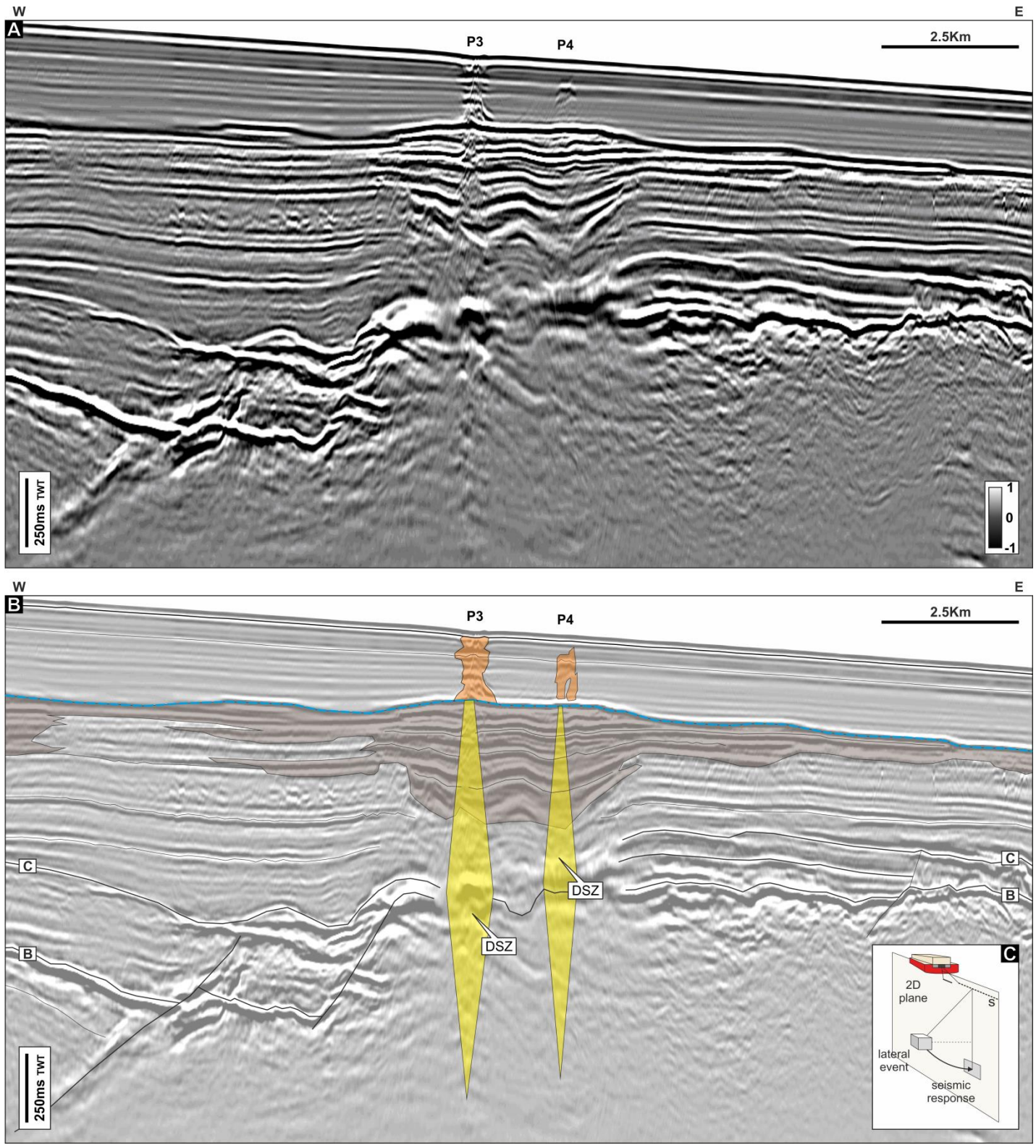

Figure 4.20 2D seismic section crossing pipes P3 and P4 (far-stack section). The pipes are located out of the seismic plane. The far angle sorting used to define the far-stack section allowed to recognise them. Amplified reflections (brown shade) are present beneath the BSR (blue dashed line). P3 and P4 are located above a prominent structural high. The strong disturbed signal zones (DSZ) do not allow a proper definition of the roots of the pipes. Data courtesy of GSI.

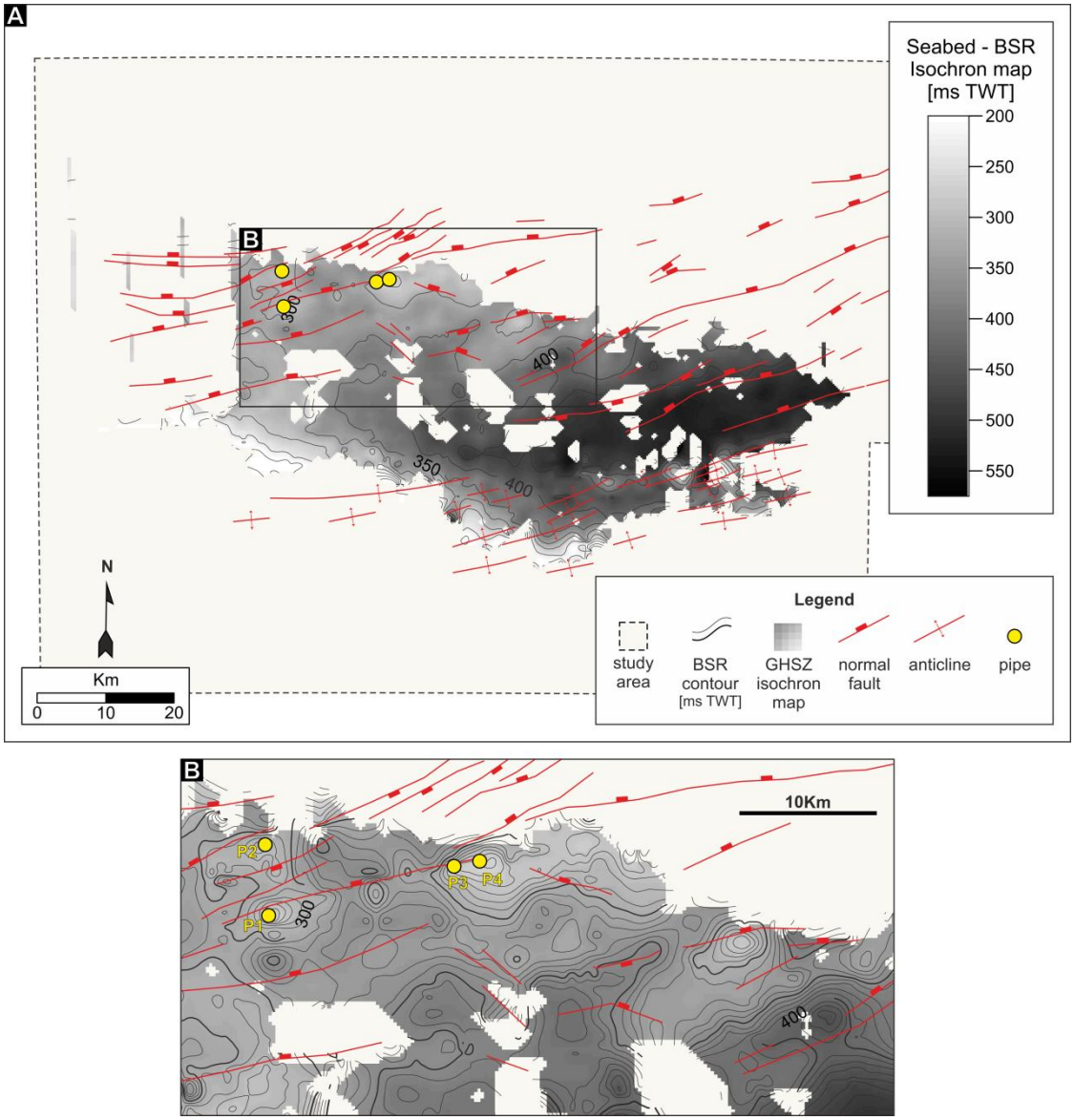

Figure 4.21 GHSZ isochron map with position of pipes and structural features of the basin. The pipes are distributed in the northern portion of the BSR in a region characterised by strong faulting (A). In detail the Pipes are related with decreasing of time thickness of the GHSZ and with some prominent normal faults trending ENE-WSW.

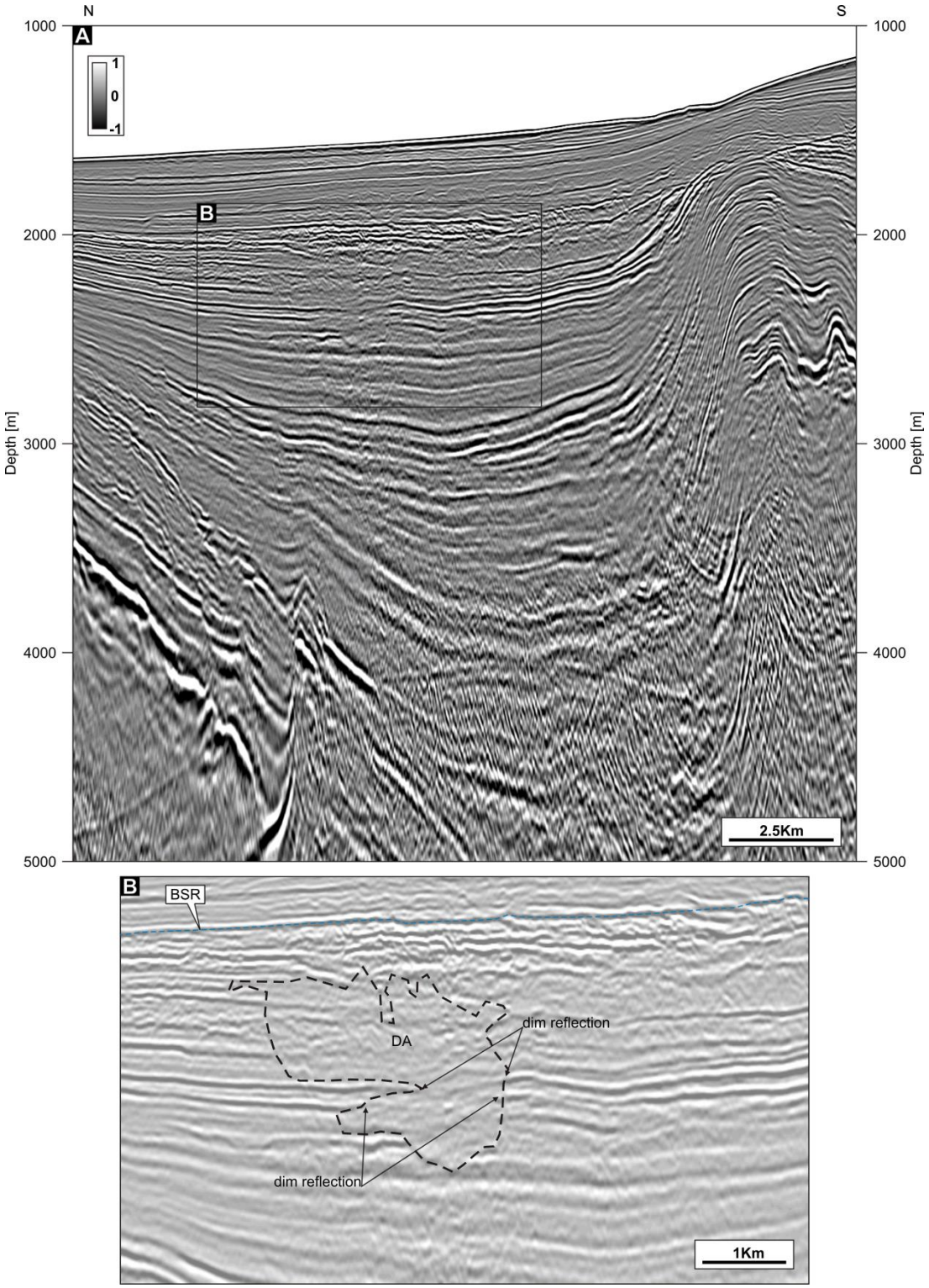

Figure 4.22 2D Seismic section crossing a region of amplitude diming. The region is located above a structural high associated with a prominent footwall crest of a basement normal fault. The dim amplitude zone is characterised by low amplitude respect to the background values (A). The dimming is clearly imaged when along an observed reflection the amplitude are dimmed and regained (B).Data courtesy of GSI.

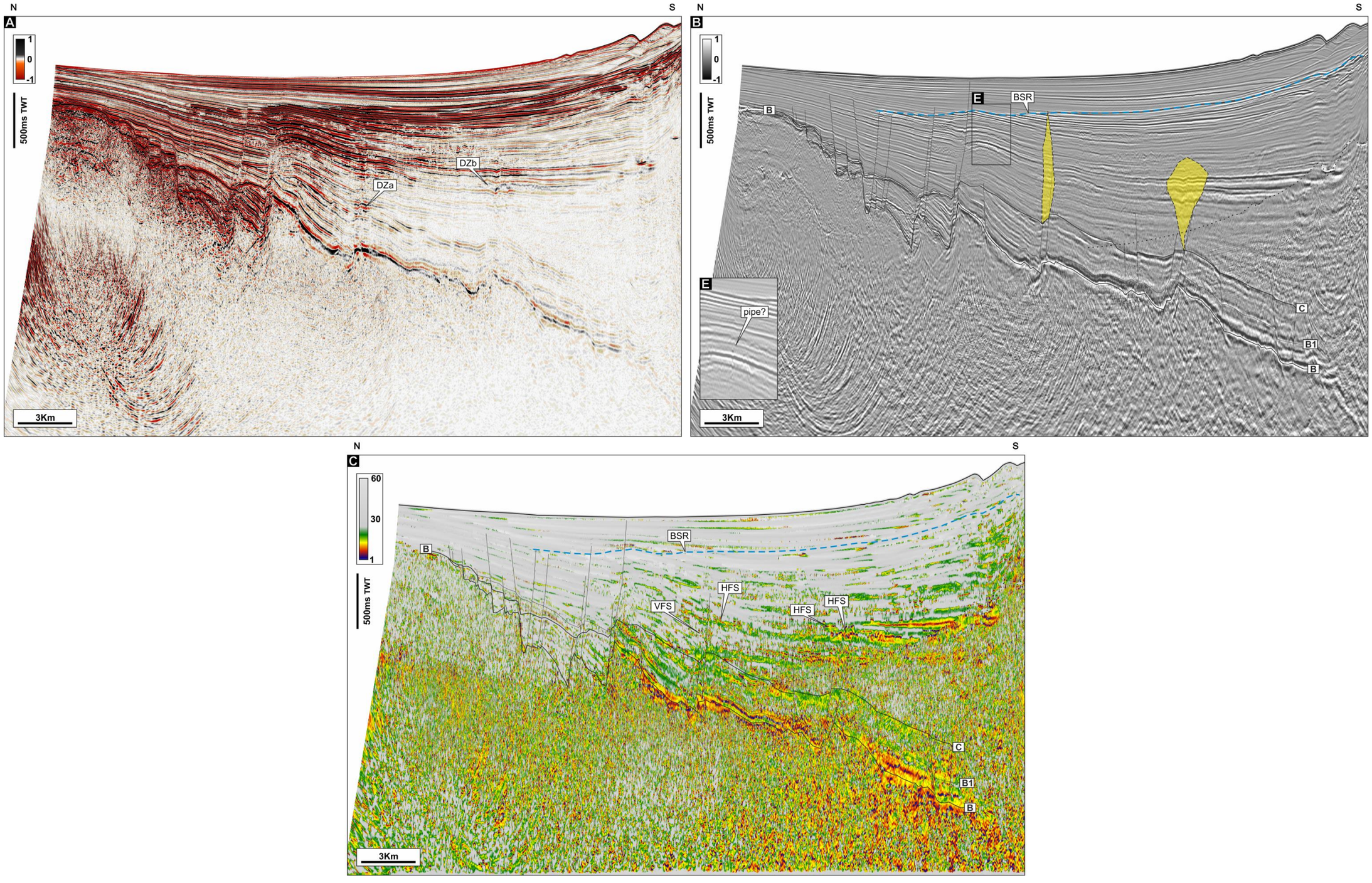

Figure 4.23 2D seismic and attribute composite depicting disturbed signal zones. The amplitude responses of the disturbed signal zones are clearly imaged on seismic data where they stand out as vertical zones of signal amplification (A). These features are interpreted to be located at the foot wall crests of basement normal faults (Horizon B, (B)). The frequency-peak response exhibits horizontal frequency shadows which are interpreted to be associated with the amplified reflections composing the disturbed signal zones (C). Data courtesy of GSI.

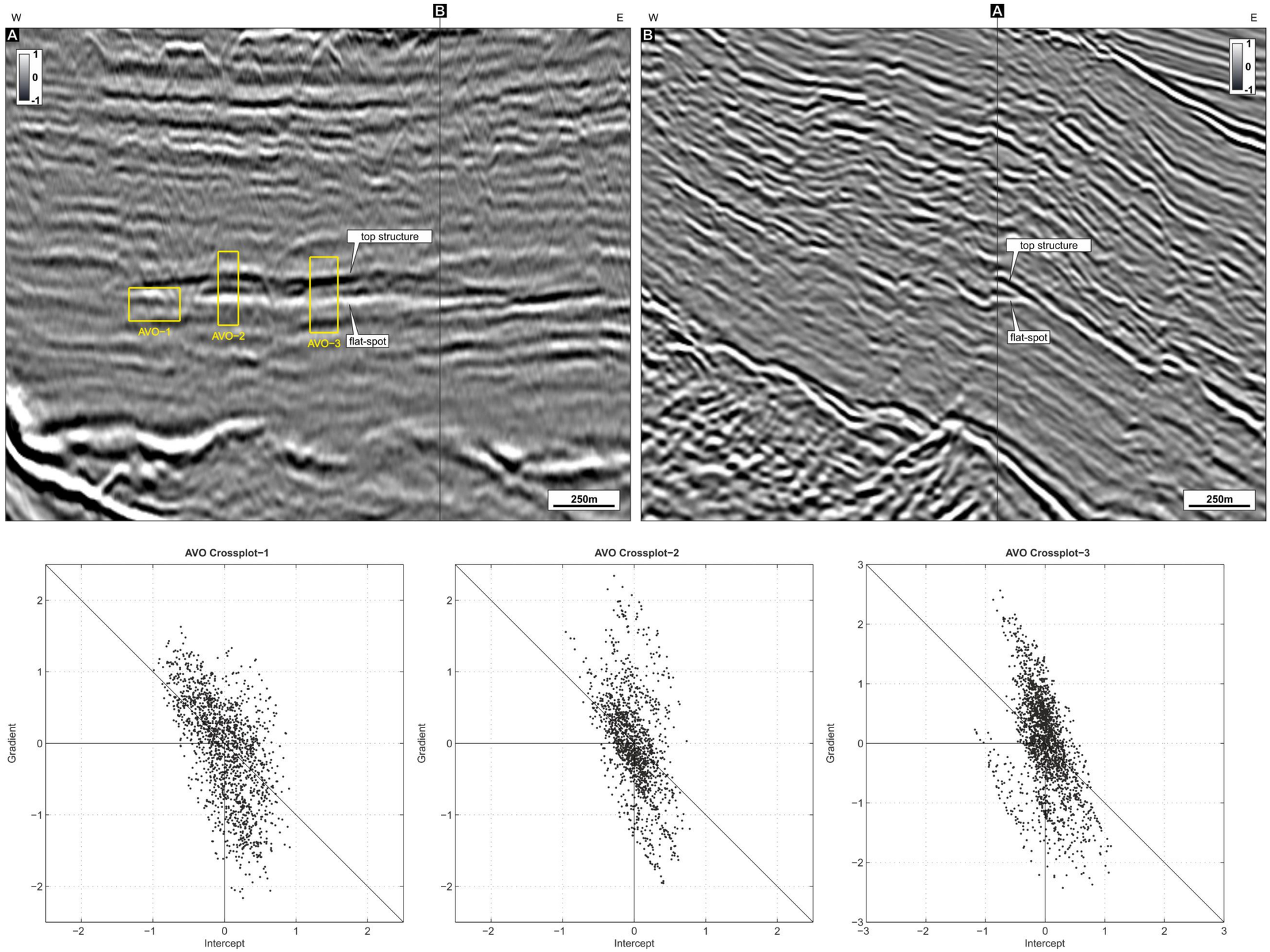

Figure 4.24 2D seismic sections crossing a flat-spot and AVO cross-plots. The flat-spot identified in SFB is located in the deeper portion of the basin (Unit 1). The flat spot composed of well-defined flat positive reflection and negative reflection top structure (A). The latter is characterised by AVO Class III. Flat spot transect the background reflectivity and top structure associated with polarity reversal (B). Data courtesy of GSI.

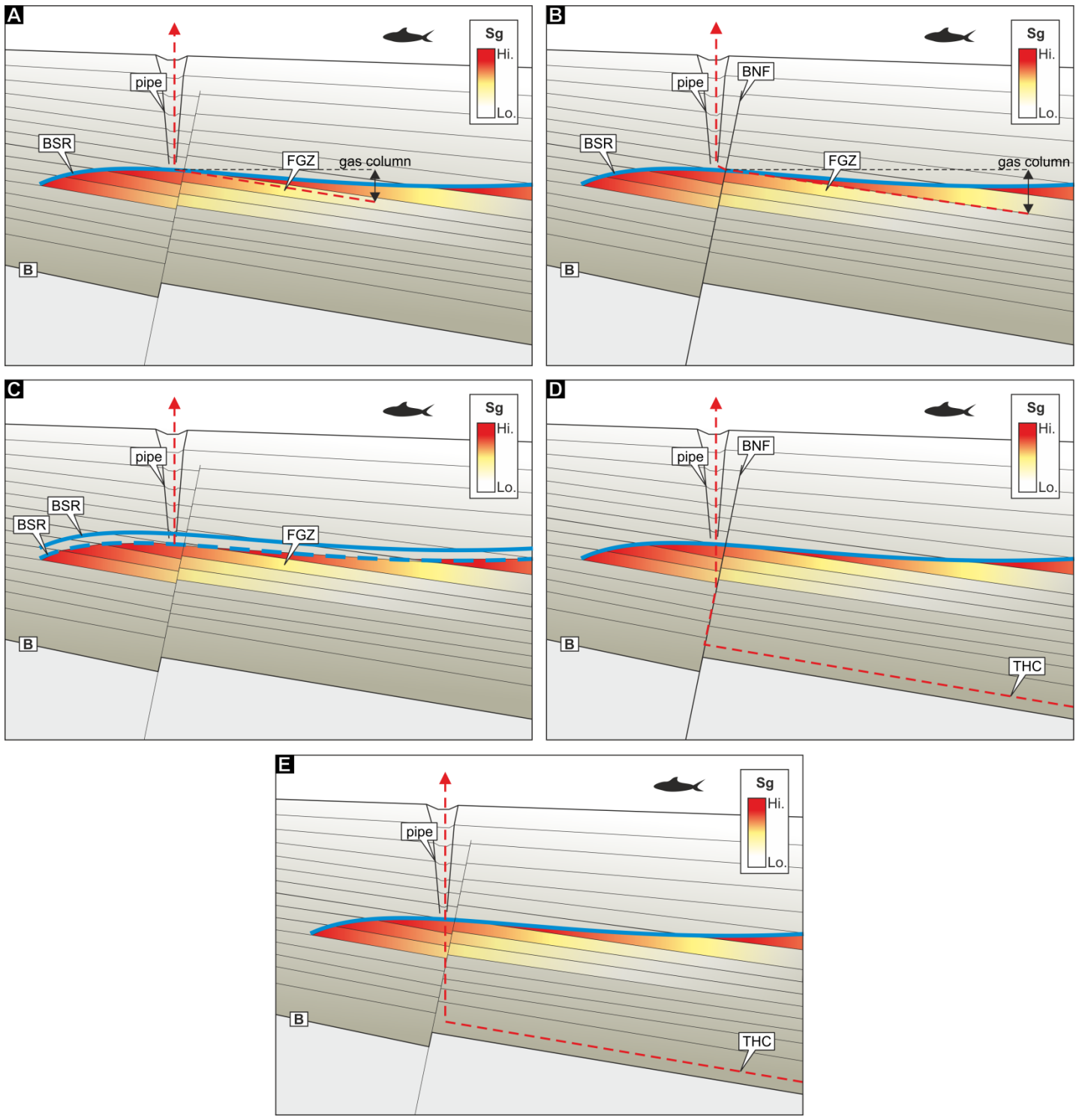

Figure 4.25 Conceptual models for the formation of pipes. The position of pipe, BSR, ERs and structural features are fixed and representative of the interpretation completed on the seismic data. The mechanisms for the formation of the pipes are: (A) the pipe is formed due to gas entering within the GHSZ caused by pressure build-up of the free gas zone beneath the BSR (GHSZ). This mechanism can explain the position of the pipe with respect to the domal shallowing of the BSR but it is not consistent to the effective gas columns of the free gas zone (FGZ); (B) the pipe is formed due to fault slip activated by pressure build-up within the FGZ. This mechanism is not feasible because the fault slip is not occurring at the location of the pipes; (C) the pipe can be generated from instability of the GHSZ caused by variation in salinity, temperature or pressure. This case is not consistent to what observed on seismic data where only one single BSR is observed in the regions surrounding the pipes; (D) the pipe can be formed by fluid migration within faults. This mechanism is feasible however is still under debate the formation of pipes associated with faults; (E) the pipe can be formed by vertical migration of hydrocarbon from shallower region of the basement (B) to the seabed. In this case the vertical migration of hydrocarbon is not affected by the presence of faults and GHSZ. The position of the pipes and the structural highs of the basement are consistent with this mechanism.

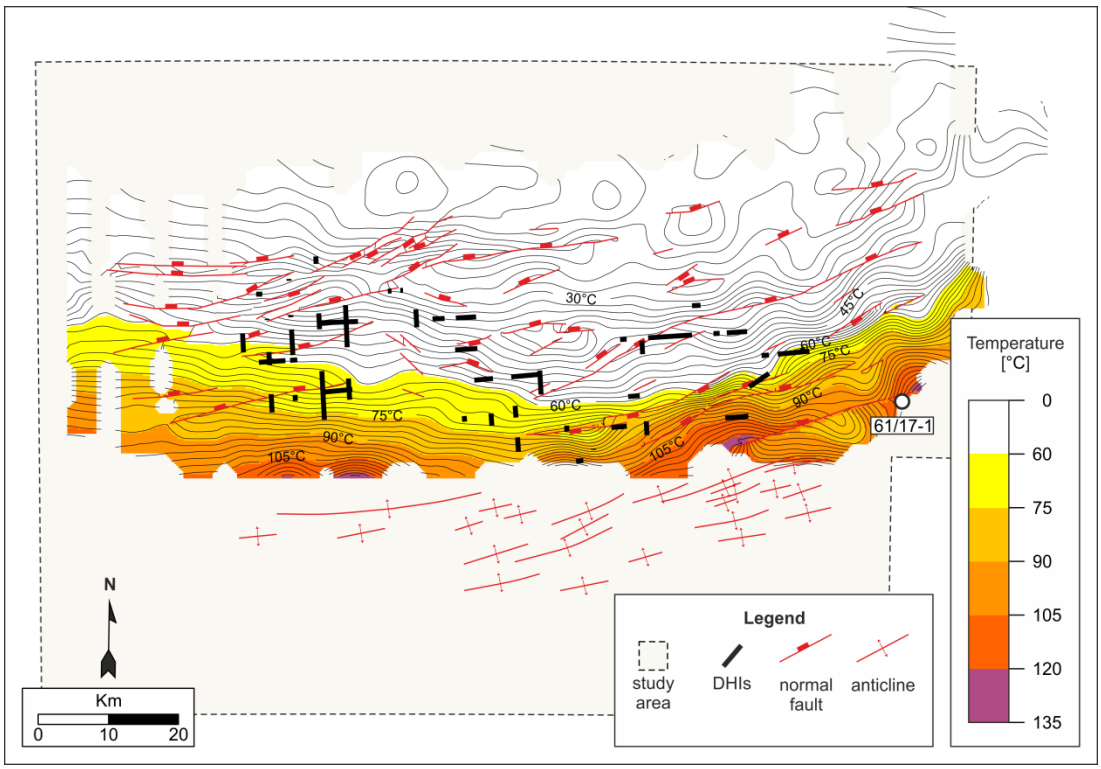

Figure 4.26 Structure map and temperature map at Horizon B using an interval velocity of 1.9km /s and a geothermal gradient of 30°C/km . Considering an initial oil generation at 60°C the expected rocks producing thermogenic fluids are located at the southern margin of the syn-rift.

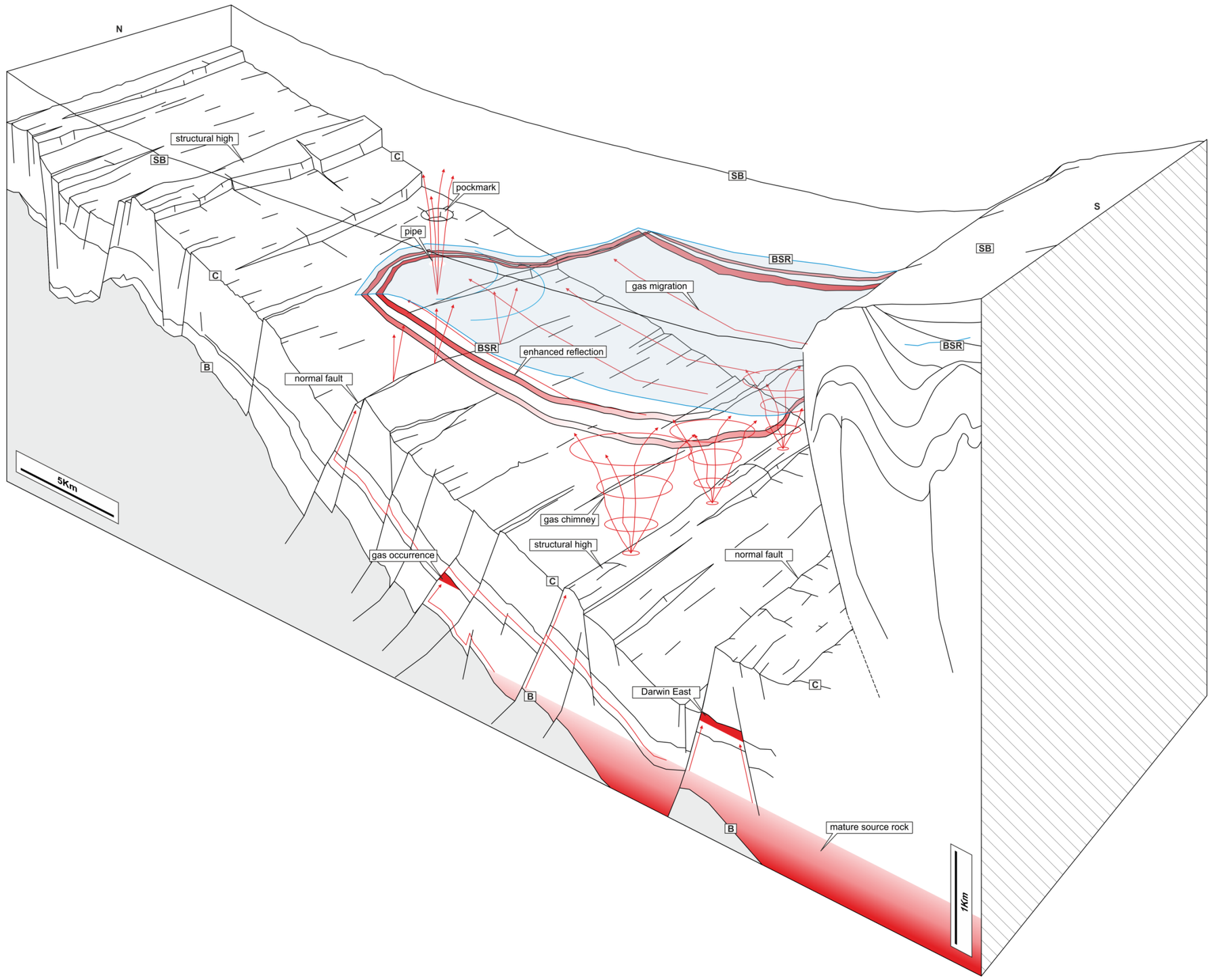

Figure 4.27 Cartoon showing the proposed conceptual plumbing system active in the South Falkland Basin (SFB) (see text). The model is based on what discussed in section 4.5. Hydrocarbon occurrences and fluid flow features are drawn in red. The position and continuity of the BSR is simplified (blue line, light blue shade).

5. Fluid expulsion structures in North-East Falkland Basin

5.1. Introduction

This chapter represents the final case study of the descriptive framework focused on fluid-related seismic anomalies present in the Falkland Basins. In detail, this Chapter is focussed on the description of a type of vertical structure which is believed to be linked to gas migration or focussed fluid flow. This type of structure is characterised by a vertical zone of depression in the overburden and associated with seismic amplitude amplifications.

5.1.1. Background

Mud volcanoes (MVs) are structures associated with the migration and expulsion of sediments and fluids to the earth surface (Graue, 2000). They can be related to the migration of thermogenic fluids, such as oil and gas, and so can represent a type of seep or leakage phenomenon associated with proliferous basins (Etiope et al., 2009; Stadnitskaia et al., 2008). On the earth surface they may produce positive structures characterised by a conical shape. In other cases they may produce depressions due to the expulsion of the remobilised material and subsequent collapse of the overburden (Somoza et al., 2012). MVs characterised by bi-conic structures are common and are due to multiple stages of expulsion and collapsing (Stewart and Davies, 2006).

Pipes are columnar shaped, vertical zone of seismic signal disturbance which are caused by fluid expulsion (Cartwright, 2007; Moss and Cartwright, 2010). Pipes may be associated with amplified reflections which are commonly stacked in a narrow columnar zone (Gay et al., 2012; Moss et al., 2012). Pipes may present upward curved reflections at their margin, which are indicative of failure of the hosting rock

layers (Riboulot et al., 2013). Pipes may terminate at the seabed and may be associated with pockmarks (Moss et al., 2012; Pilcher and Argent, 2007; Plaza-Faverola et al., 2014), or they may be isolated or aligned along structural features such faults (e.g. Leduc et al., 2013) or salt diapirs (Taylor et al., 2000). The presence at seabed of pockmarks may also be indicative of the presence of a deeper reservoir connected along pathways and pipes to the seabed (Gay et al., 2004).

Gas chimneys are zones of signal disturbance characterised by amplified and dimmed regions of chaotic reflectivity pattern (Arntsen et al., 2007; Løseth et al., 2003). Gas chimneys are normally associated with the presence of patchily or irregularly distributed gas charged regions (Granli, 1999). Gas chimneys are indicators of vertical fluid flow characterised by a vertical and unconstrained laterally extended migration (Arntsen et al., 2007). Gas chimneys are often present above hydrocarbon accumulations trapped anticlinal structures or footwall crests and are usually indicative of the presence of deeper hydrocarbon reservoirs (Løseth et al., 2009).

Vertical Anomaly Clusters (VACs) are a vertical assemblage of gas related amplitude anomalies, which are linked by the gas migration process (Chapter 3). VACs can extend for several kilometres (up to 25km) with a large horizontal aspect ratio. VACs are found in sealing sequences where cross stratal migration is expected to be along a fault and fracture network. VACs are indicative of the presence of hydrocarbon fluids migrating vertically from underlying source kitchens or reservoirs.

5.1.2. Aims

The primary aim of this case history is to describe, and account for the enigmatic vertical depression zones and all other fluid-related seismic anomalies present within the study area. The depression structures and all other potential indicators of fluid flow will be analysed in the context of the structure and stratigraphy. The secondary aim is to understand the genesis of the depression structures and to examine whether they formed as a result of the expulsion or migration of fluids.

5.1.3. Dataset

In October 2013, additional seismic data became available provided by Geophysical Service Inc. (GSI) which allowed the description of the North-East Falkland Basin (NEFB) with a dense seismic coverage (see Chapter 1).

The dataset used for this chapter is composed of 55 2D seismic lines provided by GSI and 28 2D seismic lines from FOGL (Figure 5.1). The 2D grid spacing is variable and ranges from 700 m to 10 km . Processing histories of the seismic data can be found for GSI dataset in Appendix A.1.2 and for the FOGL dataset in Appendix A.1.1. The different polarity of the two surveys has been converted to the standard American display convention, with positive peak response representing increasing acoustic impedance. The seismic display used in this Chapter is variable density (see Chapter 2). The seismic resolution of the surveys used in the previous chapters and calculated using the Widess relation (Widess, 1973) is shown in Table 5.1.

Table 5-1 **:** Seismic resolutions of the FOGL and GSI datasets.

Dataset	**Full stack**	**Near-angle stack**	**Far-angle stack**
FOGL	14m	13m	19m
GSI	12m	10m	18m

5.2. Seismic Stratigraphy

The North-east Falkland Basin (NEFB) is here defined as a region located approximately 180 km to the NE from the Falkland Islands (Figure 5.1). NEFB cover approximately a region of 4578 km^2. Bathymetrically it is represented by a gentle southeastward dipping seabed from 1600 m to approximately 2300 m deep. The bathymetry is also characterised by pronounced scarps oriented perpendicularly to the slope.

The gross seismic stratigraphy is based on the stratigraphic framework described and discussed in Chapter 3. The names and definitions of Unit 1, 2 and 3 presented in Chapter 3 are directly applicable in this Chapter and described in Section 3.3.2. The following description will include the definition of the key horizons and the units not previously defined.

The descriptive work used to define the units does not follow rigorous definitions of sequence boundaries but rather an informal subdivision of the units conveniently based on regionally correlatable reflections (e.g. Posamentier et al., 1988). The seismic stratigraphy is described with reference to a representative 2D seismic profile crossing the centre of the study area (Figure 5.2).

5.2.1. Acoustic basement (Horizon B)

The deepest recognisable horizon encountered in the 2D seismic grid (Figure 5.2) is a positive, weak to moderate amplitude laterally discontinuous reflection named here Horizon B. In many regions within the study area Horizon B is not easily detected. It appears very weak in amplitude and often it can only be recognised because it sharply divides two acoustically different seismic facies: 1) onlapping

stratified units above and, 2) featureless seismic characters. Due to the different seismic processing flows applied to the two 2D seismic surveys Horizon B exhibits variable a amplitude response but a consistent positive polarity. Only few coherent reflections are observed beneath this boundary and for this reason it has been interpreted as the base of the sedimentary package or acoustic basement.

Correlation of the best pick of Horizon B throughout the study area is shown in the time-structure map shown in Figure 5.3. The map does not represent a complete structure map since the lack of coherent signal at depth did not allowed to correlate faults and other structural elements.

The gross map geometry of Horizon B (Figure 5.3) can be synthesised as an irregular SE-dipping slope. The time map exhibits a number of prominent structural highs located to the north and west of the study area exhibiting irregular margins. These structural reliefs are divided by three major NW-SE aligned scarp-like structures (Figure 5.3). The centre of the map exhibits a number of structural lineaments oriented approximately N-S. These structures are associated with normal faulting throwing to west. The fault pattern is characterised by sequential fault blocks progressively dipping to the east. In the southeast region Horizon B reaches the maximum depth with values ranging between 6.0 and 7.5s TWT (Figure 5.3).

Due to the lack of calibration with wells, Horizon B has been here tentatively interpreted as the likely equivalent of the crystalline basement encountered in DSDP well site 330, and it is dated tentatively Precambrian in age (Backer and Daziel, 1976).

5.2.2. Unit JC1

Unit JC1 is limited by Horizon B at its base and by Horizon J at its top. Horizon J can be recognised as a positive, laterally continuous reflection which is correlatable throughout the study area (Figure 5.2). Unit JC1 is predominantly composed by parallel reflections characterised by variable amplitude response from moderate to high. In regions where the acoustic basement can be clearly recognised the reflections are seen to onlap onto Horizon B. In some regions the discontinuity of reflections can be interpreted as basement faulting (Figure 5.2).

A set of amplitude reflections is observed in this unit. These amplitudes do not show a clear relationship with specific intervals. Amplified reflections are observed in the deeper regions of Unit JC1 (Figure 5.2). Some isolated high amplitude reflections are characterised by saucer-shaped profiles. The strong positive acoustic response of these seismic anomalies and their geometry are consistent with an interpretation of igneous bodies such sills (e.g. Hansen and Cartwright, 2006). Sill intrusions, and also lava flows, have been reported in these regions by Richards et al. (1996) and Richards et al. (2013) and dated as approximately 135-121Ma (Valanginian-Aptian; Richards et al., 2013). The gross TWT time thickness of Unit JC1 ranges between c.50ms and 3300ms TWT.

Based on previous reconstructions (Platt and Philip, 1995; Richards et al., 1996) Unit JC1 is dated as Jurassic to Early Cretaceous in age. Based on this interpretation, Unit JC1 may include Oxfordian to Early Kimmerdgian source-prone marine sediments composed of interbedded silty-claystones and limestone similar to the sediments encountered in DSDP well sites 330 and 511 (see Chapter 3, Figure 3.2). The presence of potential mature source rocks is discussed later.

5.3. Depression structures

Circular to sub-circular depressions are recognised in the study area (Figure 5.4). These depressions can be recognised because they deform the background reflectivity pattern of the shallow basin with a concave upward geometry broadly circular in plain view. Three depressions, here named C1, C2 and C3 are described and analysed in detail below.

5.3.1. Depression structure C1

C1 is described with reference to two representative 2D seismic profiles (Figure 5.5a-b and 5.6, see Figure 5.4b for the line location). The profiles were selected because they allow a clear visualisation of the structures and because they are the closest to the axis of the depression (Figure 5.4b).

C1 is characterised by concave-upward reflections which extend vertically from the top reflections of Unit 3 to Horizon K covering almost 1.5s TWT (Figure 5.5a and 5.6). The depression does not have a seabed expression because of the erosion of the shallow sediments. Evidence of seabed erosional truncation of reflections is clearly observed in Figure 5.5a and 5.6. The reflections composing C1 are mostly parallel in Unit 3 but show evident variations in curvature and geometry toward the base of Unit 2 (Figure 5.5a). It is interesting to observe that Horizon K exhibits bowl-shaped geometry in Figure 5.5a and an almost flat surface in Figure 5.6.

C1 is hardly recognizable in Units 1 and JC1 where the deformation of the polygonal fault system and the loss of acoustic signal make it difficult to recognise coherent reflections and to understand if the depression extends in these units.

Horizons J1 and J (Figure 5.5a) exhibit however upward concave shape that may represent the deeper depressed reflections associated with C1.

Normal faults can be observed within the depression. They are mostly distributed in Unit 3. These faults have the same pattern of the polygonal faults present in other regions of Unit 3 and associated with Opal A-CT transition (similar to what observed by Davies and Cartwright, 2002). C1 does not exhibit clear evidence of faulting in Unit 2. However, sub-resolution faults maybe present within the depression structures.

5.3.1.1. Geometrical analysis of C1

The geometry of the depression structure was defined and analysed by interpreting the hinge points at the margins of the depression (Figure 5.5b C). Two parameters have been measured for each interpreted horizon, (1) the chord length, which represents the distance measured between two hinge points of a given concave upward reflections segment, and (2) the negative vertical relief, which represents the vertical distance between the chord and the relative upward concave reflection segments measured at the maximum vertical distance. The measurements were complicated by the presence of faults (e.g. polygonal faults in Unit 1 and 3) and undulated reflectivity pattern associated with Units 2 and 3. For these reasons only a limited number of horizons have been used.

C1, as revealed by the geometrical analysis (Figure 5.5b C), tapers systematically downward i.e. the chord lengths decrease with depth. The chord of C1 ranges from 5.55km (L2) to 2.68km (K). The negative vertical relief values ranges from 0.127s TWT (L1) to 0.082s (K1) and are not related with depth or chord length (Figure 5.5b C).

The values of chord and negative vertical relief measured for every horizon have been used to calculate the approximate volume occupied by the relative overburden (Figure 5.5b D). The singular overburden volume was approximated as a spherical cap defined by

$$V = \frac{\pi \Delta z}{6}\left(3\left(\frac{\phi}{2}\right)^2 + \Delta z^2\right)$$

, where Δz represents the negative vertical relief in km , calculated using

$$\Delta z = (\Delta t/2) \times V_p$$

, where V_p represents the average velocity of the sedimentary package (based on velocity field data provided by FOGL.plc), and ϕ the chord length which is here approximately used as average diameter. The calculated approximate overburden volume values range between 1.19km ^{3} (L2) and 0.31km ^{3} (K) with an average value of 0.66km ^{3}.

The overburden volume values have been subsequently used to calculate the effective volume variation occurring along the depression structure. This analysis was based on subtracting to the volume extracted at a given horizon the volume of the overburden located immediately above. The result of this analysis shows two prominent volume variation occurring between Horizons K and K1 (-0.44 km ^{3}) and between Horizons K2 and L (-0.33 km ^{3}) with a cumulative volume loss of -0.771 km ^{3}. This volume loss is exclusively associated with Unit 2.

5.3.1.2. **Acoustic analysis of C1**

Seismic amplitude anomalies and disrupted signal zone can be observed within C1 and in the immediate nearby regions (Figure 5.5a).

The centre of the depression is characterised by a region of strong acoustic amplification. The amplified reflections within this region are negative in amplitude and are stacked vertically with a systematic decrease of the down sag toward to the top of Unit 2 (FAA, Figure 5.5a B). These stacked amplitude anomalies are defined by an acoustic character and geometry comparable with the vertically anomaly clusters, or VACs, exhaustively discussed in the east Falkland Basin (see Chapter 3.3).

Two sets of amplitude anomalies composed of 2-3 stacked negative high amplitude reflections are present within the upper reflections of Unit 2. These amplified regions define in 2D cross-sections a gullwing-shaped structure located right above the amplified central region (Figure 5.5a). This geometry is also observed in Figure 5.6. These features may suggest the presence of a toroid-shaped amplified volume coaxial to the amplified region beneath.

A region of signal disturbance characterised by strong amplitude amplification is present above the maximum vertical negative relief of Horizon L (Figure 5.5a). The region is distributed sub-vertically and is limited at the top by the interpreted Opal CT-Q boundary.

Two columnar regions of signal disturbance are located above the hinge points of Horizon L. These vertical regions extend upward for 400-500ms TWT with a maximum width in cross-section of 1km . The regions are acoustically similar to adjacent faulted zones which characterise Unit 3 and that are associated with a cluster of closely spaced normal faults.

5.3.2. Depression structure C2

C2 is described with reference to two representatives seismic profiles (Figure 5.7a-b and 5.8, see Figure 5.4a-b for the line location). The depression feature is best mapped at Horizon L where it can be seen as a sub-circular shaped depression with its longitudinal axis oriented NE-SW (Figure 5.4a-b) and approximately perpendicular to the basin slope.

The gross geometry of C2 is similar to C1. C2 is well imaged on seismic profile (Figure 5.7a) where it exhibits clearly concave-upwards reflections from the seafloor to Horizon K (Figure 5.7a-b). These reflections appear however flat in SW-NE cross section (Figure 5.8). C2 has a vertical extent of 1.5s TWT. C2 reflections are parallel in Unit 3 without evidences of onlap reflections or erosional surfaces (Figure 5.7a), while in Unit 2 the reflections composing C2 are parallel but with asymmetric geometry. An example of this geometry is given by the non-coaxial shapes of Horizon K and K1 (Figures 5.7a-b 5.8).

C2 is not easily recognisable in Unit 1. The strong signal loss produced by the intense faulting does not allow us to define any coherent reflections. Horizon J1, tentatively interpreted in Figure 5.7b, does not exhibit a concave upward shape. Further downward, Horizons J and B1 exhibits however concave-upward shapes and they may represent deeper horizons associated with C2.

A series of major normal faults are interpreted toward the centre of C2. These faults are mostly distributed within the depression structure in Unit 3 and they exhibit the same acoustic and geometrical character of other Opal A-CT related normal faults present in this Unit. Some prominent normal faults are also observed in the basal reflections of Unit 2. These faults propagate from the underlying Unit 1 to the centre of Unit 2.

5.3.2.1. Geometrical analysis of C2

The geometry of C2 has been analysed applying the same methodology used for C1 (see 5.3.1.1 and Figure 5.5b).

The geometrical analysis evidences that C2 exhibits an irregular variation of the chord values with depth (Figure 5.7b). C2 exhibits a neck-like feature at Horizon K1 with a chord value of 2.57km . C2 exhibits a maximum width of 4.45km (L2) in the middle of Unit 3. The depression tapers locally toward the top with a chord value of 3.66km (L4). The value of negative vertical relief varies from a minimum of 0.082s TWT, at the neck-like feature (K1), to a maximum of 0.133s TWT (L1).

A calculation of the effective volume variation was done using the values of chords and negative vertical reliefs and extending the interpreted Horizons as an approximation of a spherical cap (see 5.3.1.1 and Figure 5.5b). The calculation reveals that the largest volume variations are occurring between K and K1 with a volume loss of -0.22km ^{3} and between L and L1 with -0.25km ^{3}. C2 exhibits also a positive volume variation between L3 and L4 of +0.27km ^{3} may associated with the reduction at the top of the depression of chord (diameter) and negative vertical relief. C2 is therefore associated with multiple regions of volume variations.

5.3.2.2. Acoustic analysis of C2

A number of stacked amplitude anomalies with moderate amplification are observed inside the depression zone close to Horizon K (Figure 5.7a). The amplitude anomalies are concentrated in the axis of the depression. The acoustic response of these stacked amplitude anomalies is characterised by a negative amplitude response

and by sharp lateral amplitude cut-offs. These anomalies are similar in all respect to the amplitude anomalies described in Chapter 3 and distributed in EFB and are therefore interpreted as being due to gas charged layers (Figure 3.4, see Chapter 3).

5.3.3. Depression structure C3

C3 is described using two representative 2D seismic profiles crossing the depression structure longitudinally (Figure 5.9a-b) and transversally (Figure 5.10; see Figure 5.4a-b for the line location). C3 shows a complicate sub-circular depression surface as observed on the time-structure map of Horizon L (Figure 5.4b) with its major axis oriented and parallel to the basin slope.

C3, as seen on 2D seismic profile, is composed of a number of upward concave reflections from Horizon L to the seabed. The depression at the Opal A-CT and Opal CT-Q level exhibits a upward concave shape but the Opal CT-Q reflection presents a more pronounced concave shape compared to the Opal A-CT. Opal CT-Q cross-cuts the reflectivity pattern at the base of Unit 3 (Figure 5.9a C-D). Erosional features are not observed within the depressed region.

C3 exhibits a complex seabed shape with clear truncated reflections associated with erosional surfaces (Figure 5.9a). Above the seabed surface a positive sedimentary edifice is observed (Figure 5.10). This edifice is composed of a triangle-shaped body which continues with a flat surface at SW. The internal geometry of this edifice is characterised by a number of reflections mimicking its external surface. These bodies are potentially related to later expulsion of material. This point is discussed later.

C3 is characterised by an intense disrupted signal zone in Unit 2 and at the base of Unit 3. The disrupted region does not allow us to reconstruct properly the geometry of the reflectivity pattern. C3 is not recognisable in Unit JC1 and 1 due to intense loss of signal. Importantly C3 is located approximately above an interpreted basement normal fault (Figure 5.9a and 5.10). The footwall crest of this prominent fault, as interpreted at Horizon B, is located approximately at the axis of C3.

A number of normal faults are recognisable in Unit 2 and 3. Normal faults in Unit 3 are mostly associated with the fault pattern already observed in this unit and related to the Opal A-CT transition. Normal faults in Unit 2 are mostly observed in Figure 5.9a. Their throw is oriented toward the centre of the depression (Figure #).

5.3.3.1. Geometrical analysis of C3

The geometry of C3 has been analysed applying the same methodology used for C1 and C2 (see 5.3.1.1 and Figure 5.5b). The horizons showing higher continuity across the depression have been mapped and used in this analysis. However, most horizons are strongly affected by lack of coherent signal in Unit 2 and by the effect of the divergent Opal transitions in Unit 3. Consequently two different scenarios with contrasting geometrical analyses, C3-1 and C3-2, were considered. C3-1 is consistent with an interpreted long-wave depression where the hinge points are based on broad thinning of Unit 2. C3-2 is consistent with an interpreted smaller depression based on a more localised deformation of the reflectivity (Figure 5.9b).

C3-1

The geometrical analysis reveals that C3-1 tapers downward (Figure 5.9b). The chord values range between 13.01km (L1) and 3.17km (K). The values associated

with the negative vertical relief range between 0.20s TWT (L1) and 0.056s TWT (K). These values have been used to calculate the approximate spherical cap volume of each horizon and the effective volume variations within the depression (see 5.3.1.1 and Figure 5.5b). The measurement reveals that C3-1 is characterised by a volume loss of about -7.1km ^{3} between L and L1 and -4.93km ^{3} with a cumulative volume loss between K and L1 of c.-12km ^{3}.

C3-2

C3-2 is smaller in dimension respect to C3-1 with a maximum chord value of 7.17 km (L1, Figure 5.9b). The negative vertical relief values are depth dependent with a maximum value of 0.118ms TWT (L1) to a minimum of 0.056sTWT (K). The effective volume variation within the depression is depth dependent and with a maximum volume loss of -1.34 km^3 occurring between L and L1 (Unit 3).

5.3.3.2. Acoustic analysis of C3

C3 is acoustically characterized by a strong signal disruption in Unit 2 (Figure 5.9a and 5.10). The disturbed signal zone is characterized by a patchy amplification of the background reflectivity. The layering appears completely disrupted within the depression with an almost complete disruption of the reflections. Disordered reflection segments are observed within the disrupted zone.

The disruption zone is distributed also in the regions surrounding the depression structures (Figure 5.9a and 5.10). These regions are observed at the base of Unit 2 and are characterized by a dominant decrease of acoustic amplitude and by an irregular intermittent reflectivity pattern (Figure 5.10 C).

5.3.4. Depression distribution and relationship with the basin features

The depression structures on Horizon L (Figure 5.4a) are mostly distributed in the western region of the study area. They are irregularly spaced and aligned in a NNE-SSW axis. The depressions structures occur in a middle-slope position and do not exhibit any relationship with the stratigraphic characteristics of Unit 2 and 3.

As observed in the previous seismic sections (e.g. Figure 5.6, 5.10) the distribution of the depressions seems more related with the structural features of the acoustic basement. For this reason their distribution has been compared with the time-structure map of Horizon B which represent the deeper recognisable acoustic structure in the study area.

C1 and C2 are located above a basement normal fault (F1, Figure 5.11 A-B). The footwall crest of F1 represents a local structural high of Horizon B. This structural feature is oriented NNE-SSW and has the same orientation of the depression structures distribution. This structural region is located at a depth of 4600-4700msTWT.

C3 is located as well as above a structural high of Horizon B. In this case the structural high is oriented NNW-SSE with a depth of 4500msTWT. This structural high is adjacent to prominent scarps and close to deep structures with depth of 5000-5500ms TWT.

5.4. Amplitude anomalies, pipes and gas chimneys

Different typologies of seismic anomalies have been identified in the study area. These include amplitude anomalies, (AAs and VACs), pipes and gas chimneys. A detailed description of these seismic features is given below.

5.4.1. Amplitude anomalies

Amplitude anomalies (AAs) were identified using the methodology presented in Chapter 2. Good examples of amplitude anomalies have already been described in section 5.3 in association with depression structures (e.g. Figure 5.5a, 5.6 and 5.8a). Other examples not related with depression structures are described below.

The AAs can be described as simple amplifications of the background reflectivity. They are characterised by a sharp decrease of amplitude at their margins (Figure 5.12). These AAs are negative in amplitude and not associated with phase rotations.

As observed from representative examples in Figure 5.12 and 5.13, on the vast majority of the 2D profiles AAs are normally found in groups where the singular AAs are stacked in vertical clusters. Vertical gaps of not amplified reflections are observed within stacked AAs. The amplified reflections exhibit also lateral discontinuity, yielding on seismic an intermittent pattern (Figure 5.13).

These stacked AAs are acoustically identical to the ones described in association with depression structures (Figure 5.5a), which were interpreted as vertical anomaly clusters (VACs). These VACs in NEFB and the ones discussed in EFB (see Chapter 3) are compared in Figure 5.14. The two representative examples of VACs are

characterised by a number of stacked AAs distributed in Unit 2. In these examples the stacking of AAs, considering the large variability of (1) internal AAs distribution, (2) size of individual AAs and (3) thickness of Unit 2, is clearly defined. Following the discussion presented in Chapter 3, the observed VACs in NEFS are interpreted as associated with gas charged layers (Chapter 3).

5.4.2. Pipes

Pipes are vertical or sub-vertical regions of signal disturbance. Pipes exhibit localised seismic amplifications of the background reflectivity. Upward curved reflections may surround the pipes and define their lateral extent. In the study area a number of features that can be interpreted as pipe were observed. A representative example of a potential pipe is described with reference to Figure 5.15.

In 2D seismic section it appears as a columnar region of signal disturbance. It propagates approximately from Horizon K at the bottom to the Opal A-CT transition in Unit 3 at the top. The columnar seismic feature is acoustically characterised by amplified reflections. The reflectivity pattern within the pipe is chaotic and disrupted with respect to the background. The seismic feature is characterised by a cross sectional width of approximately 600m and a vertical extent of c1.8s TWT.

Upward curved reflections are present at the margin of the columnar feature. Horizon L and a number of acoustically amplified reflections in Unit 2 exhibit a clear upward pattern in Figure 5.15B.

A region of signal disturbance is present below the seismic feature. It can be described as a region of signal dimming which propagates downward to Horizon J. The low amplitude response, coupled with the presence of polygonal faults, does not allow us to interpret any structure.

The documented structure is similar to other vertical zone of signal disturbance described by Gay et al (2007) in Lower Congo Basin and it is here interpreted as a pipe. The lack of 2D seismic lines transecting the seismic feature in other directions does not allow us to assess his three-dimensional geometry leaving some interpretational uncertainties. The low amplitude disturbed region beneath the pipe represents a common characteristic of large pipes (Moss and Cartwright, 2010) and it is often associated with migrating fluids.

5.4.3. Gas chimneys

Gas chimneys can be defined as region of signal disturbance which can be observed on seismic data (Heggland, 1998). Gas chimneys are associated with disruption and dimming of the background reflectivity. They can exhibit a large variability in shape and dimension. They are often associated with upward migration of fluids and represent a type of hydrocarbon seepage (Heggland, 1997). A number of features potentially interpretable as gas chimneys are described with reference to a representative example observed in two seismic sections crossing the feature longitudinally and transversally (Figures 5.16 and 5.17).

The putative gas chimney is located right above a structural high, from Horizon K to the interpreted Opal CT – Q boundary. It exhibits a complex structure composed of a number of amplified reflections distributed around a disturbed amplitude dim zones in the centre of the feature (ADZ, Figure 5.16). It deforms in a number of points the background reflectivity. Horizon L appears dimmed and discontinuous in two regions (BR, Figure 5.16 B and 5.17 B). Reflection amplification is also present above Horizon L and with an extent of 200-250ms TWT. Above the interpreted Opal CT – Q the AAs are present but limited at the Opal A-CT boundary. Some weak

AAs, located between the Opal A-CT and CT – Q, are possibly related to highly faulted zones which are observed in this unit.

The acoustic character of this seismic feature is similar to other examples of seismic chimneys described worldwide (e.g. Schroot et al 2003b; Sun et al., 2012; Tingdahl et al., 2001) and it has been interpreted as a seismic chimney associated with upward migrating fluids (e.g. gas). The presence of deformed reflections (e.g. Horizon L in Figure 5.16 B and 5.17 B) indicates a potential failure of the observed layers which may contribute to the remobilization of solid particles in the migrating fluids. However no intrusive bodies have been observed within the regions surrounding these features. This suggests the lack, or negligible content of remobilised solid material. Furthermore, seeps forces associated with migrating fluids only can deform permanently the hosting lithologies (Mourgues and Cobbold, 2003; Ooms et al., 1970) and account for the observed deformed horizons (BR, Figure 5.16 B and 5.17 B).

5.4.4. Distribution of the fluid related seismic features and relationship with the basin features

The documented VACs (stacked amplitude anomalies), pipes and gas chimneys interpreted as fluid related seismic features have been mapped in the study area to define and understand their distribution.

VACs were projected on the seismic grid based on the lateral extension of single constituent AAs. This methodology was already adopted in EFB (see Figure 3.8). The VACs are represented by simple vertical projections of the anomaly extents on any given seismic line intersection. Since all VACs are limited at their base by Horizon K the contour of this horizon has been included in the map. Due to the

limitations of the 2D seismic grid some AAs are mapped as individual line intersections (Figure 5.18).

The result of this analysis reveals that VACs are widely distributed and particularly well developed in the western and northern part of the study area (Figure 5.18). The dimension of the VACs is variable and ranges approximately between 1 and 16 km. The VACs exhibit variable plan geometry from simple elliptical to irregular. Examples of rounded pattern can be observed in a Figure 5.18B (VR). The VACs do not exhibit elongated or meandering plan geometry. Taking in account that they are not associated with erosion or depositional structures, as observed in 2D seismic sections (e.g. Figure 5.12, 5.13 and 5.14B), the VACs are not consistent with typical reservoir geobodies.

The VACs plan shape can be characterised by straight margins with different orientations. In the examples in Figure 5.18 B (VS) the interpreted VACs perimeters are characterised by straight margins which are oriented with different angles. The straight pattern across multiple 2D seismic lines is interpreted as associated with the normal fault system present in Unit 2.

The previously documented gas chimneys and pipes are in all the cases associated within VACs of different dimension (Figure 5.18A). The pipes (red circles) are located within small VACs in the northern portion of the study area. Gas chimneys are located within larger VACs. Gas chimneys and pipes are distributed in a narrower region respect to the other AAs and VACs.

The distribution map associated with the VACs, pipes and gas chimneys has been updated with the distribution of depression structures and subsequently compared with the time-structure maps of the interpreted Horizons. The most striking correlation was found again in association with Horizon B (Figure 5.19).

The depression structures and the other seismic features (VACs, pipes and gas chimneys) are in most of the cases distributed above structural elevated areas of Horizon B (Figure 5.19). In the previous description, (see section 5.3.4) it was observed that two depression structures were located directly above a footwall crest of an interpreted basement normal fault (F1, Figure 5.11). The distribution map, updated with the position of the documented seismic features, reveals also that a number of VACs and two gas chimneys are distributed on the same orientation of F1 and approximately along its shallower footwall crest (Figure 5.19).

Other VACs are distributed above the normal faults parallel to F1. Striking examples of this correlation can be observed above F2 with VACs V1 and V2 and also above F3 with VAC V3 (Figure 5.19). To the north the group of VACs, gas chimneys (Gs) and the pipe P1 are located above a structural high. In this case these features and the depression structure C3 define a trend oriented east- west which is parallel with the structure beneath (Figure 5.19). In a number of cases some VACs and other AAs are located above local structural lows (e.g. V4 and V5). A representative example of this observation is related to V4, which is located above a large structural low of Horizon B (Figure 5.19).

These observations show that the distribution of depression structures, AAs, VACs, pipes and gas chimneys is strongly controlled by the structural characteristics of the acoustic basement, such as the interpreted normal faults. This important relationship raised the question about the role of the deep structures in distributing the observed fluid related seismic features in the shallow portion of the study area. This point is described in the following sections.

5.5. Discussion

5.5.1. Depression structures

The most important observations associated with the documented enigmatic depression structures are here analysed to understand their origin and significance. This part of the discussion starts with the definition of their common characteristics which will be used to compare them with other examples of depression structures documented worldwide.

The documented depression structures are linked by a number of common characteristics such (1) evidence of material withdrawal (up to -1.34km ^{3} at C3), (2) upward curved reflections (0.05-0.2s TWT), (3) presence of amplitude anomalies and/or disturbed signal zones, (3) parallel reflectivity pattern (no clear evidence of erosion or onlap surfaces), and (4) diameter above 2km.

Different geological process can generate structures similar to those observed in the present study. A review of these processes and their relative output structures have been discussed by Stewart (1999) where different type of circular depressions are classified in terms of genesis, geometry and other parameters. The classification discussed by Stewart (1999) does not take in consideration other examples of circular structures caused for instance by hydrothermal venting or by expulsion of mud (e.g. mud volcanoes; Stewart and Davies, 2006). All potential mechanisms associated with the generation of the observed depression structures are here considered and discussed.

Depression structures can be produced by (1) salt withdrawal or dissolution/collapse of soluble rocks (such as evaporites, salt, etc), (2) expulsion of magma (e.g. calderas), (3) impact cratering, (4) pockmarks, and (5) mud volcanoes.

Salt bodies are recognisable on 2D and 3D seismic data because they produces a strong amplitude response at the interface separating sedimentary rocks above and salt rocks below (Aveseth et al., 2009). In most of the time salt bodies are characterised by diapir-related structures which deform the geometry of the sedimentary rocks (e.g. Stewart, 1999). Some amplitude anomalies characterised by strong positive amplitude responses are observed within JC1, however their geometry is not consistent with salt bodies. These seismic anomalies in JC1 have been previously interpreted as magmatic intrusions and lava flows as also documented by Richards et al (1996, 2013 and with older interpretations: e.g. Platt and Philip, 1996). The presence of salt has never been reported in any of the basin around the Falkland Islands and so the generation of the depression structures cannot be associated with salt rocks withdrawal or dissolution.

The presence of magma is reported by Richards et al (2013) and could be related to hydrothermal venting. Examples of depression structures associated with hydrothermal venting are described for instance by Svensen (2004) in southeast Vøring Basin. In that case the depression structures, which appear similar to those described in this work, are produced right above the margins of sill complexes. In NEFB the magmatic bodies are limited to the south-east portion of the study area and not present in the region of the depression structures. The age of the magma intrusions, recently dated as Valanginian by Richards et al (2013), is also not consistent with the later generation of the observed depression structures, which deform the shallower late Cretaceous-Cenozoic interval (Figure 5.2).

Impact craters can generate depression structures of different size and negative vertical reliefs (Salguero-Hernandez et al., 2010; Stewart and Allen, 2002). Impact craters described for instance in Morgan et al (1997) are characterised by distinctive

structural features such outer ring-shaped wall structures, breccia lenses at the floor of the impact region and ring-shaped extensional grabens. These structures are not consistent to what described in the depression structures observed in the NEFB.

Pockmarks are structures associated with migrating fluids ending at the seabed with gas-induced cratering or catastrophic expulsion (Bialas et al., 2013; Cole at al., 2000; Hovland and Judd, 1988). A consequence of superficial expulsion would be recognized on cross section as truncation of the shallow reflectivity. Some representative examples of these features are showed for instance by Betzler et al. (2011) where shallower reflections just beneath the seafloor are truncated in proximity of seabed gas pockmarks. The shallow reflectivity patterns observed here at the top of the depression structures is partially eroded at the seabed but does not exhibits evidences of lateral truncation. Gas pockmarks are associated with episodic migration of gas characterised by intermittent events of gas expulsion (Bangs et al., 2011; Davis et al., 1990; Jin et al., 2008). This characteristic would yield a reflectivity pattern characterised by staked craters or vents with evident onlapping surfaces (Andresen, 2011). This characteristic is not seen in the observed depression structures which show instead a “rigid” collapse of Unit 3 and part of Unit 2. Also the dimensions of the observed depression structures is 1-2 orders of magnitude bigger than the expected size of gas pockmarks (0.01-0.5 km; e.g. Andresen, 2011; Moss and Cartwright, 2010, Riboulot et al., 2013). However exceptional large pockmarks like those described by Bialas et al. (2013) in Chatham Rise and pockmark gullies Pilcher and Argent (2007) in west African continental margin exhibit larger extent.

Mud volcanoes or sand injections are intrusive and extrusive features related with migration of fluids associated with remobilisation and fluidisation of sediments (e.g.

Cartwright, 2007; Etiope et al., 2009; Lonke and Mascle, 2004; Planke et al., 2003). Mud volcanoes are generally caused by tectonic processes, may associated with overpressure build-up in compressional geological settings, or with maturation and degassing of organic-rich sediments and source rocks (e.g., Brown 2000; Etiope et al., 2009; Gennari et al., 2013;Hedberg 1974; Henriet et al., 1991; Milkov 2000).

The intrusion or extrusions of fluidised or remobilised materials within or above the depression structures is expected to form bodies or edifices characterised by (1) contrasting geometry respect to the country rocks and (2) different reflectivity patterns on seismic data. The lack of injected or buried bodies within the observed depression structures could be explained by a singular collapse event with a completely extrusive migration of the remobilised sediments at the seabed surface. Clear evidences of extrusive structures have been observed above C3 (Figure 5.10) where a number of bodies composed of triangular-shaped structure can be interpreted as a mud edifice characterised by cone-shaped structure. In the regions above C2 and C1 the lack of clear extrusive bodies at the seabed can be justified by the complete erosion of the seafloor sediments caused by the action of currents, which have been documented in the NEFB by Arhan et al. (2002). This interpretation is justified by evidences of erosions at the seabed observed above the depression structures (e.g. Figure 5.5a and 5.6).

Summary

Based on the discussed points the observed depression structures are interpreted to be primarily caused by release of fluidised sediments (mud) and subsequent collapse of the overburden.

Depression structure C3, due to the presence of extruded mud at the seabed, is interpreted as a mud volcano similar to those described by Westbrooke and Smith (1983) which are characterised by low positive vertical relief. Depression structures C1 and C2, taking in to account the lack of mud edifices (eroded by the activity of ocean currents), are similar to caldera-like structures described by Graue (2000) in deeper water Nigeria. In those examples the mud volcanoes were interpreted as abandoned features. Other examples of depression structures associated with mud volcanisms are also documented by Duerto and McClay (2002) in Venezuelan Basin and Tari et al. (2012) in Matruh and Herodotus basins of NW Egypt. In those cases, the depressions are buried by mud edifices.

Based on these examples and taking in to account what discussed in the previous paragraph the depression structures C1 and C2 are still interpreted as abandoned mud volcanoes but where only the depression structures are preserved.

5.5.1.1. Withdrawal regions

The interpretation of the depressions as mud volcanoes raises the question about the definition of the intervals where the depletion of material occurred and also the possible origin of the involved fluids.

The interpretation and the geometrical analysis carried out in all depression structures revealed that the regions characterised by appreciable volume variation where identified within Unit 2 and 3. These regions may be interpreted as a system of depleted multi-mud chambers like those described by Cooper (2001) or Capozzi and Picotti (2002).

It is important to note that there are not common layers or intervals within Unit 2 and 3 where the material withdrawal occurs systematically. The lack of calibration in

the geometrical analyses and the variation in thickness of Unit 2 and 3 has not allowed us to define a specific interval of depletion. This observation may however suggest the effective lack of precise intervals apt to work as mud chamber or intervals potentially associated with fluidisation of sediment (mud formation). However, a number of broad intervals associated with negative volume variation which were interpreted to be caused by material withdrawal were defined in every depression structure. According to the geometrical analysis applied to the depression structures, higher values of depletion are observed within Unit 2 (Figure 5.5b and 5.7b).

5.5.1.2. Sources of fluids

Mud volcanoes are strongly linked to the presence of fluids which enrich fine-grained sediments and promote buoyancy (Kopf, 2002). The presence of mud volcanoes implies therefore a relative high concentration of fluids. Different fluids generated at different stages or depths can be involved in this process. The most important include (1) pore fluids from compaction, lateral migration (from overpressured regions) and diagenesis (e.g. opal A-CT), (2) hydrocarbon fluids (biogenic and thermogenic), and (3) hydrothermal fluids (Deville et al., 2003; Kopf, 2002).

As shown previously (Figure 5.11 and 5.18) the distribution of the depression structures is clearly linked with the structural features of the deeper portions of the basin (e.g. fault F1, Figure 5.4) and particularly with the interpreted acoustic basement (Horizon B, Figure 5.4). Evidences of geographical, structural and stratigraphical relationship with the shallower Units 1, 2 and 3 were not observed (e.g. Figure 5.4a).

This observation suggests that fluids derived from compaction (e.g. of fine-grained sediments composing the shallow intervals, e.g Swarbrick and Osborne, 1996 and 1998; Swarbrick et al., 2004) or diagenesis (e.g. from the chemical transformation from Opal A to Opal CT; Davies and Cartwright, 2002) within Units 1, 2 and 3 are not however directly linked to the formation of mud and to the position mud volcanoes.

This important implication suggests that the main source fluids apt to enrich the fine grained sediments, in some intervals within Unit 2 (see section 5.6.1.1), have a deeper origin and necessarily associated with Unit JC1.

Evaluation of deep fluid sources

Potential sources of fluids in Unit JC1 can be associated with different causes including (1) later-stage dewatering of fluid-filled porous sediments, (2), hydrothermal fluids and (3) fluids generated from maturation of source rocks.

High sedimentation rate of low permeable sediments is a critical condition able to reduce escape of fluids and generate overpressure (Swarbrick et al., 2004). Overpressured conditions are transient features which may end to episodes of seals failure and release of fluids (Reilly and Flemings, 2010; Rozhko et al., 2007).

Release of overpressured fluids from Unit JC1 could be linked to the formation of the observed mud volcanoes structures. As observed from long-range well calibration (see Chapter 3, Figure 3.2), Unit JC1 is associated with sedimentation rates of 5.2 – 15.2m/m.y. (Ludwig, 1983) and it is not expected to retain fluids and generate high pressure conditions (e.g. Mello & Karner, 1996). Unit JC1 exhibits also evidence of deformation associated with post-rift reactivation of basement normal faults (e.g. Figure 5.2, 5.16 and 5.17). These conditions are not favourable

for the retention of fluids and generate overpressure. The lack of important parameters about pressure, porosity and burial history associated with Unit JC1 does not allow however to determine the presence of overpressured conditions in the deep portion of the basin. Therefore, the formation of mud volcanoes due to escape of overpressured fluids from Unit JC1 cannot be completely ruled out.

Hydrothermal fluids in NEFB are not responsible for the formation of the mud volcanoes (see section 5.6.1). However these fluids expelled during and after the formation of magmatic sills and lava bodies (Valanginian-Hautervian, Richards et al., 2013) could be present in some small amount (not here evaluated due to the lack of parameters) within Unit JC1. Since Unit JC1 represents the most probable source of fluids it is expected in this Unit a potential contamination of hydrothermal compounds in the fluid-rich sediments associated with mud-volcanoes structures (e.g. Planke et al., 2003).

The maturation of source rocks and especially the conversion from kerogene to oil and gas are one the most significant volume expansion mechanisms which occur in the subsurface (Peng et al., 2013). Migration of hydrocarbons and other maturation-derived fluids and gasses, such as water and CO_2, can increase locally the pore fluid pressure and generate overpressure conditions (e.g. Wiprut and Zoback, 2002). Mud volcanoes, as observed in land environment are mostly associated with migrating hydrocarbons from deep sources to the earth surface (Etiope et al., 2009). A large number of examples from marine environment, synthesised for instance by Dimitrov (2002), suggest again that mud volcanisms are primarily associated with generation and expulsion of thermogenic fluids.

A large number of amplitude anomalies, pipes and gas chimneys were observed within and in the regions surrounding the depression structures. These seismic

features have been discussed to be primarily indicators of hydrocarbons migrating to the shallow sequences of the study area (see section 5.4). Potential expulsion of hydrocarbons and other maturation-derived fluids from Unit JC1 and migration to the shallow section of the study area can be the primary mechanism for the formation of the observed mud volcano-related depression structures. This important point is discussed in the following section.

5.5.1.3. Distribution, maturation of source rock and fluid migration pathways

In order to determine a potential relationship between formation of the observed mud volcanoes and hydrocarbons a qualitative evaluation of the possible maturation and migration of thermogenic fluids has been undertaken.

Source rock maturation

Multiple source rock intervals encountered by DSDP well sites 330 and 511 (Backer and Dalziel, 1976) were interpreted to be stratigraphically distributed from Horizon B to approximately the centre of Unit 2 (Figure 3.2, see Chapter 3). A precise interpretation of source rock layers within these units was not possible due to the lack of precise well calibration. However a qualitative description of the potential location of mature source rocks has been undertaken.

In order to evaluated the maturity of the source rocks the thickness of the overburden has been calculated using the isochronal map calculated between the acoustic basement (Horizon B) and the seabed. The isochronal map has been

converted in thickness map (in metre) applying the velocity data provided by FOGL.plc. The interval velocity calculated between the seabed and Horizon B was approximately 2000m/s (1991m/s).

The result of this analysis (Figure 5.20) shows that the thickness of the entire sedimentary package ranges approximately between 1500 and 5000m. The gross geometry of the map is strongly influenced by the morphology of Horizon B (Figure 5.3). The map exhibits therefore a thick sediment column located in the SE portion of the study area with values of almost 5000m. The sedimentary package thins then westward mimicking the morphology of the basement. To the NE of the study area the thickness of the sedimentary package is 1700m.

Applying a nominal geothermal gradient of 30˚C/km a number of regions potentially mature for oil and gas are defined in the basin (Figure 5.20). The calculation approximates for simplicity that the maturation of source rocks are stratigraphically consistent with the deepest regions above the acoustic basement (at the maximum thickness of the sedimentary columns). Therefore in this calculation it is implicit that a number of shallower source rocks may be mature (or immature) at shallower intervals.

The highlighted 90˚C and 120˚C contours (which represent to the contouring of 3000m and 4000m, respectively) define approximately peak-oil (red) and peak-gas windows (yellow). Since the depression structures are approximately of the same age of the seabed (erosive events observed at the seabed are considered recent as well) the calculation is approximately consistent with present day maturation. The maturation was based on nominal values for hydrocarbon generation in sedimentary basins (e.g. England et al, 1987; Selley, 1985).

If source rocks are present in the observed geological interval, the regions associated with potential peak-gas generation are limited within the eastern portion of the study area. The regions associated with potential maturation of oil are instead wide-spread within the study area. These regions are distributed mostly in the eastern portion of the study area where they occupy a large region which covers entirely the thicker portion of the sedimentary fill. Smaller peak-oil mature regions are also located also to the west of the study area.

Migration in Unit JC1

The stratigraphic configuration which characterise Unit JC1 was defined as a system dominated by fine grained sedimentation and characterised by parallel reflectivity (see 5.2.2.1, Figure 5.2). The lithology of these sediments was calibrated with DSDP well and was consistent with clay-rich sediments onlapping the acoustic basement (Horizon B; see section 5.2.2).

The presence of continuous high amplitude reflections within Unit JC1 may indicate the presence of inter-bedded layers characterised by coarser-grain sediments. These sediments may potentially work as carrier-beds allowing updip migration of hydrocarbon from the eastern portion of the study area to the documented relatively higher structural regions located to the centre and to the west. It is not uncommon for thermogenic fluids to migrate horizontally for hundreds of kilometres from the source point to the reservoir bodies (England et al., 1987).

Migration in Unit 1

Once the thermogenic fluids reach the base of Unit 1 they have to migrate across a ~1km thick fine-grained succession which is strongly affected by a polygonal fault system. Polygonal faults are developed in many sedimentary basins worldwide (e.g. Cartwright and Dewhurst, 1998; Ostanin et al., 2012b). The polygonal faults are thought to be a major fluid pathway system and allow vertical migration of hydrocarbon when reactivated (e.g. Cartwright et al., 2007; Gay et al., 2006; Losh et al., 1999; Sun et al., 2012a). The polygonal faults developed in Unit 1 are therefore thought to actively contribute to transfer fluids from the top of Unit JC1 to the base of Unit 2. The lack of horizontal continuous reflections within the east-dipping Unit 1 suggests the lack of potential carrier beds able to promote up-dip westward migration of fluids. This observation is consistent with the limited distribution of amplitude anomalies and other fluid flow features in the westernmost portion of the basin which, considering the slope of the basin (east), should be expected if carrier beds were present.

Taking in to account the clear link between the observed fluid-related seismic anomalies and the structural features of Horizon B the migration of gas within Unit 1 is assumed mostly vertical and relatively focussed. For instance, the precise alignment observed between the structural highs associated to the basement normal fault F1 and a number of depression structures, pipes and gas chimneys above, suggest that the gas is migrating vertically. As documented by Gay et al., 2006; Gay et al., 2004 fluid migration could be achieved within the triple-junctions of polygonal-shaped elements composing Unit 1 and allowing a direct connection with straight vertical pathways from the top of Unit JC1 to the base of Unit 2.

5.5.2. Conceptual model for the formation of the mud volcanoes-related depression structures

The genesis of the observed depression structures based on the discussed observations is described with reference to a conceptual model and here synthesised in a number of points. The model shown in Figure 5.21 considers only the process at the stage of the expected migration of thermogenic fluids at the base of Unit 2:

1. Thermogenic fluids (gases, oil and water) and probably other fluids (e.g. hydrothermal fluids) are generated within the deeper portion of the basin, between the interpreted acoustic basement (Horizon B) to the top of Unit JC1 (Horizon J).
2. These fluids migrate up-dip along eastward-dipping carrier-like layers from the deeper portions of Unit JC1 to the east to the shallower regions to the west. In the structural high regions these fluid are expected to concentrate and be released in Unit 1.
3. Fluids migrate in Unit 1 where the polygonal fault system allows vertical to sub-vertical migration pathways.
4. Fluids reach Horizon K (A, Figure 5.21) and at a given point will start to migrate within Unit 2 (B, Figure 5.21).
5. Fluid migration within pre-existing normal faults is believed to be one of the potential migration mechanisms (e.g. Ingram and Urai, 1999; Moretti, 1998). Fluid will bypass infill of low permeability layers instead of reservoir-like layers (B-C, Figure 5.21).

6. The high concentration of fluids in some key layers will trigger the formation of mud (e.g. Nichols et al., 1994; D-E, Figure 5.21). A number of multiple-mud chambers are expected to form primarily in Unit 2. The amount of thermogenic fluids (hydrocarbons and water) necessary for the fluidisation of the host sediments has not been here calculated because of the limited knowledge of the host lithology and nature of the thermogenic fluids involved (e.g. gas-oil ratio, water-hydrocarbon ratio).
7. The mud generated within these Units will escape with a complete extrusive event to seabed surface (F, Figure 5.21). Mud migration within faults is considered a leading mechanism for the formation of mud volcanoes (Milkov, 2000).
8. The release of mud is then followed by a collapse of Unit 2 and 3 generating the observed depression structures (E, Figure 5.21).
9. The mud expelled at the seabed is in some cases eroded by the action of ocean currents. Some mud structures are however preserved.

Although the proposed model can justify the formation of the observed mud volcano-related depression structures it remains unclear the transient nature of these features. The previously documented geometrical analyses (see section 5.3) and the discussed model points firmly that the depressions have been generated by one single expulsion event. If these features are associated with hydrocarbon fluids, this model is potentially in contrast with the expulsion of fluids from source rocks which, in favourable conditions (e.g. constant burial or lack of uplifts events), is characterised by constant expulsion rates. This point requires further analysis.

5.6. Conclusion

The main conclusions are:

- In North-East Falkland Basin a number of depression structures have been described and documented.
- These depression structures are interpreted to be associated with mud volcanisms and release of fluids and sediments from the deeper basin.
- A number of evidences support the case that these mud volcano-related depression structures are associated with migrating hydrocarbons generated in the deeper units of the basin.
- A number of VACs, pipes and gas chimneys support the case of an active petroleum system.
- The distribution of hydrocarbon indicators in NEFB is suggested to be controlled by the structural features of the acoustic basement and not related to the hydraulic properties of the shallow basin.

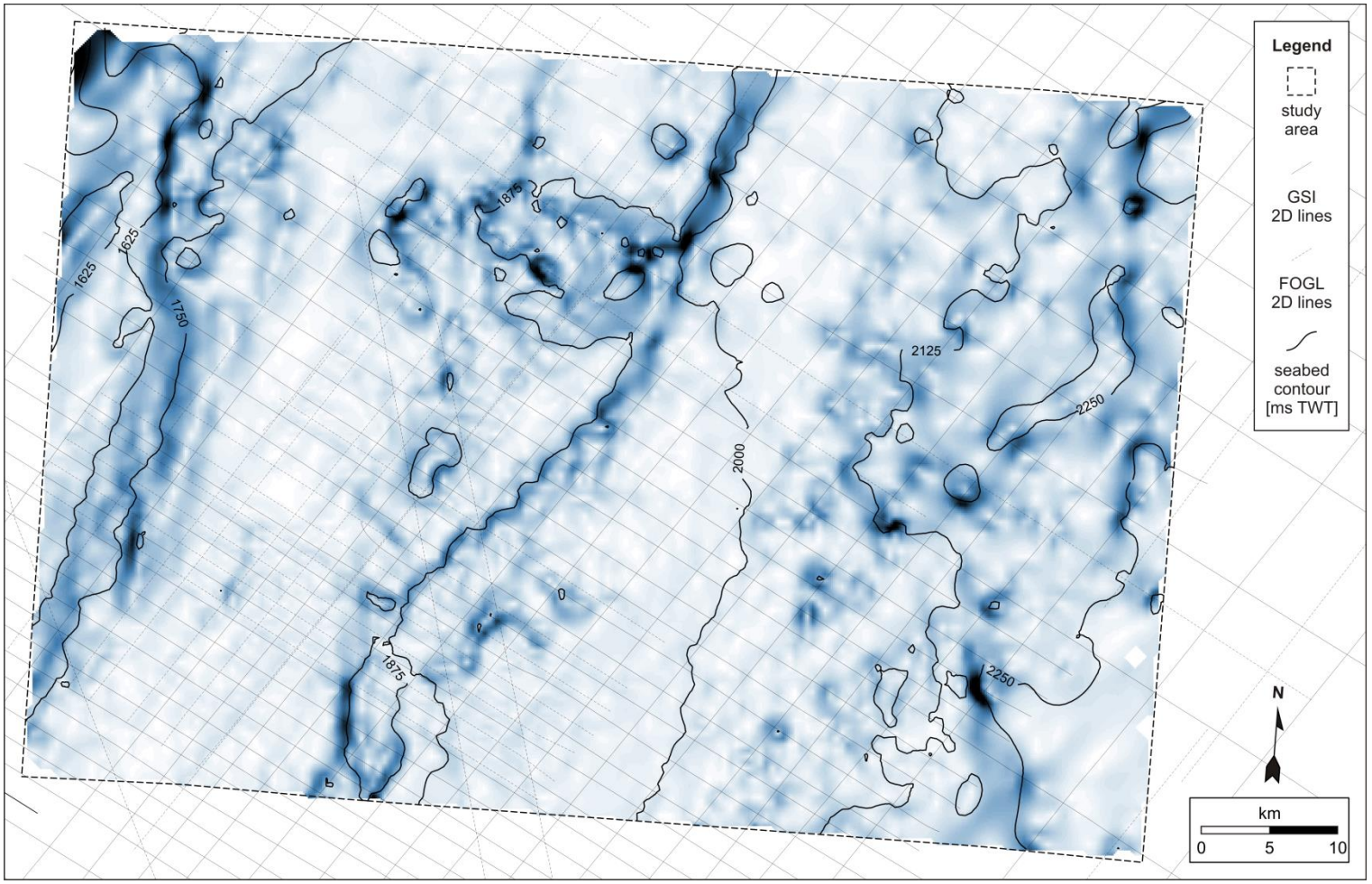

Figure 5.1 Bathymetric map of the study area and position of the 2D seismic lines. Seabed dipping ESE and characterised by irregular surface consisting in NE-SW oriented scarp-like structures.

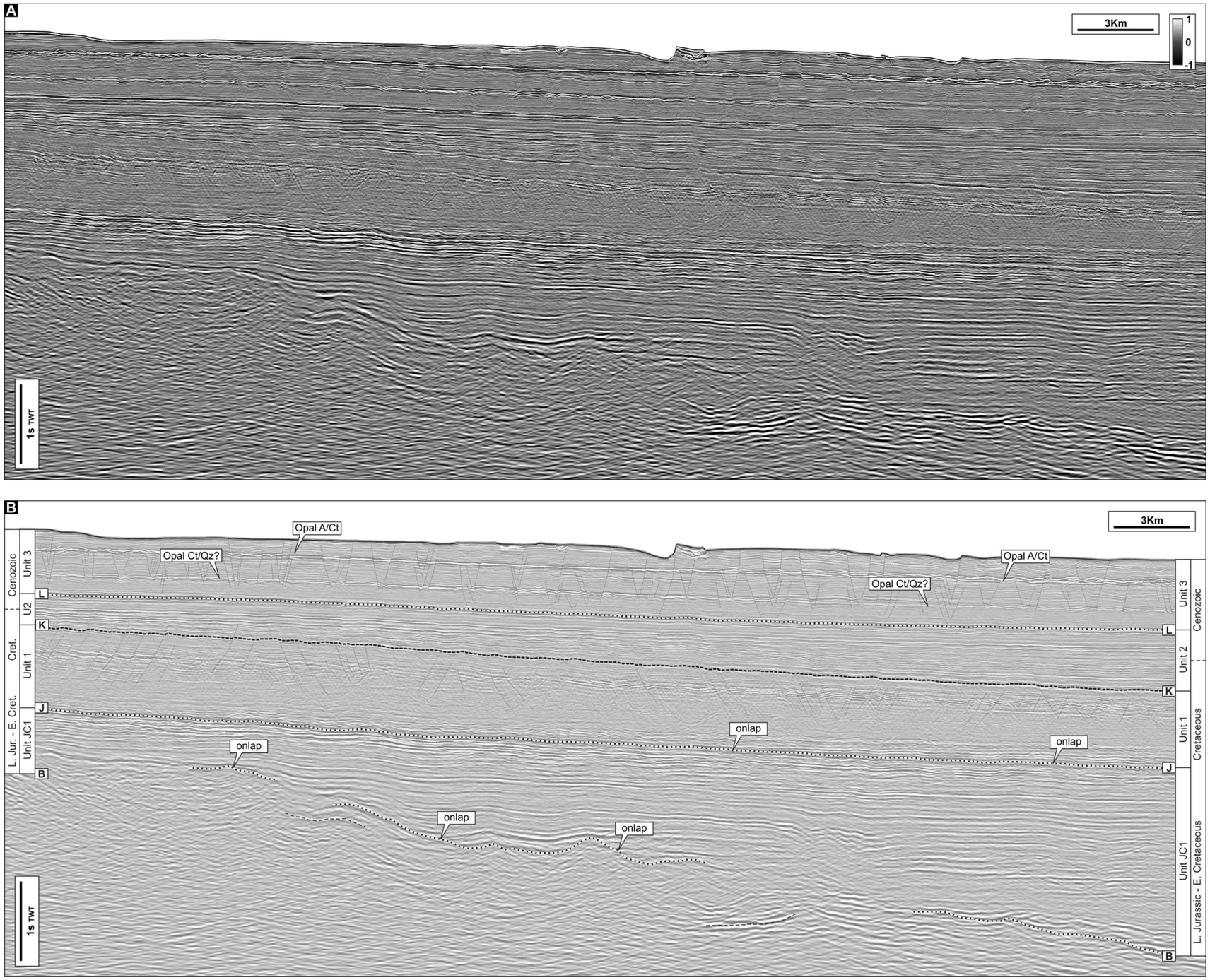

Figure 5.2 Representative 2D seismic line passing across the study area (A). Interpreted seismic line with the interpretation of the acoustic basement (Horizon B) and definition of the Units: onlapping wedge characterised by weak to moderate amplitude highly continuous reflections (Unit JC1), onlapping reflection affected by polygonal faults (Unit 1), onlapping weakly divergent wedge composed of highly continuous reflections (Unit 2), polygonally faulted contourite deposit and Opal A - CT transition and Opal Ct - Quartz (?) (Unit 3). See text. See Chapter 3.3.2 and Figure 3.3 for comparison.

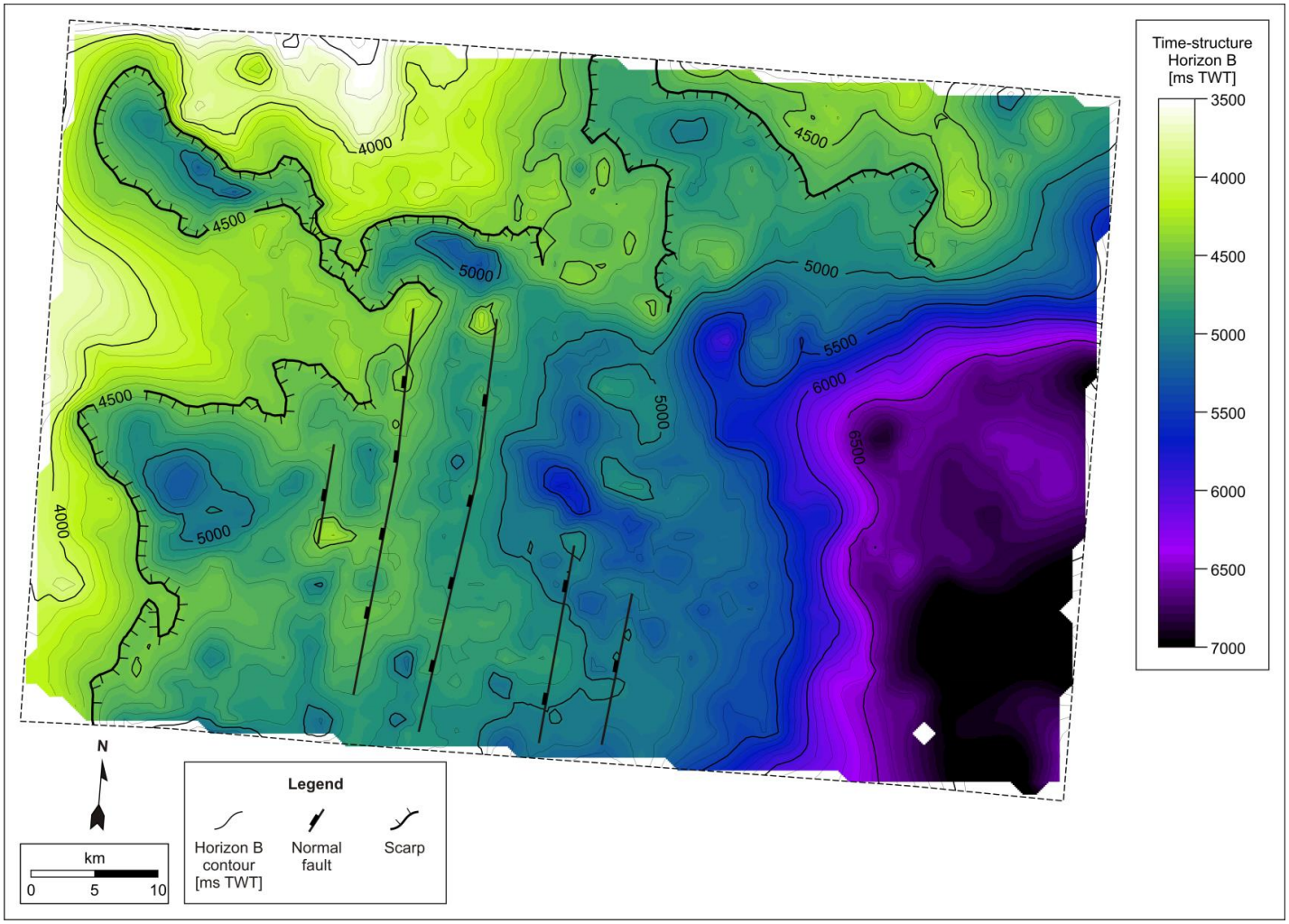

Figure 5.3 Time-structure map of the acoustic basement (Horizon B). Structural features are interpreted on the basis of the few recognised acoustic features on seismic section and on the reconstructed structural trends on time map. ESE dipping acoustic basement characterised by scarp structures at west and normal faults throwing to west. Maximum depth of 7200ms TWT at east.

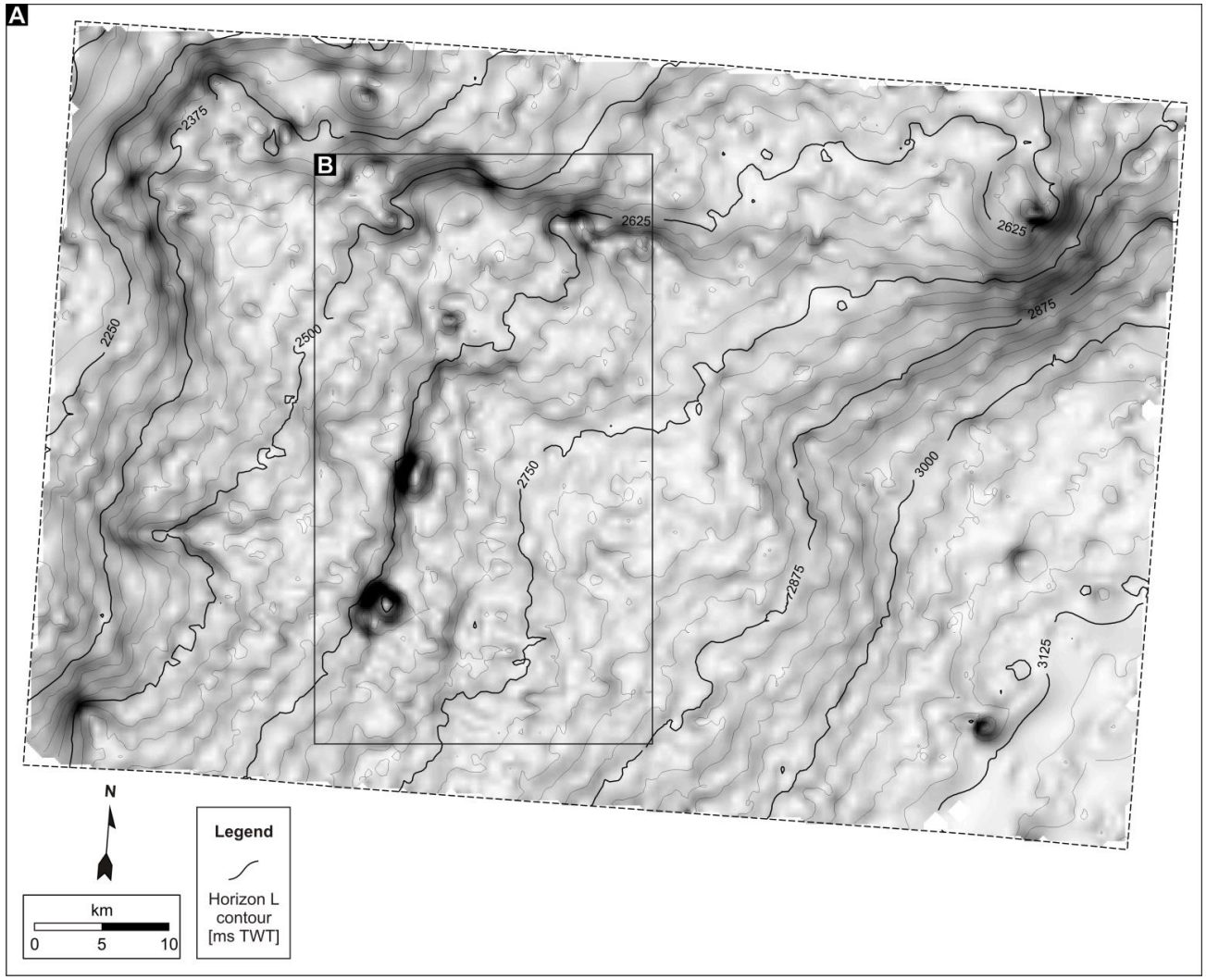

Figure 5.4a Time map of Horizon L. Horizon L characterised by eastward dipping geometry. Imprint from the underlying interpreted acoustic basement is clearly observed (Figure 5.3). Selection used for 2D line location and depression description (B, Figure 5.4b).

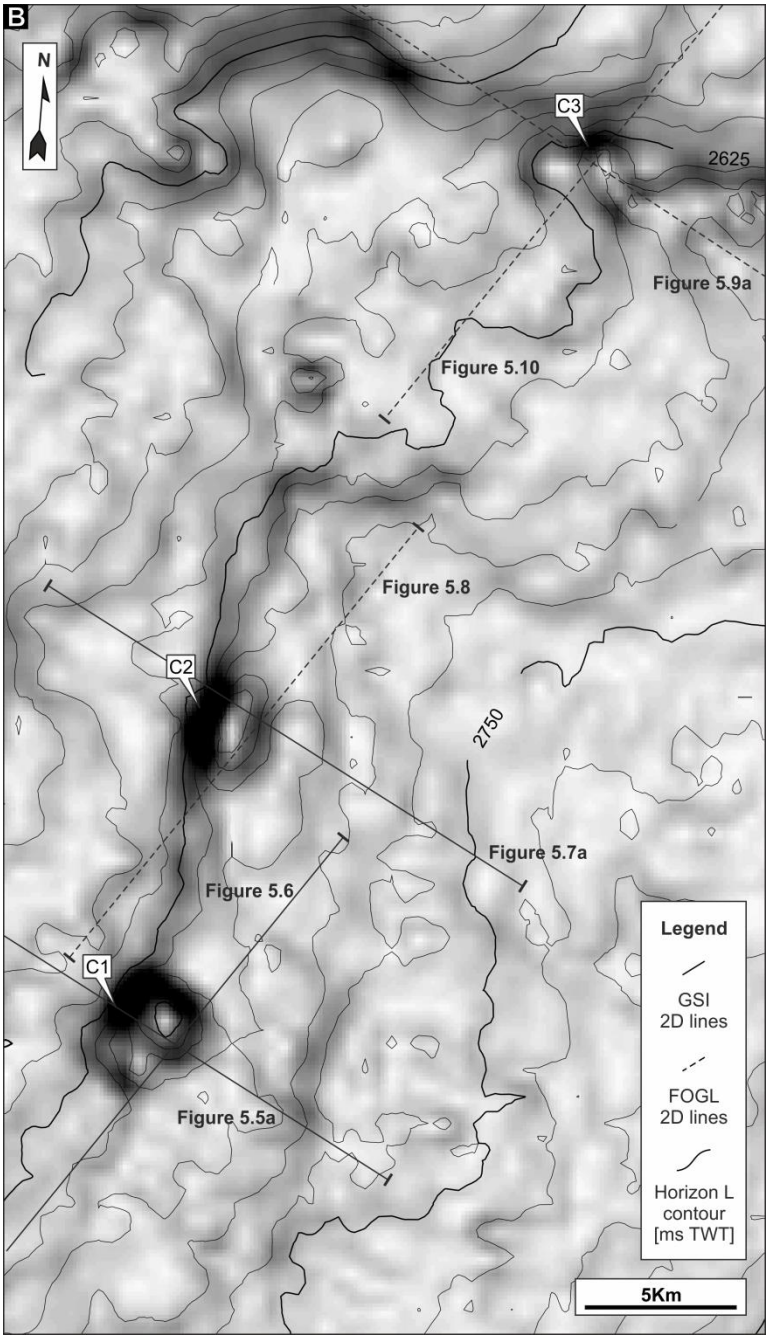

Figure 5.4b Close-up of Horizon L showing the depression structures (C1, C2 and C3) and position of the 2D seismic lines used for description of the depression structures (see Figure 5.4a for location). C1 represent a well-defined sub-circular depression with an average diameter of 3km . C2 and C3 are more elliptical in shape and oriented approximately NE-SW and NW-SW, respectively.

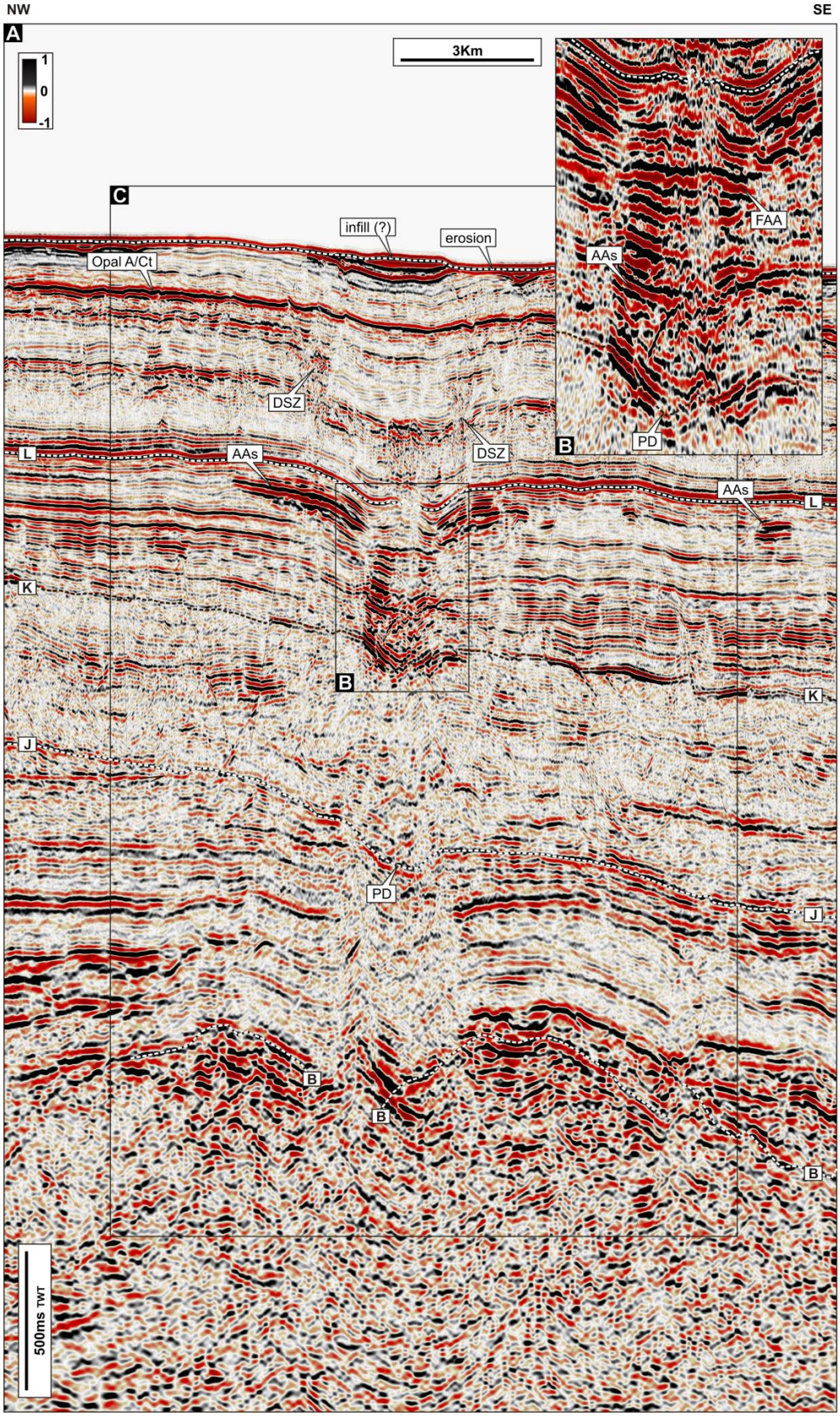

Figure 5.5a 2D seismic section crossing depression structure C1 (see Figure 5.4b for location). The depression structure is clearly recognisable between Horizon K and Opal A-CT. Upward concave reflections at Horizons k, J, B interpreted as push-down (PD, see text). Amplitude anomalies (AAs), disturbed signal zones (DSZs) within the depression structure.

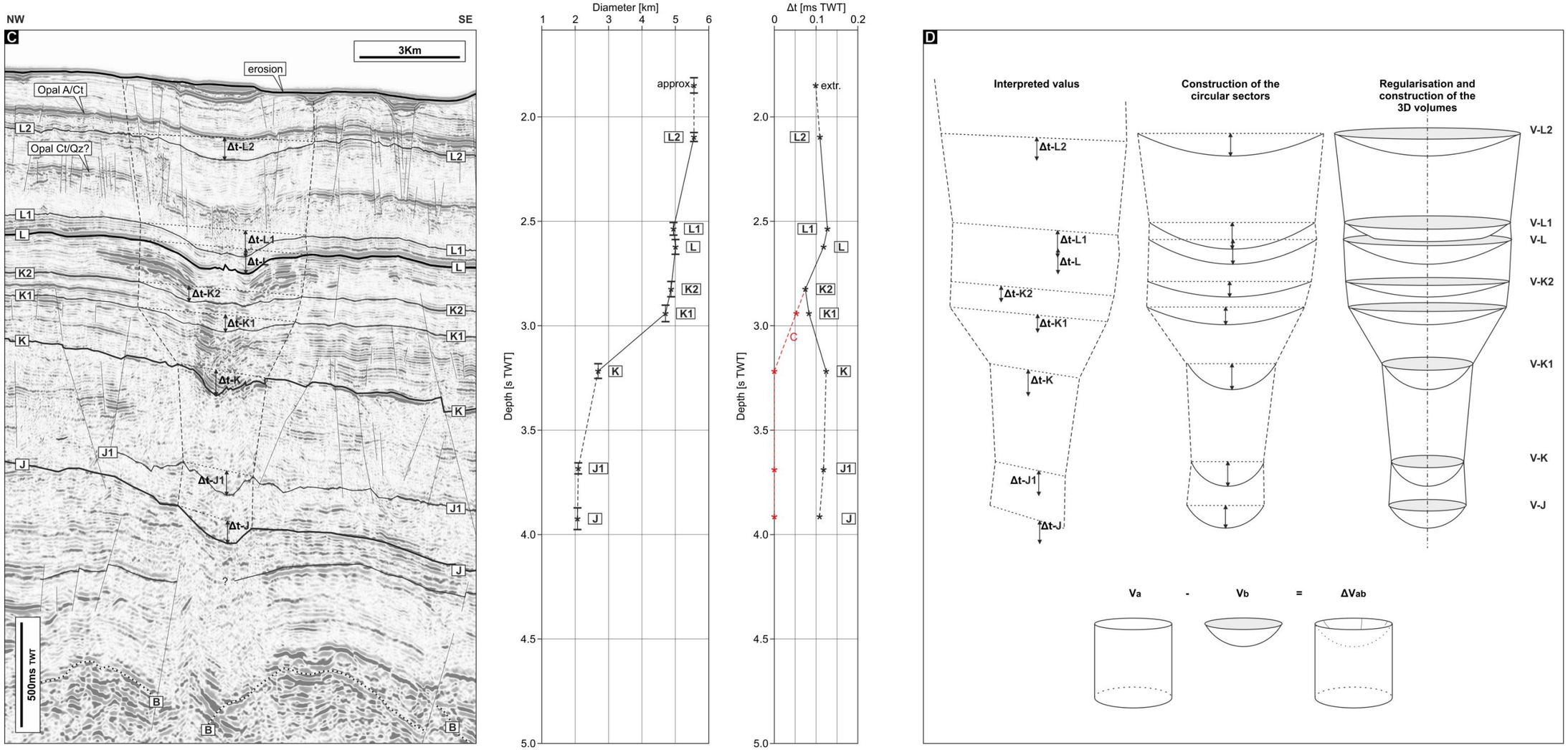

Figure 5.5b Close-up of the depression structure C1 (see Figure 5.4b for location and Figure 5.5a for position), geometrical analysis and volume loss approximation work flow (D). A total of 6 horizons (9 with interpretational uncertainties) have been used to define the geometry of C1. Hinge points are defined as interpreted points of maximum curvature of the horizons associated with depression structures. Chords (dotted lines, C) constructed between two hinge points related to the same horizons and negative vertical relief values (e.g. Δt-K) based on calculation of the maximum distance (in s TWT) between the chord and the associated horizon (see text). Cross-plots of Diameter (in km) Vs depth (s TWT) and Δt (s TWT) Vs depth (s TWT) of the measured values showing tapering of C1 from Horizon L2 and Horizon K. Interpreted values at Horizon K, J1 and J are potentially associated with push down effect (dashed lines). A qualitative removal of push-down effects from Horizon K to J may suggest a corrected linear trend of the decrease of the negative vertical relief values (c, red dashed line) and a subsequent location of the base of the depression structure (i.e. shallowest flat horizon beneath the depression structure) at Horizon K. Chord and negative vertical relief values are used to calculate circular sectors as an approximation of the shape of the depressed reflections. The sectors are extended to simplified 3D volume (spherical caps). The difference between spherical caps provides the approximate volume change (ΔV, loss or fill) associated with the different sectors of the depression structures (D, see text).

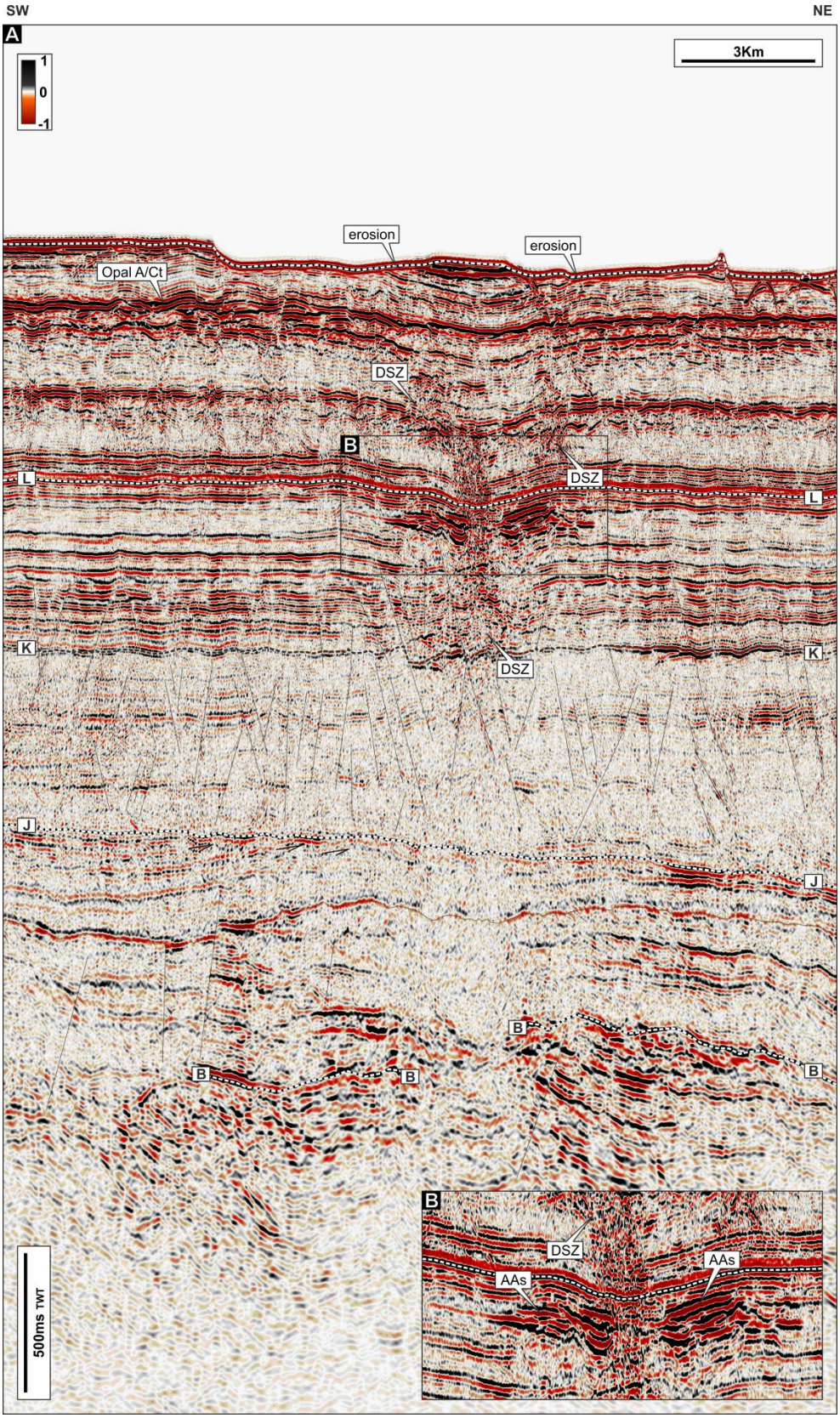

Figure 5.62D seismic section crossing depression structure C1 (see Figure 5.4b for location). Amplitude anomalies (AAs) are present below Horizon L (B). Horizon K is flat in this section. Truncated reflections at the seabed are indicative of erosion. Disturbed signal zones (DSZs) are distributed in both within and at the margins of the depression structure.

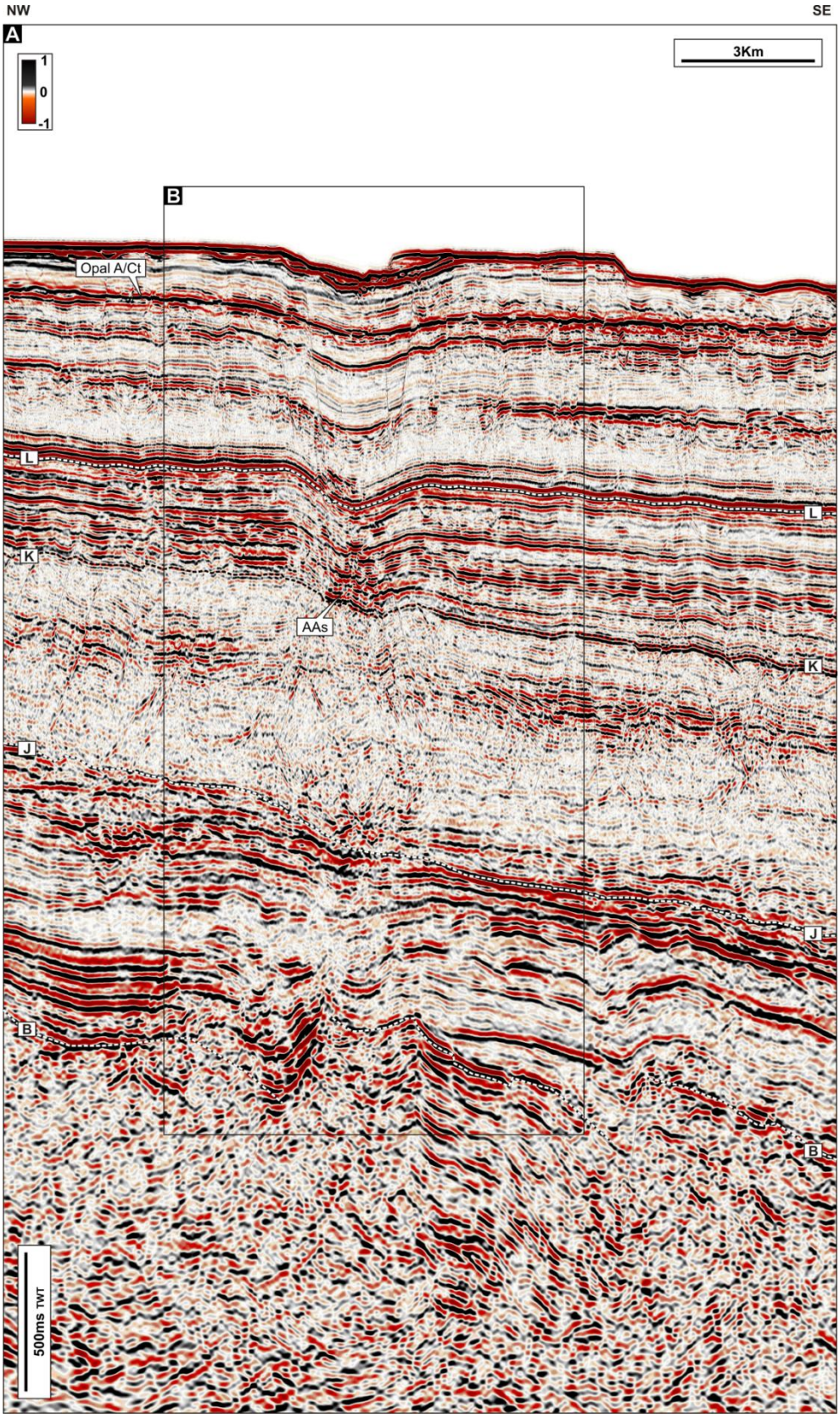

Figure 5.7a 2D seismic section crossing depression structure C2 (see Figure 5.4b for location). Depression structure defined by parallel upward concave-shaped reflections between Horizons K and the seabed. Amplitude anomalies (AAs) present above Horizon K. Opal A-CT cross cuts the reflectivity pattern close to the seabed.

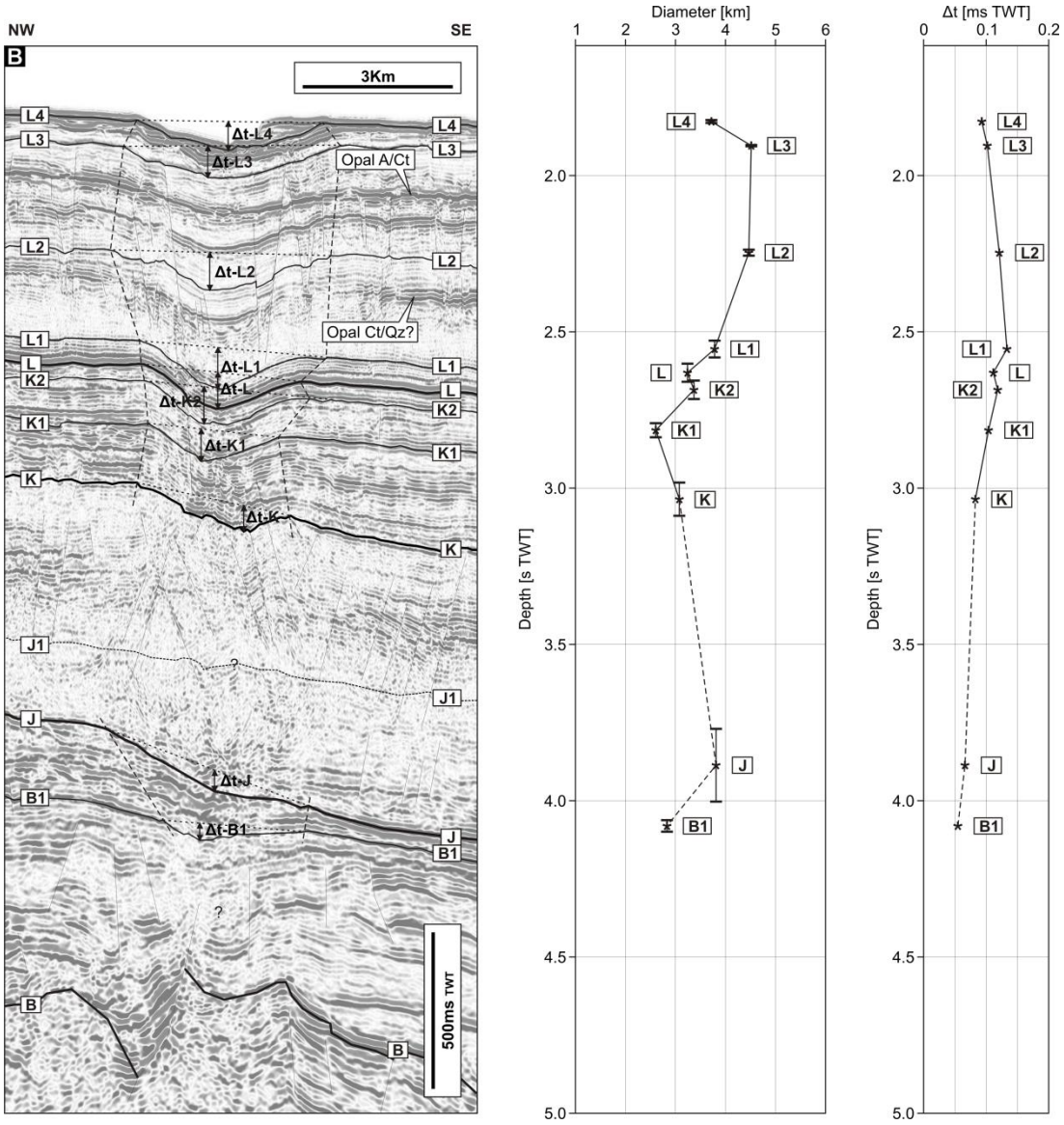

Figure 5.7b Close-up of the depression structure C2 (see Figure 5.4b for location) and geometrical analysis. A total of 8 horizons (10) have been used to measure the geometry of C2.

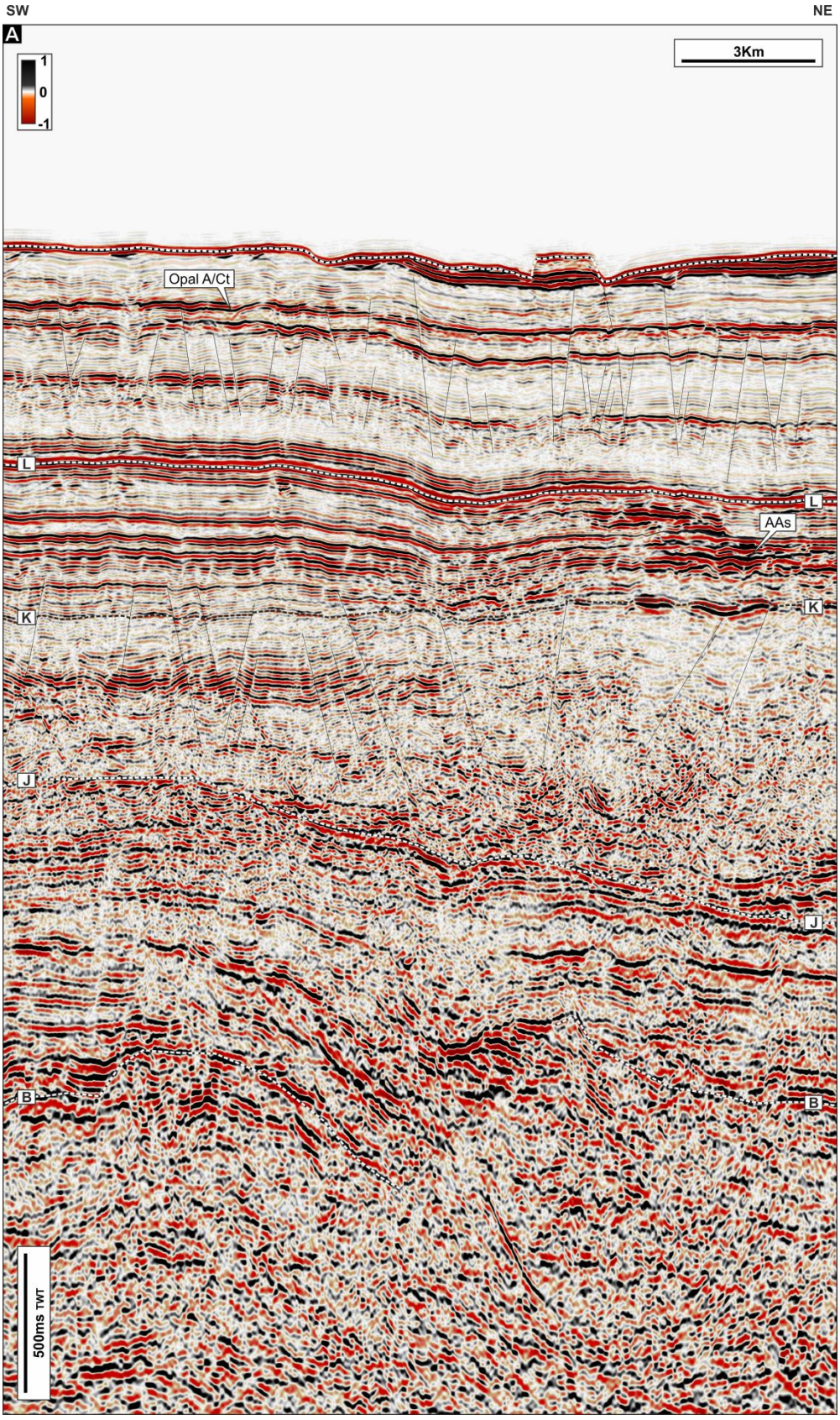

Figure 5.8 2D seismic section crossing depression structure C2 (see Figure 5.4b for location). The depression is mostly recognisable at Horizon L and terminate right above Horizon K. C2 is not associated with AAs however some AAs are observed in the nerby regions between Horizons K and L.

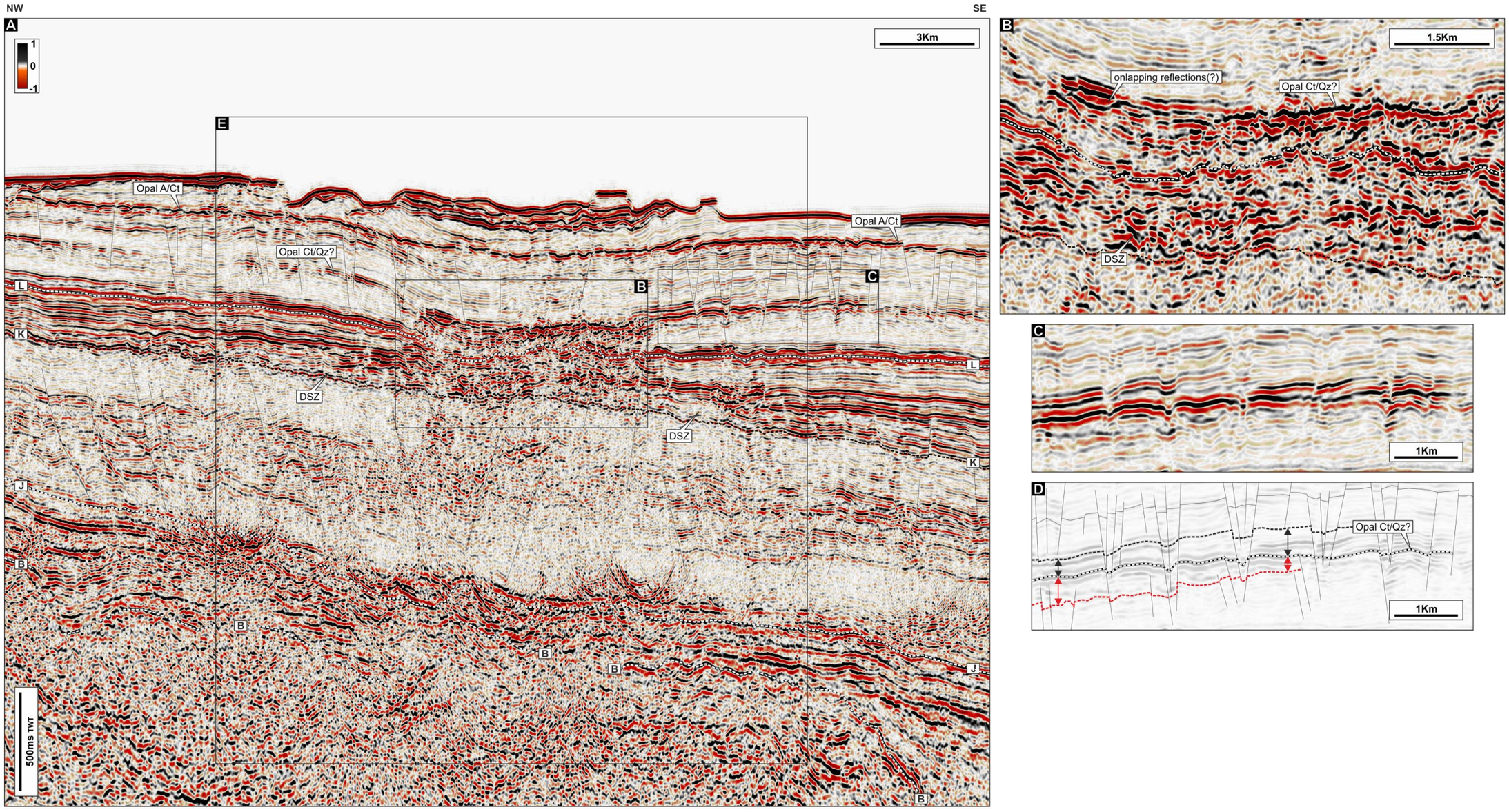

Figure 5.9a 2D seismic section crossing depression structure C3 (see Figure 5.4b for location). Depression structure characterised by upward-concave reflections between Horizon L and the seabed. Strong signal disturbance region between Horizon K and L within the depression. Disturbed signal zones (DSZ) are present in proximity of Horizon K and laterally distributed (A). Onlapping reflections above Horizon L are associated with Opal CT-Quartz (B). Opal CT-Quartz characterised by discordant reflection respect to the reflectivity pattern (see black and red guide arrows, C-D).

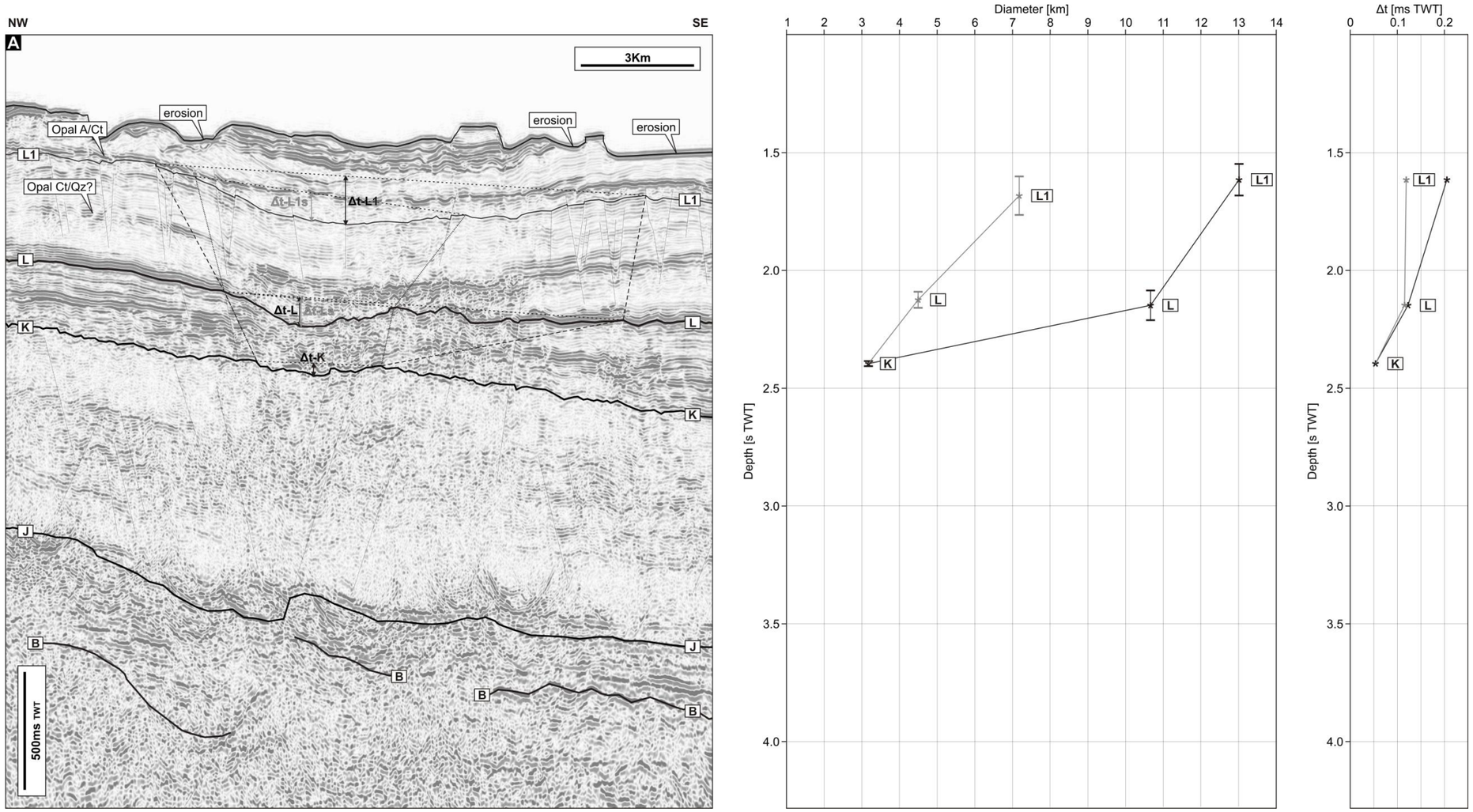

Figure 5.9b Close-up of the depression structure C3 (see Figure 5.4b for location) and geometrical analysis. The analysis is here based on two potential interpretations based on 3 horizons. The first analysis (black lines) is consistent with an interpretation where C3 is associated with a large depressed region. The second analysis (grey lines) considers a thinning of Unit 2 and is consistent with a smaller depression.

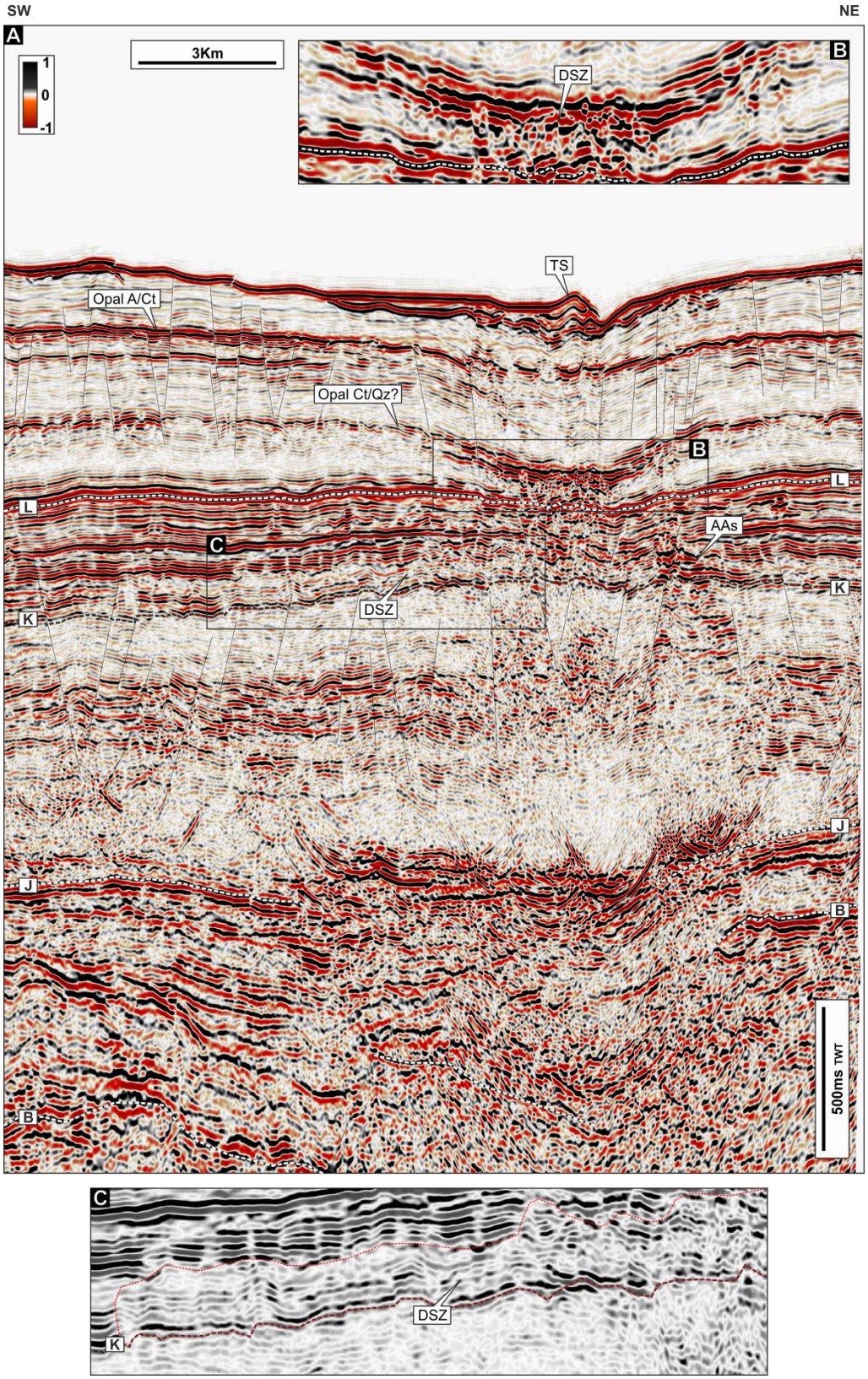

Figure 5.10 2D seismic section crossing depression structure C3 (see Figure 5.4b for location). Depression structure characterised by upward-concave reflections between Horizon L and the seabed. Strong signal disturbance region between Horizon K and L. Triangular structure (TS) at the seabed may indicative of mud expulsion (A). Disturbed signal zone (DSZ) distributed in proximity of Horizon L (B) and K (C).

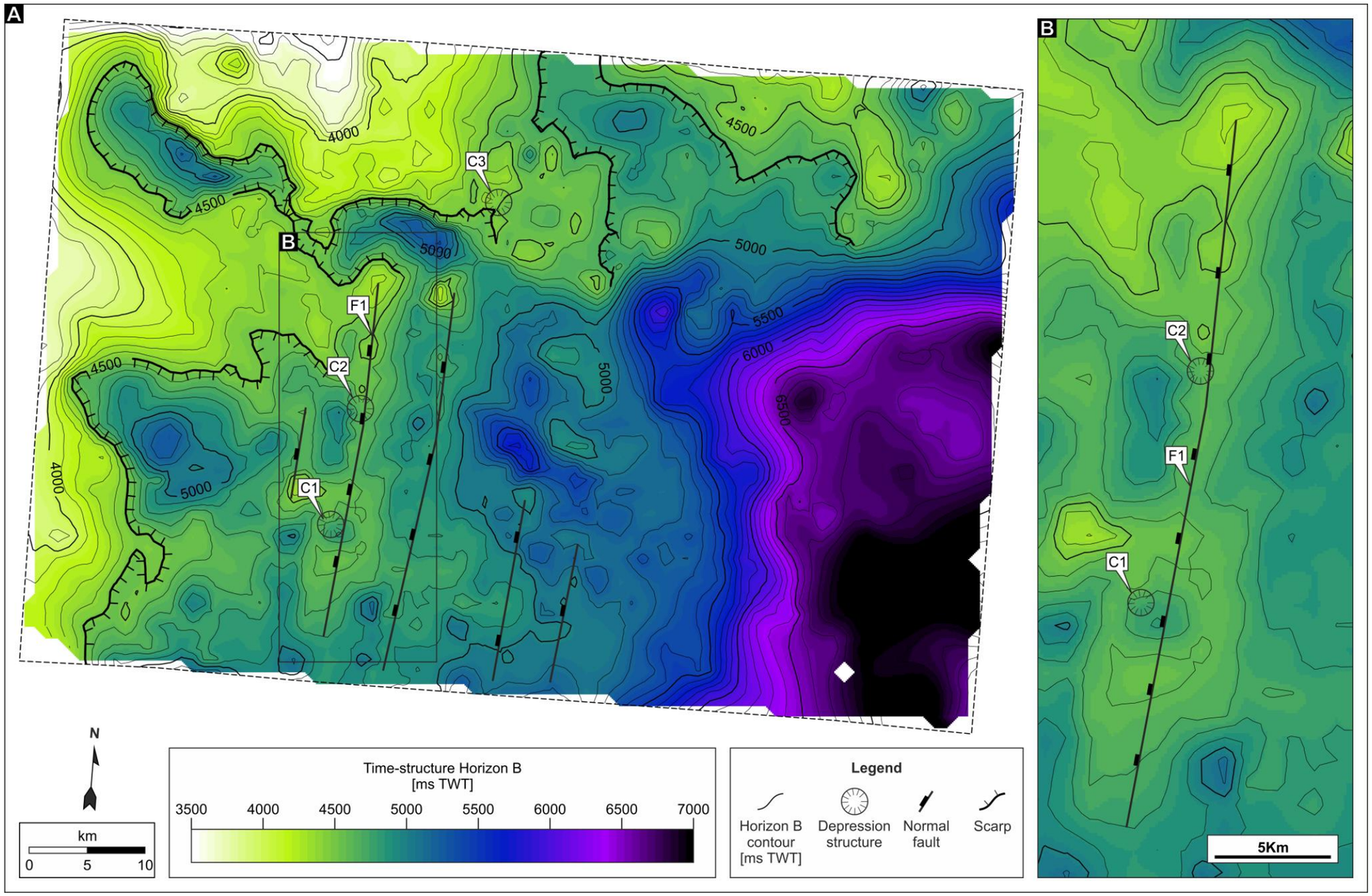

Figure 5.11 Time-structure map of the acoustic basement (Horizon B, see Figure 5.3) and position of the depression structures. The three depression structures interpreted on seismic data are primarily located above prominent basement related structural highs. C1 and C2 are located above the footwall crest of fault F1 (close-up, B). C3 is located above a scarp structures immediately at NE of fault F1.

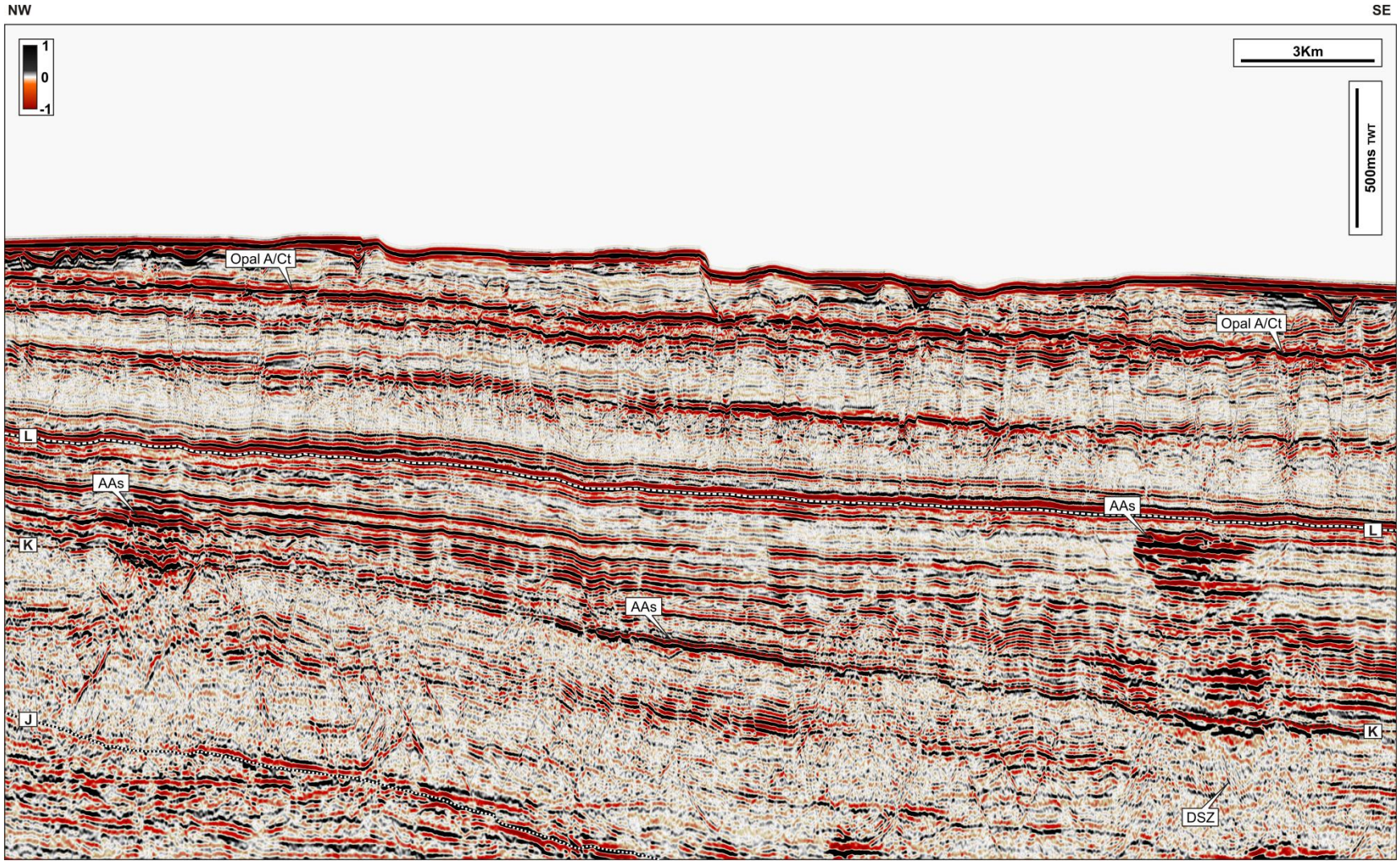

Figure 5.12 2D seismic section depicting two distinct groups of stacked amplitude anomalies. The anomalies (AAs) are stacked vertically in columns with cross sectional length of 1.5-2.0km . Note the sharp amplitude cut offs at the margin of the individual anomalies. Disturbed signal zone are observed (DSZ).

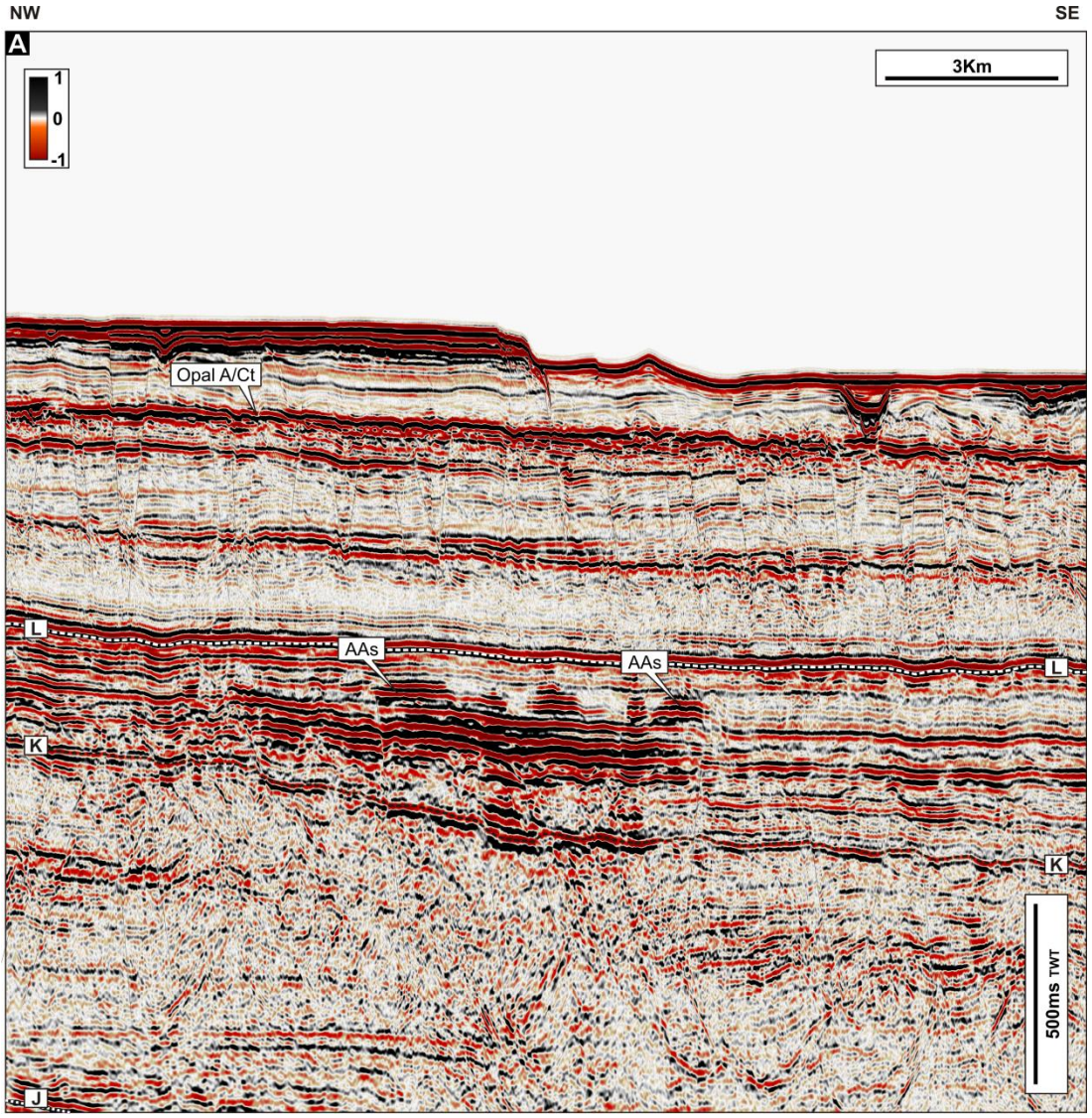

Figure 5.13 2D seismic section cross cutting a number of stacked amplitude anomalies. Individual anomalies (AAs) staked vertically in small piles yield intermittent amplifications of the reflectivity pattern. Cross-sectional length of individual amplitude anomalies over >6km .

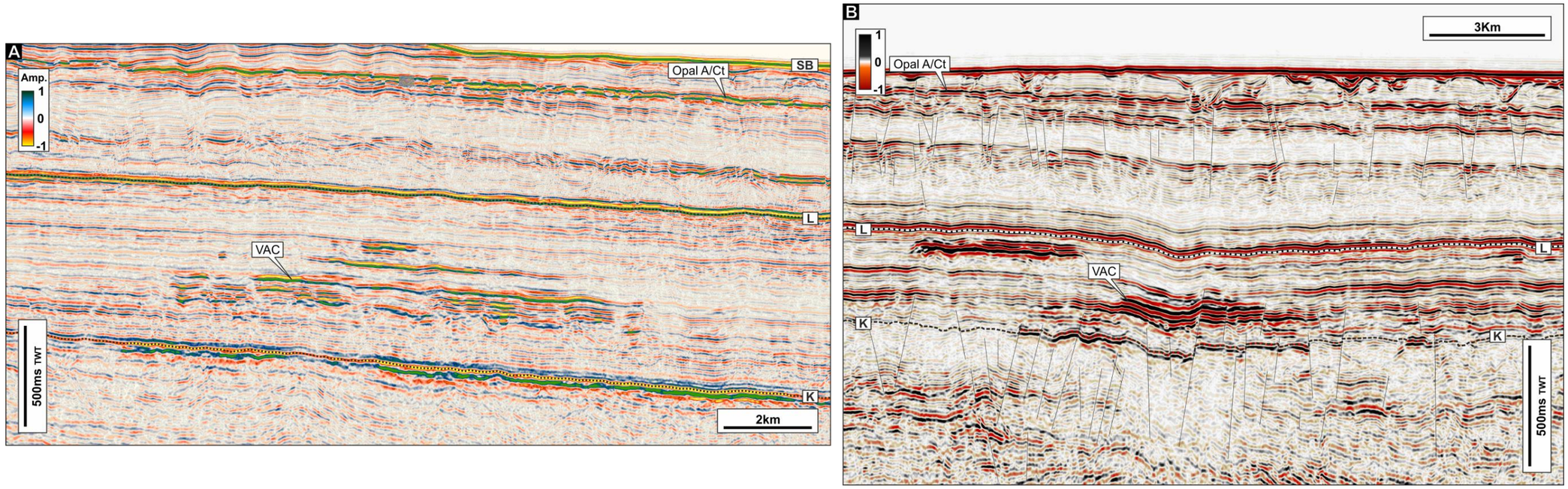

Figure 5.14 2D seismic sections cross cutting two VACs. VAC encountered in east Falkland Basin (EFB, Figure 3.4) composed of a number of stacked amplitude anomalies distributed vertically from Horizon K. Outer shape of the VAC can be inscribed in a triangle with base of ~18km and height of 600ms TWT (A). VAC interpreted in North east Falkland Basin (NEFB) composed of few stacked amplitude anomalies. The outer shape is sub-rectangular and distorted by the geometry of the reflectivity pattern and segmented by a number of normal faults propagating from the underline unit. The VAC is consistent with a cross sectional length of approximately 7km and height of 300ms TWT (B).

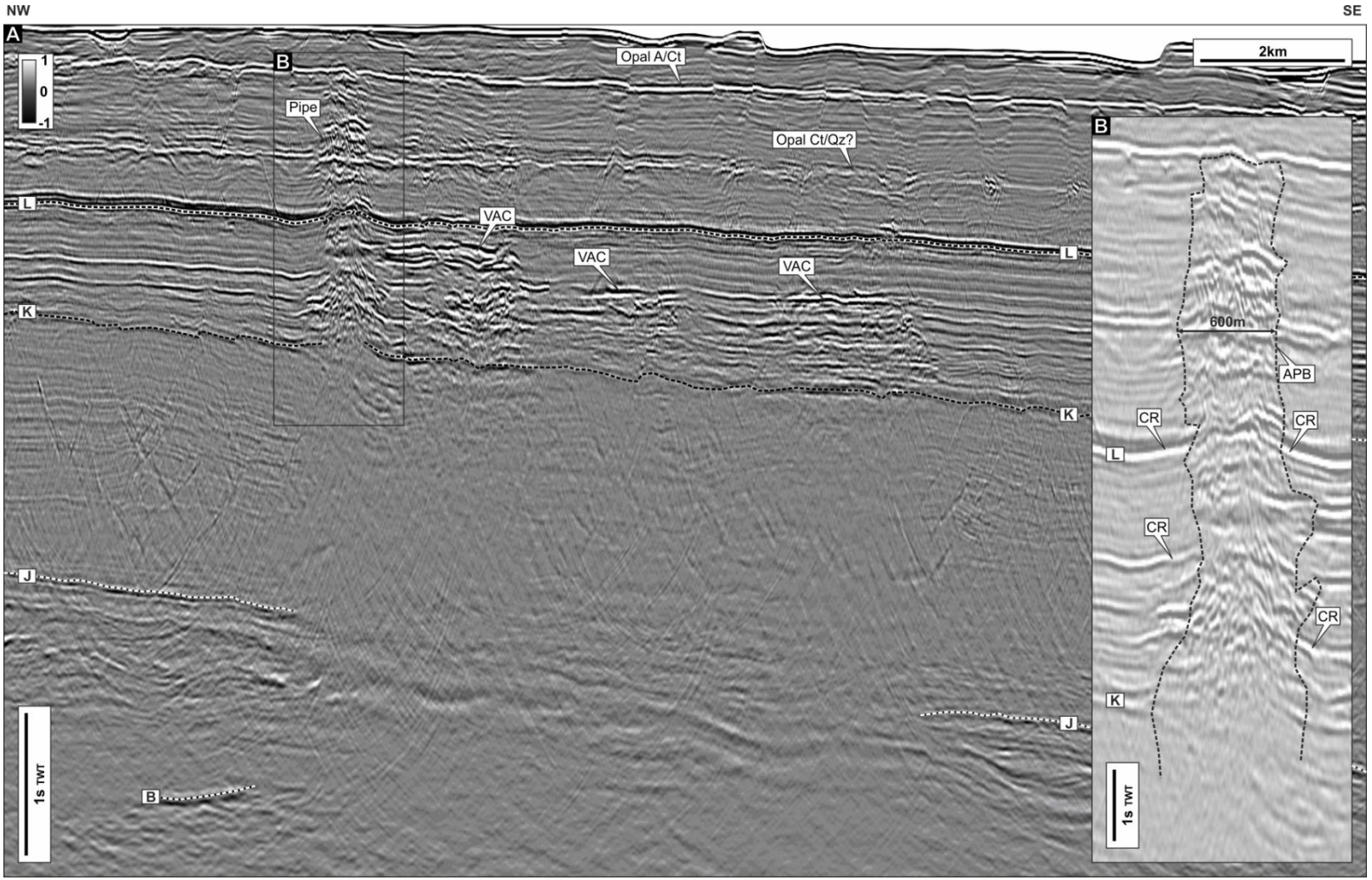

Figure 5.152D seismic sections cross cutting a pipe and a number of VACs. The pipe stands out as a columnar region of vertical disturbance. Pipe and VACs are primarily visible between Horizon K and L. The pipe, based on an interpreted approximate pipe boundary (APB), is consistent with a cross sectional width (or diameter) of 600m. The pipe deforms the background reflectivity curving upward a number of reflections (CR) (B).

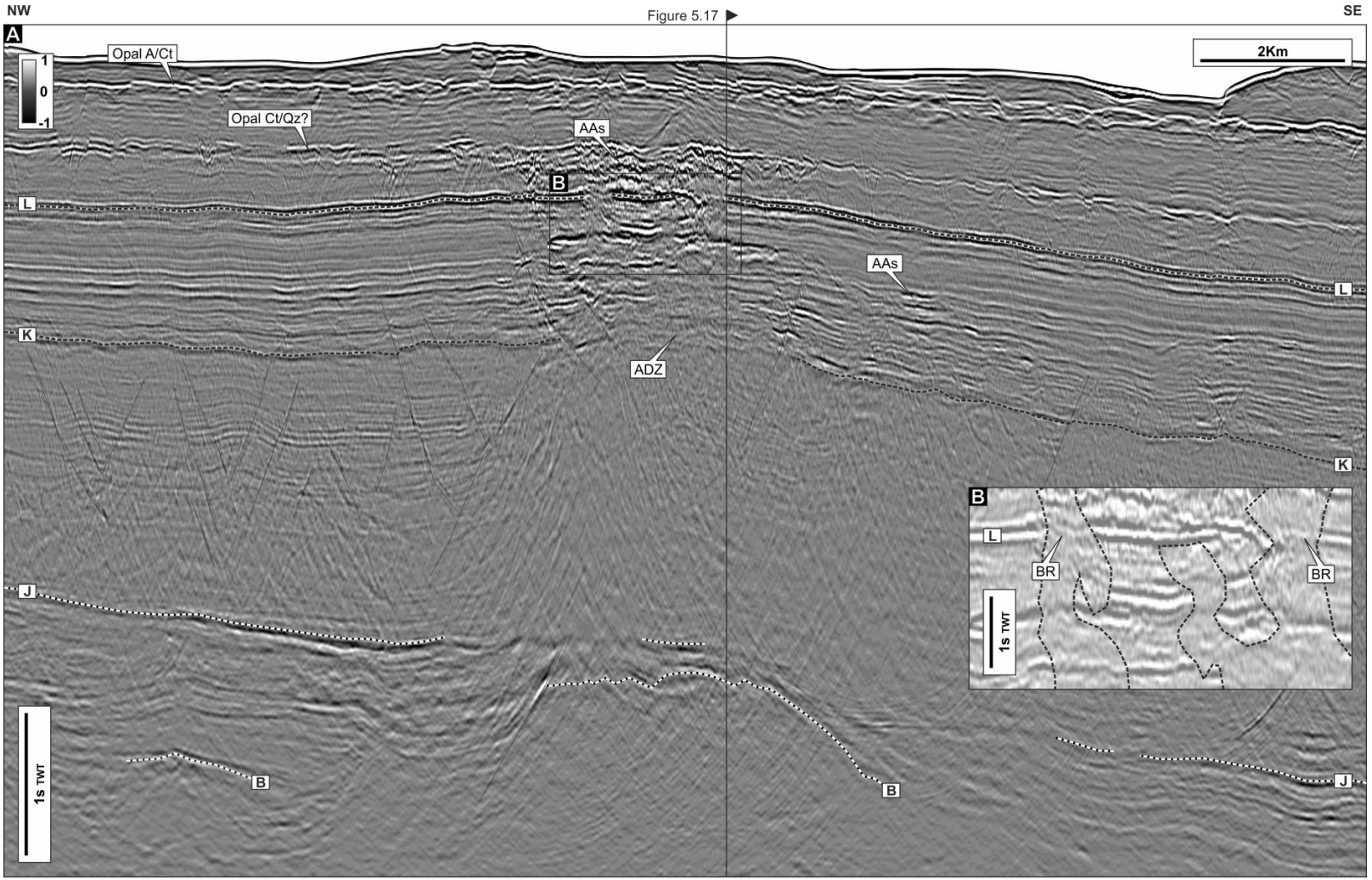

Figure 5.162D seismic sections depicting a gas chimney (see also Figure 5.17). The gas chimney is located in the centre of the section above a basement structural high. The seismic feature is composed of a number of amplitude anomalies (AAs) distributed around a number of anomaly dim zone (ADZ). The interpreted gas chimney is also associated with normal faults and with broken reflections as evidence by intermittent reflectivity of Horizon L (B).

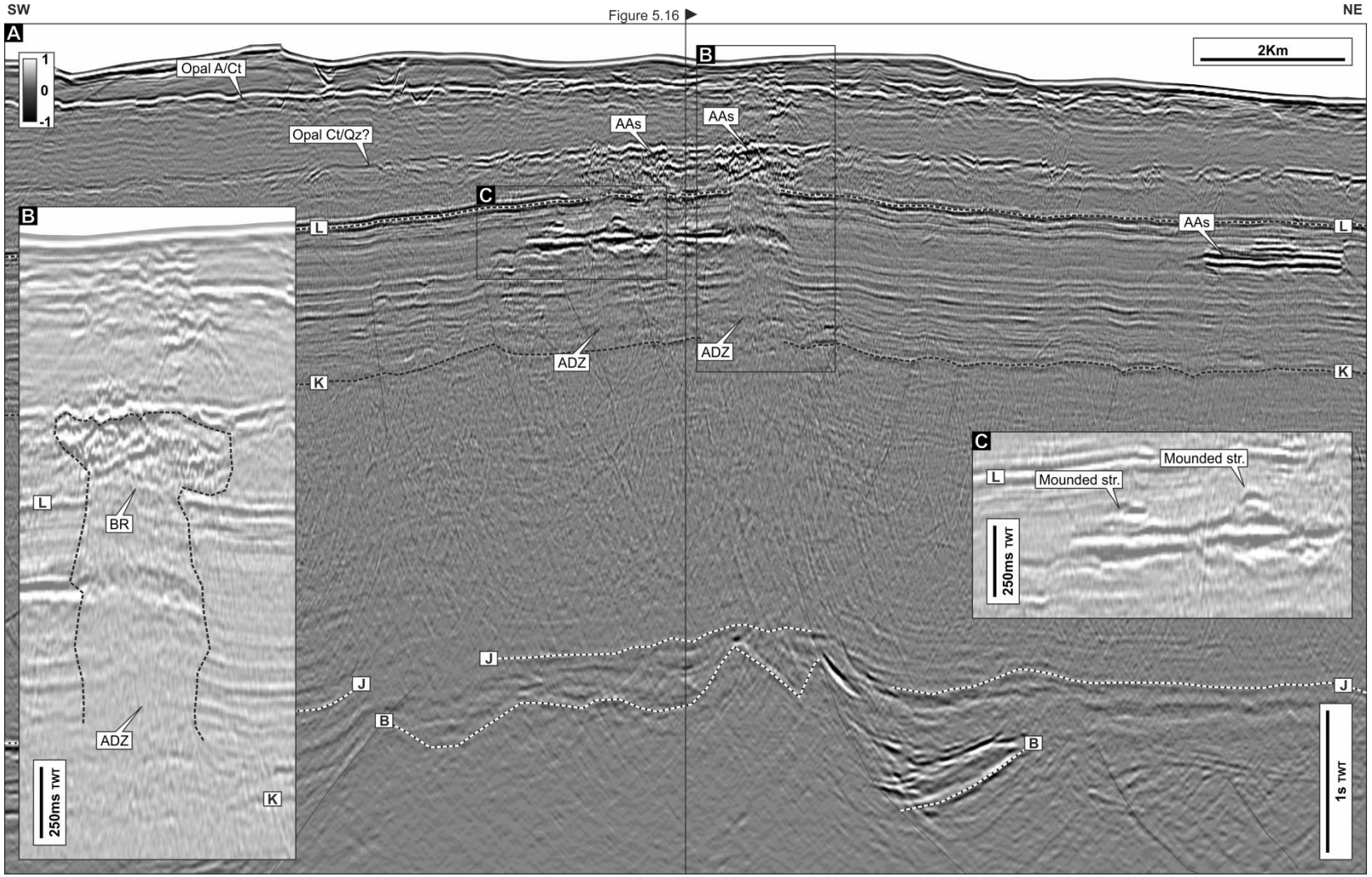

Figure 5.17 2D seismic sections depicting a gas chimney (see also Figure 5.16). The gas chimney is located above a structural high. It is composed of amplitude anomalies and amplitude dim zones (ADZ). The amplitude anomalies reach the interpreted Opal CT-Quartz transition. In a number of points the gas chimney is associated with broken reflections (Horizon L, B). The amplitude anomalies are staked in small mounded shapes (C).

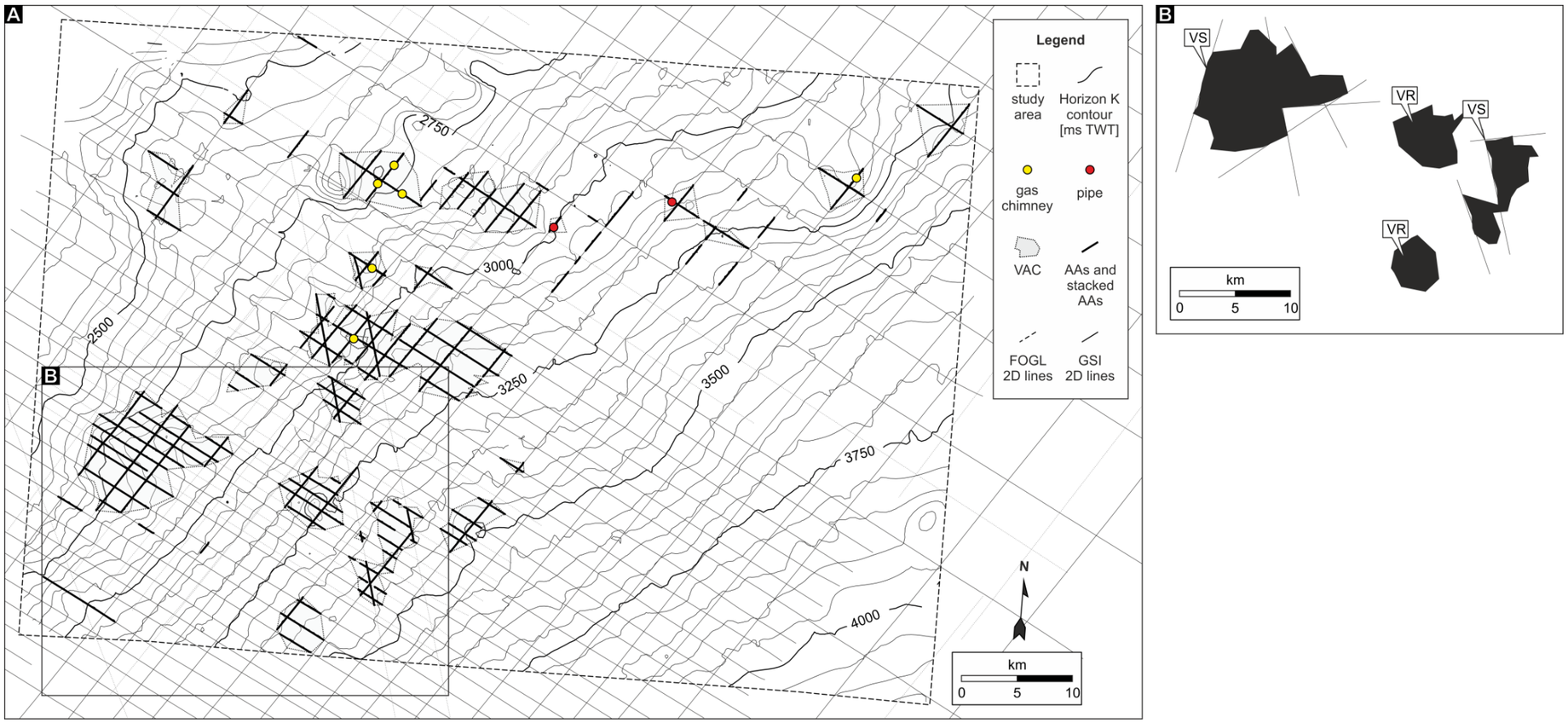

Figure 5.18 Distribution maps of amplitude anomalies, VACs, gas chimneys, pipes and contour of Horizon K. Amplitude anomalies are drawn projecting vertically their lateral extension as observed on 2D cross section. Adjacent stacked AAs define the boundary of the VACs. Approximately 20 VACs have been defined. VACs may present rounded shapes (VR) or angular shape characterised by sharp margins (VS) (B).

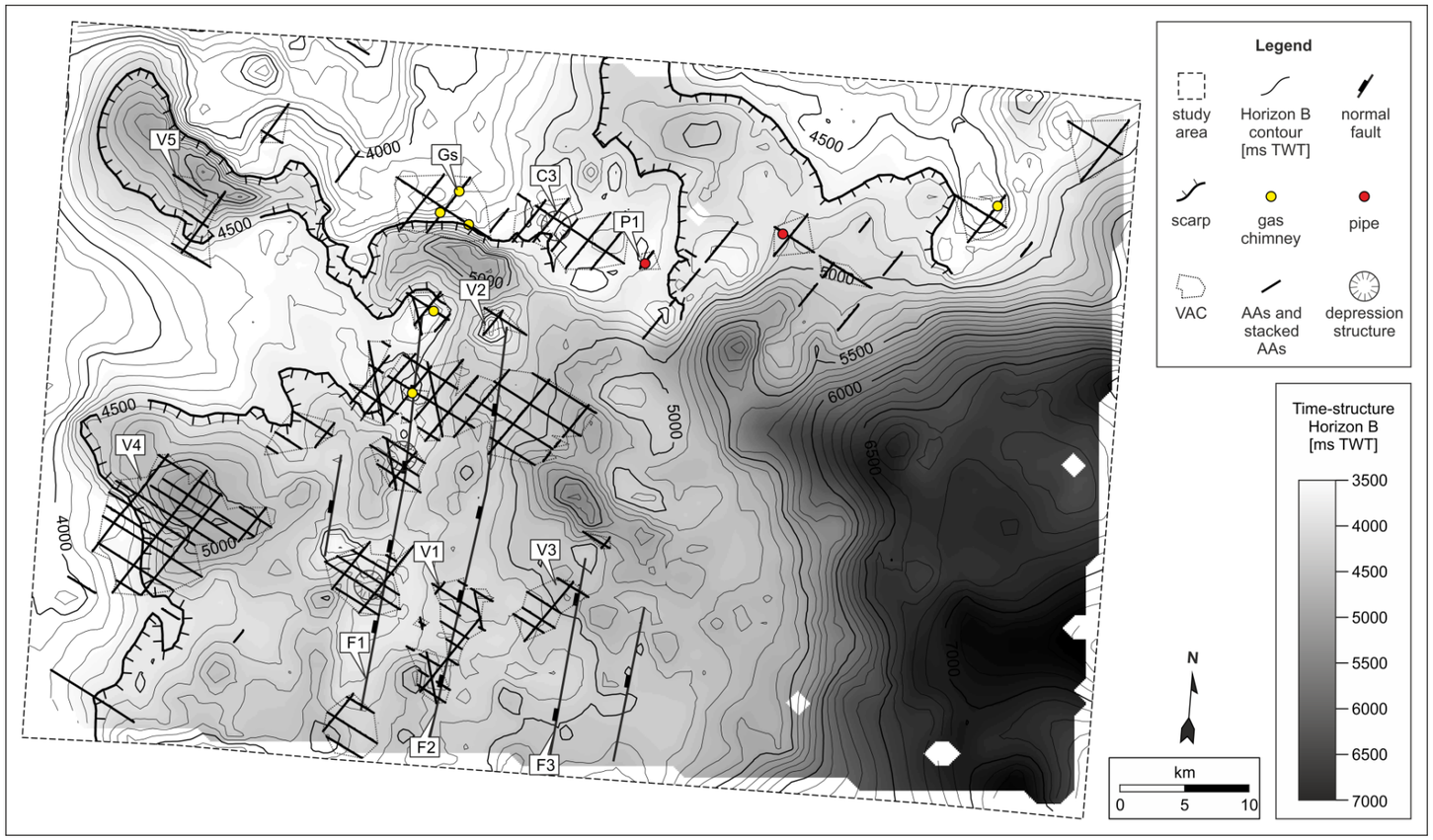

Figure 5.19 Distribution maps of depression structures, amplitude anomalies, VACs, gas chimneys, pipes and time–structure map of the acoustic basement (Horizon B). The map puts in evidence the strong relationship between the distribution of depression structures, amplitude anomalies, VACs, gas chimneys, pipes with the interpreted features of the basement. A number of depression structure, VACs and gas chimneys are located above the normal faults F1, F2 and F3. A number of gas chimneys (Gs), depression C3 and pipe P1 are located above a scarp-like structure interpreted on Horizon B. VACs V4 and V5 are located above local structural low, characterised by downward curved shape. Isolated VACs and gas chimney at NE corner of the map.

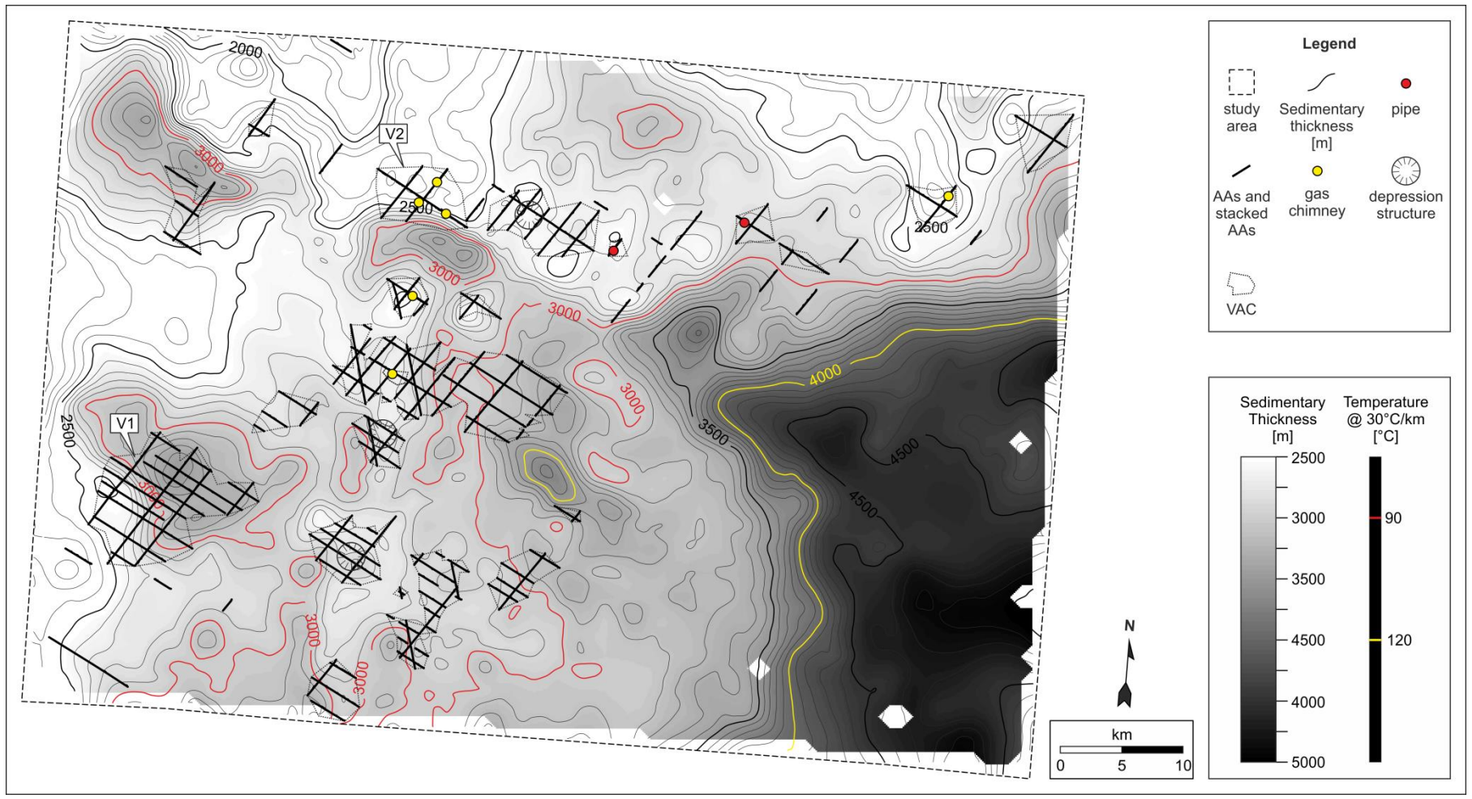

Figure 5.20 Potential maturation map and distribution of the documented depression structures, VACs, gas chimneys, and pipes. Sedimentary thickness based on an average velocity of 1991m/s. Maximum sedimentary thickenss of 4900m. Geothermal gradient applied of 30°C/km . Maximum potential temperature reached in the basin of 147°C. Definition of potential oil maturation window and gas generation window at 90°C and 120°C, respectively. Potential distribution of oil-mature source rock in the south-east quadrant of the study area. Patchy distribution of potential oil-mature source rock in the north and west regions of the map. Potential gas-mature source rock limited in the south-east quadrant of the study area. VACs above oil-mature source rock are observed (e.g. V1). In most of the case the fluid related seismic feature are located above immature source rock (e.g. V2). The documented fluid related seismic features are not observed above gas-mature source rock.

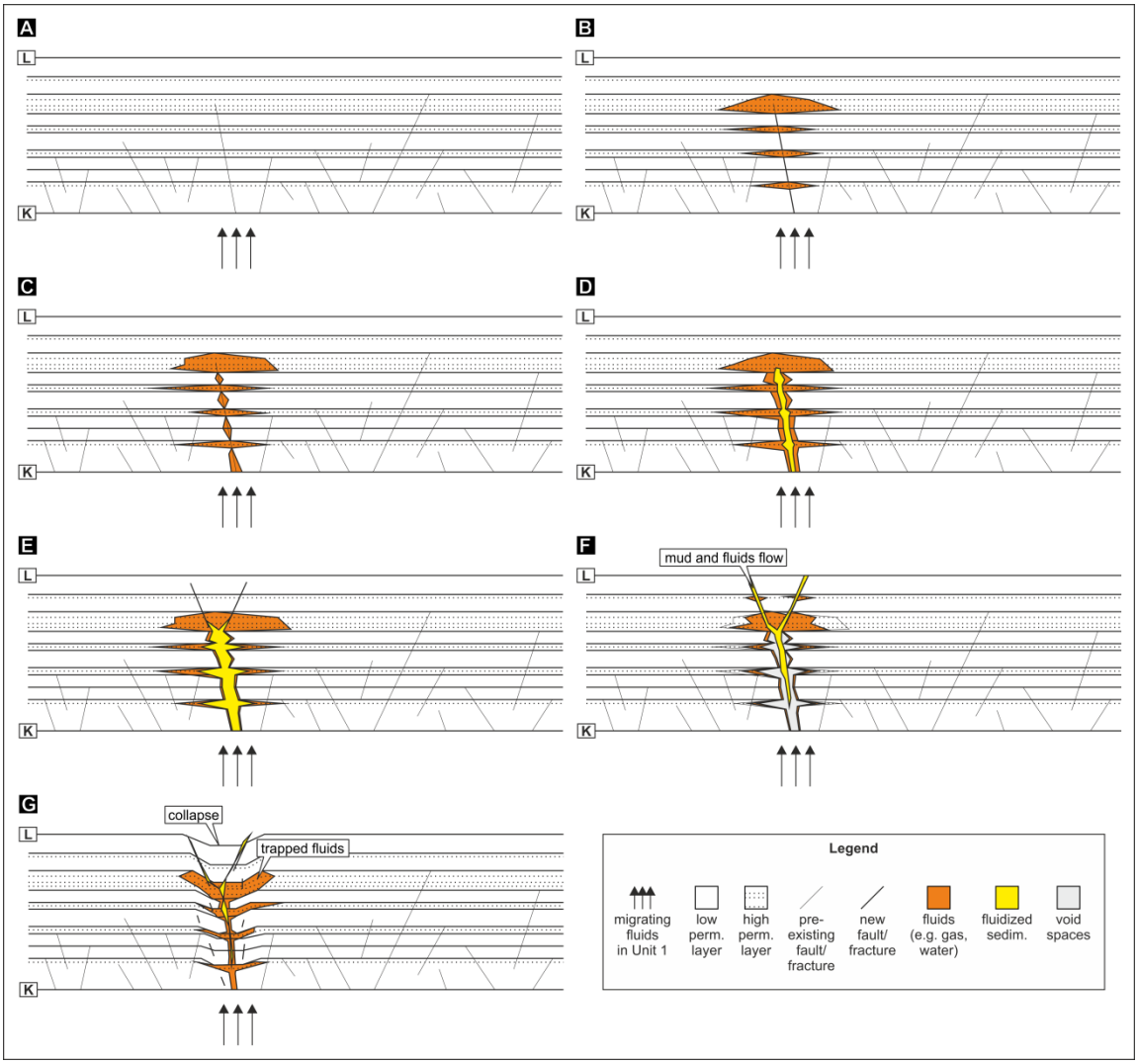

Figure 5.21 Conceptual migration model for the formation of mud volcano-related depression structures in NEFB. A given amount of thermogenic fluids hits Horizon K (A). Fluids start to invade Unit 2 migrating vertically across pre-existing faults (e.g. VAC formation; see Chapter 3, Figure 3.14) (B-C). Once the gas reaches a given flow rate or pressure sediments start to be mobilised and a number of chambers will form (D-E). Once the mud is formed and the pressure rise the mud is expelled (F). The expelled material will leave void spaces which are subsequently reduced by the collapsing of the overburden (G).

6. Discussion

6.1. Introduction

6.1.1. Introduction

A number of topics, examples and case histories related to the seismic evidence of hydrocarbon migration have been presented in the previous chapters. In Chapter 1, a detailed background of the scientific literature focussed on hydrocarbon migration has been documented. In Chapter 2, a series of methodologies used to recognise hydrocarbons in 2D and 3D seismic data have been provided. In Chapters 3, 4 and 5 a number of observations related to the migration of hydrocarbons in three different basins defined around the Falkland Islands have been described and discussed.

The seismic scale of some of the processes involved in producing the observed direct hydrocarbon indicators (DHIs) have been discussed (e.g. VAC formation, Chapter 3). However, at the sub-seismic scale and at the basin scale some important questions remain unanswered. Some of these topics have relevant importance, such as the migration of hydrocarbons in fine-grained sediments or the migration of hydrocarbon through faults.

In the following sections of this chapter the results from the case histories (Chapter 3, 4, and 5) will be synthesised and analysed to improve the understanding behind hydrocarbon migration, using the Falkland Basin. These results will be then compared with other evidence of hydrocarbon migration in other basins worldwide in order to find potential similarities which can improve our discussion.

The limitations and the future developments of this research work will be defined and proposed in the final session of the Chapter.

6.2. Summary of key results

6.2.1. Summary of key results

Chapter 3

In Chapter 3 a newly defined class of direct hydrocarbon indicator (DHI) has been defined. Vertical anomaly clusters (VACs) represent assemblages of constituent amplitude anomalies (e.g. bright spot) which define regions of amplitude amplification as compared with the background reflectivity. The constituent amplitude anomalies are linked by the migration process which is dominated by cross-stratal migration associated with the transient opening (or reactivation) of faults and fractures.

Semi-quantitative analysis of the observed amplitude anomalies and VACs included AVO, TFR and compressional velocity variation. These observations revealed that the amplitude anomalies are associated with compressible fluids like a gas phase. Drilling campaigns competed by FOGL plc in 2012 (Appendix A.2) confirmed that the observed seismic amplitude anomalies are associated with thermogenic hydrocarbons (gas).

The VACs are mostly distributed within the shallow section of the East Falkland Basin (Unit 2). Their vertical distribution is inhomogeneous and reveals a high concentration of amplitude anomalies in the centre of Unit 2 (e.g. Reflection 21). The different concentration of AAs has been associated with vertical variation of permeability of Unit 2 and linked with some key reservoir-like layers embedded in the Unit.

VACs are geographically distributed in a corridor (VAC corridor, Chapter 3, Figure 3.8). Their geographical distribution is characterised by patchy patterns at the

different horizons (e.g. Reflection K and Reflection 21, Figure 3.10). The geographical distribution of VACs remains still uncertain due to the lack of evidence of hydrocarbon migration features below the base of Unit 2 (Horizon K).

Chapter 4

In Chapter 4 a widespread Bottom Simulating Reflection (BSR) and a large number of DHIs, comprising enhanced reflections, pipes, disturbed signal zones and flat spots, have been observed.

The large BSR is interpreted to be the base of the gas hydrate stability zone. It is associated with enhanced reflections which are the results of the presence of free gas phase. The BSR is characterised by a non-uniform distance respect to the seabed. Modelling of geothermal gradient depth BSR profiles (G_GDBSRs) using different geothermal gradients revealed that the BSR is consistent with the shape of the acoustic basement (Figure 4.16). The gas generating the observed hydrates is interpreted to be mostly thermogenic. Biogenic gas cannot be excluded due to the lack of geochemical data.

The observed pipes are evidence of dramatic fluid expulsion events and are related to basement normal faults. The origin of the involved fluids has been interpreted to be thermogenic gas. Disturbed signal zones have been observed and interpreted as resulting from upward migration of fluids. A prominent flat spot has been observed in the deep parts of the SFB. It represents clear evidence for thermogenic gas.

The plumbing system is strongly dependent on the structural configuration of the basin. The distribution of pipes and other DHIs are linked with basement normal

faults. Thermogenic gas is interpreted to be the main fluids involved in the formation of the observed DHIs.

Chapter 5

In Chapter 5 a series of depression structures interpreted as mud volcano and volcano conduits are associated with a large number of amplitude anomalies, VACs, pipes and gas chimneys have been documented and discussed.

The mud volcanoes are characterised by a stacked depression structure which extends vertically for about 2km . They are characterised by concave upward reflections with diameters ranging between 2.0 and 7.1 km. VACs and disturbed signal zones are present within and in the nearby regions surrounding the mud volcanoes.

The mud volcanoes were interpreted and discussed to be associated with the upward migration of deep sourced fluids. A detailed discussion of the nature of these potential fluid sources suggests that these fluids are primarily derived from the deep source rocks and so associated with hydrocarbons. The hydrocarbons are interpreted to be the main fluids involved in the remobilisation of sediments. Mud volcanoes do not exhibit clear mud edifices and this is interpreted to be the result of erosion at the seabed.

6.3. Synthesis and comparison of DHIs

The direct hydrocarbon indicators (DHIs) observed in the previous case histories can be synthesised in a more convenient way in order to be analysed as function of their common seismic response and similar habitats.

6.3.1. Comparison of DHIs

The DHIs have been interpreted and classified according to the scientific terminology developed in the last decades (see Chapter 1). An objective analysis of what it is really observed on 2D seismic data (neglecting the strict terminology) allows us to compare the DHIs by a number of common acoustic characteristics, such as amplifications, polarity or distortion of the seismic signal. In most of the cases these features constitute singularly simple elements (Chapter 1) which are constituents of specific classes of DHI (e.g. amplitude anomalies composing vertical anomaly clusters, Chapter 3).

6.3.2. Permeability-controlled DHIs

Amplitude anomalies observed in east Falkland Basin and NE Falkland Basin, and associated with VACs (e.g. Figure 3.4, 3.6 and 5.5, 5.6), are acoustically similar to enhanced reflections associated with the BSR (e.g. Figure 4.17B) or again amplitude anomalies located at the top of disrupted signal zones (Figure 4.23) in South Falkland Basin. All these DHIs are strongly comparable because they represent simple amplifications of the background reflectivity and because they are in the observed examples soft reflections.

Table 6-1 Composite of representative examples of amplitude anomalies (see text).

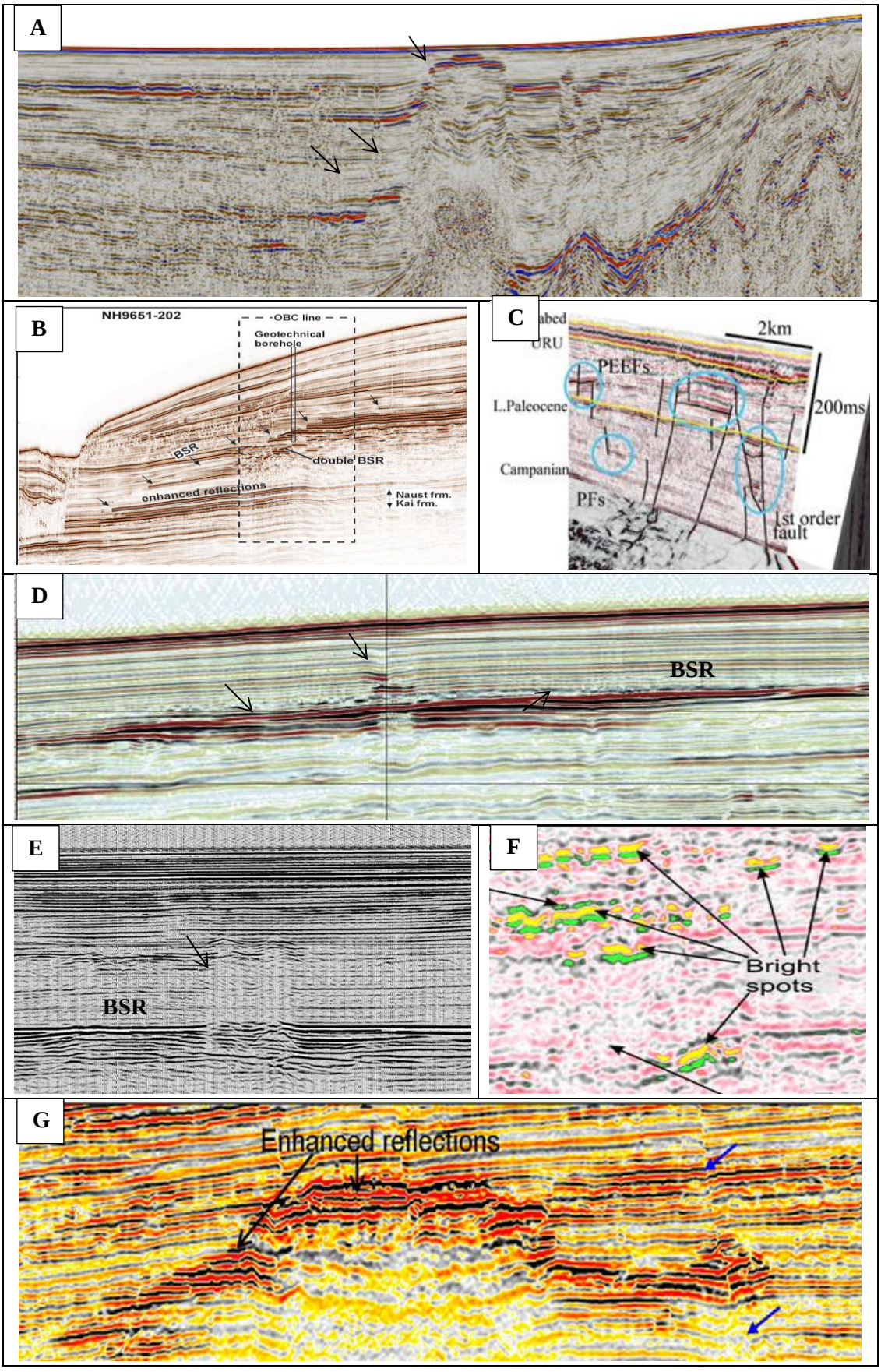

Similar amplitude anomalies are documented by Baristeas et al (2012) in the near Malvinas Basin (Table 6.1 A, black arrows). In these examples the amplitude anomalies on seismic data exhibit the same acoustic characteristics of the observed seismic features in the studied Falkland basins.

Other representative examples of amplitude anomalies form in other basins worldwide and include, for instance, enhanced reflections described by Bünz and Mienert (2004) in the mid-Norwegian Margin (Storegga Slide) (Table 6.1 B), enhanced reflections documented by Ostanin et al (2012a-b) in SW Barents Sea (Table 6.1 C), high amplitude anomalies described by Calves et al (2008) in Indus Fan (Arabian Sea) located below the BSR (Table 6.1 D, black arrows), shallow amplitude anomalies interpreted by Gorman et al (2002) within the GHSZ (Table 6.1 E, black arrows), soft bright spots documented by Andreassen et al (2007) in SW Barents Sea (Table 6.1 F) and enhanced reflections at the top of disturbed signal zones described by Sun et al (2012a) in South China Sea (Table 6.1 G).

The amplitude anomalies observed in the Falkland basins and the examples proposed in Table 6.1, occur in different geological settings, in dipping and sup-horizontal sedimentary layers and are associated with different depositional systems. These amplitude anomalies seem controlled by a series of mechanisms that prevent up-dip or lateral migration of hydrocarbons. We observe that amplitude anomalies composing VACs are sharply delimited by faults and fractures (e.g. Figure 3.7). Similar examples are shown also in Table 6.1 C (Ostanin et al., 2012a). Enhanced reflections are delimited by phase boundaries such as the BSR, in the South Falkland Basin (Figure 4.17) or, as previously documented, in the examples in Table 6.1 B (Bünz and Mienert, 2004) and D (Calves et al., 2008).

The similar acoustic response observed in these fluid related seismic features (e.g. AAs, VACs and enhanced reflections) is therefore primarily associated with their passive impact on the hosting lithologies. These fluid occurrences, mostly associated with hydrocarbons, are predominantly controlled by the permeably structure of the hosting media which controls the migration processes and their formation. These seismic features are therefore termed *permeability-controlled DHIs* and defined as hydrocarbon occurrences where the fluid migration passively responds to a pre-existing permeability structure. Under this DHI style fall also other occurrences, such as flat-spots, disturbed signal zones and also BSR. The BSR, which is not typically considered a DHI, potentially falls in this DHI style because it represents a seismic reflection caused by the presence of gas hydrates and free gas zone and so indicative of presence of hydrocarbons (e.g. Koh and Sloan, 2007).

6.3.3. Fluid-controlled DHIs

Gas pipes observed in South Falkland Basin (Figure 4.19) are similar to gas pipes and gas chimneys observed in NE Falkland Basin (Figure 5.15). They are both characterised by columnar regions of vertical disturbance. The hosting lithologies are in both cases deformed by the action of the migrating fluids as clearly imaged on seismic data. Similar examples of pipes are described by Dumke et al (2014) in Giant Gjallar Vent (Norwegian Sea) (Table 6.2 A), Moss and Cartwright (2010) in offshore Namibia (Table 6.2 C) or Cartwright (2007) offshore Norway (Table 6.2 D). Other pipes showing different impact on the hosting lithology are for instance documented by Hustoft et al (2007) in mid Norwegian margin (Table 6.2 B) or again by Cartwright (2007) (Table 6.2 E). In the first example the pipe is characterised by a narrower region of deformation which is mostly represented by stacked upward

curved reflections (Table 6.2 B, black arrows). In the second case the pipe is associated with dissolution and characterised by a complete disruption of the reflections (Table 6.2 E, black arrow).

The dominant characteristic of these features - the deformation of the hosting structure - can be also linked to the documented mud-volcano (Figure 5.10) and conduits of mud-volcanoes (Figure 5.5). These seismic features observed in NE Falkland Basin (Chapter 5) clearly deform the shallow section of Unit 2 and 3 with strong impact on the original sedimentary structure. Similar mud-volcano and conduits of mud-volcano are documented by Dimitrov (2002) in Black Sea (Table 6.3 A) and by Medialdea et al (2009) in Gulf of Cádiz (Table 6.3 D). Other similar type of mud volcanoes showing buried depression structures are for instance documented by Mascle et al. (2014) in Mediterranean Sea (Table 6.3 B and C, black arrows). The last examples are considered similar to what observed in NE Falkland Basin in the expected case of preserved mud edifices (see Chapter 5.6.1).

The acoustic character of these seismic features underlines their destructive impact on the hosting lithologies. These seismic features, which are often associated with hydrocarbons (e.g. Etiope et al., 2009), respond actively on the pre-existing permeability setting. Hence the permeability of the hosting lithologies evolves dynamically allowing the formation of new migration pathways or routes where the migration processes take place. These seismic features are termed here *fluid-controlled DHIs* and are defined as hydrocarbon migration structures able to create their own migration pathways in the hosting media. Under this style of DHIs fall pipes, gas chimneys and also potentially mud volcanoes.

Table 6-2 Composite of representative examples of pipes (see text).

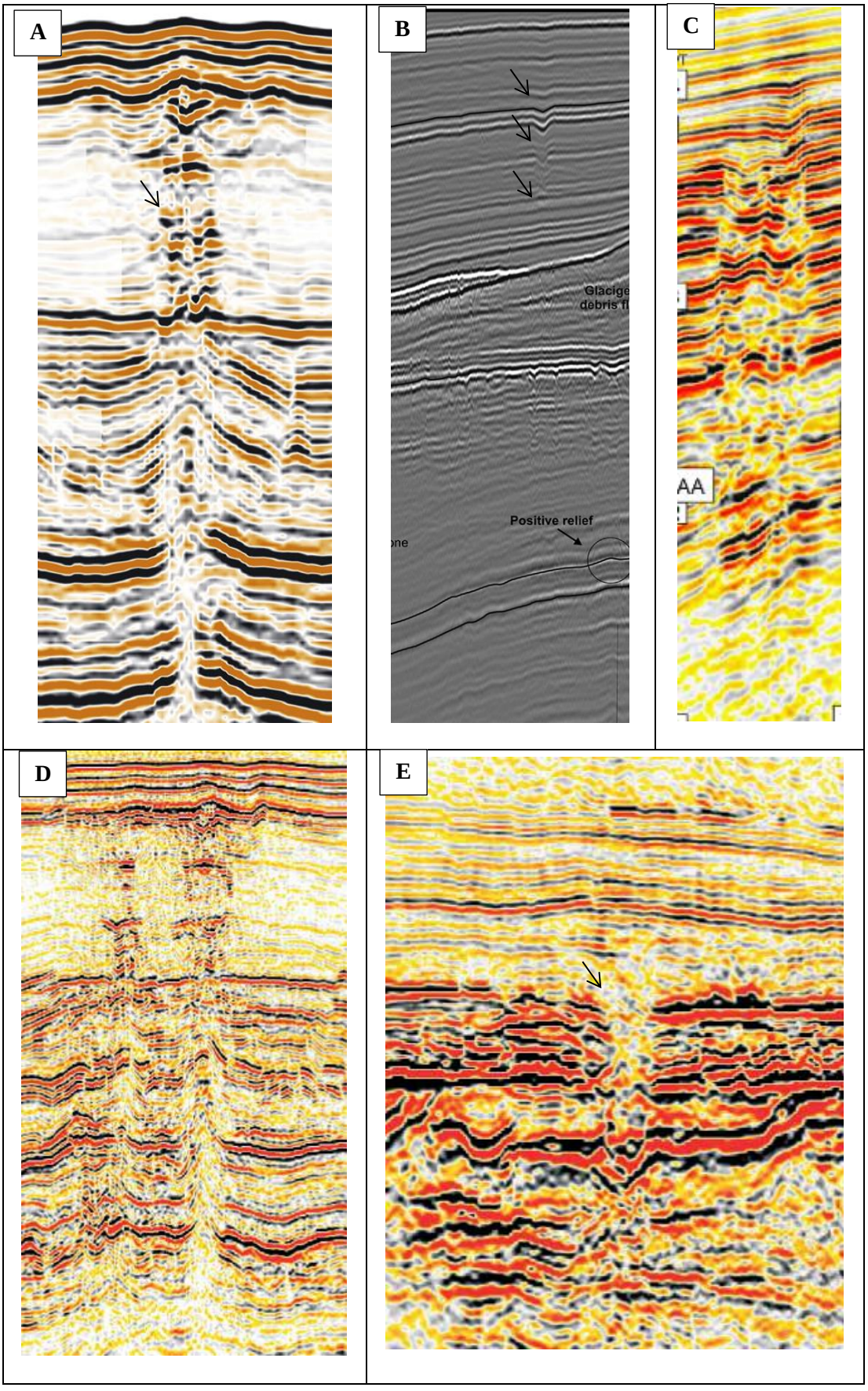

Table 6-3 Composite of representative examples of mud volcanoes (see text).

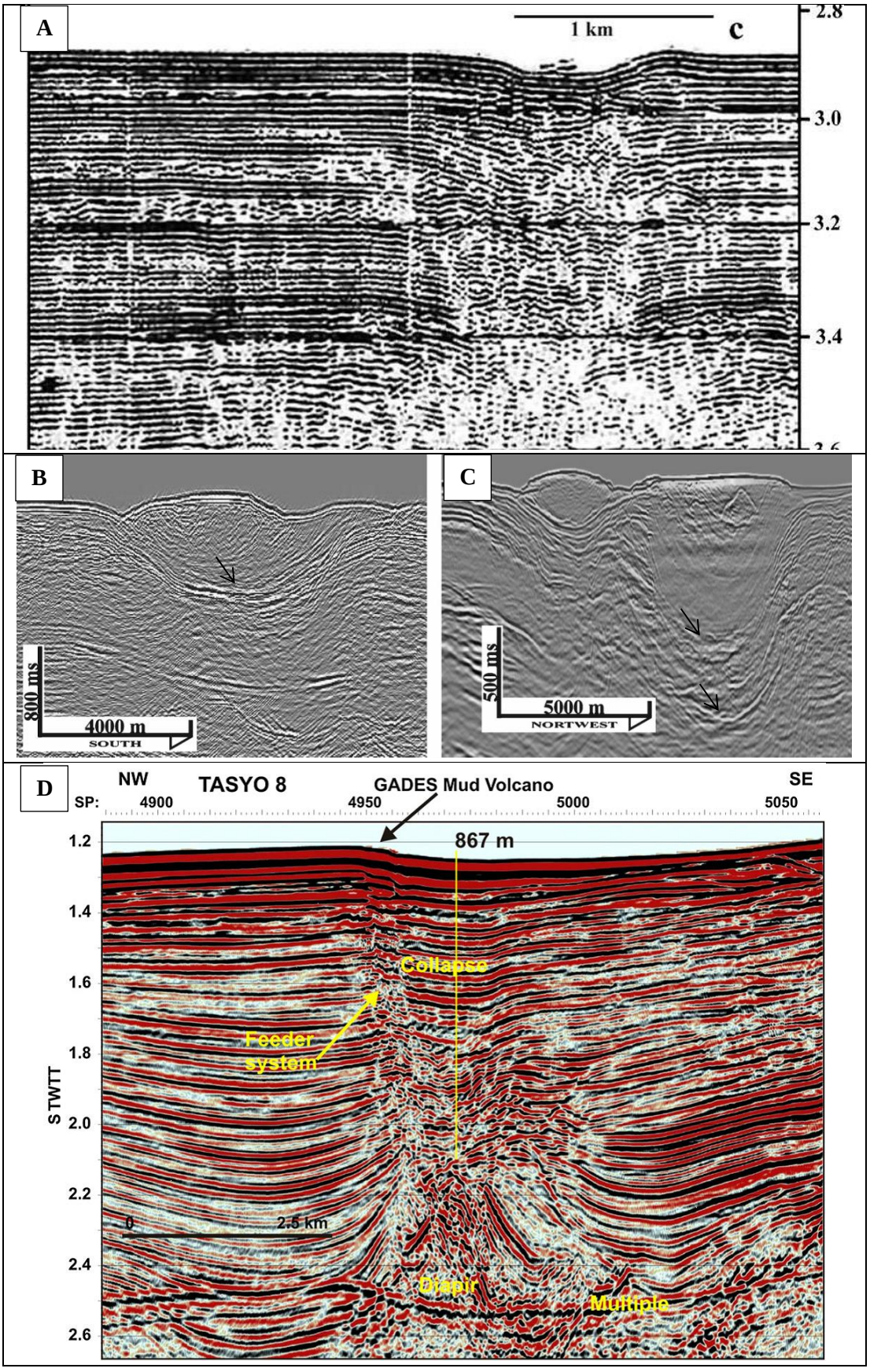

The acoustic character of these seismic features underlines their destructive impact on the hosting lithologies. These seismic features, which are mostly associated with hydrocarbons, respond actively on the pre-existing permeability setting. Hence the permeability of the hosting lithologies evolves dynamically allowing the formation of new migration pathways or routes where the migration processes take place. These seismic features are termed here *fluid-controlled DHIs* and are defined as hydrocarbon migration structures able to create their own migration pathways in the hosting media. Under this style of DHIs fall pipes, gas chimneys and also potentially mud volcanoes.

6.3.4. Limitations of the classification

Some hydrocarbon related seismic features are potentially termed permeability- and fluid controlled DHIs. In the NE Falkland Basin are observed to be associated with dimming and disruption of the seismic signal. This response was interpreted to be caused by potential breaking the sedimentary layers, as observed in a number of regions (e.g. Horizon L, Figures 5.16 and 5.17). This observation supports the proposed classification that gas chimneys, defined as vertical migration of gas observed on seismic data as regions where the seismic amplitude and phase of the reflections is distorted (Heggland, 1997), are fluid-controlled DHIs. However it has been observed, using shear-wave data and forward modelling, that some gas chimneys generate regions of disturbed signal zone associated with fluid migrating through faults, without appreciable deformations of the structures (e.g. Arntsen, 2007; Granli et al., 1999). Therefore in some conditions they can be termed as permeability-controlled DHIs.

The formation of VACs was interpreted and discussed to be potentially favoured by the transient aperture of pre-existing faults and fractures (e.g. at the base of Unit 2; Foschi et al., 2014). In these conditions the structure is partially deformed (or opened, e.g. Capuano, 1993) in order to allow the gas to migrate vertically and connect a number of layers potentially characterised by higher permeability. However a number of faults and fractures, which allow cross-stratal migration, also delimit lateral migration of hydrocarbons. Given that direct evidence of vertical fluid escape features (e.g. pipes) or seal breaching have not been observed (see for example Figures 3.5, 3.6, 3.7), the VACs are still interpretable as permeability-controlled DHIs.

Mud volcanoes and conduits of mud-volcanoes, as already discussed in Chapter 5.6.1.2-3, were interpreted to be probably associated with migrating sediments enriched by fluids of thermogenic origin. As suggested by Etiope et al (2009) also most of the terrestrial mud volcanism (>80%) is associated with hydrocarbons. Again, in marine environment mud volcanisms is frequently associated with migrating methane as documented by Dimitrov (2002), Etiope and Klusman (2002), Milkov (2000) and Prinzhofer and Deville (2013), among others. Taking in account these hydrocarbon-related examples it is suggested to consider mud volcanoes as indicators of the presence of migrating hydrocarbons and since they clearly create their own pathways during the ascending migration of sediments and fluids they potentially represent fluid-controlled DHIs.

Table 6-4 DHIs classification (see text)

DHIs	Classification	Definition	Seismic response
Amplitude anomaly (AA) Bottom simulating reflection (BSR) Enhanced reflection (ER) Flat-spot Vertical anomaly cluster (VAC)	permeability-controlled	It defines DHIs where the hydrocarbon migration passively responds to a pre-existing permeability structure.	The seismic response resulting from the presence or formation of these DHIs is mostly characterised by amplification or dimming of the background seismic amplitudes.
Gas chimney Gas pipe Mud volcano (MV)	fluid-controlled	It defines DHIs where the fluid migration creates its own permeability structure.	The seismic response of these DHIs is a clear damaging of the reflectivity pattern. Scattering, amplification and dimming may present.

6.4. DHIs and migration processes

6.4.1. Introduction

The classification of DHIs proposed in the previous section was based on the qualitative seismic interpretation of the potential interaction of the migrating fluids (e.g. free gas) with the hosting lithologies.

At a seismic scale the migration of hydrocarbons is however visible only under specific dimensions (or volumes, e.g. Widess, 1976; Partyka et al., 1999). The resolution of seismic data and so the detection of certain seismic features is indeed controlled by a number of factors, such as the lateral dimension of the occurrences of hydrocarbons (Fresnel zone, Sheriff 1975), velocity of the media involved and layer thickness (Chopra et al., 2006 and 2009; Rubino and Velis, 2009), and spacing of the seismic traces (horizontal resolution due to acquisition parameters; Yilmaz, 2001). These factors limit the detection of the DHIs and the migration processes acting at a sub-seismic scale. Never the less some considerations about the specific migration processes, based solely on seismic resolvable evidence associated with the observed DHIs, are proposed in the following sections.

The wide spectrum of DHIs is produced by a few but important migration processes. These include: 1) Darcy flow (e.g. Krooss and Leythaeuser, 1996; Li and Li, 2010; Li, 2004; Losh et al., 1999; Qiao et al., 2005; Rudkiewicz et al., 1994; Sandvik and Mercer, 1990; Shi, 2006; Swarbrick et al., 2004; Yu and Lerche, 1995; Zou et al., 2009), 2) hydraulic fracturing (e.g. Capuano, 1993; Cartwright, 1994b; Heum, 1996; Leduc et al., 2013; Moss and Cartwright, 2010; Petersen et al., 2010; Xie et al., 2003) and migration through faults and fractures (e.g. Abid and Hesse, 2007; Aiello, 2005; Annunziatellis et al., 2008; Aydin, 2000; Bense and Person,

2006; Caillet and Batiot, 2003; Chen and Zha, 2008; Childs et al., 2009; Childs et al., 2002; De Boever et al., 2011; Marynowski et al., 2001; Moretti, 1998; Xiang et al., 2010), 3) diffusion (e.g. Arntsen et al., 2007; Bourg et al., 1993; Etiope and Martinelli, 2002; Krooss and Leythaeuser, 1996; Leythaeuser et al., 1979; Leythaeuser et al., 1982; Stainforth and Reinders, 1990; Thomas and Clouse, 1990; Volynskii et al., 1988), and 4) flow in solution (e.g. Bjørkum et al., 1998; Durand, 1988; Etiope and Martinelli, 2002; Hunt, 1984; MacDonald et al., 2002; Teige et al., 2005). The formation of permeability- and fluid-controlled DHIs are discussed in detail in association with these processes.

6.4.2. Migration processes associated with permeability-controlled DHIs.

The permeability-controlled DHIs are controlled by migration mechanisms which are responding passively to a pre-existing permeability structure (Table 6.4). This means that the migrating fluids will occupy the pore spaces where the stratal water was present before the migration phenomena. The pore spaces can be related to pores within porous media or associated with elongated pores associated with fracture and fractures network (e.g. Brown, 2000). The permeability-controlled DHIs, taking into account also the points discussed in the previous sections, can be formed by 1) the displacement of pore water and the replacement with the migrating fluids, or 2) molecular diffusion into the pore water.

Displacement of stratal water from the pore spaces is strongly influenced by the nature of the migrating fluids. If the migrating fluids are represented by a free gas phase (e.g. methane) the system will be governed by multiphase flow, such as water and gas (e.g. multi-phase Darcy flow; e.g. Burrus et al., 1991; Li and Li, 2010; Li, 2004; Losh et al., 1999; Qiao et al., 2005; Rudkiewicz et al., 1994; Sandvik and

Mercer, 1990; Yu and Lerche, 1995; Zou et al., 2009). The migration process will be strongly influenced by the variation of relative permeability of the two phases which will reduce the migration of the free gas phase (e.g Kuo, 1997). A complete displacement of water will never be reached (irreducible water saturation; Bjorkum et al., 1998) and therefore only a partial gas saturation of the pores will be present in the water wet system. The partial saturation of free gas (e.g. methane or CO_2), is responsible for a strong decrease of the acoustic impedance ("fizz" water; Domenico, 1974) generating on seismic appreciable variations of amplitude. The observed amplitude anomalies distributed in VACs (Chapter 3, e.g. Figure 3.5) or the enhanced reflections observed beneath the BGHSZ (Chapter 4, e.g. Figure 4.17) are believed to be associated with these phenomena.

However water wet system can be permeable to water but not necessarily to other phases like gas methane (Bjorkum et al., 1998; Teige et al., 2005). The limited migration of gas may be therefore limited by barrier of low permeability. These barriers, such faults, chemical boundaries (BSR, Opal A-CT, etc) will "shape" the distribution of the migrating gas. This could explain the sharp margins of the amplitude cut-off of some enhanced reflections (e.g. Figure 4.18) or the number of sharply defined amplitude anomalies observed in VACs associated with major normal faults (e.g. Figure 3.7).

The limited migration of gas phases across structural barriers or seals suggests that diffusive migration processes (Burrus et al., 1991; Li and Li, 2010; Li, 2004; Losh et al., 1999; Qiao et al., 2005; Rudkiewicz et al., 1994; Sandvik and Mercer, 1990; Yu and Lerche, 1995; Zou et al., 2009) or flow of gas in solution (water carrier; e.g. Etiope and Martinelli, 2002) do not play a relevant role in the development of permeability controlled DHIs. This argument is consistent with the

slowness of the diffusion mechanism which is well known to play a prominent role in primary migration within source rocks (Hunt, 1984; Leythaeuser et al., 1982; Stainforth and Reinders, 1990; Thomas and Clouse, 1990).

6.4.3. Migration processes associated with fluid-controlled DHIs.

Some of the most striking fluid-controlled DHIs (e.g. gas chimneys, Figure 5.15, Chapter 5) are clearly associated with deformation of the shallow section of the studied basins. It is suggested that the migrating hydrocarbons are in some way associated with local and transient deformation of the host sediments (e.g. Unit 2 and 3 in NE Falkland Basin) producing deformed reflections, disruption and strong scattering on seismic data (e.g. Figures 4.19, 5.5; Tables 6.2, 6.3). In the regions surrounding the fluid-controlled DHIs, some permeability-controlled DHIs are present and may be associated with the result of residual hydrocarbon accumulations, which may generate amplitude anomalies (e.g. AAs in Figure 5.5a).

The formation of these fluid-controlled DHIs is associated with migration mechanisms able to produce (1) the pathways and (2) the hydrocarbon occurrences. The formation of pathways, like the observed pipes (Figure 4.19) and mud volcano conduits (Figure 5.5) suggest that the behaviour of the hydrocarbon is primarily associated with hydraulic fracturing (e.g. Capuano, 1993; Cartwright, 1994a; Duranti and Hurst, 2004; Jain and Juanes, 2009; Leduc et al., 2013; Mandl and Harkness, 1987; Moss and Cartwright, 2010).

The hydraulic fracturing is suggested to be the most likely mechanism able to generate the observed pipes in the South Falkland Basin (e.g. P1, Figure 4.19). In NE Falkland Basin the hydraulic fracturing is associated with the pre-existing fault systems which are well developed in Unit 1 and partially in Unit 2 and 3. The

presence of faults and fractures can change completely the permeability structure and allow a faster flow of the hydrocarbons in pre-existing or partially opened migration pathways (Abid and Hesse, 2007; Aydin, 2000; Bense and Person, 2006; Caillet and Batiot, 2003; Childs et al., 2002; Gay et al., 2006; Ilg et al., 2012; Ingram and Urai, 1999; Moretti, 1998).

Some prominent fluid-controlled DHIs, like the documented mud volcanoes and mud volcano conduits (Chapter 5), are also associated with strong remobilisation of sediments and have a greater impact, in terms of deformation of the host, in comparison to the observed gas chimneys and gas pipes (e.g. Figure 5.15, Chapter 5). Remobilisation of sediments to form mud volcanoes elsewhere is known to be associated with migrating hydrocarbons (e.g. Etiope et al., 2009; Loncke and Mascle, 2004; Planke et al., 2003) and active buoyant migration of hydrocarbons (and other fluids) may exert frictional forces on the hosting lithologies (Abel et al., 2005; Mourgues and Cobbold, 2003; Ooms et al., 1970; Rozhko, 2010). The expulsion (extrusion) of remobilised material and collapse of the overburden represent a secondary effect on the hosting lithologies with formation of depression structures (e.g. Figure 5.7a).

However, the observed fluid-controlled DHIs may not necessarily be associated with hydrocarbons. As documented by Bjorkum et al. (1998, 1999) only pore water is able to produce hydraulic fracturing of low permeability seal rocks. This statement is supported by laboratory results (e.g. Teige et al., 2005), and suggested by other works focussed on hydrocarbon migration (e.g. Leduc et al., 2013). In a recent work has been demonstrated that oil phase in water wet systems may potentially migrate through non-fractured caprocks by flow in narrow oil-wet films (Teige and Hermanrud, 2012) suggesting again that hydrocarbon may ultimately flow in low

permeability rocks without necessarily fracture the rocks. These last points require further investigations.

6.4.4. Cross-plot of DHIs

Following the last discussed observations, the most diffuse and important permeability-controlled and fluid-controlled DHIs observed in the three case histories (Chapters 3, 4 and 5), and documented in the broad scientific literature (e.g. Tables 6.1, 6.2 and 6.3), have been organised in relation to their impact on the host sediments. A qualitative organisation of the observed DHIs, following the increasingly dynamic behaviour of the migrating fluids (hydrocarbons and water) with their horizontal size (as measured on 2D/3D seismic data) has been synthesised in a qualitative cross-plot shown in Figure 6.1.

Starting from the observed AAs, which includes (1) AAs of VACs, (2) enhanced reflections (BSR), (3) AAs associated with disturbed signal zones and (4) all AAs located at the margins of fluid controlled DHIs, it is possible to define a broad region (Figure 6.1) which spans over different scales (from seismic resolvable to >25km ; VAC, Figure 3.5) and which is mostly consistent with water displacement (or replacement, see previous section).

By considering the increasing impact of the fluid on the host sediments we can define a region where fault and fracture reactivation allows vertical and cross-stratal migration. In this region of the cross-plot (Figure 6.1) we can place the documented VACs. The VACs have a larger size with respect to single AAs. VACs have been observed only with minimum cross sectional extent above 200m. Some gas chimneys and disturbed signal zones, as documented before (e.g. Granli, 1999), may be associated with migrating hydrocarbons through faults and so their region may

partially overlap with that related to VACs. The relatively smaller dimensions of gas chimneys and disturbed signal zones, compared to VACs, is perhaps associated with a faster migration of hydrocarbons within larger faults (e.g. Annunziatellis et al., 2008; Aydin, 2000; Bense and Person, 2006; Caillet and Batiot, 2003; Chen and Zha, 2008) and a less time to develop large DHIs.

Gas pipes represent a specific region in this cross-plot. Pipes are characterised by small size and focussed hydrocarbon migration. The hydraulic fracturing migration mechanism and the formation of pathways are specific characteristics of these features (Leduc et al., 2013; Løseth et al., 2011; Moss and Cartwright, 2010; Sun et al., 2013a). The small number of these DHIs described in the observed Falkland basins suggested us to plot their diameter range observing other examples from previous publications (50-500m; e.g. Moss and Cartwright, 2010).

Gas chimneys and mud volcanoes and mud volcano conduits (Chapter 5), associated with strong hydraulic fracturing and structural damages, represent the most extreme DHIs observed in the Falkland Basins and in other basins worldwide (Andresen et al., 2010; Davies and Stewart, 2005; Dimitrov, 2002; Etiope et al., 2009; Graue, 2000; Loncke and Mascle, 2004; Mastalerz et al., 2007; Medialdea et al., 2009; Milkov, 2000; Planke et al., 2003; Prinzhofer and Deville, 2013; Somoza et al., 2012; Stadnitskaia et al., 2008; Stewart and Davies, 2006; Westbrook and Smith, 1983). Their position within the cross-plot is located at the highest level associated with the strongest fluid pressure impact on the hosting structures (e.g. Figure 5.5, Chapter 5). Their dimension (interpreted diameter from 2D seismic profiles) is here plotted following the examples observed in the Falkland Basins only.

6.5. DHI style: possible causes

As documented in the previous chapters the observed direct hydrocarbon indicators (DHIs) are interpreted as being primarily associated with migration of thermogenic fluids (see discussion sections 3.6, 4.6, 5.5). The hydrocarbons generating these structures are thought to have been generated in kitchens in the deeper portions of the basin and are hence distributed following the structural elements of the (acoustic) basement.

Although the position of the DHIs is reasonably well constrained (e.g. see Chapter 5, Figure 5.20) it remains still unclear and unsolved why migrating hydrocarbons are able to develop specific DHIs in the shallow units. What is the controlling factor acting to differentiate fluid-controlled and structure controlled DHIs? Is the formation of specific DHIs time-related and unrelated to the structure of the basin?

Since the migrating fluids are inferred to be in all the cases hydrocarbons it is expected that their behaviour is in some ways related to the properties of the media involved or with their variable flux rate over the time. Some speculative and preliminary hypotheses, associated with the qualitative behaviour of the hydrocarbons versus the structures and the time, are proposed in the following sections.

6.5.1. DHI style versus structures

In the shallow sections of the observed basins (especially Unit 1, 2 and 3 in east Falkland Basin and NE Falkland Basin) a wide spectrum of permeability-controlled and fluid-controlled DHIs was present. Contrasting DHIs have been indeed observed

in similar lithologies and in many cases in the same sedimentary packages. A number of supporting evidence can be observed for the showed case histories in Figure 5.5a and 5.15.

This important evidence seems support the case that the hydraulic properties of the hosting media may have a limited effect on the differentiation of the observed DHIs. This therefore may suggests that the differentiation of the DHIs is not only associated with the properties of the hosting lithologies but may represent the results of different processes which presumably act in the deeper portions of the observed basins.

6.5.1.1. The possible role of deep structures

In the South Falkland Basin (SFB, Chapter 4) and in the NE Falkland Basin (NEFB, Chapter 5), a number of contrasting DHIs were observed in the shallow units. Arguing that these units do not play a role in the differentiation of the observed DHIs (see above), the latter have been therefore analysed in relation to the deep structural elements of these two basins in order to find any structural control which can justify their differentiation.

This description is based on representative seismic profiles showed in Figure 6.2 (for SFB) and 6.3 (for NEFB) which include different and contrasting DHIs.

In the South Falkland Basin (SFB, Figure 6.2 and 6.4) the distribution of pipes was previously interpreted to be related with local structural highs associated with foot wall crests of basement normal faults. Other DHIs, such disturbed signal zones and amplitude anomalies are observed above similar basement normal faults but in these cases these structures are deeper with respect to those related to the pipes.

The positions of pipes, AAs and disturbed signal zones exhibit a direct relationship between their differentiations and the depth of the acoustic basement (Figure 6.2). Hence, the pipes are focussed where the basement is shallower meanwhile the other DHIs are located where the basement is relatively deeper. Taking as reference the DHIs distribution (plotted on the basemap of SFB, Figure 6.3) the pipes are focussed in the northern regions and close to his northern margin. The pipe distribution represents, within the DHIs distribution, a region where the basement reaches a relatively shallower position.

In North east Falkland Basin (*NEFB*, Figure 6.4) the distribution of MVs, pipes, gas chimneys and some VACs were associated with structural highs and with shallow footwall crests of interpreted basement normal faults (e.g. F1, Figure 5.11). Other VACs and individual amplitude anomalies were observed above similar geological setting located in deeper positions.

Also in this case there is a direct relationship between the differentiation of the DHIs and their relative position within the basin (Figure 6.5). The position of MVs, pipes and gas chimneys is clearly focussed at the north-west margin of the DHIs distribution. Other DHIs, such VACs and amplitude anomalies, are instead located in a more central position respect to the DHIs distribution.

6.5.1.2. Summary

These observations reveal that fluid-controlled DHIs are mostly located at the margin of the defined DHI distributions. Given the particular geometry of the observed acoustic basements (SFB and NEFB) and the differentiation of the observed DHIs it is clear that particular structures located at shallow regions produce more frequently fluid-controlled DHIs rather than permeability-controlled DHIs. The

structure of the basin can therefore help to control the differentiation of the observed DHIs and define precise regions where specific DHIs are preferentially formed. A preliminary conceptual model is shown in Figure 6.6.

Considering the large number of variables involved in these processes these preliminary hypotheses need however to be verified in the future leaving however some strong evidence supporting that the DHI style may be function of the specific positions within the observed rift-basins.

6.5.2. Style DHIs as function of the time

Given the wide spectrum of DHIs observed in the Falkland basins and their specific responses on the hosting lithologies, is it plausible to group them as a unique fluid flow feature which evolves during the stages of the migration process and so during the time?

A number of DHIs have been selected following the increasing hydrocarbon effect as qualitative interpretation of seismic data. The selection of these DHIs followed therefore an imaginary evolution as observed in Figure 6.5 (black arrow). In this imaginary evolution the migration of hydrocarbons will start to flow toward a water-wet region (Figure 6.7-A). Under specific hydraulic condition a hydrocarbon occurrence within a given permeable layer will form and on seismic an amplitude anomaly will be visible (Figure 6.7-B). If hydrocarbons are present and continue to migrate there will be a point in which the capillary entry pressure will be achieved and the hydrocarbon will start to migrate vertically. The presence of faults and fractures will allow the hydrocarbon to flow vertically more easily due to the lower rock strength. Layers characterised by lower entry pressure will be filled first (e.g. Luo, 2011) generating on seismic a number of stacked amplitude anomalies or a

VAC (Figure 6.7-C). These steps have been already described for the VAC formation (for more details see Chapter 3.6). At this stage an increase in hydrocarbon pressure will promote the hydraulic fracturing of certain sealing layers (e.g. Horizon L, Figure 5.16) producing new migration pathways. At this stage, it is supposed that there is a change from permeability-controlled DHIs and fluid controlled DHIs. On seismic data, the resulting breaching of these layers and the scattering of seismic waves due to the presence of pockets of hydrocarbons will appear as a gas chimney (e.g. Arntsen, 2007; Figure 6.7-D). Once the newly formed pathways associated with the establishment of a gas chimney reach the seabed surface a rapid release of hydrocarbons and remobilised sediment will occur. The system will remain open until the hydrocarbon pressure drops sufficiently to close the pathways. The voids previously occupied by hydrocarbons and remobilised sediments will collapse under the pressure of the overburden. At this stage depression structures will be formed. Residual hydrocarbon occurrences will remain trapped in some regions within and surrounding the depression structures (Figure 6.7-E).

6.6. Limitations and further developments

6.6.1. Limitations of the 2D seismic data and lack of well calibration

The entire thesis work was based on a large 2D seismic dataset which provided a good coverage of the analysed basins but suffered from handicaps in resolution, reconstruction and definition of the observed seismic features.

The seismic resolution prevented observation and definition of subtle seismic features that may be associated with hydrocarbon. The lack of a clear definition of the geometries of the observed DHIs may have led to a complete misunderstanding of the phenomenon associated with the migration of hydrocarbons and so to a wrong definition of the causes associated with the generation of some important hydrocarbon-related seismic features (primarily VACs, Chapter 3).

The 2D seismic method represents a delicate method, which does not allow a complete reconstruction of the geometry of the structure present in subsurface. The interpretational uncertainties may lead to potential errors and uncertainties of what it are occurring in the gaps between 2D seismic lines. Most of the interpretations, such as mud volcanoes or VACs, have been helped by observed analogies with the wide scientific literature focussed in this research field.

Some limitations derived also by the use of different seismic datasets which have not allowed a proper interpretation of seismic horizons and other structural elements (e.g. near and far-stack sections of the GSI dataset are without automatic gain control (agc); see Appendix A.1). Some important stratigraphic and structural features within the interpreted basins have been therefore reconstructed from 2D seismic data with all uncertainties associated with the limitations defined before.

The entire work suffered also by the lack of well calibration. The information used in two of the observed case histories (Chapter 3 and 4) was based on long range well calibration which, as documented, allowed only a very broad definition of the units involved. The lack of these constrains, has led to a limited interpretation of the structures involved and a limited quantitative analysis of the DHIs.

In one of the case histories (South Falkland Basin) has been possible to use some limited well information which however have been useful to define roughly some important horizons and define the age of the lithologies involved.

Some useful information has been derived from oil company reports (see Appendix A.2) which has been extremely useful and encouraging due to the positive feedback on some key interpretations (e.g. VAC are associated with thermogenic gas as predicted in Chapter 3).

The small number of papers focussed in the area required a partial reinterpretation of the Units involved, limited description of the sequence boundaries and a definition of other important stratigraphic features.

6.6.2. Further developments

The extremely variability of the DHIs observed in the Falkland Basins leaves open a large number of arguments related to their identification, quantitative interpretation, and understanding.

Chapter 3

VACs represent novel DHIs which need to be explored more in detail and evaluate their shape using a 3D seismic reconstruction. The presence of a well

calibration could permit to analyse also they internal structure and define a better formation model. Quantitative analyses also may be required to observe the variation in saturation within the constituent amplitude anomalies and their evolution.

A further development of the stacking factor versus variation on compressional velocity requires a quantitative approach. It could represent a potential methodology to define a direct correlation between hydrocarbon saturated layers and push down effect. Further analyses can be done starting from other important works such Rubino (2009).

Time-frequency representation (TFR) can be improved implementing algorithms based on reassignment methods (e.g. Auger and Flandrin, 1995; Han et al., 2014; Wu and Liu, 2009). This implementation can be useful to eliminate completely cross-term interference (CTI, see Chapter 2) and provide a more focussed instantaneous response on frequency domain.

Chapter 4

The most interesting feature of this case history, which leaves still open many unanswered questions due to the lack of proper well calibration, is the bottom simulating reflection (BSR). Its distribution and its relationship with the deep structures represent a formidable example to study the effect of the stability of the gas hydrate stability zone (GHSZ) in regions characterised by shallow basement. Further research would ideally require the use of precise geothermal gradient and other important parameters such porosity thermal conductivity of the shallow sediments involved. Also an analysis of the gas associated with the gas hydrates could be useful to determine if the hypothesis of a predominantly thermogenic origin is correct.

Other remaining questions are associated with the formation of pipes. As already extensively documented in the scientific literature there are still many uncertainties about the relationship between pipes and faults.

Chapter 5

The interpreted mud volcanoes and mud volcano conduits require a reinterpretation with the use of 3D seismic data. A correct definition of their geometry and their relationship with the complicated deep structures can reveal a different mechanism for their formation. In particular a detailed definition of the discussed chambers (or multi-chambers) is needed to assess the origin of the fluidised materials and the withdrawal regions beneath the depression structures.

A more detailed definition of the fluid involved and especially the amount of solid phase expelled at the seabed could explain and justify in a more robust way the lack of extrusive and intrusive edifices.

Also a geochemical analysis of the mud involved or expelled by expulsion features can finally resolve their association them with the other hydrocarbon migration features.

Chapter 6

In the last chapter a number of interesting points were raised from the synthesis and discussion of the presented case histories.

The determination of common acoustic features associated with the response of specific DHIs suggests that they are caused by similar processes and that their response is associated with the behaviour of the fluids involved (hydrocarbons and

water). Since the variation in fluid behaviour is potentially associated with more specific parameters, such fluid pressure, rock strength or permeability of the rock involved, it is may be possible to define in the future a particular parameter able to justify the style of the observed DHIs in a more quantitative way.

The DHI style, or differentiation between fluid controlled or permeability controlled DHIs, was previously hypothesised to be potentially associated with the structural characteristics of deep basins. This preliminary hypothesis deserves to be explored with more detail and taking as reference a large number of examples.

The DHI style could be also the result of the migration of hydrocarbons which, at different stages, express on seismic and on the structures involved different and contrasting DHIs. This hypothesis needs a complete work to assess his feasibility.

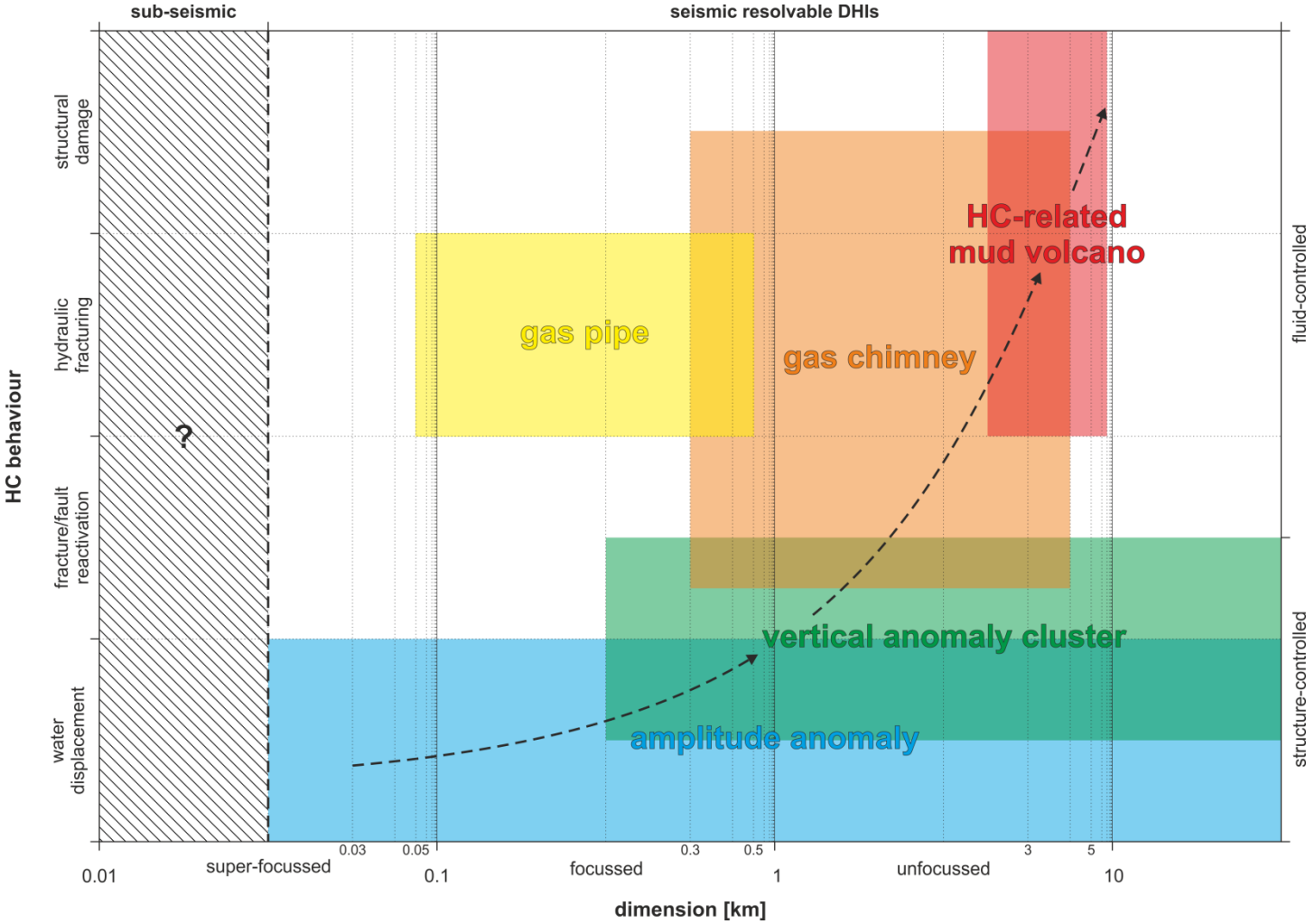

Figure 6.1 DHIs cross-plot. The plot summarises the qualitative interpretation of DHI observed in the three Falkland Basins. Some of the DHIs plotted in the figure represent group of DHIs (see text). A hypothetical evolution of specific DHIs is underlined by the black dashed line (see text; section 6.4.2). In the plot the threshold of seismic resolvability is set to 20m.

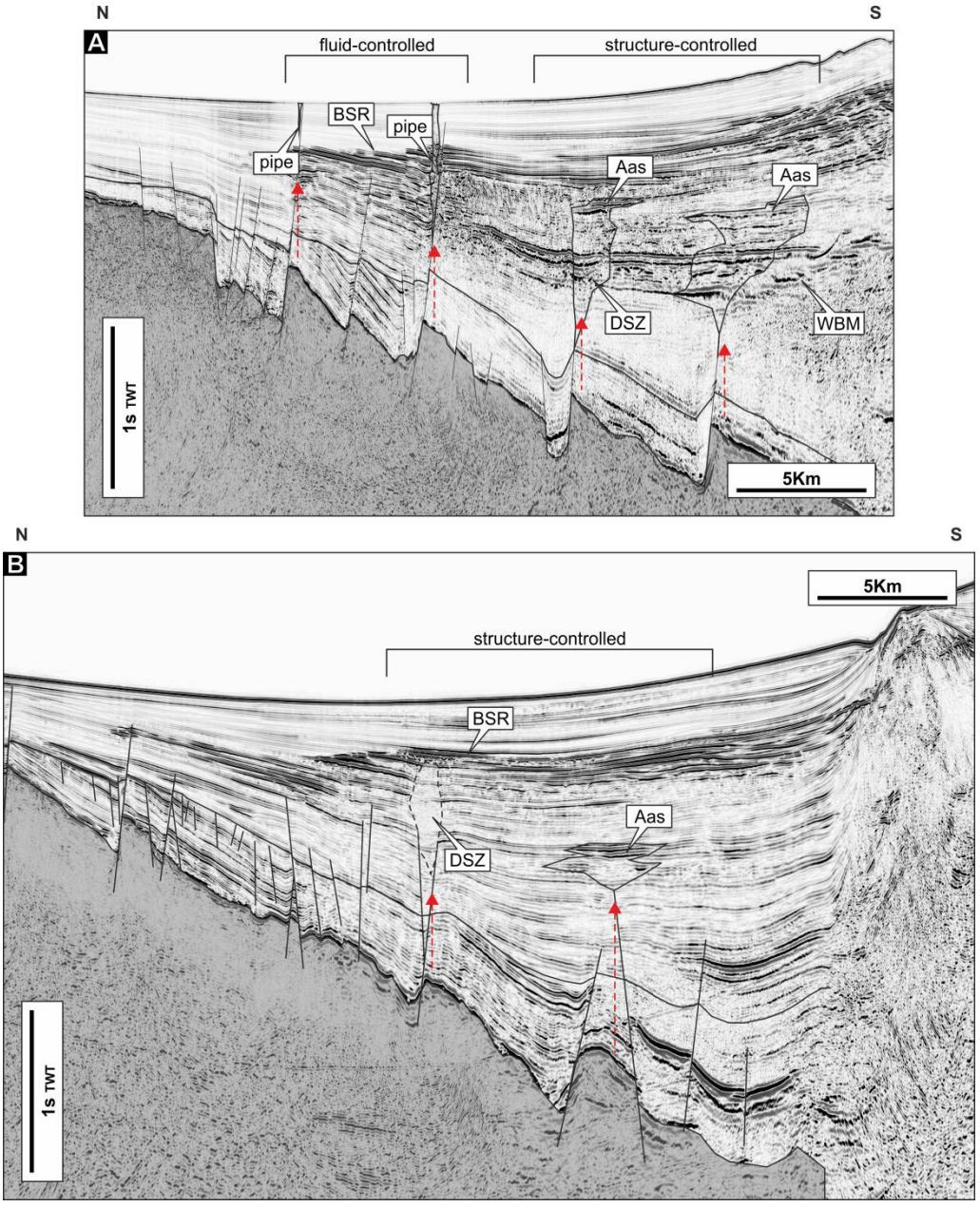

Figure 6.2 Representative seismic sections from South Falkland Basin (Chapter 4). Fluid-controlled and structure controlled-DHIs are located above basement highs located at different depths. Fluid controlled DHIs are in this case located above relatively shallower basement structures respect to the structure-controlled DHIs ones.

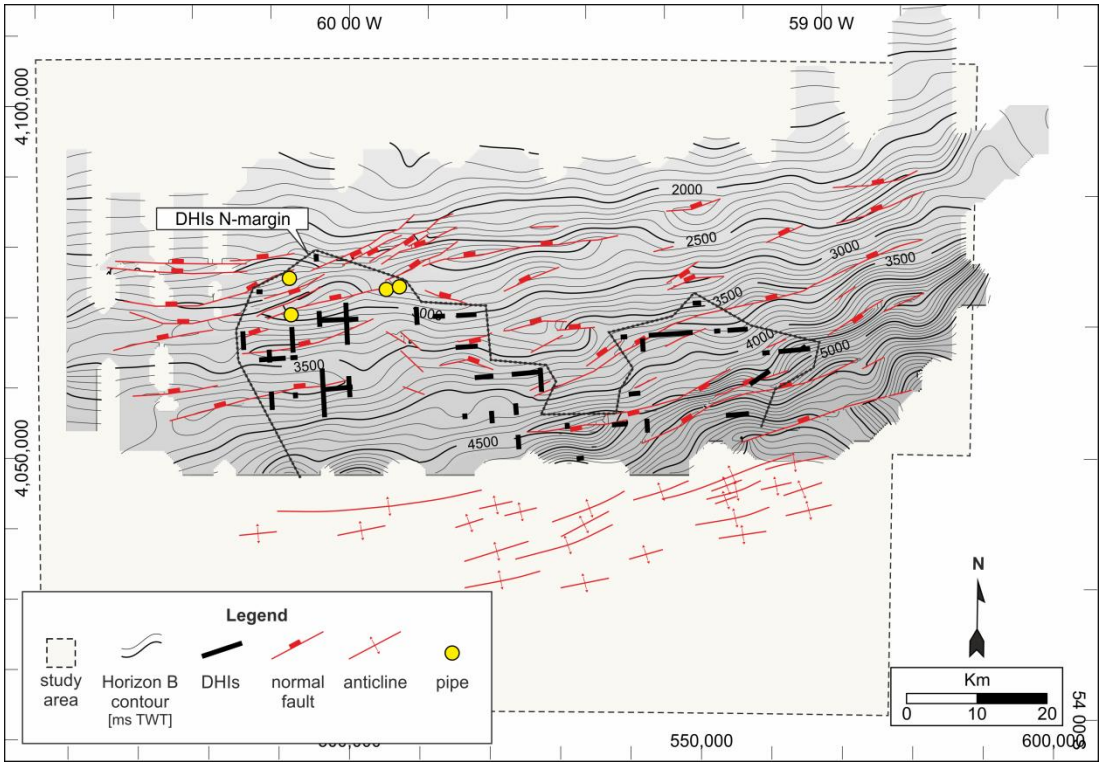

Figure 6.3 South Falkland Basin (SFB) time-structure map of the acoustic basement (Horizon B; see Chapter 4). The basemap exhibits a number of DHIs spread above the normal fault system. The fluid-controlled DHIs (pipes) clearly define a region in the northern margin of the DHI distribution.

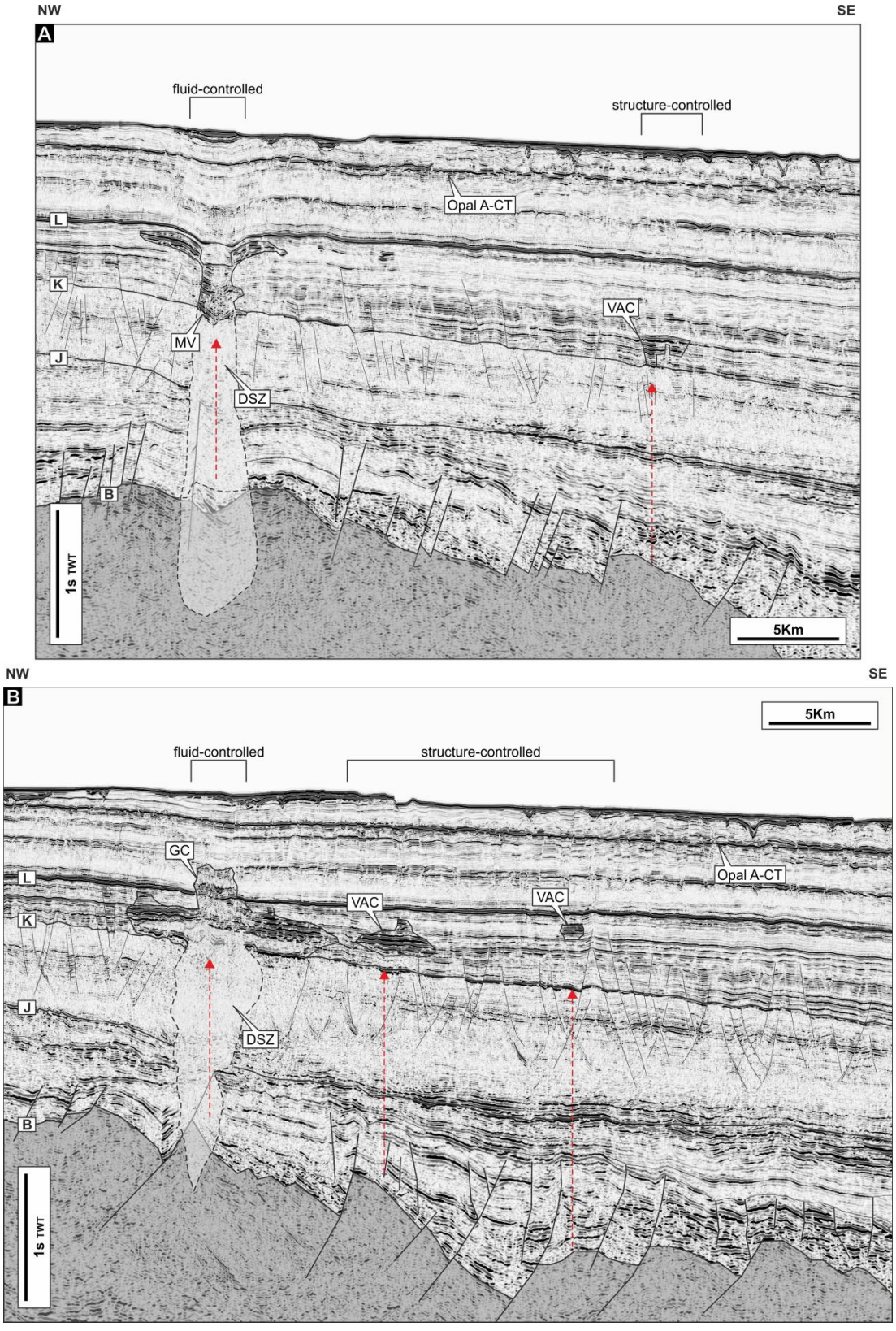

Figure 6.4 Representative seismic sections from North-east Falkland Basin (Chapter 5). Fluid-controlled and structure controlled-DHIs are located above basement highs located at different depth. Fluid controlled DHIs are in this case located above relatively shallower position respect to the structure controlled DHIs.

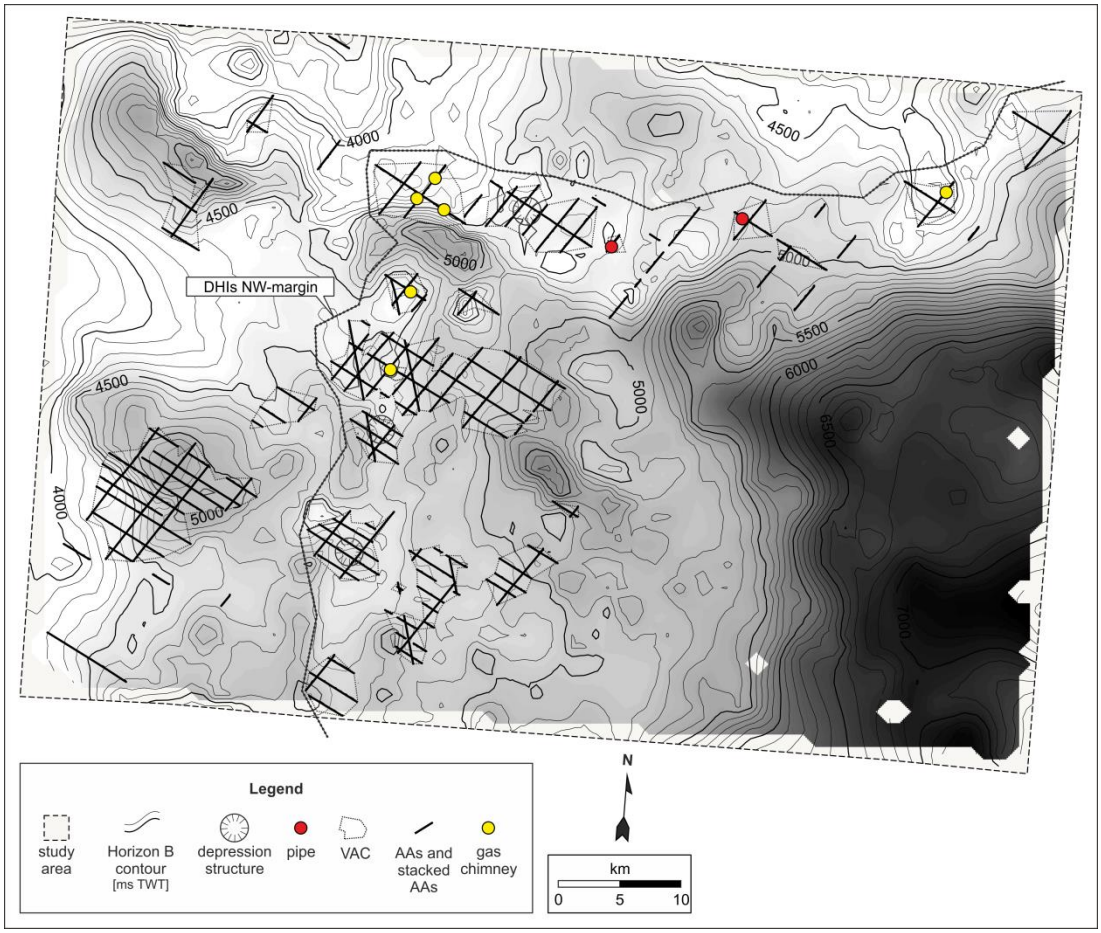

Figure 6.5 North east Falkland Basin (NEFB) time-structure map of the acoustic basement (Horizon B; see Chapter 5). The basemap exhibits different DHIs spread above the main slope. Interpreted normal faults are clearly linked with all fluid-controlled DHIs and some structure controlled DHIs. The latter are interpreted to be associated with the fluid controlled DHIs. Taking as reference the DHI distributed above the main slope (see Chapter 5) the fluid controlled DHIs are located at the north- west margin.

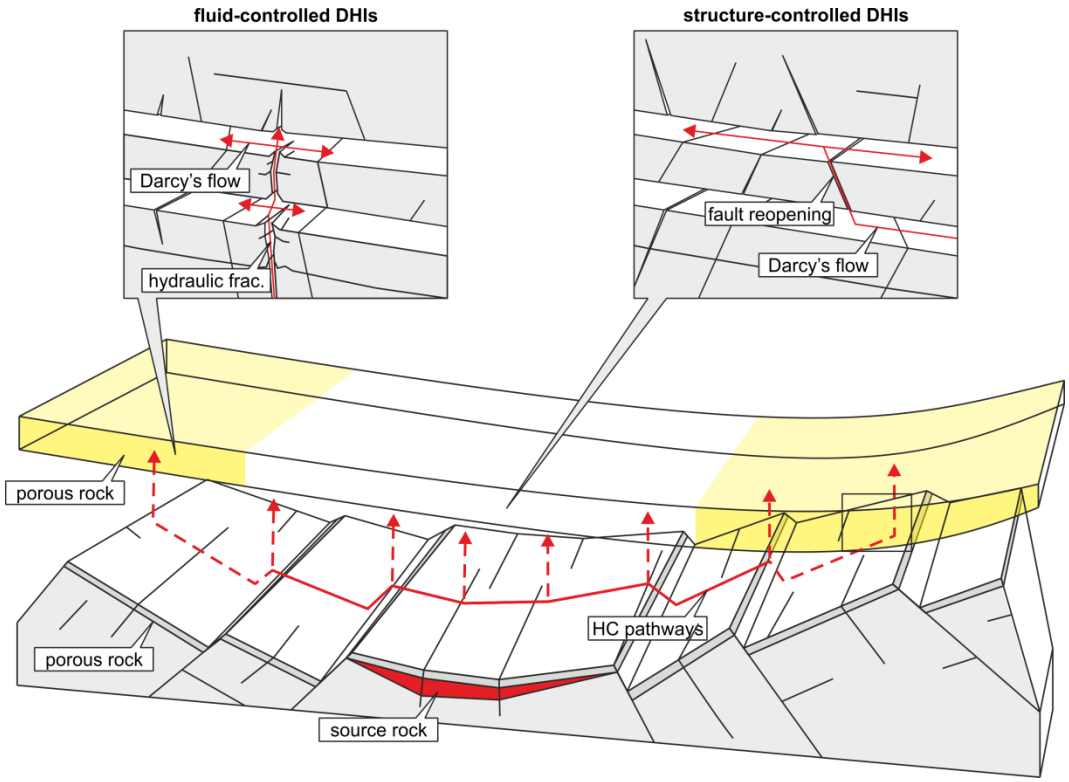

Figure 6.6 Hypothetical differentiation of DHIs associated with a simplified system dominated by a rift basin. The hydrocarbons generated in a given source rock migrate horizontally along deep porous rocks. The vertical migration is focussed at the footwall crest of the normal fault system. From these relative structural highs the hydrocarbons migrate to the above porous rocks forming specific DHIs. In the yellowish regions fluid controlled DHIs are formed.

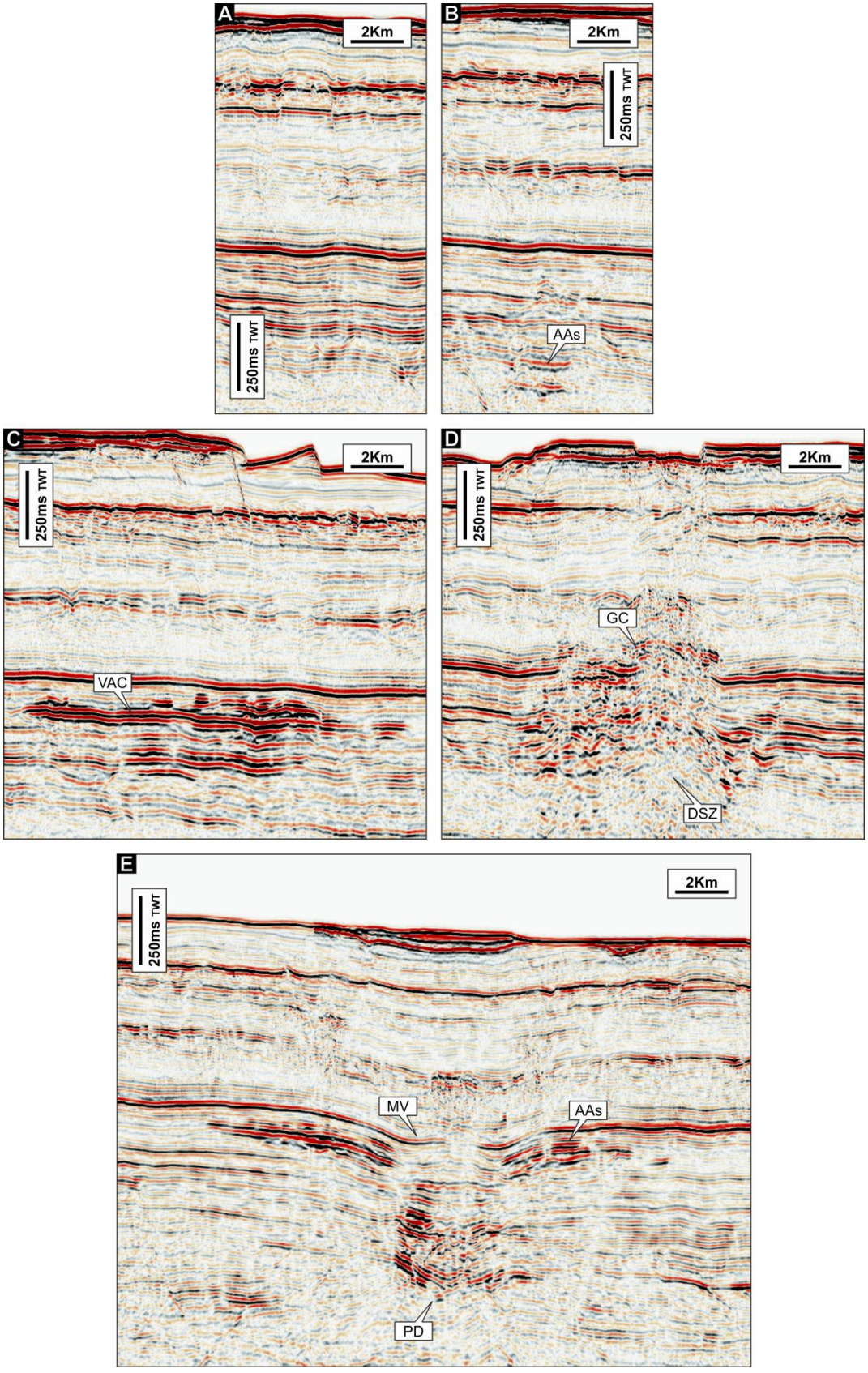

Figure 6.7Hypothetical DHI evolution. A) No hydrocarbons, B) settlement of amplitude anomalies, C) VAC formation, D) gas chimney and E) mud volcano-related depression structure after the expulsion of hydrocarbons and remobilised sediments.

7. Conclusions

7.1. Introduction

In this last Chapter a number of conclusions and key findings based on the research work carried out during the PhD course are presented. These conclusions are here summarised and divided following key arguments previously discussed and revisited in Chapter 6.

7.2. Vertical anomaly cluster

Vertical anomaly clusters (VACs), described in Chapter 3, represent a new class of DHI where a systematic migration of hydrocarbons produce a number of spatially-related occurrences observable on seismic data as assemblages of stacked amplitude anomalies. VACs are interpreted to be genetically associated with migration mechanisms acting at sub-seismic scale within faults and fractures.

VACs are important because they may be associated with region of non-focussed migration of hydrocarbons (size <25km) and also associated to a low impact on the pre-existing permeability structures. For this reason they have been classified as permeability-controlled DHIs. VACs can be however the result of a transient stage of the migration of hydrocarbons and evolve, if hydrocarbon flux is present, to other migration structures such as gas chimney or to more extreme migration features such as mud volcanoes.

VACs are believed to be present in other regions worldwide. For this reason it is expected a feedback from other researchers to evaluate their importance as DHI and also as evidence for hydrocarbon migration.

7.3. South Falkland Basin

The South Falkland Basin revealed a series of interesting features such as the dome-shaped bottom simulating reflection or the interpreted hydrocarbon plumbing system.

7.3.1. Bottom simulating reflection

The documented BSR is characterised by domal-shallowing which have been interpreted as an effect of the shallow basement. The observed deformation was consistent with the geometry of footwall crest of basement normal faults which are believed to be also the potential migration system/mechanism for the formation of the documented pipes.

The BSR observed in South Falkland Basin requires additional work which may lead to important implication for the stability of the gas hydrate stability zone in basin characterised by shallow basement.

7.3.2. Hydrocarbon plumbing system

The documented DHIs in the South Falkland Basin are interpreted as associated with a hydrocarbon plumbing system. This hydrocarbon plumbing system is able to deliver hydrocarbons in a broad area and reach the seafloor with extraordinary fluid expulsion structures (pipes). A number of potential targets have been documented in the deeper portion of the basin (flat spots) which indicate that a potential large amount of hydrocarbons is still present in the subsurface and accumulated in the

rotated fault blocks traps. Further investigation are needed to asses this preliminary and speculative conclusion.

7.4. NE Falkland Basin

7.4.1. Mud volcano and mud volcano conduits

A number of depression structures interpreted to be caused by mud volcanoes have been reported in the NE Falkland Basin. They represent the most dramatic fluid flow structure observed in the three study areas. These structures are potentially associated with hydrocarbons and so may correlated to other DHIs documented in the study area

7.4.2. DHI differentiation

The DHIs documented in NE Falkland Basin represent an important study of this research on the hypothesis of the DHI differentiation. The DHI differentiation is believed and discussed to be the result of the migration of hydrocarbons (and fluids) which is controlled, in the South Falkland Basin and in particular in the NE Falkland Basin, by the structural features of the deep structures. In particular the basin is proposed to be the main factor controlling the behaviour of the hydrocarbons and their impact of the shallow structures. This hypothesis was supported by the depth of the basement and the distribution of permeability controlled DHIs and fluid controlled DHIs occurring at the same geological interval.

7.5. Discussion

7.5.1. DHI synthesis and differentiation

The large number of DHIs have been documented and compared with the scientific literature. The DHIs have been then classified following their qualitative responses observed on seismic data. This work allowed us to divide the DHIs in permeability-controlled DHIs and fluid-controlled DHIs. These two classes are controlled by specific migration mechanisms.

The way in which the DHIs respond actively or passively to a pre-existing permeability structure has been explained in two speculative theories, which has already stated require further analyses to be tested. The first one is associated with focussing at specific deep structures, which are able to deliver flux of hydrocarbon fluids at different rate at specific positions of the basins. The second is related to a potential evolution of one single fluid migration event which evolves during the time and that is able to produce contrasting DHIs.

Reference

Abel, S., K. V. Prasad, and A. Mahaboob, 2005, Buoyancy force and thermal radiation effects in MHD boundary layer visco-elastic fluid flow over continuously moving stretching surface: International Journal of Thermal Sciences, v. 44, p. 465-476.

Abid, I., and R. Hesse, 2007, Illitizing fluids as precursors of hydrocarbon migration along transfer and boundary faults of the Jeanne d'Arc Basin offshore Newfoundland, Canada: Marine and Petroleum Geology, v. 24, p. 237-245.

Abrams, M. A., 2005, Significance of hydrocarbon seepage relative to petroleum generation and entrapment: Marine and Petroleum Geology, v. 22, p. 457-477.

Aiello, I. W., 2005, Fossil seep structures of the Monterey Bay region and tectonic/structural controls on fluid flow in an active transform margin: Palaeogeography, Palaeoclimatology, Palaeoecology, v. 227, p. 124-142.

Aminzadeh, F., P. De Groot, T. Berge, and G. Valenti, 2001, Using gas chimneys as an exploration tool: World Oil, v. 222, p. 50-56.

Andreassen, K., Nilssen, E. G., and Ødegaard, C. M., 2007, Analysis of shallow gas and fluid migration within the Plio-Pleistocene sedimentary succession of the SW Barents Sea continental margin using 3D seismic data: Geo-Marine Letters, v. 27, no. 2-4, p. 155-171.

Andresen, K. J., 2012, Fluid flow features in hydrocarbon plumbing systems: What do they tell us about the basin evolution?: Marine Geology, v. 332-334, p. 89-108.

Andresen, K. J., O. R. Clausen, and R. B. Jørgensen, 2010, A composite mud volcano system in the Chalk Group of the North Sea Central Graben: Journal of the Geological Society, v. 167, p. 1209-1224.

Andresen, K. J., and M. Huuse, 2011, 'Bulls-eye' pockmarks and polygonal faulting in the Lower Congo Basin: Relative timing and implications for fluid expulsion during shallow burial: Marine Geology, v. 279, p. 111-127.

Andresen, K. J., M. Huuse, N. H. Schødt, L. F. Clausen, and L. Seidler, 2011, Hydrocarbon plumbing systems of salt minibasins offshore Angola revealed by three-dimensional seismic analysis: AAPG Bulletin, v. 95, p. 1039-1065.

Anka, Z., C. Berndt, and A. Gay, 2012, Hydrocarbon leakage through focused fluid flow systems in continental margins: Marine Geology, v. 332-334, p. 1-3.

Anka, Z., R. Ondrak, A. Kowitz, and N. Schødt, 2013, Identification and numerical modelling of hydrocarbon leakage in the Lower Congo Basin: Implications on the genesis of km -wide seafloor mounded structures: Tectonophysics, v. 604, p. 153-171.

Annunziatellis, A., S. E. Beaubien, S. Bigi, G. Ciotoli, M. Coltella, and S. Lombardi, 2008, Gas migration along fault systems and through the vadose zone in the Latera caldera (central Italy): Implications for CO2 geological storage: International Journal of Greenhouse Gas Control, v. 2, p. 353-372.

Arhan, M., Naveira Garabato, A. C., Heywood, K. J., and Stevens, D. P., 2002, The Antarctic Circumpolar Current between the Falkland Island and South Georgia: Journal of Physical Oceanography, v. 32, no. 6, p. 1914-1931.

Arntsen, B., L. Wensaas, H. Løseth, and C. Hermanrud, 2007, Seismic modeling of gas chimneys: Geophysics, v. 72, p. 251-259.

Arts, R., O. Eiken, A. Chadwick, P. Zweigel, B. van der Meer, and G. Kirby, 2004a, Seismic monitoring at the Sleipner underground CO 2 storage site (North Sea), p. 181-191.

Arts, R., O. Eiken, A. Chadwick, P. Zweigel, L. van der Meer, and B. Zinszner, 2004b, Monitoring of CO2 injected at Sleipner using time-lapse seismic data: Energy, v. 29, p. 1383-1392.

Arts, R., and V. Vandeweijer, 2011, The challenges of monitoring CO2 storage: Leading Edge (Tulsa, OK), v. 30, p. 1026-1033.

Auger, F., and P. Flandrin, 1995, Improving the readability of time-frequency and time-scale representations by the reassignment method: IEEE Transactions on Signal Processing, v. 43, p. 1068-1089.

Avseth, P., T. Mukerji, and G. Mavko, 2009, Quantitative Seismic Interpretation. Applying Rock Physics to Reduce Interpretation Risk: Cambridge, Cambridge University Press.

Aydin, A., 2000, Fractures, faults, and hydrocarbon entrapment, migration and flow: Marine and Petroleum Geology, v. 17, p. 797-814.

Bangs, N. L. B., M. J. Hornbach, and C. Berndt, 2011, The mechanics of intermittent methane venting at South Hydrate Ridge inferred from 4D seismic surveying: Earth and Planetary Science Letters, v. 310, p. 105-112.

Baristeas, N., Z. Anka, R. di Primio, J. F. Rodriguez, D. Marchal, and F. Dominguez, 2012, Distribution of hydrocarbon leakage indicators in the Malvinas Basin, offshore Argentine continental margin: Marine Geology, v. 332-334, p. 56-74.

Barker, P. F., and I. W. D. Dalziel, 1976, Initial Reports of the Deep Sea Drilling Project, Leg 36. : Washington, US Government Printing Office.

Barry, K. M., and T. R. Shugart, 1974, Seismic hydrocarbon migration and models, Offshore Technological Conference, Houston, TX, Offshore Technol Conf, c/o David L. Riley,Dallas, Tex, p. 659-672.

Bear, J., and C. Braester, 1972, On the Flow of Two Immscible Fluids in Fractured Porous Media, Developments in Soil Science, p. 177-202.

Ben-Brahim, L., R. Petton, M. Couderc, and A. Djamhoer, 1999, Characterisazion of seismic anomalies using converted waves: a case history from east Natuna Basin: 27th Annual Convention Proceedings, p. 1-9.

Bense, V. F., and M. A. Person, 2006, Faults as conduit-barrier systems to fluid flow in siliciclastic sedimentary aquifers: Water Resources Research, v. 42.

Berg, R. R., 1975, Capillary pressures in stratigraphyc traps: AAPG Bulletin (American Association of Petroleum Geologists), v. 59, p. 939-956.

Berndt, C., 2005, Focused fluid flow in passive continental margins: Philosophical Transactions of the Royal Society A: Mathematical, Physical and Engineering Sciences, v. 363, p. 2855-2871.

Berndt, C., J. Mienert, M. Vanneste, and S. Bünz, 2005, Gas hydrate dissociation and sea-floor collapse in the wake of the Storegga Slide, Norway, Norwegian Petroleum Society Special Publications, p. 285-292.

Bertoni, C., and Cartwright, J. A., 2005, 3D seismic analysis of circular evaporite dissolution structures, Eastern Mediterranean: Journal of the Geological Society, v. 162, no. 6, p. 909-926.

Betzler, C., S. Lindhorst, C. Hübscher, T. Lüdmann, J. Fürstenau, and J. Reijmer, 2011, Giant pockmarks in a carbonate platform (Maldives, Indian Ocean): Marine Geology, v. 289, p. 1-16.

Bialas, J., I. Pecher, B. Davy, C. Papenberg, F. Gross, J. Hillman, S. Koch, K. Kroeger, and A. Sark, 2013, Seismic studies of giant pockmark-like features in southern chatham rise, New Zealand: 75th EAGE Conference and Exhibition Incorporating SPE EUROPEC 2013.

Biot, M. A., 1962, Mechanics of deformation and acoustic propagation in porous media: Journal of Applied Physics, v. 33, p. 1482-1498.

Bjørkum, P. A., O. Walderhaug, and P. H. Nadeau, 1998, Physical constraints on hydrocarbon leakage and trapping revisited: Petroleum Geoscience, v. 4, p. 237-239.

Boait, F., N. White, A. Chadwick, D. Noy, and M. Bickle, 2011, Layer spreading and dimming within the CO 2 plume at the Sleipner Field in the North Sea, p. 3254-3261.

Bourg, A. C. M., P. Degranges, C. Mouvet, and J. P. Sauty, 1993, Migration of chlorinated hydrocarbon solvents through Coventry sandstone rock columns: Journal of Hydrology, v. 149, p. 183-207.

Brooks, J. M., M. E. Field, and M. C. Kennicutt Ii, 1991, Observations of gas hydrates in marine sediments, offshore northern California: Marine Geology, v. 96, p. 103-109.

Brown, A., 2000, Evaluation of possible gas microseepage mechanisms: AAPG Bulletin, v. 84, p. 1775-1789.

Brown, A., 2003a, Capillary effects on fault-fill sealing: AAPG Bulletin, v. 87, p. 381-395.

Brown, A., 2003b, Improved interpretation of wireline pressure data: AAPG Bulletin, v. 87, p. 295-311.

Brown, A. R., 2004, Interpretation of Three-Dimensional Seismic Data: AAPG Memoir/SEG Investigations in Geophysics No. 9, AAPG.

Brown, L. F., and W. L. Fisher, 1977, Seismic-stratigraphic interpretation of depositional systems: Examples from Brazilian rift and pull-apart basins, in C. E. Payton, ed., Seismic Stratigraphy—applications to hydrocarbon exploration, v. 26, AAPG, p. p. 213-248.

Bry, M., N. White, S. Singh, R. England, and C. Trowell, 2004, Anatomy and formation of oblique continental collision: South Falkland basin: Tectonics, v. 23, p. TC4011 1-20.

Bünz, S., and J. Mienert, 2004, Acoustic imaging of gas hydrate and free gas at the Storegga slide: Journal of Geophysical Research B: Solid Earth, v. 109, p. B04102 1-15.

Bünz, S., J. Mienert, and C. Berndt, 2003, Geological controls on the Storegga gas-hydrate system of the mid-Norwegian continental margin: Earth and Planetary Science Letters, v. 209, p. 291-307.

Burrus, J., A. Kuhfuss, B. Doligez, and P. Ungerer, 1991, Are numerical models useful in reconstructing the migration of hydrocarbons? A discussion based on the northern Viking Graben: Petroleum migration, p. 89-109.

Caillet, G., and S. Batiot, 2003, 2D modelling of hydrocarbon migration along and across growth faults: An example from Nigeria: Petroleum Geoscience, v. 9, p. 113-124.

Calvès, G., M. Huuse, A. Schwab, and P. Clift, 2008, Three-dimensional seismic analysis of high-amplitude anomalies in the shallow subsurface of the northern Indus Fan: Sedimentary and/or fluid origin: Journal of Geophysical Research B: Solid Earth, v. 113.

Caminos, R., Cingolani, C. A., Hervé, F., and Linares, E., 1982, Geochronology of the pre-Andean metamorphism and magmatism in the Andean Cordillera between latitudes 30° and 36°S: Earth Science Reviews, v. 18, no. 3-4, p. 333-352.

Cao, Q., and J. Ye, 2011, Modeling of the pressure evolution and hydrocarbon migration in the Moliqing fault-depression, Yitong Basin, NE China: Shiyou Kantan Yu Kaifa/Petroleum Exploration and Development, v. 38, p. 174-181.

Capozzi, R., and Picotti, V., 2002, Fluid migration and origin of a mud volcano in the Northern Apennines (Italy): The role of deeply rooted normal faults: Terra Nova, v. 14, no. 5, p. 363-370.

Capuano, R. M., 1993, Evidence of fluid flow in microfractures in geopressured shales: American Association of Petroleum Geologists Bulletin, v. 77, p. 1303-1314.

Carcione, J. M., and U. Tinivella, 2000, Bottom-simulating reflectors: Seismic velocities and AVO effects: Geophysics, v. 65, p. 54-67.

Carman, P. G., 1997, Fluid flow through granular beds: Chemical Engineering Research and Design, v. 75, p. S32-S46.

Cartwright, J., 2007, The impact of 3D seismic data on the understanding of compaction, fluid flow and diagenesis in sedimentary basins: Journal of the Geological Society, v. 164, p. 881-893.

Cartwright, J., and Huuse, M., 2005, 3D seismic technology: The geological 'Hubble': Basin Research, v. 17, no. 1, p. 1-20.

Cartwright, J., M. Huuse, and A. Aplin, 2007, Seal bypass systems: AAPG Bulletin, v. 91, p. 1141-1166.

Cartwright, J. A., 1994a, Episodic basin-wide fluid expulsion from geopressured shale sequences in the North Sea Basin: Geology, v. 22, p. 447-450.

Cartwright, J. A., 1994b, Episodic basin-wide hydrofracturing of overpressured Early Cenozoic mudrock sequences in the North Sea Basin: Marine and Petroleum Geology, v. 11, p. 587-607.

Cartwright, J., 2011, Diagenetically induced shear failure of fine-grained sediments and the development of polygonal fault systems: Marine and Petroleum Geology, v. 28, no. 9, p. 1593-1610.

Cartwright, J. A., and D. N. Dewhurst, 1998, Layer-bound compaction faults in fine-grained sediments: Bulletin of the Geological Society of America, v. 110, p. 1242-1257.

Castagna, J. P., and S. W. Smith, 1994, Comparison of AVO indicators: a modeling study: Geophysics, v. 59, p. 1849-1855.

Castagna, J. P., and S. Sun, 2006, Comparison of spectral decomposition methods: First Break, v. 24, p. 75-79.

Castagna, J. P., S. Sun, and R. W. Siegfried, 2003, Instantaneous spectral analysis: Detection of low-frequency shadows associated with hydrocarbons: Leading Edge (Tulsa, OK), v. 22, p. 120+122+124-127.

Castagna, J. P., and H. W. Swan, 1997, Principles of AVO crossplotting: Leading Edge (Tulsa, OK), v. 16, p. 337.

Castagna, J. P., H. W. Swan, and D. J. Foster, 1998, Framework for AVO gradient and intercept interpretation: Geophysics, v. 63, p. 948-956.

Cathles, L. M., Z. Su, and D. Chen, 2010, The physics of gas chimney and pockmark formation, with implications for assessment of seafloor hazards and gas sequestration: Marine and Petroleum Geology, v. 27, p. 82-91.

Chen, Z., and M. Zha, 2008, Mechanism of overpressured fluid compartment and its controlling on hydrocarbon migration and accumulation in faulted lacustrine basin: A case study from the Dongying Sag, Bohai Bay Basin: Scientia Geologica Sinica, v. 43, p. 50-64.

Childs, C., Ø. Sylta, S. Moriya, N. Morewood, T. Manzocchi, J. J. Walsh, and D. Hermanssen, 2009, Calibrating fault seal using a hydrocarbon migration model of the Oseberg Syd area, Viking Graben: Marine and Petroleum Geology, v. 26, p. 764-774.

Childs, C., Ø. Sylta, S. Moriya, J. J. Walsh, and T. Manzocchi, 2002, A method for including the capillary properties of faults in hydrocarbon migration models, p. 127-139.

Chopra, S., J. Castagna, and O. Portniaguine, 2006, Thin-bed reflectivity inversion, p. 2057-2061.

Chopra, S., J. Castagna, and Y. Xu, 2009, Thin-bed reflectivity inversion and some applications: First Break, v. 27, p. 55-62.

Clarke, S. M., S. D. Burley, G. D. Williams, A. J. Richards, D. J. Meredith, and S. S. Egan, 2006, Integrated four-dimensional modelling of sedimentary basin architecture and hydrocarbon migration, p. 185-211.

Clennell, M. B., M. Hovland, J. S. Booth, P. Henry, and W. J. Winters, 1999, Formation of natural gas hydrates in marine sediments 1. Conceptual model of gas hydrate growth conditioned by

host sediment properties: Journal of Geophysical Research B: Solid Earth, v. 104, p. 22985-23003.

Cohen, L., 1995, Time-Frequency Analysis: Prentice Hall Signal Processing: New Jersey, Prentice Hall.

Cole, D., S. A. Stewart, and J. A. Cartwright, 2000, Giant irregular pockmark craters in the Palaeogene of the Outer Moray Firth Basin, UK North Sea: Marine and Petroleum Geology, v. 17, p. 563-577.

Cooley J.W. and J.W. Tukey, 1965, An algorithm for the machine calculation of complex Fourier series, Mathematics of Computation, v. 19,297-301.

Cooper, C., 2001, Mud volcanoes of Azerbaijan visualized using 3D seismic depth cubes: the importance of overpressured fluid and gas instead of non-extant diapirs. In: Abstr Vol Subsurface Sediment Mobilization Conf, 10–13 September, Ghent, Belgium, p 71.

Cunningham, A. P., and Barker, P. F., 1996, Evidence for westward-flowing Weddell Sea Deep Water in the Falkland Trough, western South Atlantic: Deep-Sea Research Part I: Oceanographic Research Papers, v. 43, no. 5, p. 643-654.

Davies, R., B. R. Bell, J. A. Cartwright, and S. Shoulders, 2002, Three-dimensional seismic imaging of Paleogene dike-fed submarine volcanoes from the northeast Atlantic margin: Geology, v. 30, p. 223-226.

Davies, R. J., 2003, Kilometer-scale fluidization structures formed during early burial of a deep-water slope channel on the Niger Delta: Geology, v. 31, p. 949-952.

Davies, R. J., and J. Cartwright, 2002, A fossilized Opal A to Opal C/T transformation on the northeast Atlantic margin: Support for a significantly elevated palaeogeothermal gradient during the Neogene?: Basin Research, v. 14, p. 467-486.

Davies, R. J., and S. A. Stewart, 2005, Emplacement of giant mud volcanoes in the South Caspian Basin: 3D seismic reflection imaging of their root zones: Journal of the Geological Society, v. 162, p. 1-4.

Davis, E. E., R. D. Hyndman, and H. Villinger, 1990, Rates of fluid expulsion across the northern Cascadia accretionary prism: constraints from new heat flow and multichannel seismic reflection data: Journal of Geophysical Research, v. 95, p. 8869-8889.

De Boever, E., P. Muchez, R. Swennen, and L. Dimitrov, 2011, Evolution of deformation and fault-related fluid flow withan ancient methane seep system (Eocene, Varna, Bulgaria): Geofluids, v. 11, p. 166-183.

Del Ben, A., and A. Mallardi, 2004, Interpretation and chronostratigraphic mapping of multichannel seismic reflection profile I95167, eastern Falkland Plateau (South Atlantic): Marine Geology, v. 209, p. 347-361.

Demirbas, A., 2010, Methane hydrates as potential energy resource: Part 1 - Importance, resource and recovery facilities: Energy Conversion and Management, v. 51, p. 1547-1561.

Deville, E., A. Battani, R. Griboulard, S. Guerlais, J. P. Herbin, J. P. Houzay, C. Muller, and A. Prinzhofer, 2003, The origin and processes of mud volcanism: New insights from Trinidad, Geological Society Special Publication, p. 475-490.

Dilay, A. J., 1982, DIRECT HYDROCARBON INDICATORS LEAD TO CANADIAN GAS FIND: WORLD OIL, v. V 195.

Dillon, W. P., W. S. Holbrook, R. Drury, J. Gettrust, D. Hutchinson, J. Booth, and M. Taylor, 1997, Faulting of gas-hydrate-bearing marine sediments - contribution to permeability: Proceedings of the Annual Offshore Technology Conference, p. 8296.

Dimitrov, L. I., 2002, Mud volcanoes-the most important pathway for degassing deeply buried sediments: Earth-Science Reviews, v. 59, p. 49-76.

Domenico, S., 1974, EFFECT OF WATER SATURATION ON SEISMIC REFLECTIVITY OF SAND RESERVOIRS ENCASED IN SHALE: GEOPHYSICS, v. 39, p. 759-769.

Duerto, L., and McClay, K., 2011, Role of the shale tectonics on the evolution of the Eastern Venezuelan Cenozoic thrust and fold belt: Marine and Petroleum Geology, v. 28, no. 1, p. 81-108.

Dumke, I., Berndt, C., Crutchley, G. J., Krause, S., Liebetrau, V., Gay, A., and Couillard, M., 2014, Seal bypass at the Giant Gjallar Vent (Norwegian Sea): Indications for a new phase of fluid venting at a 56-Ma-old fluid migration system: Marine Geology, v. 351, p. 38-52.

Durand, B., 1988, Understanding of HC migration in sedimentary basins (present state of knowledge): Organic Geochemistry, v. 13, p. 445-459.

Duranti, D., and A. Hurst, 2004, Fluidization and injection in the deep-water sandstones of the Eocene Alba Formation (UK North Sea): Sedimentology, v. 51, p. 503-529.

Ecker, C., J. Dvorkin, and A. Nur, 1998, Sediments with gas hydrates: Internal structure from seismic AVO: Geophysics, v. 63, p. 1659-1669.

England, W. A., A. S. Mackenzie, D. M. Mann, and T. M. Quigley, 1987, The movement and entrapment of petroleum fluids in the subsurface: Journal of the Geological Society, v. 144, p. 327-347.

Etiope, G., A. Feyzullayev, and C. L. Baciu, 2009, Terrestrial methane seeps and mud volcanoes: A global perspective of gas origin: Marine and Petroleum Geology, v. 26, p. 333-344.

Etiope, G., and Klusman, R. W., 2002, Geologic emissions of methane to the atmosphere: Chemosphere, v. 49, no. 8, p. 777-789.

Etiope, G., and G. Martinelli, 2002, Migration of carrier and trace gases in the geosphere: An overview: Physics of the Earth and Planetary Interiors, v. 129, p. 185-204.

Fish, P., 2005, Frontier South, east Falkland basins reveal important exploration potential: Oil and Gas Journal, v. 45, p. 34-40.

Fisher, Q. J., S. D. Harris, E. McAllister, R. J. Knipe, and A. J. Bolton, 2001, Hydrocarbon flow across faults by capillary leakage revisited: Marine and Petroleum Geology, v. 18, p. 251-257.

Flemings, P. B., X. Liu, and W. J. Winters, 2003, Critical pressure and multiphase flow in Blake Ridge gas hydrates: Geology, v. 31, p. 1057-1060.

Foucher, J. P., H. Nouzé, and P. Henry, 2002, Observation and tentative interpretation of a double BSR on the Nankai slope: Marine Geology, v. 187, p. 161-175.

Foschi, M., Cartwright, J. A., Peel, F. J., 2014. Vertical anomaly cluster: evidence for vertical gas migration across multi-layered sealing sequence. AAPG Bulletin, V. 98, No. 9, P. 1859–1884.

Francis, A., 1997, Acoustic impedance inversion pitfalls and some fuzzy analysis: Leading Edge (Tulsa, OK), v. 16, p. 275.

Galeazzi, J. S., 1996, Cuenca de Malvinas. In V. A. Ramos, & M. A. Turic (Eds.), Geologı´a y recursos naturales de la plataforma continental Argentina (pp. 273–309). XIII Congreso Geolo´gico Argentino y III Congreso de Exploracion de Hidrocarburos (Buenos Aires).

Gamage, K., E. Screaton, B. Bekins, and I. Aiello, 2011, Permeability-porosity relationships of subduction zone sediments: Marine Geology, v. 279, p. 19-36.

Gay, A., M. Lopez, C. Berndt, and M. Séranne, 2007, Geological controls on focused fluid flow associated with seafloor seeps in the Lower Congo Basin: Marine Geology, v. 244, p. 68-92.

Gay, A., M. Lopez, P. Cochonat, M. Séranne, D. Levaché, and G. Sermondadaz, 2006, Isolated seafloor pockmarks linked to BSRs, fluid chimneys, polygonal faults and stacked

Oligocene–Miocene turbiditic palaeochannels in the Lower Congo Basin: Marine Geology, v. 226, p. 25-40.

Gay, A., M. Lopez, P. Cochonat, and G. Sermondadaz, 2004, Polygonal faults-furrows system related to early stages of compaction - upper Miocene to recent sediments of the Lower Congo Basin: Basin Research, v. 16, p. 101-116.

Gay, A., M. Lopez, P. Cochonat, N. Sultan, E. Cauquil, and F. Brigaud, 2003, Sinuous pockmark belt as indicator of a shallow buried turbiditic channel on the lower slope of the Congo basin, west African margin, Geological Society Special Publication, p. 173-189.

Gay, A., R. Mourgues, C. Berndt, D. Bureau, S. Planke, D. Laurent, S. Gautier, C. Lauer, and D. Loggia, 2012, Anatomy of a fluid pipe in the Norway Basin: Initiation, propagation and 3D shape: Marine Geology, v. 332-334, p. 75-88.

Gennari, G., S. Spezzaferri, M. C. Comas, A. Rüggeberg, C. Lopez-Rodriguez, and L. M. Pinheiro, 2013, Sedimentary sources of the mud-breccia and mud volcanic activity in the western Alboran Basin: Marine Geology, v. 339, p. 83-95.

Ghiglione, M. C., Quinteros, J., Yagupsky, D., Bonillo-Martínez, P., Hlebszevtich, J., Ramos, V. A., Vergani, G., Figueroa, D., Quesada, S., and Zapata, y. T., 2010, Structure and tectonic history of the foreland basins of southernmost South America: Journal of South American Earth Sciences, v. 29, no. 2, p. 262-277.

Gorman, A. R., W. S. Holbrook, M. J. Hornbach, K. L. Hackwith, D. Lizarralde, and I. Pecher, 2002, Migration of methane gas through the hydrate stability zone in a low-flux hydrate province: Geology, v. 30, p. 327-330.

Graue, K., 2000, Mud volcanoes in deepwater Nigeria: Marine and Petroleum Geology, v. 17, p. 959-974.

Grauls, D., 2001, Gas hydrates: importance and applications in petroleum exploration: Marine and Petroleum Geology, v. 18, p. 519-523.

Gray, S. H., J. Etgen, J. Dellinger, and D. Whitmore, 2001, Seismic migration problems and solutions: Geophysics, v. 66, p. 1622-1640.

Granli, J. R., Arntsen, B., Sollid, A., and Hilde, E., 1999, Imaging through gas-filled sediments using marine shear-wave data: Geophysics, v. 64, no. 3, p. 668-677.

Haacke, R. R., G. K. Westbrook, and R. D. Hyndman, 2007, Gas hydrate, fluid flow and free gas: Formation of the bottom-simulating reflector: Earth and Planetary Science Letters, v. 261, p. 407-420.

Hammond, A., 1974, Bright Spot: Better seismological indicator of oil and gas: Science, 185, 515-517

Han, L., M. D. Sacchi, and L. Han, 2014, Spectral decomposition and de-noising via time-frequency and space-wavenumber reassignment: Geophysical Prospecting, v. 62, p. 244-257.

Hansen, D. M., and Cartwright, J., 2006, Saucer-shaped sill with lobate morphology revealed by 3D seismic data: Implications for resolving a shallow-level sill emplacement mechanism: Journal of the Geological Society, v. 163, no. 3, p. 509-523.

Hashemi, H., D. M. J. Tax, R. P. W. Duin, A. Javaherian, and P. De Groot, 2008, Gas chimney detection based on improving the performance of combined multilayer perceptron and support vector classifier: Nonlinear Processes in Geophysics, v. 15, p. 863-871.

Heggland, R., 1997, Detection of gas migration from a deep source by the use of exploration 3D seismic data: Marine Geology, v. 137, p. 41-47.

Heggland, R., 1998, Gas seepage as an indicator of deeper prospective reservoirs. A study based on exploration 3D seismic data: Marine and Petroleum Geology, v. 15, p. 1-9.

Helgerud, M. B., J. Dvorkin, A. Nur, A. Sakai, and T. Collett, 1999, Elastic-wave velocity in marine sediments with gas hydrates: Effective medium modeling: Geophysical Research Letters, v. 26, p. 2021-2024.

Henriet, J. P., M. De Batist, and M. Verschuren, 1991, Early fracturing of Palaeogene clays, southernmost North Sea: relevance to mechanisms of primary hydrocarbon migration: Generation, accumulation, and production of Europe's hydrocarbons, p. 217-227.

Heum, O. R., 1996, A fluid dynamic classification of hydrocarbon entrapment: Petroleum Geoscience, v. 2, p. 145-158.

Holbrook, W. S., H. Hoskins, W. T. Wood, R. A. Stephen, and D. Lizarralde, 1996, Methane hydrate and free gas on the Blake Ridge from vertical seismic profiling: Science, v. 273, p. 1840-1843.

Hood, K. C., L. M. Wenger, P. GrossO, and S. C. Harrison, 2002, Hydrocarbon Systems Analysis of the Northern Gulf of Mexico: Delineation of Hydrocarbon Migration Pathways Using Seeps and Seismic Imaging, in Schumacher and L. A. LeSchack, ed., Surface exploration case histories: Applications of geochemistry, magnetics, and remote sensing, , v. 48, p. 25–40.

Hornbach, M. J., D. M. Saffer, and W. S. Holbrook, 2004, Critically pressured free-gas reservoirs below gas-hydrate provinces: Nature, v. 427, p. 142-144.

Horozal, S., G. H. Lee, B. Y. Yi, D. G. Yoo, K. P. Park, H. Y. Lee, W. Kim, H. J. Kim, and K. Lee, 2009, Seismic indicators of gas hydrate and associated gas in the Ulleung Basin, east Sea (Japan Sea) and implications of heat flows derived from depths of the bottom-simulating reflector: Marine Geology, v. 258, p. 126-138.

Hovland, M., 1983, Elongated depressions associated with pockmarks in the western Slope of the Norwegian Trench: Marine Geology, v. 51, p. 35-46.

Hovland, M., J. V. Gardner, and A. G. Judd, 2002, The significance of pockmarks to understanding fluid flow processes and geohazards: Geofluids, v. 2, p. 127-136.

Hovland, M., and A. G. Judd, 1988, Seabed pockmarks and seepages: impact on geology, biology and the marine environment: Seabed pockmarks and seepages: impact on geology, biology and the marine environment.

Hovland, M., H. Svensen, C. F. Forsberg, H. Johansen, C. Fichler, J. H. Fosså, R. Jonsson, and H. Rueslåtten, 2005, Complex pockmarks with carbonate-ridges off mid-Norway: Products of sediment degassing: Marine Geology, v. 218, p. 191-206.

Hunt, J. M., 1984, Generation and migration of light hydrocarbons: Science, v. 226, p. 1265-1270.

Hustoft, S., Mienert, J., Bünz, S., and Nouzé, H., 2007, High-resolution 3D-seismic data indicate focussed fluid migration pathways above polygonal fault systems of the mid-Norwegian margin: Marine Geology, v. 245, no. 1-4, p. 89-106.

Hustoft, S., S. Bünz, J. Mienert, and S. Chand, 2009, Gas hydrate reservoir and active methane-venting province in sediments on < 20 Ma young oceanic crust in the Fram Strait, offshore NW-Svalbard: Earth and Planetary Science Letters, v. 284, p. 12-24.

Hustoft, S., S. Bünz, and J. Mienert, 2010, Three-dimensional seismic analysis of the morphology and spatial distribution of chimneys beneath the Nyegga pockmark field, offshore mid-Norway: Basin Research, v. 22, p. 465-480.

Hyndman, R. D., and G. D. Spence, 1992, A seismic study of methane hydrate marine bottom simulating reflectors: Journal of Geophysical Research, v. 97, p. 6683-6698.

Ilg, B. R., S. Hemmings-Sykes, A. Nicol, J. Baur, M. Fohrmann, R. Funnell, and M. Milner, 2012, Normal faults and gas migration in an active plate boundary, southernTaranaki Basin, offshore New Zealand: AAPG Bulletin, v. 96, p. 1733-1756.

Imbert, P., 2009, Seismic-scale expression of fluid sourcing, circulation and expulsion in sedimentary series: Society of Petroleum Engineers - International Petroleum Technology Conference 2009, IPTC 2009, p. 3224-3237.

Imbert, P., and S. Ho, 2012, Seismic-scale funnel-shaped collapse features from the Paleocene-Eocene of the North west Shelf of Australia: Marine Geology, v. 332-334, p. 198-221.

Ingram, G. M., and J. L. Urai, 1999, Top-seal leakage through faults and fractures: the role of mudrock properties, p. 125-135.

Ivanov, M., A. Mazzini, V. Blinova, E. Kozlova, J. S. Laberg, T. Matveeva, M. Taviani, and N. Kaskov, 2010, Seep mounds on the Southern Vøring Plateau (offshore Norway): Marine and Petroleum Geology, v. 27, p. 1235-1261.

Jain, A. K., and R. Juanes, 2009, Preferential mode of gas invasion in sediments: Grain-scale mechanistic model of coupled multiphase fluid flow and sediment mechanics: Journal of Geophysical Research B: Solid Earth, v. 114.

Jin, Z., J. Cao, W. Hu, Y. Zhang, S. Yao, X. Wang, Y. Zhang, Y. Tang, and X. Shi, 2008, Episodic petroleum fluid migration in fault zones of the northwestern Junggar Basin (nortwest China): Evidence from hydrocarbon-bearing zoned calcite cement: AAPG Bulletin, v. 92, p. 1225-1243.

Koh, C. A., and Sloan, E. D., 2007, Natural gas hydrates: Recent advances and challenges in energy and environmental applications: AIChE Journal, v. 53, no. 7, p. 1636-1643.

Kopf, A. J., 2002, Significance of mud volcanism: Reviews of Geophysics, v. 40, no. 2, p. 2-1 - 2-52.

Korenaga, J., W. S. Holbrook, S. C. Singh, and T. A. Minshull, 1997, Natural gas hydrates on the southeast U.S. margin: Constraints from full waveform and travel time inversions of wide-angle seismic data: Journal of Geophysical Research B: Solid Earth, v. 102, p. 15345-15365.

Korneev, V. A., G. M. Goloshubin, T. M. Daley, and D. B. Silin, 2004, Seismic low-frequency effects in monitoring fluid-saturated reservoirs: Geophysics, v. 69, p. 522-532.

Krooss, B. M., and D. Leythaeuser, 1996, Molecular diffusion of light hydrocarbons in sedimentary rocks and its role in migration and dissipation of natural gas: AAPG Memoir, p. 173-183.

Kuo, L. C., 1997, Gas exsolution during fluid migration and its relation to overpressure and petroleum accumulation: Marine and Petroleum Geology, v. 14, p. 221-229.

Law, B. E., 2002, Basin-centered gas systems: AAPG Bulletin, v. 86, no. 11, p. 1891-1919.

Leduc, A. M., R. J. Davies, R. E. Swarbrick, and J. Imber, 2013, Fluid flow pipes triggered by lateral pressure transfer in the deepwater western Niger Delta: Marine and Petroleum Geology, v. 43, p. 423-433.

Leythaeuser, D., R. G. Schaefer, C. Cornford, and B. Weiner, 1979, Generation and migration of light hydrocarbons (C2C7) in sedimentary basins: Organic Geochemistry, v. 1, p. 191-204.

Leythaeuser, D., R. G. Schaefer, and A. Yukler, 1982, Role of diffusion in primary migration of hydrocarbons: American Association of Petroleum Geologists Bulletin, v. 66, p. 408-429.

Li, K., X. Zhao, X. Zhang, and B. Ye, 2007, Hydrocarbon migration pathway system types and evolution in the akekule rise, Tarim Basin: Scientia Geologica Sinica, v. 42, p. 766-778.

Li, L., X. Lei, X. Zhang, and Z. Sha, 2013, Gas hydrate and associated free gas in the Dongsha Area of northern South China Sea: Marine and Petroleum Geology, v. 39, p. 92-101.

Li, Y. P., P. Y. Sun, G. Y. Wei, D. L. Tang, and Y. Q. He, 2009, Using 3-C land seismic data to improve structural imaging in gas chimney area: Shiyou Diqiu Wuli Kantan/Oil Geophysical Prospecting, v. 44, p. 417-424.

Liu, X., and P. B. Flemings, 2006, Passing gas through the hydrate stability zone at southern Hydrate Ridge, offshore Oregon: Earth and Planetary Science Letters, v. 241, p. 211-226.

Liu, X., and P. B. Flemings, 2007, Dynamic multiphase flow model of hydrate formation in marine sediments: Journal of Geophysical Research B: Solid Earth, v. 112.

Loizou, N., Liu, E., and Chapman, M., 2008, AVO analyses and spectral decomposition of seismic data from four wells west of Shetland, UK: Petroleum Geoscience, v. 14, no. 4, p. 355-368.

Loncke, L., and J. Mascle, 2004, Mud volcanoes, gas chimneys, pockmarks and mounds in the Nile deep-sea fan (eastern Mediterranean): Geophysical evidences: Marine and Petroleum Geology, v. 21, p. 669-689.

Lorenzo, J. M., and J. C. Mutter, 1988, Seismic stratigraphy and tectonic evolution of the Falkland/Malvinas Plateau: Revista Brasileira de Geociencias, v. 18, p. 191-200.

Løseth, H., M. Gading, and L. Wensaas, 2009, Hydrocarbon leakage interpreted on seismic data: Marine and Petroleum Geology, v. 26, p. 1304-1319.

Løseth, H., L. Wensaas, B. Arntsen, N. M. Hanken, C. Basire, and K. Graue, 2011, 1000 m long gas blow-out pipes: Marine and Petroleum Geology, v. 28, p. 1040-1060.

Løseth, H., L. Wensaas, B. Arntsen, and M. Hovland, 2003, Gas and fluid injection triggering shallow mud mobilization in the Hordaland Group, North Sea, Geological Society Special Publication, p. 139-157.

Losh, S., L. Eglinton, M. Schoell, and J. Wood, 1999, Vertical and lateral fluid flow related to a large growth fault, South Eugene Island Block 330 field, offshore Louisiana: AAPG Bulletin, v. 83, p. 244-276.

Loughlin, P. J., Pitton, J. W., and Atlas, L. E., 1993, Bilinear time-frequency representations. New insights and properties: IEEE Transactions on Signal Processing, v. 41, no. 2, p. 750-767.

Lu, Z., and N. Sultan, 2008, Empirical expression for gas hydrate stability law, its volume fraction and mass-density at temperatures 273.15 K to 290.15 K: Geochemical Journal, v. 42, p. 163-175.

Ludwig, W. J., 1983, Geologic framework of the Falkland Plateau: Initial reports DSDP, Leg 71, Valparaiso to Santos, 1980, part 1, p. 281-293.

Luo, X., 2011, Simulation and characterization of pathway heterogeneity of secondary hydrocarbon migration: AAPG Bulletin, v. 95, p. 881-898.

Luo, X., Y. Lei, L. Zhang, R. Chen, Z. Chen, J. Xu, and J. Zhao, 2012, Characterization of carrier formation for hydrocarbon migration: Concepts and approaches: Shiyou Xuebao/Acta Petrolei Sinica, v. 33, p. 428-436.

Macdonald, D., I. Gomez-Perez, J. Franzese, L. Spalletti, L. Lawver, L. Gahagan, I. Dalziel, C. Thomas, N. Trewin, M. Hole, and D. Paton, 2003, Mesozoic break-up of SW Gondwana: Implications for regional hydrocarbon potential of the southern South Atlantic: Marine and Petroleum Geology, v. 20, p. 287-308.

MacDonald, I. R., I. Leifer, R. Sassen, P. Stine, R. Mitchell, and N. Guinasso Jr, 2002, Transfer of hydrocarbons from natural seeps to the water column and atmosphere: Geofluids, v. 2, p. 95-107.

Macelloni, L., A. Simonetti, J. H. Knapp, C. C. Knapp, C. B. Lutken, and L. L. Lapham, 2012, Multiple resolution seismic imaging of a shallow hydrocarbon plumbing system, Woolsey Mound, Northern Gulf of Mexico: Marine and Petroleum Geology, v. 38, p. 128-142.

Mandl, G., and R. M. Harkness, 1987, Hydrocarbon migration by hydraulic fracturing, p. 39-53.

Manzocchi, T., C. Childs, and J. J. Walsh, 2010, Faults and fault properties in hydrocarbon flow models: Geofluids, v. 10, p. 94-113.

Martin, A. K., 1986, Plate tectonics: Microplates in Antartica: Nature, v. 319, p. 100-101.

Martin, A. K., S. W. Goodlad, C. J. H. Hartnady, and A. Du Plessis, 1982, Cretaceous palaeopositions of the Falkland Plateau relative to southern Africa using Mesozoic seafloor spreading anomalies: Geophysical Journal, v. 71, p. 567-579.

Marynowski, L., A. Gaweda, S. Cebulak, and M. Jędrysek, 2001, Hydrocarbons migration in tectonic zones of the western Tatra Mountains Crystalline basement (Central western Carpathians): Geologica Carpathica, v. 52, p. 3-14.

Mastalerz, V., G. J. de Lange, A. Dählmann, and T. Feseker, 2007, Active venting at the Isis mud volcano, offshore Egypt: Origin and migration of hydrocarbons: Chemical Geology, v. 246, p. 87-106.

Mascle, J., Mary, F., Praeg, D., Brosolo, L., Camera, L., Ceramicola, S., and Dupré, S., 2014, Distribution and geological control of mud volcanoes and other fluid/free gas seepage features in the Mediterranean Sea and nearby Gulf of Cadiz: Geo-Marine Letters, v. 34, no. 2-3, p. 89-110.

Mavko, G., T. Mukerji, and J. Dvorkin, 2009, The Rock Physics Handbook: Tools for Seismic Analysis in Porous Media, 2nd edition: Cambridge, Cambridge University Press.

Max, M. D., and A. Lowrie, 1996, Oceanic methane hydrates: A "Frontier" gas resource: Journal of Petroleum Geology, v. 19, p. 41-56.

McKerrow, W. S., C. R. Scotese, and M. D. Brasier, 1992, Early Cambrian continental reconstructions: Journal - Geological Society (London), v. 149, p. 599-606.

Medialdea, T., L. Somoza, L. M. Pinheiro, M. C. Fernández-Puga, J. T. Vázquez, R. León, M. K. Ivanov, V. Magalhaes, V. Díaz-del-Río, and R. Vegas, 2009, Tectonics and mud volcano development in the Gulf of Cádiz: Marine Geology, v. 261, p. 48-63.

Meldahl, P., R. Heggland, B. Bril, and P. De Groot, 2001, Identifying faults and gas chimneys using multiattributes and neural networks: Leading Edge (Tulsa, OK), v. 20, p. 474-476+478+481-482.

Mello, U. T., and Karner, G. D., 1996, Development of sediment overpressure and its effect on thermal maturation: Application to the Gulf of Mexico basin: AAPG Bulletin, v. 80, no. 9, p. 1367-1396.

Milkov, A. V., 2000, Worldwide distribution of submarine mud volcanoes and associated gas hydrates: Marine Geology, v. 167, p. 29-42.

Millahn, K. O., H. Koitka, D. Jurczyk, and W. S. Jankowsky, 1978, Direct detection of hydrocarbons using seismic procedures. p. 133. Hanover, Germany, Prakla-Seismos GmbH.

Mitchell, C., G. K. Taylor, K. G. Cox, and J. Shaw, 1986, Are the Falkland Islands a rotated microplate?: Nature, v. 319, p. 131-134.

Moretti, I., 1998, The role of faults in hydrocarbon migration: Petroleum Geoscience, v. 4, p. 81-94.

Morgan, J., M. Warner, G. the Chicxulub Working, J. Brittan, R. Buffler, A. Camargo, G. Christeson, P. Denton, A. Hildebrand, R. Hobbs, H. Macintyre, G. Mackenzie, P. Maguire, L. Marin, Y. Nakamura, M. Pilkington, V. Sharpton, D. Snyder, G. Suarez, and A. Trejo, 1997, Size and morphology of the Chicxulub impact crater: Nature, v. 390, p. 472-476.

Moss, J. L., and J. Cartwright, 2010, 3D seismic expression of km -scale fluid escape pipes from offshore Namibia: Basin Research, v. 22, p. 481-501.

Moss, J. L., J. Cartwright, and R. Moore, 2012, Evidence for fluid migration following pockmark formation: Examples from the Nile Deep Sea Fan: Marine Geology, v. 303-306, p. 1-13.

Mourgues, R., D. Bureau, L. Bodet, A. Gay, and J. B. Gressier, 2012, Formation of conical fractures in sedimentary basins: Experiments involving pore fluids and implications for sandstone intrusion mechanisms: Earth and Planetary Science Letters, v. 313-314, p. 67-78.

Mourgues, R., and P. R. Cobbold, 2003, Some tectonic consequences of fluid overpressures and seepage forces as demonstrated by sandbox modelling: Tectonophysics, v. 376, p. 75-97.

Mullins, O.C. and Sheu, E.Y., 1999, Structures and Dynamics of Asphaltenes, 1st ed: Springer, 31.

Nichols, R. J., R. S. J. Sparks, and C. J. N. Wilson, 1994, Experimental studies of the fluidization of layered sediments and the formation of fluid escape structures: Sedimentology, v. 41, p. 233-253.

Norton, I. O., 1982, Paleomotion between Africa, South America, and Antarctica, and implications for the Antarctic Peninsula: Antarctic geoscience. 3rd symposium on Antarctic geology and geophysics, Madison, August 1977, p. 99-106.

Ooms, G., P. F. Mijnlieff, and H. L. Beckers, 1970, Frictional force exerted by a flowing fluid on a permeable particle, with particular reference to polymer coils: The Journal of Chemical Physics, v. 53, p. 4123-4130.

Osborne, M. J., and R. E. Swarbrick, 1997, Mechanisms for generating overpressure in sedimentary basins: A reevaluation: AAPG Bulletin, v. 81, p. 1023-1041.

Ostanin, I., Z. Anka, R. Di Primio, and A. Bernal, 2012a, Hydrocarbon leakage above the Snohvit gas field, Hammerfest Basin SW Barents Sea: First Break, v. 30, p. 55-60.

Ostanin, I., Z. Anka, R. di Primio, and A. Bernal, 2012b, Identification of a large Upper Cretaceous polygonal fault network in the Hammerfest basin: Implications on the reactivation of regional faulting and gas leakage dynamics, SW Barents Sea: Marine Geology, v. 332-334, p. 109-125.

Ostanin, I., Z. Anka, R. di Primio, and A. Bernal, 2013, Hydrocarbon plumbing systems above the Snøhvit gas field: Structural control and implications for thermogenic methane leakage in the Hammerfest Basin, SW Barents Sea: Marine and Petroleum Geology, v. 43, p. 127-146.

Othman, A., 1994, Seismic signal analysis in partially fluid saturated media: Modelled by seismogram synthesis, Journal of King Saud University,Science:6(2):237-263.

Partyka, G., J. Gridley, and J. Lopez, 1999, Interpretational applications of spectral decomposition in reservoir characterization: Leading Edge (Tulsa, OK), v. 18.

Pecher, I. A., N. Kukowski, C. Huebscher, J. Greinert, and J. Bialas, 2001, The link between bottom-simulating reflections and methane flux into the gas hydrate stability zone - New evidence from Lima Basin, Peru Margin: Earth and Planetary Science Letters, v. 185, p. 343-354.

Peng, B., H. Y. Zou, C. Y. Teng, and F. Hao, 2013, Evolution of overpressure and dynamic mechanism of hydrocarbon migration and accumulation in Damintun depression: Zhongguo Shiyou Daxue Xuebao (Ziran Kexue Ban)/Journal of China University of Petroleum (Edition of Natural Science), v. 37, p. 10-16.

Petersen, C. J., S. Bünz, S. Hustoft, J. Mienert, and D. Klaeschen, 2010, High-resolution P-Cable 3D seismic imaging of gas chimney structures in gas hydrated sediments of an Arctic sediment drift: Marine and Petroleum Geology, v. 27, p. 1981-1994.

Pilcher, R., and J. Argent, 2007, Mega-pockmarks and linear pockmark trains on the west African continental margin: Marine Geology, v. 244, p. 15-32.

Pinet, N., M. Duchesne, and D. Lavoie, 2010, Linking a linear pockmark train with a buried Palaeozoic structure: A case study from the St. Lawrence Estuary: Geo-Marine Letters, v. 30, p. 517-522.

Planke, S., H. Svensen, M. Hovland, D. A. Banks, and B. Jamtveit, 2003, Mud and fluid migration in active mud volcanoes in Azerbaijan: Geo-Marine Letters, v. 23, p. 258-267.

Platt, N. H., and P. R. Philip, 1995, Structure of the southern Falkland Islands continental shelf: initial results from new seismic data: Marine and Petroleum Geology, v. 12, p. 759-771.

Plaza-Faverola, A., I. Pecher, G. Crutchley, P. M. Barnes, S. Bünz, T. Golding, D. Klaeschen, C. Papenberg, and J. Bialas, 2014, Submarine gas seepage in a mixed contractional and shear deformation regime: Cases from the Hikurangi oblique-subduction margin: Geochemistry, Geophysics, Geosystems, v. 15, p. 416-433.

Popescu, I., M. De Batist, G. Lericolais, H. Nouzé, J. Poort, N. Panin, W. Versteeg, and H. Gillet, 2006, Multiple bottom-simulating reflections in the Black Sea: Potential proxies of past climate conditions: Marine Geology, v. 227, p. 163-176.

Popescu, I., G. Lericolais, N. Panin, M. De Batist, and H. Gillet, 2007, Seismic expression of gas and gas hydrates across the western Black Sea: Geo-Marine Letters, v. 27, p. 173-183.

Posamentier, H. W., R. J. Davies, J. A. Cartwright, and L. J. Wood, 2007, Seismic geomorphology - An overview, p. 1-14.

Posamentier, H. W., M. T. Jervey, and P. R. Vail, 1988, Eustatic controls on clastic deposition I: conceptual framework: Sea-level changes: an integrated approach, p. 109-124.

Posamentier, H. W., and V. Kolla, 2003, Seismic geomorphology and stratigraphy of depositional elements in deep-water settings: Journal of Sedimentary Research, v. 73, p. 367-388.

Posamentier, H. W., and P. R. Vail, 1988, Eustatic controls on clastic deposition II: sequence and systems tract models: Sea-level changes: an integrated approach, p. 125-154.

Prather, B. E., J. R. Booth, G. S. Steffens, and P. A. Craig, 1998, Classification, lithologic calibration, and stratigraphic succession of seismic facies of intraslope basins, deep-water Gulf of Mexico: AAPG Bulletin, v. 82, p. 701-728.

Prinzhofer, A., and E. Deville, 2013, Origins of hydrocarbon gas seeping out from offshore mud volcanoes in the nile delta: Tectonophysics, v. 591, p. 52-61.

Qiao, Y. F., X. P. Mao, and G. Z. Xin, 2005, Quantitative simulation of hydrocarbon migration: Diqiu Kexue - Zhongguo Dizhi Daxue Xuebao/Earth Science - Journal of China University of Geosciences, v. 30, p. 617-622.

Rajput, S., T. M. Müller, M. B. Clennell, P. P. Rao, and N. K. Thakur, 2012, Constraints on seismic reflections and mode conversions at bottom simulating reflectors associated with gas hydrates: Journal of Petroleum Science and Engineering, v. 88-89, p. 48-60.

Rajput, S., M. K. Sen, and S. Chopra, 2009, Seismic indicators of gas hydrates and associated free gas, SEG Technical Program Expanded Abstracts, p. 2622-2626.

Reilly, M. J., and P. B. Flemings, 2010, Deep pore pressures and seafloor venting in the Auger Basin, Gulf of Mexico: Basin Research, v. 22, p. 380-397.

Riboulot, V., A. Cattaneo, N. Sultan, S. Garziglia, S. Ker, P. Imbert, and M. Voisset, 2013, Sea-level change and free gas occurrence influencing a submarine landslide and pockmark formation and distribution in deepwater Nigeria: Earth and Planetary Science Letters, v. 375, p. 78-91.

Rice, D. D. (1993), Biogenic gas: Controls, habitats, and resource potential, Journal Name: United States Geological Survey, Professional Paper; (United States); Journal Volume: 1570, Medium: X; Size: Pages: 583–606.

Richards, P., I. Duncan, C. Phipps, G. Pickering, J. Grzywacz, R. Hoult, and J. Merritt, 2006, Exploring for fan and delta sandstones in the offshore Falklands Basins: Journal of Petroleum Geology, v. 29, p. 199-214.

Richards, P. C., R. W. Gatliff, M. F. Quinn, J. P. Williamson, and N. G. T. Fannin, 1996, The geological evolution of the Falkland Islands continental shelf, p. 105-128.

Richards, P. C., P. Stone, G. S. Kimbell, W. C. McIntosh, and E. R. Phillips, 2013, Mesozoic magmatism in the Falkland Islands (South Atlantic) and their offshore sedimentary basins: Journal of Petroleum Geology, v. 36, p. 61-73.

Rise, L., J. Sættem, S. Fanavoll, T. Thorsnes, D. Ottesen, and R. Bøe, 1999, Sea-bed pockmarks related to fluid migration from Mesozoic bedrock strata in the Skagerrak offshore Norway: Marine and Petroleum Geology, v. 16, p. 619-631.

Rollet, N., S. McGiveron, T. Hashimoto, R. Hackney, P. Petkovic, K. Higgins, E. Grosjean, and G. A. Logan, 2012, Seafloor features and fluid migration in the Capel and Faust basins, offshore eastern Australia: Marine and Petroleum Geology, v. 35, p. 269-291.

Rozhko, A. Y., 2010, Role of seepage forces on seismicity triggering: Journal of Geophysical Research B: Solid Earth, v. 115.

Rozhko, A. Y., Y. Y. Podladchikov, and F. Renard, 2007, Failure patterns caused by localized rise in pore-fluid overpressure and effective strength of rocks: Geophysical Research Letters, v. 34.

Rubino, J. G., and Velis, D., 2009, Thin-bed prestack spectral inversion: Geophysics, v. 74, no. 4, p. R49-R57.

Rudkiewicz, J. L., O. Brévart, J. Connan, and F. Montel, 1994, Primary migration behaviour of hydrocarbons: from laboratory experiments to geological situations through fluid flow models: Organic Geochemistry, v. 22, p. 631-639,IN7-IN8.

Ruppel, C., G. R. Dickens, D. G. Castellini, W. Gilhooly, and D. Lizarralde, 2005, Heat and salt inhibition of gas hydrate formation in the northern Gulf of Mexico: Geophysical Research Letters, v. 32, p. L04605.

Rutherford, S. R. and Willimas, R. H., 1989, Amplitude-versus-offset variations in gas sands: Geophysics, 54, 680–688.

Salguero-Hernández, E., J. Urrutia-Fucugauchi, and L. Ramírez-Cruz, 2010, Fracturing and deformation in the Chicxulub crater - Complex trace analysis of instantaneous seismic attributes: Revista mexicana de ciencias geológicas, v. 27, p. 175-184.

Sandvik, E. I., and J. N. Mercer, 1990, Primary migration by bulk hydrocarbon flow: Organic Geochemistry, v. 16, p. 83-89.

Satyavani, N., N. K. Thakur, N. Aravind Kumar, and S. I. Reddi, 2005, Migration of methane at the diapiric structure of the western continental margin of India - Insights from seismic data: Marine Geology, v. 219, p. 19-25.

Satyavani, N., N. K. Thakur, U. Shankar, S. I. Reddi, A. R. Sridhar, P. Prasada Rao, K. Sain, and R. Khanna, 2003, Indicators of gas hydrates: Role of velocity and amplitude: Current Science, v. 85, p. 1360-1363.

Schowalter, T. T., 1979, Mechanics of secondary hydrocarbon migration and entrapment: AAPG Bulletin, v. 63, p. 723-760.

Schroot, B. M., G. T. Klaver, and R. T. E. Schüttenhelm, 2005, Surface and subsurface expressions of gas seepage to the seabed - Examples from the Southern North Sea: Marine and Petroleum Geology, v. 22, p. 499-515.

Schroot, B. M., and R. T. E. Schüttenhelm, 2003b, Shallow gas and gas seepage: Expressions on seismic and other acoustic data from the Netherlands North Sea: Journal of Geochemical Exploration, v. 78-79, p. 305-309.

Selley, R. C., 1985, Elements of petroleum geology: Elements of petroleum geology.

Shankar, U., and M. Riedel, 2013, Heat flow and gas hydrate saturation estimates from Andaman Sea, India: Marine and Petroleum Geology, v. 43, p. 434-449.

Shelander, D., J. Dai, and G. Bunge, 2010, Predicting saturation of gas hydrates using pre-stack seismic data, Gulf of Mexico: Marine Geophysical Researches, v. 31, p. 39-57.

Shelander, D., J. Dai, G. Bunge, S. Singh, M. Eissa, and K. Fisher, 2012, Estimating saturation of gas hydrates using conventional 3D seismic data, Gulf of Mexico Joint Industry Project Leg II: Marine and Petroleum Geology, v. 34, p. 96-110.

Sheriff, R. E., 1975, Factors affecting seismic amplitudes: Geophysical Prospecting, v. 23, p. 125-138.

Sheriff, R. E., and Geldart, L. P., 1982, Exploration seismology. Volume 1: history, theory, and data acquisition: Exploration seismology. Volume 1: history, theory, and data acquisition.

Shuey, R.T., 1985, A simplification of the Zoeppritz equations: Geophysics, 50, 609-614.

Shurr, G. W., and J. L. Ridgley (2002), Unconventional shallow biogenic gas systems, American Association of Petroleum Geologists Bulletin, 86(11), 1939–1969.

Sloan Jr, E. D., 2003, Fundamental principles and applications of natural gas hydrates: Nature, v. 426, no. 6964, p. 353-359.

Somoza, L., T. Medialdea, R. León, G. Ercilla, J. T. Vázquez, M. Farran, J. Hernández-Molina, J. González, C. Juan, and M. C. Fernández-Puga, 2012, Structure of mud volcano systems and pockmarks in the region of the Ceuta Contourite Depositional System (western Alborán Sea): Marine Geology, v. 332-334, p. 4-26.

Spinelli, G. A., E. R. Giambalvo, and A. T. Fisher, 2004, Sediment permeability, distribution, and influence on fluxes in oceanic basement, in E. E. D. a. H. Elderfield, ed., Hydrogeology of the Oceanic Lithosphere, Cambridge University Press.

Stadnitskaia, A., M. K. Ivanov, E. N. Poludetkina, R. Kreulen, and T. C. E. van Weering, 2008, Sources of hydrocarbon gases in mud volcanoes from the Sorokin Trough, NE Black Sea, based on molecular and carbon isotopic compositions: Marine and Petroleum Geology, v. 25, p. 1040-1057.

Stainforth, J. G., and J. E. A. Reinders, 1990, Primary migration of hydrocarbons by diffusion through organic matter networks, and its effect on oil and gas generation: Organic Geochemistry, v. 16, p. 61-74.

Stauffer, D., 1979, Scaling theory of percolation clusters: Physics Reports, v. 54, p. 1-74.

Stewart, S. A., 1999, Seismic interpretation of circular geological structures: Petroleum Geoscience, v. 5, p. 273-285.

Stewart, S. A., and P. J. Allen, 2002, A 20-km -diameter multi-ringed impact structure in the North Sea: Nature, v. 418, p. 520-523.

Stewart, S. A., and R. J. Davies, 2006, Structure and emplacement of mud volcano systems in the South Caspian Basin: AAPG Bulletin, v. 90, p. 771-786.

Sultan, N., P. Cochonat, J. P. Foucher, and J. Mienert, 2004, Effect of gas hydrates melting on seafloor slope instability: Marine Geology, v. 213, p. 379-401.

Sun, Q., J. Cartwright, S. Wu, and D. Chen, 2013, 3D seismic interpretation of dissolution pipes in the South China Sea: Genesis by subsurface, fluid induced collapse: Marine Geology, v. 337, p. 171-181.

Sun, Q., S. Wu, J. Cartwright, and D. Dong, 2012a, Shallow gas and focused fluid flow systems in the Pearl River Mouth Basin, northern South China Sea: Marine Geology, v. 315-318, p. 1-14.

Sun, Q., S. Wu, M. Hovland, P. Luo, Y. Lu, and T. Qu, 2011, The morphologies and genesis of mega-pockmarks near the Xisha Uplift, South China Sea: Marine and Petroleum Geology, v. 28, p. 1146-1156.

Sun, Y., S. Wu, D. Dong, T. Lüdmann, and Y. Gong, 2012b, Gas hydrates associated with gas chimneys in fine-grained sediments of the northern South China Sea: Marine Geology, v. 311-314, p. 32-40.

Svenson, H., S. Planke, A. Maithe-Sørensen, B. Jamtveit, R. Myklebust, T. R. Eidem, and S. S. Rey, 2003, Release of methane from a volcanic basin as a mechanism for initial Eocene global warming: Nature, v. 429, p. 542-545.

Swarbrick, R. E., and M. J. Osborne, 1996, The nature and diversity of pressure transition zones: Petroleum Geoscience, v. 2, p. 111-116.

Swarbrick, R. E., and M. J. Osborne, 1998, Mechanisms that generate abnormal pressures: An overview: AAPG Memoir, p. 13-34.

Swarbrick, R. E., M. J. Osborne, and G. S. Yardley, 2004, Comparison of overpressure magnitude resulting from the main generating mechanisms: AAPG Memoir, p. 1-12.

Taner, M. T., Koehler, F., and Sheriff, R. E., 1979, COMPLEX SEISMIC TRACE ANALYSIS: Geophysics, v. 44, no. 6, p. 1041-1063.

Tari, G., Kohazy, R., Hannke, K., Hussein, H., Novotny, B., and Mascle, J., 2012, Examples of deep-water play types in the matruh and herodotus basins of NW Egypt: Leading Edge, v. 31, no. 7, p. 816-823.

Taylor, M. H., W. P. Dillon, and I. A. Pecher, 2000, Trapping and migration of methane associated with the gas hydrate stability zone at the Blake Ridge Diapir: New insights from seismic data: Marine Geology, v. 164, p. 79-89.

Taylor, G. K., and J. Shaw, 1989, The Falkland Islands: New palaeomagnetic data and their origin as a displaced terrane from southern Africa: Deep Structure and Past Kinematics of Accreted Terranes, v. 50, p. 59-72.

Teige, G., and C. Hermanrud, 2012, Membrane seal leakage in non-fractured caprocks by the formation of oil-wet flow paths: Fault and Top Seals: From Characterization to Modelling.

Teige, G. M. G., C. Hermanrud, W. H. Thomas, O. B. Wilson, and H. M. Nordgård Bolås, 2005, Capillary resistance and trapping of hydrocarbons: A laboratory experiment: Petroleum Geoscience, v. 11, p. 125-129.

Thomas, M. M., and J. A. Clouse, 1990, Primary migration by diffusion through kerogen: II. Hydrocarbon diffusivities in kerogen: Geochimica et Cosmochimica Acta, v. 54, p. 2781-2792.

Tingdahl, K. M., A. H. Bril, and P. F. De Groot, 2001, Improving seismic chimney detection using directional attributes: Journal of Petroleum Science and Engineering, v. 29, p. 205-211.

Tinivella, U., and M. Giustiniani, 2013, Variations in BSR depth due to gas hydrate stability versus pore pressure: Global and Planetary Change, v. 100, p. 119-128.

Vérard, C., K. Flores, and G. Stampfli, 2012, Geodynamic reconstructions of the South America-Antarctica plate system: Journal of Geodynamics, v. 53, p. 43-60.

Volynskii, A. L., T. Y. Grokhovskaya, A. Sanchez, G. M. Lukovkin, and N. F. Bakeyev, 1988, Mechanism of the migration of a low molecular weight component in the system natural rubber vulcanizate-low molecular weight hydrocarbon: Polymer Science U.S.S.R., v. 30, p. 2220-2227.

Wan, Y., Y. F. Zhang, and J. Y. Zhang, 2014, Hydrocarbon migration mechanisms of Hailar - Tamsag basin, p. 1415-1418.

Westbrook, G. K., and Smith, M. J., 1983, Long decollements and mud volcanoes: evidence from the Barbados Ridge Complex for the role of high pore-fluid pressure in the development of an accretionary complex: Geology, v. 11, no. 5, p. 279-283.

White, R. S., 1977, Seismic bright spots in the Gulf of Oman: Earth and Planetary Science Letters, v. 37, p. 29-37.

Widess, M., 1973, How thin is a bed?: Geophysics, v. 38, p. 1176-1180.

Winefield, P., R. Gilham, and R. Elsinger, 2005, Plumbing the depths of the Central Graben: Towards an integrated pressure, fluid and charge model for the Central North Sea HPHT play, Petroleum Geology Conference Proceedings, p. 1301-1315.

Wiprut, D., and Zoback, M. D., 2002, Fault reactivation, leakage potential, and hydrocarbon column heights in the northern north sea, Norwegian Petroleum Society Special Publications, Volume 11, p. 203-219.

Wood, W. T., J. F. Gettrust, N. R. Chapman, G. D. Spence, and R. D. Hyndman, 2002, Decreased stability of methane hydrates in marine sediments owing to phase-boundary roughness: Nature, v. 420, p. 656-660.

Wu, X., and T. Liu, 2009, Spectral decomposition of seismic data with reassigned smoothed pseudo Wigner-Ville distribution: Journal of Applied Geophysics, v. 68, p. 386-393.

Xie, X., J. J. Jiao, Z. Tang, and C. Zheng, 2003a, Evolution of abnormally low pressure and its implications for the hydrocarbon system in the southeast uplift zone of Songliao basin, China: AAPG Bulletin, v. 87, p. 99-119.

Xie, X., S. Li, H. He, and X. Liu, 2003b, Seismic evidence for fluid migration pathways from an overpressured system in the South China Sea: Geofluids, v. 3, p. 245-253.

Yilmaz O., 2001, Seismic data analysis: processing, inversion and interpretation of seismic data. SEG, Tulsa, Oklahoma, 2027 pp.

Yoo, D. G., N. K. Kang, B. Y. Yi, G. Y. Kim, B. J. Ryu, K. Lee, G. H. Lee, and M. Riedel, 2013, Occurrence and seismic characteristics of gas hydrate in the Ulleung Basin, east Sea: Marine and Petroleum Geology, v. 47, p. 236-247.

Yu, Z., and I. Lerche, 1995, Three-phase fluid migration with solubilities in a two-dimensional basin simulation model: Marine and Petroleum Geology, v. 12, p. 3-16.

Zabanbark, A., 2011, Geological structure and prospect of the oil and gas bearing of the Falkland Islands region: Oceanology, v. 51, p. 511-517.

Zhang, Q., and Lu, W. 2009, Spectral decomposition of seismic data with pseudo Margenau-Hill distribution, in Proceedings 71st European Association of Geoscientists and Engineers Conference and Exhibition 2009: Balancing Global Resources. Incorporating SPE EUROPEC, Volume 2, p. 798-802.

Zhou, Y., and R. Littke, 1999, Numerical simulation of the thermal maturation, oil generation and migration in the Songliao Basin, Northeastern China: Marine and Petroleum Geology, v. 16, p. 771-792.

Zoeppritz, K. (1919) On the reflection and penetration of seismic waves through unstable layers. Erdbebenwellen Viii B, (Goettinger Nachr, Ed.), p. 66-84.

Zou, C., S. Tao, X. Yuan, R. Zhu, L. Hou, L. Wang, X. Gao, and Y. Gong, 2009, The formation conditions and distribution characteristics of continuous petroleum accumulations: Shiyou Xuebao/Acta Petrolei Sinica, v. 30, p. 324-331.

Appendix A

A.1 Dataset processing flows

A.1.1 FOGL dataset

In the following tables are synthesised the acquisition parameters (Table A.1) and the processing flow (Table A.2) applied to the FOGL dataset. The processing flows have been provided by FOGL. The dataset is composed of 3 different sub-datasets:

1. Full stack
2. Near-angle stack
3. Far-angle stack

The datasets have been processed following the same processing flow of Table A.2. In order to produce the range stack datasets the CDPs have been sorted following these angle ranges: 4-22 degrees for near Near-angle stack and, 22-40 degrees for Far-angle stack

Table A.1: Acquisition parameters FOGL data

Acquisition parameters
Recorded by Wavefield
Vessel M.V. Bergen Surveyor
Source Air Guns
Volume 2425 cu in
Source Depth 7m
Offset 100m
Streamer Length 6000m
No of Groups and Group Interval 480 x 12.5m
Total No of Channels 480 (+12 aux.)
Streamer Depth 8m
Shot point Interval 25m
Nominal Fold of Cover 120
Recording Format SEG D
Sample Rate 2ms

Low Cut Filter 4.6 Hz, 6 dB/octave
High Cut Filter 206 Hz, 276 dB/Octave
Record Length 8 seconds
Date Spring 2007

Table A.2: Processing flow FOGL data

Processing Flow
Transaction From SEGD Field Tapes
System Delay Correction -164ms
Signature Deconvolution From supplied far field signature. Output to minimum phase.
Amplitude Compensation T-Squared
Filter 3Hz low cut
Resample From 2 to 4ms with 90Hz anti-alias filter
Noise Attenuation Swell noise attenuation
Surface Related Multiple Elimination (SRME)
Trace Bination From 480 at 12.5m to 240 traces at 25m using spatial anti-alias filter and trace drop
CDP Gather 120 fold from 25m shot, 12.5m groups
Navigation Merge Merge of navigation onto seismic data
Velocity Analysis “MGIVA” located at 2km intervals
NMO 4^{th} order
Demultiple Via parabolic radon transformation using 401p traces between -500 and 3500 m/s. Mute in Tau-p space derived from initial velocity analysis revised by -10% at wb + 2s; -15% at wb + 5s, -20% at 8s. Shot interpolation performed prior to demultiple and interpolated traces dropped after.
Reverse NMO
Pre-stack Time Migration (PSTM) Full Kirchhoff PSTM for velocity analysis using all offset planes
Velocity Analysis “MGIVA” PSTM analysis located at 1.0km intervals
Scaling T-squared from 4 above backed out. Replaced with TV^2
Noise Attenuation FX deconvolution on common offset planes. Over 50 traces, 5 trace operators
Pre-stack Time Migration Final full Kirchhoff PSTM using velocities from 17

above. 4km aperture, 90% NMO stretch mute with anti-alias protection.

Demultiple Via parabolic radon transformation using 401p traces between -500 and 3500 m/s. Mute in Tau-p space derived from initial velocity analysis revised by -10% at wb + 2s; -15% at wb + 5s; -20% at 8s

NMO Application Velocities derived from final PSTM analysis located at 1.0km intervals

Noise Attenuation (option) Random Noise Attenuation (Ranna). The method is based on the Forward-Backward Linear prediction (FBLP) theory of (Tufts and Kamaresan, 1982). Filter length 9, 60 trace block size; 1-% white noise.

Far Trace Mute Time and space varied. Length of taper 120ms. Near trace wb – 500ms, far trace 6500ms

Inner Trace Mute Time and space varied. Length of taper 120ms. Application time, near trace wb x 1.5; offset 1628m 5000 to 6000ms dependent upon water bottom times

Stack 120 fold with 1/N mute compensation

Datum Correction Static correction for shot and cable depth to mean sea level +8ms

Phase Rotation 180° (+RC trough, European)

Scaling 4dB/s from water bottom to water bottom plus 2s

BANDPASS FILTER

SLOPE (DB/OCT)	**FILTER (HZ)**	**SLOPE (DB/OCT)**	**TIME (MS)**
18	10-80	36	WB
18	10-60	36	WB + 1000 MS
18	10-50	36	WB + 2000 MS
18	5-30	36	WB + 3000 MS

Equalisation AGC 1.0s windows. Dual window AGC. Windows of 750 ms and 250 ms, 60%.

A.1.2 GSI dataset

In the following tables (Table A.3 and A.4.1-4) are synthesised SEG-Y header and processing flow applied to the GSI dataset. The information listed below has been extracted from the SEG-Y header of the seismic lines. For this reason only a limited description for acquisition and processing flow is available. The dataset is composed of 4 different sub-datasets:

1. Enhanced Anisotropic Time Migration
2. Raw TimeMigration
3. Near-angle stack
4. Far-angle stack

The 4 different processing flows are listed from Table A.4.1 to A.4.4

Table A.3: GSI SEG-Y information

SEG-Y
SEG-Y data format IBM real
Unit meter
Data type 2D seismic section in time
Acquisition date 2005, 2006
Units milliseconds
Projection Falkland Customised Zone 20S
Spheroid WGS 84
CDP interval 6.25m
Length 8.0s
Sample Rate 4ms
Samples 2001
Polarity +RC peak (American)
Phase zero

Table A.4.1: Enhanced Anisotropic Time Migration processing flow GSI data

Processing Flow
Navigation merge Merge of navigation onto seismic data
Debubble
Designature
Shot domain denoise
Surface Related Multiple Elimination (SRME)
Linear noise removal
CDP domain denoise
High Resolution Radon Transform
CDP domain denoise
Shot/channel Amp
Time-variant Filter
Velocity model building
Eta Calculation Anisotropic factor
Anisotropic time migration
Residual NMO/Eta
Inside trace mute
STACK
F-K Filter
F-X deconvolution
Time-variant Filter
Wrap Scaling
Source-Cable-Line tie static correction

Table A.4.2: Raw Time Migration processing flow GSI data

Processing Flow
Navigation merge Merge of navigation onto seismic data
Debubble
Designature
Shot domain denoise
Surface Related Multiple Elimination (SRME)
Linear noise removal
CDP domain denoise

High Resolution Radon Transform
CDP domain denoise
Shot/channel Amp
Time-variant Filter
Velocity model building
Eta Calculation Anisotropic factor
Anisotropic time migration
Residual NMO/Eta
Radon Transform
Inside trace mute
STACK
Source-Cable-Line tie static correction

Table A.4.3: Near-angle stack processing flow GSI data

Processing Flow
Navigation merge Merge of navigation onto seismic data
Debubble
Designature
Shot domain denoise
Surface Related Multiple Elimination (SRME)
Linear noise removal
CDP domain denoise
High Resolution Radon Transform
CDP domain denoise
Shot/channel Amp
Time-variant Filter
Velocity model building
Eta Calculation Anisotropic factor
Anisotropic time migration
Residual NMO/Eta
Angle STACK 5-20 Degrees

Table A.4.4: Far-angle stack processing flow GSI data

Processing Flow
Navigation merge Merge of navigation onto seismic data
Debubble
Designature
Shot domain denoise
Surface Related Multiple Elimination (SRME)
Linear noise removal
CDP domain denoise
High Resolution Radon Transform
CDP domain denoise
Shot/channel Amp
Time-variant Filter
Velocity model building
Eta Calculation Anisotropic factor
Anisotropic time migration
Residual NMO/Eta
Angle STACK 25-40 Degrees

A.2 Reports and Presentations

A.2.1 FOGL reports and presentation

In this section are present a number of reports and presentations of public domain published by FOGL (http://www.fogl.com/fogl/en/home) and used in the thesis.

Loligo (42/07-01) Well Results - Gas Discovery

(http://www.fogl.com/fogl/templates/fogl/modules/regulatorynews_item.jsp?ric=FOGL.L.TK&ref=62597)

RNS Number : 3639M
Falkland Oil and Gas Limited
17 September 2012

17 September 2012

Falkland Oil and Gas plc

("FOGL" or "the Company")

Loligo (42/07-01) Well Results - Gas Discovery

FOGL, the oil and gas exploration company focused on its extensive licence areas to the South and east of the Falkland Islands, is pleased to announce that the Loligo exploration well is a gas discovery.

The Loligo well has proven a working hydrocarbon system in the northern part of the east Falkland basin. The results also demonstrate that Loligo is a viable stratigraphic trap. It is clear from the initial well results that the main hydrocarbon phase within the T1 to T5 aged reservoir objectives is gas, but it has not been possible to determine whether this gas has any liquid content.

Well 42/07-01 has been drilled to a depth of 4,043 metres. FOGL is the operator of the well, holding a 75% interest; its joint venture partner Edison International Spa ("Edison"), holds the remaining 25% interest. The well penetrated six Tertiary aged reservoir objectives on prognosis. These comprise the T1, T1 deep, T2 (Trigg), T2 deep (Trigg deep), T3 (Three Bears) and T5 targets. These objectives had all been identified on the basis of their seismic amplitude responses. Very strong gas shows (C1 to C5) were encountered whilst drilling through each of these horizons. Analysis of the wireline log data indicates that all six targets comprise fine grained

sandstones, siltstones and claystones. FOGL interprets that these sediments have been deposited either outside, or at the distal (outer) end of the slope channel system.

Gas bearing zones were encountered over a 1,300 metre vertical interval from 2,420 to 3,720 metres. Petrophysical analysis of the T1 to T3 intervals inclusive (2,420 to 2,885 metres) indicates porosities ranging from 18% to 35% in the gas bearing zones. Due to the thin bedded nature of these sediments it is difficult to assess precisely both hydrocarbon saturation and the total net hydrocarbon bearing reservoir. Preliminary estimates however, suggest hydrocarbon saturations ranging from 40% to 60% and net hydrocarbon bearing reservoir of between 10 and 20 metres.

Within the T5 target two main hydrocarbon bearing zones were encountered (3,462 to 3,558 metres and 3,608 to 3,705 metres). The net hydrocarbon bearing reservoir in these two zones was 46 and 59 metres respectively. Porosities ranged between 23% and 30%, averaging 24% and hydrocarbon saturations between 40% and 75%.

Attempts were made to obtain pressure data and collect fluid samples. This was unsuccessful, probably due to the fine grained nature of sediments in the gas bearing zone and also, not having access to the specialised test equipment appropriate for this type of formation.

Further detailed evaluation of all the well data, together with the existing seismic is now required in order to better define reservoir distribution and more precisely map the channel systems. Determining the reservoir potential of the thin bedded sandstones and siltstones using detailed petrophysical evaluation will be undertaken once the sidewall core samples have been analysed back in the UK. These studies will facilitate a better assessment of resource potential and also help define the work that will be required to further appraise this discovery over what is a large complex. The area of the previously mapped amplitude response at the target horizons range from approximately 250 square kilometres at T2 to over 600 square kilometres at T1. The T5 hydrocarbon zones were better than expected based on pre-drill estimates, but more work will now be required to define their areal extent.

FOGL now intends to plug and abandon the well, which is expected to take approximately 10 days. FOGL and Edison believe that it would be premature to drill a second well on Loligo at the current approved location (Loligo north-west) before having undertaken detailed analysis of the current well results. Accordingly the decision has been taken that the next well will be on the Scotia prospect in the Mid Cretaceous fan play. On the basis that Scotia is also drilled within budget, it is estimated that the Company's cash balance post the 2012 exploration campaign will not be less than US$200m. A further announcement will be made when the Scotia well is spudded.

Tim Bushell, Chief Executive of FOGL said:

"The initial results of the Loligo well are encouraging. They have demonstrated that hydrocarbons have migrated into the Tertiary Channel Play. It is also clear that

Loligo is a valid trap that contains multiple gas bearing zones, with over 100 metres of hydrocarbon bearing reservoir. We now need to focus on reservoir distribution within Loligo in order to find the sweet spots. A work programme will be undertaken to achieve this, assess the resource potential and commercial viability of this discovery.

"We now have a positive result from one of our major exploration prospects. This, together with the results from our next well, will help determine the priorities for our future exploration efforts. With our partners Noble Energy and Edison, we have the technical resources and funding in place to carry out substantial 3D surveys, followed by further drillingin 2014."

Enquiries:

Falkland Oil and Gas
+44 (0) 207 563 1260
Tim Bushell, Chief Executive
Oriel (Nominated Advisor and Joint Broker)
+44 (0) 207 710 7600
David Arch / Gareth Price / Ashton Clanfield
Jefferies Hoare Govett (Joint Broker)
+44 (0) 207 029 8000
Alex Grant / Chris Zeal / Graham Hertrich
FTI Consulting
+44 (0) 207 831 3113
Ben Brewerton / Ed westropp

The technical information included in this announcement has been reviewed, verified and compiled by the Company's geological staff, including a qualified person, Colin More BSc., MSc. (Exploration Director), who has over 26 years of experience in petroleum exploration, for the purpose of the Guidance Note for Mining, Oil and Gas Companies issued by the London Stock Exchange in respect of AIM companies, which outline standards of disclosure for mineral projects. Mr. More is a member of the Geological Society of London, the American Association of Petroleum Geologists and the Society of Exploration Geophysicists.

ENDMSCDGGDCDUBBGDL

AGM presentation 9 June 2011

(http://www.fogl.com/fogl/uploads/companypresentations/AGMpresentation2011website.pdf - slides 3 and 4)

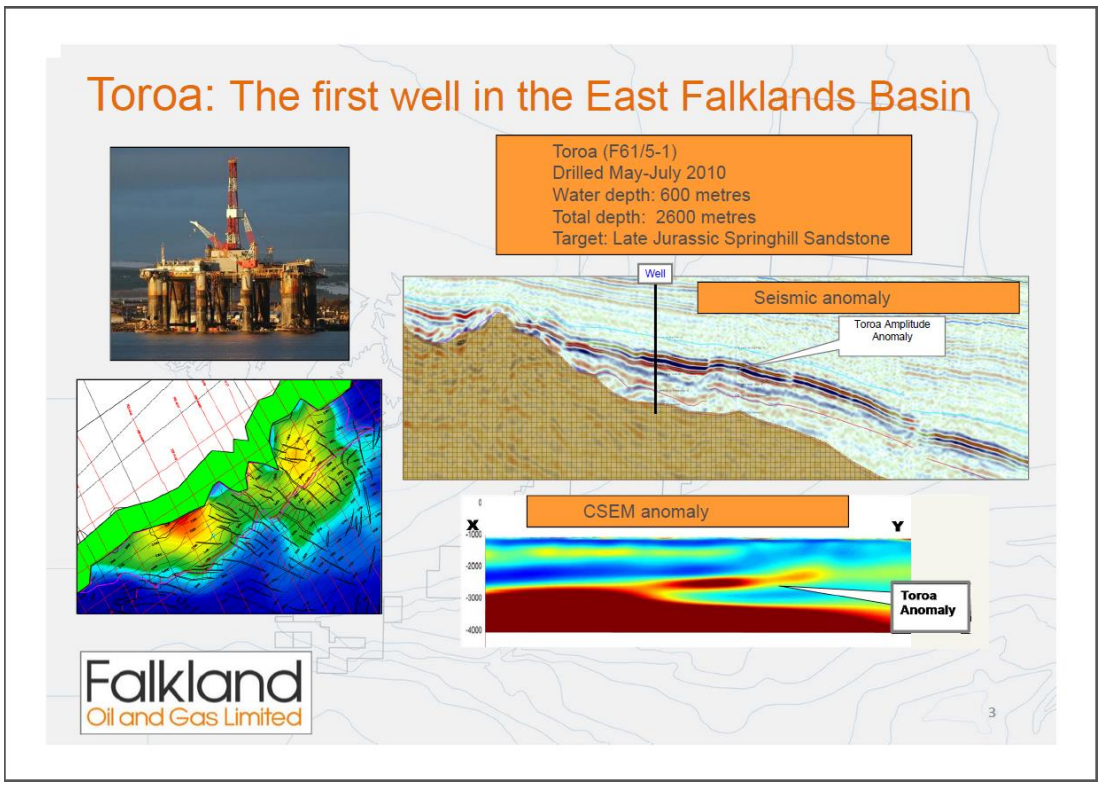

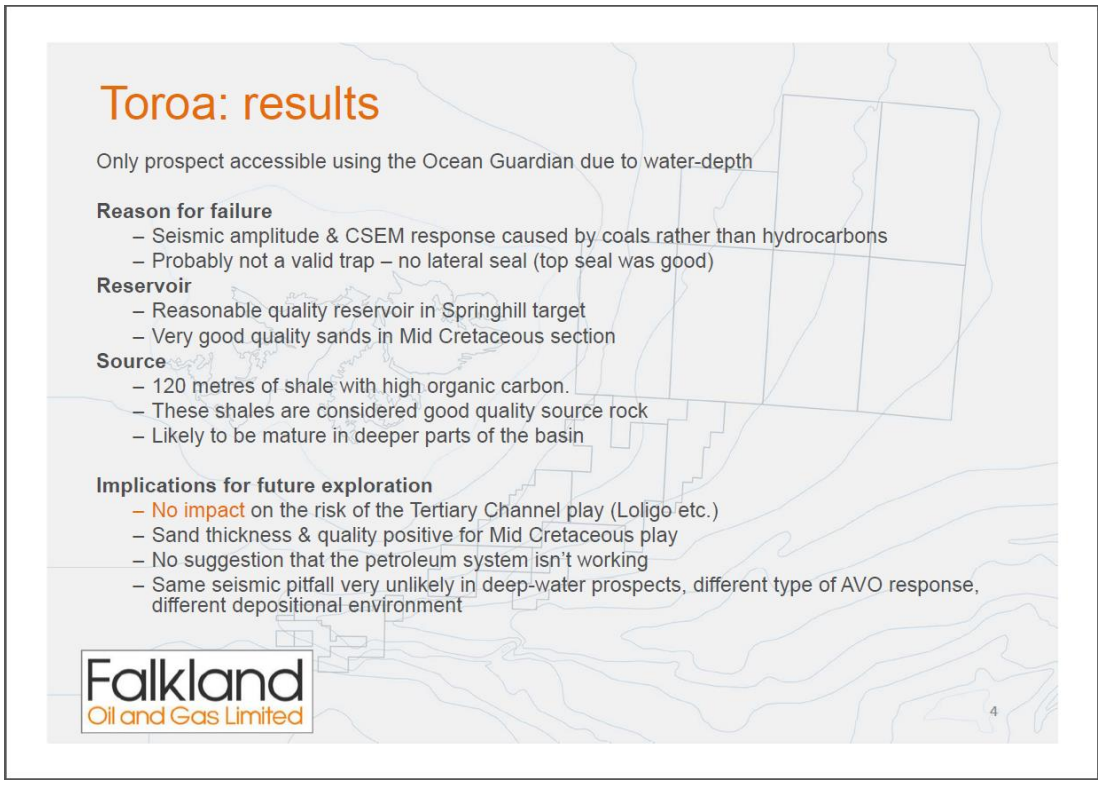

A.2.2 Border and Southern reports and presentation

In this section are present a number of reports and presentations of public domain published by Border and Southern (http://www.bordersandsouthern.com/) and used in the thesis.

61/17-1 (Darwin east) Well Result

(http://www.bordersandsouthern.com/news/rns_viewer.php?id=20044683)

RNS Number : 8142B
Borders & Southern Petroleum plc
23 April 2012

23 April 2012

Borders & Southern Petroleum plc

("Borders & Southern" or "the Company")

61/17-1 (Darwin east) Well Results

Borders & Southern (AIM: BOR) is pleased to announce a significant gas condensate discovery.

Well 61/17-1 was drilled to a total depth of 4876m and came in very close to prognosis. As predicted, the strong AVO anomaly represented a porous sandstone reservoir containing hydrocarbons.

Whilst drilling, the well encountered good hydrocarbon shows from 4633m down to 4810m. The main reservoir interval, comprising good quality massive sandstone, was found to be 84.5m thick with net pay of 67.8m. Average porosity for this interval is 22%, with maximum values reaching 30%.

Fluid samples from the reservoir have been recovered and will be brought back to the UK for analysis. Once the lab analysis is complete and the results integrated with other data collected from the well, the Company will be able to comment on the liquid content of the reservoir.

It is too early to give an accurate resource estimate, but this large simple structure, with a seismic amplitude anomaly measuring 26 square kilometres, is likely to contain significant volumes.

The well has successfully proven a working source rock, good quality reservoir and competent seals in the South Falkland Basin. The Company has an extensive prospect inventory to exploit this success.

The Company now intends to complete wireline logging operations, plug and abandon the well in line with regulatory requirements and move to the Stebbing prospect, the second well in the current drilling programme. An announcement will be made once this well has spudded.

Chief Executive, Howard Obee, commented:

"We're delighted to have made a discovery with the Company's first exploration well and to have opened up a new hydrocarbon basin. There is clearly a lot of work ahead of us to understand the size and value of the discovery, but it is a great start and the potential of the basin is exciting. I'd like to thank all the many people that have contributed to this project for their fantastic efforts."

For further information please visit www.bordersandsouthern.com or contact:

Howard Obee, Chief Executive
Borders & Southern Petroleum plc
Tel: 020 7661 9348
Katherine Roe / Brett Jacobs
Panmure Gordon (UK) Limited
Tel: 020 7459 3600
Simon Hudson / Paul Youens
Tavistock Communications
Tel: 020 7920 3150

Notes:

Borders & Southern Petroleum plc is an oil & gas exploration company listed on the London Stock Exchange AIM (BOR). The Company operates and has a 100% interest in five Production Licences in the South Falkland Basin covering an area of nearly 20,000 square kilometres. The Company has acquired 2,862 km of 2D seismic, 1,492 square kilometres of 3D seismic and drilled one exploration well. This statement has been reviewed, verified and approved by Dr Howard Obee, (a petroleum geologist with 25 years relevant experience, Fellow of the Geological Society and member of the American Association of Petroleum Geologists and the Petroleum Exploration Society of Great Britain), in accordance with the Guidance Note for Mining, Oil and Gas Companies issued by the London Stock Exchange in respect of AIM companies.

-ends-

END

MSCBKBDKOBKDKQB

Darwin Fluid Analysis

(http://www.bordersandsouthern.com/news/rns_viewer.php?id=20315808)

RNS Number : 6716K
Borders & Southern Petroleum plc
23 August 2012

23 August 2012

Borders & Southern Petroleum plc

("Borders & Southern" or "the Company")

Darwin Fluid Analysis

Borders & Southern (AIM: BOR) is pleased to announce the results of the Darwin fluid sample analysis. As previously reported, well 61/17-1 encountered a good quality sandstone reservoir comprising 67.8m of net pay with an average porosity of 22%. The gas condensate reservoir was sampled at four separate levels with 3 fluid samples taken at each level.

The initial condensate yield from the Darwin gas samples, as measured in a laboratory separator test, varies from 123 to 140 stb/MMscf. The API gravity of the condensate is 46 to 49 degrees. Based on the condensate yield and ongoing reservoir modelling, the Company estimates the recoverable volume of condensate to be 130 to 250 million barrels with a mid case of 190 million barrels.

Following these positive laboratory results, the Board will approve a work programme that includes appraisal drilling of the Darwin discovery. Additional wells are necessary to confirm the initial resource estimates and establish a commercial development. In the coming months, activity will focus on a comprehensive technical evaluation of all the data collected from well 61/17-1 and a review of potential development concepts along with project economics.

These results have exciting implications for the Company's prospect and lead inventory and particularly for those prospects in the Lower Cretaceous play fairway to the south of the Falkland Islands. Borders & Southern's prospect inventory contains further relatively low risk structural prospects of a similar size to Darwin along with stratigraphically trapped fans of slightly higher risk but larger scale. Some of these prospects will be targeted in the next drilling phase with the objective of adding to the discovered resources of Darwin and building a core development area.

Discussions with a seismic contractor regarding the acquisition of additional 3D seismic are in progress and we plan to have a vessel in the Falklands at the start of 2013 to commence the survey. This survey will focus on similar prospects to Darwin currently outside our existing 3D area. Whilst the final costs of the 2012 drilling programme will not be fully known until after the demobilisation of the rig later in the year, the Company can state that it is fully funded for the 3D seismic acquisition and processing, the reprocessing of the Company's 2007 3D seismic data and all the technical studies that need to be undertaken on the samples collected from the two wells.

Given the encouraging results from the Darwin well, the Company will start planning the next drilling programme, which is likely to include both exploration and appraisal wells. The timing of drilling will be dependent on rig availability, but realistically this will not occur before 2014. The Company is currently exploring the best way to fund the next phase of the programme, including the possibility of now bringing in partners.

For further information please visit www.bordersandsouthern.com or contact:

Howard Obee, Chief Executive
Borders & Southern Petroleum plc
Tel: 020 7661 9348
Katherine Roe
Panmure Gordon (UK) Limited
Tel: 020 7459 3600
Simon Hudson / Kelsey Traynor
Tavistock Communications
Tel: 020 7920 3150

Notes:

Borders & Southern Petroleum plc is an oil & gas exploration company listed on the London Stock Exchange AIM (BOR). The Company operates and has a 100% interest in five Production Licences in the South Falkland Basin covering an area of nearly 20,000 square kilometres. The Company has acquired 2,862 km of 2D seismic, 1,492 square kilometres of 3D seismic and drilled two exploration wells. This statement has been reviewed, verified and approved by Dr Howard Obee, (a petroleum geologist with 25 years relevant experience, Fellow of the Geological Society and member of the American Association of Petroleum Geologists and the

Petroleum Exploration Society of Great Britain), in accordance with the Guidance Note for Mining, Oil and Gas Companies issued by the London Stock Exchange in respect of AIM companies.

-ends-

This information is provided by RNS
The company news service from the London Stock Exchange

END

MSCEAAPDAESAEFF

Investor presentation January 2013

(http://www.bordersandsouthern.com/media/pdf/Investor%20Presentation%20January%202013.pdf – slide 6)

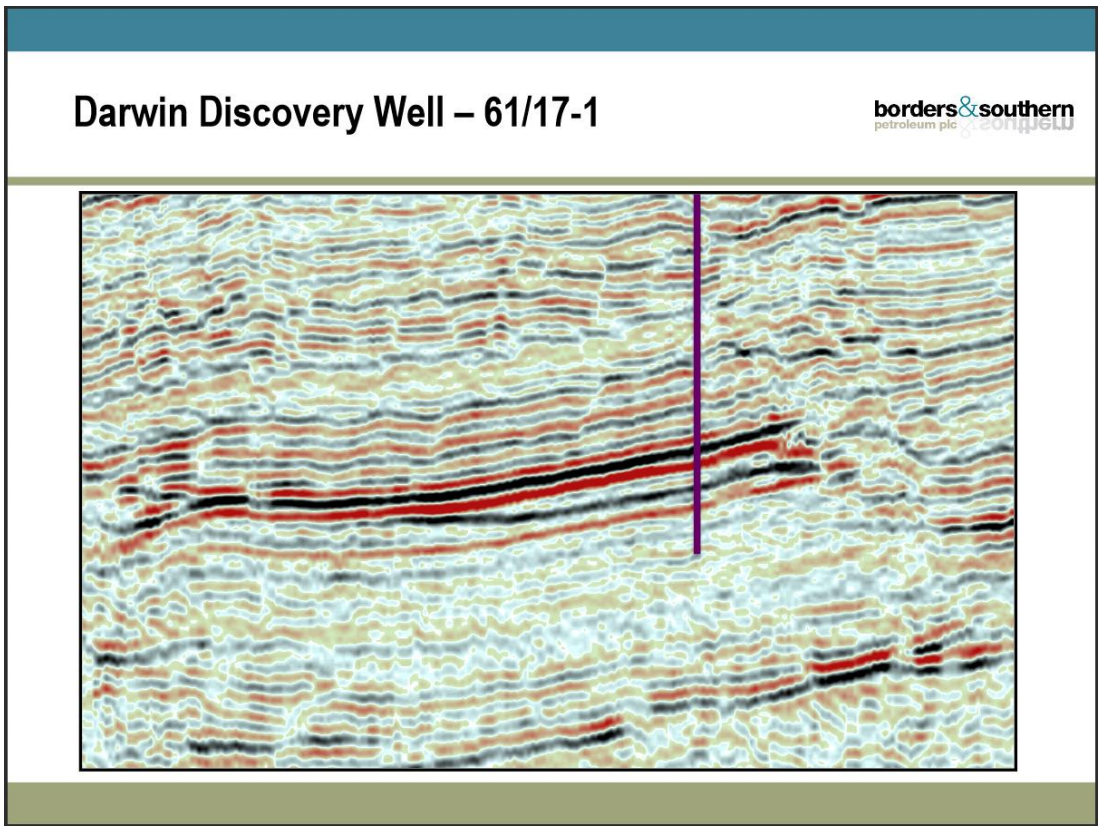

Environmental Impact Statement Offshore Falkland Islands Exploration Drilling

(http://www.epd.gov.fk/wp-content/uploads/B&S%20Falklands%20EIS.pdf – page 281)